# Numerical Analysis of Radio-Frequency Sheath-Plasma Interactions in the Ion Cyclotron Range of Frequencies

by

Haruhiko Kohno

Submitted to the Department of Nuclear Science and Engineering
in partial fulfillment of the requirements for the degree of

Doctor of Science in Applied Plasma Physics

at the

MASSACHUSETTS INSTITUTE OF TECHNOLOGY

June 2011

Author . . . . . . . . . . . . . . . . . . . . . . . . . . . . . . . . . . . . . . . . . . . . . . . . . . . . . . . . . . . .
Department of Nuclear Science and Engineering
May 9, 2011

Certified by. . . . . . . . . . . . . . . . . . . . . . . . . . . . . . . . . . . . . . . . . . . . . . . . . . . . . . .
Jeffrey P. Freidberg
Professor, Department of Nuclear Science and Engineering
Thesis Supervisor

Certified by. . . . . . . . . . . . . . . . . . . . . . . . . . . . . . . . . . . . . . . . . . . . . . . . . . . . . . .
Paul T. Bonoli
Senior Research Scientist, MIT Plasma Science and Fusion Center
Thesis Reader

Certified by. . . . . . . . . . . . . . . . . . . . . . . . . . . . . . . . . . . . . . . . . . . . . . . . . . . . . . .
John C. Wright
Research Scientist, MIT Plasma Science and Fusion Center
Thesis Reader

Accepted by . . . . . . . . . . . . . . . . . . . . . . . . . . . . . . . . . . . . . . . . . . . . . . . . . . . . . . .
Mujid S. Kazimi
Chair, Department Committee on Graduate Students

# Numerical Analysis of Radio-Frequency Sheath-Plasma Interactions in the Ion Cyclotron Range of Frequencies

by

Haruhiko Kohno


Submitted to the Department of Nuclear Science and Engineering
on May 9, 2011, in partial fulfillment of the
requirements for the degree of
Doctor of Science in Applied Plasma Physics

## Abstract

Electromagnetic plasma waves in the ion cyclotron range of frequencies (ICRF) are routinely used in magnetic fusion experiments to heat plasmas and drive currents. However, many experiments have revealed that wave energy losses in the plasma edge and at the wall are significant, and detected that the acceleration of ions into the walls due to the formation of radio-frequency (RF) sheaths is one of the root causes of this problem. Since the RF-enhanced sheaths have many undesirable effects, such as impurity production and hot spot generation, a predictive numerical tool is required to quantitatively evaluate these effects with complicated boundary shapes of tokamaks taken into account.

In this thesis the numerical code that solves self-consistent RF sheath-plasma interactions in the scrape-off layer for ICRF heating is developed based on a nonlinear finite element technique and is applied to various problems in the one-dimensional (1D) and two-dimensional (2D) domains corresponding to simplified models for the poloidal plane of a tokamak. The present code solves for plasma waves based on the cold plasma model subject to the sheath boundary condition, in which the most important physics that happens in the sheath is captured without using the field quantities in the sheath.

Using the developed finite element code, several new properties of the RF sheath-plasma interactions are discovered. First, it is found in the 1D domain that multiple roots can be present due to the resonance of the propagating slow wave and its nonlinear interaction with the sheath. Second, sheath-plasma waves are identified in a 2D slab geometry, and it is proved in conjunction with an electrostatic 2D sheath mode analysis that the sheath-plasma wave only appears in the vicinity of the sheath surface if the plasma density is greater than the lower hybrid density, and its wavelength depends on various parameters. Third, as a consequence of the self-consistent interaction between the propagating slow wave and the sheath, it is shown

that the electric field distribution pattern in the plasma smoothly varies along the magnetic field lines between the conducting-wall and quasi-insulating limits.

In the numerical analysis employing the 2D domain whose scale is equivalent to the Alcator C-Mod device, it is demonstrated that the calculated sheath potential can reach the order of kV, which is sufficient to yield enhanced sputtering at the wall. In addition, it is shown that the sheath potential in the close vicinity of the antenna current strap can be insensitive to the direction of the background magnetic field in the RF sheath dominated regime. Further, it is found from a series of nonlinear calculations that the sheath potential sensitively varies depending on the plasma density and electron temperature, which is consistent with the scaling derived from the Child-Langmuir law and the definition of the RF sheath potential.

Lastly, a new finite element approach, which is named the finite element wavepacket method, is developed for the purpose of solving for multiscale plasma waves in the tokamak poloidal plane accurately with reasonable computational cost. This method is established by combining the advantages of the finite element and spectral methods, so that important properties in the finite element method, such as the sparsity of the global matrix and the ease in satisfying the boundary conditions, are retained. The present scheme is applied to some illustrative 1D multiscale problems, and its accuracy improvement is demonstrated through comparisons with the conventional finite element method.

Thesis Supervisor: Jeffrey P. Freidberg
Title: Professor, Department of Nuclear Science and Engineering

Thesis Reader: Paul T. Bonoli
Title: Senior Research Scientist, MIT Plasma Science and Fusion Center

Thesis Reader: John C. Wright
Title: Research Scientist, MIT Plasma Science and Fusion Center

# Thesis Errata Sheet

**Author** Haruhiko Kohno

**Primary Dept.** Nuclear Science and Engineering

**Degree** Doctor of Science    **Graduation date** Jun 2011

## Thesis title

Numerical Analysis of Radio-Frequency Sheath-Plasma Interactions

in the Ion Cyclotron Range of Frequencies

## Brief description of errata sheet

The errata sheet contains a couple of major errors that have been discovered in my

thesis. Although they do not affect the conclusions, they should be pointed out here for

~~the sake of correctness of the thesis.~~

**Number of pages** _2_ (11 maximum, including this page)

▶ **Author**: I request that the attached errata sheet be added to my thesis. I have attached two copies prepared as prescribed by the current *Specifications for Thesis Preparation*.

Signature of author ___Signature Redacted___ Date _7/25/2011_

▶ **Thesis Supervisor** or **Dept. Chair**: I approve the attached errata sheet and recommend its addition to the student's thesis.

Signature ___Signature Redacted___ Date _7/26/11_

Name ___Jeffrey Freidberg___  ☑ Thesis supervisor ☐ Dept. Chair

▶ **Dean for Graduate Education**: I approve the attached errata sheet and direct the Institute Archives to insert it into all copies of the student's thesis held by the MIT Libraries, both print and electronic.

Signature ___Signature Redacted___ Date _07/28/11_

Name ___CHRISTINE ORTIZ___

# Errata Sheet

**This errata sheet contains corrections of errors in the doctoral thesis.**

**Page 18**

16 lines down from the top of the page: The numerator should be $\left(b_{\mathrm{n}}\varepsilon_{\parallel}E_{\parallel}\right)^4$ because $\varepsilon_{\parallel}$ depends on plasma density. Therefore, replace the evaluation of $V_0$ with $V_0 \sim \left(b_{\mathrm{n}}\varepsilon_{\parallel}E_{\parallel}\right)^4 / \left(n_{\mathrm{e}0}^2 T_{\mathrm{e}}\right)$.

**Page 50**

Equation (2.97): $dn$ should be replaced with $dv$.

**Pages 66, 67, 69, and 70**

Equations (3.25), (3.26), (3.33), (3.39), and (3.43): $N_i^{\mathrm{S}}$ should be replaced with $\tilde{N}_i^{\mathrm{S}}$.

**Pages 67, 68, 69, and 180**

Equations (3.31), (3.32), (3.35), (3.41), and (B.3): $\left[N_i^{\mathrm{S}}\tilde{N}_j^{\mathrm{S}}\tilde{N}_k^{\mathrm{S}}\right]$ should be replaced with $\left[N_i^{\mathrm{S}}\check{N}_j^{\mathrm{S}}\check{N}_k^{\mathrm{S}}\right]$ in order not to be confused with the definition of $\tilde{N}_i^{\mathrm{S}}$ in Equation (3.21).

**Page 130**

Equation (4.17): Insert $\varepsilon_{\parallel}$ into the numerator, i.e.,

$$V_0 \sim C_{\mathrm{sh}} V_{\mathrm{sh}} \sim \mathcal{C}\frac{\left(b_{\mathrm{n}}\varepsilon_{\parallel}E_{\parallel}\right)^4}{n_{\mathrm{e}0}^2 T_{\mathrm{e}}}$$

**Page 137**

Insert the following sentences at the end of the second sentence: "Note that although $\varepsilon_{\parallel}$ depends on plasma density, $\varepsilon_{\parallel}E_{\parallel}$ remains approximately constant when plasma density is varied at fixed antenna current, because the parallel component of Equation (2.10) implies that $J_{\mathrm{ext}\parallel} \sim \varepsilon_{\parallel}E_{\parallel}$. Therefore, the rectified sheath potential $V_0$ can be evaluated as $V_0 \sim \left(n_{\mathrm{e}0}^2 T_{\mathrm{e}}\right)^{-1}$."

**Page 180**

Add the following sentence to make the definition of the coefficients $A_l^{\mathrm{e}(m)}$ and $B_l^{\mathrm{e}(m)}$ more clear: "The coefficients $A_l^{\mathrm{e}(m)}$ and ... the element e($m$), and their values are zero at the other grid nodes."

# Acknowledgments

This thesis work could not have happened without the support of a number of people.

First of all, I would like to thank the staff and graduate students in the PSFC at MIT for their collaboration and cooperation. I am deeply grateful to Paul Bonoli, my thesis reader, for his all thoughtful support, not only relating to research, but also for various affairs which cannot be mentioned in a word. He has been kind enough to entirely read this thesis and provide me with valuable feedback. My deepest appreciation also goes to John Wright, my thesis reader, for his great support in running the rfSOL code on Loki and NERSC. I would never have been able to conduct high performance simulation without his deep knowledge of the computer field. I am indebted to Jeff Freidberg, my thesis supervisor, for giving me a thorough education on plasma physics and valuable comments on my research. It has become a cherished memory that Jeff Freidberg generously organized a group study for preparation of the qualifying exams. I cordially would like to express my gratitude to Ron Parker for the time that he spent answering my many questions when I took his courses. His lecture notes of plasma physics and electrodynamics will serve as a valuable reference for many years to come. Special thanks to Antoine Julien Cerfon and Roark Marsh for tutoring me in the basics of plasma physics as teaching assistants. Their assistance was indeed invaluable when I struggled to understand the material in the plasma physics course.

Soon after I passed the qualifying exams, my research was directed to the simulation of RF sheath-plasma interactions. My heartfelt appreciation goes to Jim Myra and Dan D'Ippolito at Lodestar Research Corporation whose teaching, comments, and suggestions about RF sheath physics were inestimable value for my study. They were always kind enough to answer many of my trivial questions in detail by e-mail, and in particular, it was a great experience for me to visit them in Boulder and have intensive discussions with them. I am very honored that I could have an opportunity to collaborate with them in the course of my doctoral research, and it is surely my

# Contents

# List of Figures

viii

# Chapter 1

# Introduction

## 1.1 Sustainable Energy

Achieving sustainable energy is a monumental challenge. To paraphrase the definition in Reference [1], sustainable energy means achieving "a living harmony between the equitable availability of energy services to all people and the preservation of the earth for future generation." Let us first think about "the equitable availability of energy services to all people." In 2009 the world primary energy consumption was 11 billion tonnes of oil equivalent [2]. Suppose all the people in the world consume the primary energy at the same rate as for the US citizens. Then the energy required is more than 50 billion tonnes of oil equivalent, i.e., approximately five times larger than the current level. For a goal of energy sustainability we have to generate this huge amount of energy for many centuries to come stably in an evenly-distributed manner without being affected by any political uncertainties. In addition, for "the preservation of the earth for future generation," the energy resources should not yield any harmful substance to the environment and world peace.

Although sustainable energy should be pursued with multiple means of energy production, we still need a "key player" to satisfy the above-mentioned tremendous energy demand. In the next section several candidates will be examined to answer

1

the question which option could play a major role for this purpose.

## 1.2 Practical Solutions to the Energy Problem

### 1.2.1 Possible Primary Source of Energy after 100 Years

The world energy consumption is steadily increasing. For example, some estimates indicate that the total primary energy in the USA may rise up to 150 quads annually after 100 years [3]. If this did happen, which of the existing energy options can be a primary source that supports the expected massive energy consumption after a century?

This question can be answered by examining the energy use trends and each of the energy options. Figure 1-1 shows the variations of the US energy production by major source for the last 50 years [1] and a prediction for the coming 100 years. We notice that for the last 20 years coal, natural gas, and nuclear electric power are increasing on the whole, while crude oil is rapidly decreasing, and renewable energy sources are kept at a lower level. Some environmentalists insist that the increasing energy needs should be met only by renewable energy sources. This might appear to be an ideal solution since using renewable energy is surely the most environmentally-friendly way for the preservation of the earth. However, to achieve this goal, the use of renewable energy must be "exponentially" increased in this century, which is clearly an impossibility due to limitations on land, high costs of power generation, and the intrinsic downsides of each renewable option (see Chapter 1 of Reference [4] for detailed description). Among them, low competitiveness in costs would be a crucial issue. For example, currently the construction of the photovoltaic facility costs 20 times as much as that of a nuclear power plant for the same amount of energy production, and of course this affects the price of electricity. There is no reason to abandon much cheaper energy options from an economic point of view, so that renewable energy should not be a primary source of energy (or electricity) even

By Major Source, 1949-2006
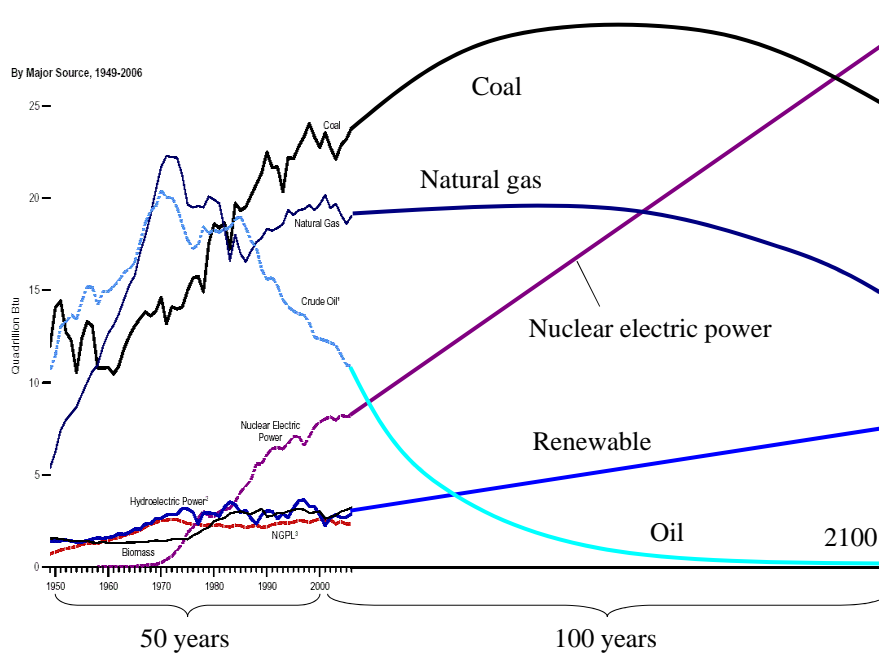
Figure 1-1: US energy production by major source during 1949–2006 and a prediction for the coming 100 years. Source EIA (2006).

after 100 years.

Next, consider crude oil. As we know, oil is one of the most useful (and thus the most consumed) fuels in the world. However, for example, according to a prediction shown in Figure 1-2, it is highly possible that crude oil will be virtually depleted sometime in the present century. This would not be hard to believe considering the steady growth in worldwide population and energy consumption [3]. Due to this problem of scarcity, and according to the recent trend in energy production, we could conclude that oil will not be a primary source of energy in the far future.

Despite the recent overall increase in energy production, natural gas would also be destined to follow the same trend as oil due to the problem of scarcity, since the current natural gas reserves are estimated to be exhausted after less than 100 years at the present rate of usage [4]. Also, contributions to the greenhouse effect will be considered more seriously in the future, which may curb the use of this fossil fuel.

Coal has been taking on an important role in electricity production; more than
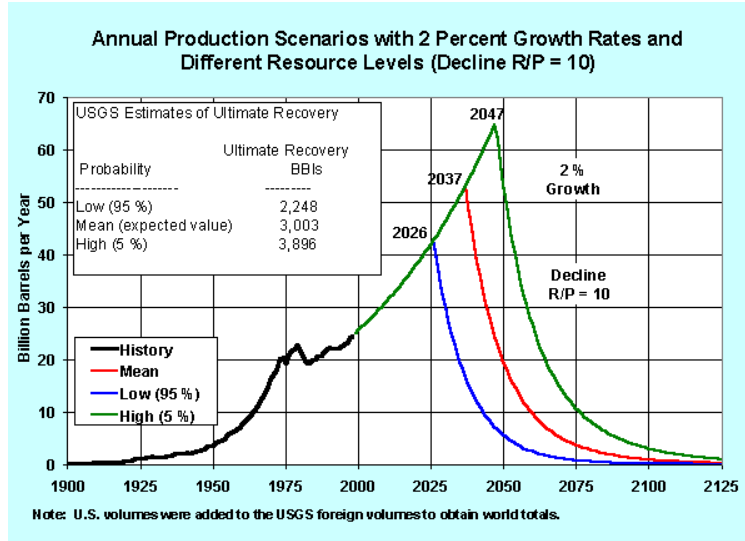
Figure 1-2: A prediction of the worldwide oil production peaks. Source EIA (2004).

50% of the electricity in the USA is currently generated by this fossil fuel. The cost of coal-fired electricity generation is relatively cheap, and unlike oil and natural gas, sufficient reserves, which are capable of supplying for hundreds of years, are assured. Nevertheless, there is a possibility that coal-based energy will rapidly shrink in the latter half of this century. The main cause would be the imposition of a high carbon tax with the expectation of a deterrent effect against several environmentally-related problems, including global warming, and the resultant physical and economic damage.

Considering the arguments above, only nuclear electric power remains as a viable energy option. The following subsection is intended to clarify whether this option has the potential to become a primary source of energy in the distant future.

## 1.2.2  Sustainability of Nuclear Electricity Generation

The generation of electricity by the nuclear fission reaction has many attractive features. There are many references which cover this topic in full detail (e.g., see Chapter 1 of Reference [4]). One definite advantage is that this form of electricity production does not emit any greenhouse gases, which is the consequence of a nuclear reaction in-

4

stead of a chemical reaction. The second important advantage is that the reserves are virtually inexhaustible. A current mainstream approach is to use low-enriched uranium, which is formed by enriching $U^{235}$ to 3–5%. The reserves of $U^{235}$ are estimated to be available for several hundreds of years, but even if this resource was depleted sometime in the latter half of this century, one could still continue the nuclear power generation with another approach, namely with a fast-breeder nuclear reactor which utilizes $U^{238}$ with an availability of more than ten thousand years. It is true that the high-level radioactive waste is extremely harmful to human bodies. However, its amount is estimated to be sufficiently small, and safe methods for disposing of nuclear waste are established.

On the other hand, there exist several disadvantages in fission-based nuclear power generation. They are political and manufacturing safety issues. First, plutonium, which is extracted from the spent fuel of light water reactors, can be diverted to nuclear weapons. This problem will be far more serious when the fast-breeder nuclear reactors start full production of electricity, since the amount of plutonium is amplified in these reactors. Second, safe operation of the future fast-breeder reactor will be more difficult than that of a light-water reactor since (1) metallic sodium used for cooling is strongly reactive, which leads to an explosion when exposed to water; and (2) the radiation strength of plutonium is much higher than that of $U^{235}$.

Nevertheless, overall, one could conclude that the presently-used nuclear electric power has a sufficient potential to be sustainable for many years to come. However, we should not rush into a conclusion that the above-mentioned fission-based power is the ultimate source of energy on earth. There is another form of nuclear power, which can supply equivalently large amount of energy with sufficient reserves in a safe and environmentally-friendly way when success is achieved — the power generated by the nuclear fusion reaction. The fundamental physics in fusion and the future prospects of the technology are briefly described in the next section.

## 1.3 Overview and Prospects for Fusion Energy

Fusion energy is the energy released in a nuclear reaction between light elements. For example, the D-T reaction yields

$$D + T \rightarrow \alpha + n + 17.6 \text{ MeV} \tag{1.1}$$

where D, T, $\alpha$, and n represent the deuterium, tritium, alpha particle (helium nucleus), and neutron, respectively. The released energy is equivalent to slightly decreased total nuclear mass, i.e., $E = \Delta mc^2 = 17.6$ MeV. This D-T reaction is considered to be the easiest of all the fusion reactions and thus extensively studied in the world (for other types of reactions, see Chapter 2 of Reference [4]).

There are two main reasons that make the fusion reaction particularly difficult. First, every nucleus is surrounded by the "electron cloud," whose radius is much larger than that of a nucleus (one frequently cited example is to compare the electron cloud and a nucleus to a stadium and a coin, respectively). Second, even if the electron clouds are completely removed, the mutually approaching nuclei normally repel each other at some point, since both nuclei have a positive electric charge and thus the Coulomb repulsive force works on both particles. In order to remove the electron cloud and then bring two nuclei close to each other to the range where the nuclear force is dominant, every particle must have extremely high kinetic energy to overcome the Coulomb force. For this purpose one needs to extraordinary increase the temperature and make a gas the state in which a certain portion of the particles is ionized — a plasma.

Considering the above-mentioned physical background, it would not be hard to imagine that the reaction rate depends on the density of nuclei and temperature. In fact, the fusion power of the D-T reaction is expressed by multiplying the reaction

rate by an energy $E_\mathrm{f}$ generated by each fusion collision:

$$P_\mathrm{DT} = n_\mathrm{D} n_\mathrm{T} \left\langle \sigma v \right\rangle_\mathrm{DT} E_\mathrm{f} \tag{1.2}$$

where $n_\mathrm{D}$ and $n_\mathrm{T}$ are the number densities of deuterium and tritium, respectively, and $\left\langle \sigma v \right\rangle_\mathrm{DT}$ is the reaction rate coefficient for the D-T reaction. It can be numerically demonstrated that the reaction rate coefficient increases with a rise in temperature up to approximately 70 keV [4].

Another important point is that the plasma should not touch the reactor wall in order to maintain itself. An approach which enables the plasma to be kept floating apart from the wall is to confine the plasma in a toroidal geometry and apply the magnetic fields in the toroidal, poloidal, and vertical directions. This is one of the most widely used magnetic confinement schemes, and the corresponding reactor is called a tokamak. Confinement of a tokamak plasma can be successfully achieved if the ratio of the plasma pressure to magnetic pressure does not exceed a certain critical value [4]. However, since the magnitude of the magnetic field is usually limited by technology or cost, there exists an allowable range for the plasma pressure in practice.

Due to many difficulties and uncertainties, fusion energy production is still unrealized. Particularly, two main difficulties that exist with a tokamak are that confinement is anomalous and that the devices are pulsed, whereas steady state operation is needed for a tokamak to operate as a commercial reactor. However, tremendous advances in theory and experiment have been made for more than half a century, and now we are in a transition period before realizing full scale electricity-producing fusion power plants. In particular, the International Thermonuclear Experimental Reactor (ITER), which is under construction, will be a significant milestone in the history of fusion research. If the ITER project is successful, a demonstration power plant (DEMO) will be constructed in the middle part of this century, and the development for commercialization will be rapidly facilitated.

Nuclear-fusion power generation has the potential to become one of the realistic

solutions to satisfy a large share of expanding energy demand in an environmentally benign way without the concerns of radiation contamination and proliferation of nuclear weapons. Although it is still hard to be optimistic considering the current performance of fusion reactors (for example, we have to eventually achieve full steady state operation with the power gain $Q = 30$–$50$, while the current performance is $Q \sim 1$), continuous efforts in technology development will be the only way to acquire sustainable energy and achieve sustainable human development.

## 1.4 Ion Cyclotron Heating of a Tokamak Plasma

As mentioned in the previous section, the highest performance magnetic confinement scheme to date is the tokamak. To enable a plasma to be ignited in a tokamak reactor, it must be heated with temperature of about 15 keV according to the ignition condition (see Chapter 4 of Reference [4]). Since the alpha power becomes dominant above 5–7 keV and heats the plasma to the required temperature for ignition, the task is to achieve the transition temperature by applying sophisticated heating techniques.

The first-step approach is based on the fact that a plasma conducts current, unlike normal gases. In tokamak operation, the toroidal current, which is induced by the transformer to yield the poloidal background magnetic field, produces ohmic heating and it raises the plasma temperature. However, since the resistivity of a plasma decreases with temperature in such a manner that $\eta \propto T^{-3/2}$, one cannot achieve the required transition temperature solely by ohmic heating. For this reason, various auxiliary heating methods have been proposed, including the neutral beam heating, electron and ion cyclotron (resonance) heating. The details of these techniques are given in many references (e.g., see Chapter 15 of Reference [4]), so that only ion cyclotron heating (ICH) will be briefly described below as this is closely related to the present research.

ICH is one of the auxiliary heating methods using radio-frequency (RF) waves.

This method is aimed at heating a plasma employing the electromagnetic waves whose applied frequencies correspond to the cyclotron frequencies of ions and their cyclotron harmonics. Since the ion cyclotron frequencies are one of the natural resonant frequencies of the plasma, a strong absorption of energy occurs when electromagnetic waves at the ion cyclotron frequencies are launched into the plasma (same applies to electron cyclotron heating (ECH)). Although the heating mechanism is similar to that in a microwave oven, the resonance mechanism is quite different; for a plasma the resonance occurs by the "collisionless damping." The ICH is produced by high power vacuum tubes, transmitted via a coaxial transmission line, and launched into the plasma by means of an antenna placed inside the vacuum chamber. Here, the geometric structure of the antenna determines the spectrum of the wavenumber component $k_{\parallel}$ parallel to the background direct-current (DC) magnetic field. Compared to ECH, ICH is considered to be achievable at a lower cost with well-established technology.

Regarding ICH, there are several issues that need to be pointed out. First, the particle resonance does not occur in a pure deuterium plasma at the fundamental frequency (i.e., the deuterium cyclotron frequency) since the polarization of the fast wave (FW), which propagates in a high-density plasma, is exactly in the opposite direction of the ion particle's motion. One of the methods to overcome this difficulty is to add a dilute, minority ion species, which is lighter than the majority species, into the plasma. This is so-called the minority ICH and in Alcator C-Mod, hydrogen is used as a minority ion species (approximately 5 % of the plasma consists of hydrogen, while the rest is deuterium). When the minority ions are added to the plasma, it turns out that the FW polarization yields a component which corresponds to the ion rotational direction; the wave can then interact with the hydrogen ion when its applied frequency is chosen at the hydrogen cyclotron frequency. In Alcator C-Mod the frequency of the FWs is set at 80 MHz, which matches the hydrogen cyclotron frequency at the center of the tokamak poloidal plane (where the magnetic field is

9

adjusted at 5.4 T). The detail of this mechanism is described in Reference [5].

Second, there is a challenge in the ICH. As will be described in Section 2.4, the FW branch has an evanescent layer at the edge of the plasma, where the plasma density is lower than the wave cutoff density. Thus, from this point of view, the antenna should be placed at the position where the plasma density is higher than the cutoff density, so that the wave power can be transmitted to the hot plasma region without decay. However, in reality, the antenna cannot be placed that close to the surface of the plasma since heat damage becomes more serious due to high temperature and plasma breakdown can occur. Therefore, the antenna position is determined by the balance between these effects; as a result, the antenna faces the plasma in the scrape-off-layer (SOL) — the region where the flux surfaces intersect with solid structures in a tokamak.

However, even if the antenna is placed in a low density and low temperature area, the metal structures in the vicinity of the antenna can be seriously damaged due to the effect of "RF sheaths," which is the central theme of this thesis and described in detail in the next section.

## 1.5   Radio-Frequency Sheaths

Although RF waves in the ion cyclotron range of frequencies (ICRF) have been successfully applied to heating experiments in fusion plasmas, many experimental and theoretical studies have shown that deleterious edge plasma interactions can occur due to various nonlinear mechanisms (see Reference [6] and the references therein). One of the most important nonlinear effects is RF sheath formation, in which the sheath potential on the walls and limiters of the tokamak device is enhanced by the ICRF waves in an unfavorable way [6, 7]. Plasma sheath formation by RF waves was studied in the 1960's [8], and the basic physical mechanism for RF sheaths is now well known. However, in a tokamak device with ICRF power, RF sheaths are

associated with plasma waves, which have quite-complicated structures, and they are often classified into the following two broad categories.

First, sheaths on the antenna surface and nearby material boundaries, such as limiters, are referred to "near-field sheaths." A root cause of them is considered to be the generation of the parasitic slow wave (SW), which has a large $E_\parallel$ component (electric field component parallel to the background magnetic field) driven by the current straps. Since the background magnetic field in a tokamak has both poloidal and toroidal components, there must exist some position where the antenna current has a component parallel to the magnetic field line. This parallel component of the antenna current is coupled to the $E_\parallel$ field of the SW, which propagates until it reaches a material surface. Due to the presence of the SW with a large-amplitude $E_\parallel$ field, electrons, which have lighter mass and thus stronger response to the RF $E_\parallel$ field, near surfaces are more encouraged to be expelled from the plasma when the electric field points into the plasma (than ions when the electric field points into the sheath), leading to the development of the net positive DC voltage, namely, "rectified" sheath potential to maintain charge ambipolarity (or quasi-neutrality; the former expression is used to describe equal fluxes of charge, while the latter is the resulting state of plasma, i.e., charge neutrality) [9]. When the current source is large, the rectified sheath potential can reach the order of kV and has important consequences. As a result of the increased sheath potential, ions are significantly accelerated in the close vicinity of wall material causing enhanced sputtering, impurity generation, and power dissipation.

The significance of near-field sheaths was appreciated in the 1980's; from then on, much experimental and theoretical work was conducted at the end of the past century to investigate the effect of sheaths on nearby antenna structures [9–13], and its various secondary effects, such as sheath currents and RF sheath-driven edge plasma convection [14–18]. Several ideas to mitigate the RF sheath problem on ICRF antennas were proposed [19,20]. Recently, important evidence for the effects of
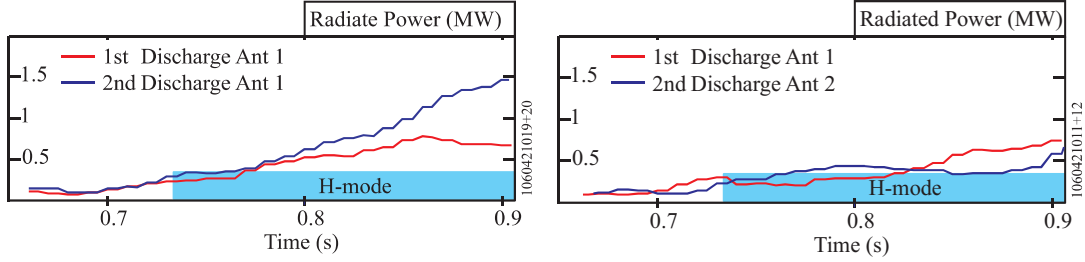
Figure 1-3: Comparison of the radiated power utilizing different antennas (courtesy of S.J. Wukitch).

RF sheaths was observed in experiments on Alcator C-Mod [21–23] and Tore Supra [24]. The quantities measured in the experiments are (1) RF-generated impurities (measurement of the increased impurity influx to the core plasma), (2) missing power and reduced heating efficiency (e.g., due to sheath power dissipation), (3) hot spots on the antenna and surrounding limiters (also due to sheath power dissipation), and (4) effects of RF sheath-driven convection (e.g., work on JET and Tore Supra). Figure 1-3 shows an example of experimental evidence for impurity production that may be related to RF sheath formation in the Alcator C-Mod tokamak [23]. It is seen that the radiated power significantly increases when the second discharge is heated by the same antenna, which indicates the acceleration of impurity generation, while low radiated power is maintained when the second discharge is heated by the different antenna.

Second, RF sheaths are also generated on material surfaces when a launched FW propagates to a wall due to SOL propagation or poor central absorption [25, 26], and the flux surfaces do not match the wall shape. These kinds of sheaths are referred to "far-field sheaths." In this case the incident FW typically generates a reflected FW and an evanescent SW (due to high plasma density) at the wall together with the rectified sheath potential. Efforts to develop efficient analytical models to understand the mechanism of far-field sheath formation have continued [27, 28]. The sheath potentials for far-field sheaths are considered to be less important than near-field sheaths from the standpoint of local damage to material structures. However, if

far-field sheaths cover a substantial portion of the wall, their total integrated contribution to the sheath power dissipation could be significant, leading to reduced heating efficiency.

There are other interesting phenomena relating to RF sheath-plasma interactions. Particularly, sheath-plasma waves [29, 30] and sheath-plasma resonances [28, 31, 32] were identified as early as the 1960's, and it is still an open question whether these physical phenomena yield significant effects on tokamak operations.

In order to unravel these complicated issues, numerous analytical approaches have been proposed thus far. If one seeks a truly accurate description of RF-sheath interactions, of course, one must consider kinetic effects and detailed sheath structures. However, if the research aim is directed at the evaluation of practically important matters, such as the effect of sheaths on waves in the SOL and sheath potentials, these details may be considered as high-order effects. Based on this philosophy, Myra, D'Ippolito, and their collaborators have established various analytical models including most notably a derivation of the "sheath boundary condition" [27], which is the idea that essential sheath effects on a main plasma are captured through the boundary condition for plasma analysis without using the field quantities in the sheath.

As will be shown in Chapter 2, the derivation of the sheath boundary condition is based on the assumption that the sheath is effectively a vacuum region, which corresponds to the zeroth-order approximation for the sheath description. Although this is seemingly a rough approximation, the sheath boundary condition captures the most important physics that happens in the sheath, that is, the rapid variation of the very large dielectric tensor component $\varepsilon_\parallel$ (later shown in Equation (2.13)) in the sheath region. D'Ippolito and Myra recently improved the sheath boundary condition to a self-consistent form [33], and demonstrated various important results, such as threshold-like turn-on of the sheath potential variation, existence of multiple roots, and sheath-plasma resonances, in their subsequent papers [28, 34–37].

For more detailed understanding and predictive capability useful for quantitative

evaluation, numerical simulation of sheath-plasma interactions with realistic geometry and plasma profiles is required. In the next section previous studies aiming at numerically solving the RF sheath interaction problems in the framework of the above-mentioned concept are overviewed, which will clarify the motivation for this thesis research.

## 1.6    Previous Studies on RF Sheath Simulation

There have been several reports that numerically solve RF sheath-plasma interaction problems. If the numerical simulation covers the main plasma (the edge and/or core plasma in a tokamak), where its characteristic length is several orders of magnitude greater than a typical sheath width, one has to approximate the sheath physics with an appropriate model; otherwise, prohibitively large computational cost would be required even for the analysis in a one-dimensional (1D) domain (see the description in the first paragraph of Section 2.7). The sheath boundary condition is one of such models, since the sheath region and the field quantities in the sheath are excluded from the calculation domain owing to the vacuum approximation and the continuity conditions. Other notable examples are the Godyak-Lieberman sheath models [38,39], which were incorporated into the numerical schemes developed by Jaeger et al. [40] and Carter et al. [41] for plasma processing. Their numerical treatments for the RF sheath may be summarized as follows.

A paper by Jaeger et al. takes into account the effect of the RF sheath by introducing the effective dielectric constant $K_{\text{eff}}$ in a grid that contains the sheath. The normalized sheath width $\delta$ is a function of the fundamental of the sheath voltage, which is calculated using a solution of Maxwell's equation. The calculated sheath potential yields reasonable values; however, there are some drawbacks with their method. First, although the sheath region is not directly resolved by grids, their definition of the effective dielectric constant requires a grid cell sandwiching the sheath

region to be sufficiently small anyway since otherwise the normalized sheath width can be so small that the sheath contribution becomes negligible. On the other hand, even if the "sheath grid" is adjusted to be a comparable size with the sheath width, some unwanted numerical oscillation could occur since the values of the dielectric tensor components abruptly change from $K = K_{\text{plasma}}$ (at the grid lines in the close vicinity of the sheath) to $K = K_{\text{sheath}} = 1$ in the adjacent grid cells. Second, two components of the electric field are assumed to be electrostatic, which is not a good approximation for a general two-dimensional (2D) analysis.

Carter et al. adopted a similar method to that in Reference [40]; however, several generalizations were made. First, the RF sheath effect is evaluated under the full electromagnetic formulation. Second, the finite sheath width is retained without normalizing it by the grid size. The local dielectric tensor components in the sheath region are defined using the effective nonlinear conductivity of the sheath and allows a smooth transition between the plasma and vacuum. The expression for the sheath width is similar to that proposed by D'Ippolito and Myra [33], although they use a different model; both consist of the sum of the RF sheath and thermal sheath contributions. Their 2D sheath solver employing the Lieberman's model is combined with the bulk 2D plasma transport and RF Maxwell solvers, and the RF sheath voltages in the plasma region are successfully calculated. A drawback in their method would be that the normal component of the electric field across the sheath (normal to the sheath surface) is fixed at a given value, which is calculated by Maxwell's equation in cold plasma, so that the RF sheath effect on the plasma waves is not taken into account. Also, their finite difference formulation would not be amenable to the problem that has a spatially complicated geometry (the plasma region considered in their paper is rectangular, and so the finite difference technique suffices).

Besides the work conducted by Jaeger and Carter et al., there was an attempt to incorporate sheath effects into a numerical code by means of the sheath boundary condition proposed by D'Ippolito and Myra [33]. Compernolle et al. tried to imple-

ment the sheath boundary condition into their TOPICA code [42, 43] using a realistic ICRF antenna model [44]. However, it would probably be fair to say that their work is stopped at a primitive level for the following reasons. First, the sheath boundary condition is introduced to a vacuum RF model, which means that the boundary condition is not coupled with the plasma dielectric tensor, yielding unphysical consequences. Second, as they mention in their paper, the power lost by the ions accelerated in the DC sheath potential increases in an unexpected way possibly due to problems in their code.

In summary, up to this point there has been no numerical code that solves RF sheath-plasma interactions truly in a self-consistent way in the domains with complicated boundary shapes. As mentioned in the previous section, experiments show that impurities are generated in the ICRF regime, which is serious because they limit heating of plasma. The difficulty is that in some cases it is hard to identify the source of impurities unless specific areas of the tokamak are covered with specific types of impurities. Therefore, developing a predictive numerical tool which possesses the above-mentioned features is essential to a complete understanding of the source; one can then consider various measures to mitigate the unwanted effects. In particular, such a numerical tool will answer the question whether rotating the antenna has a significant effect on the wall sputtering as a source of impurities. This is the motivation for this thesis research. The major achievements obtained in the present study are summarized in the following section.

## 1.7    Thesis Outline and Summary of Results

The major achievements of this thesis work are summarized as follows:

(1) Development of a novel numerical scheme that solves self-consistent RF sheath-plasma interactions in the SOL for an ICRF heating system.

(2) Discovery of various new 1D and 2D effects caused by the mutual interaction

between the sheath and cold plasma in the SOL.

(3) Quantitative predictions of the localized RF sheath potential observed in an Alcator C-Mod scale device.

(4) Development of the finite element wave-packet method that solves multiscale wave problems accurately with low computational cost.

The numerical code that solves RF sheath-plasma interactions strictly in a self-consistent way in the 1D and 2D domains with an arbitrary boundary shape is developed for the first time with use of a nonlinear finite element technique. A novel approach is that two independent weight functions are defined for the discretization of a combined form of Maxwell's equations and the sheath boundary condition, and the obtained discretized equations are combined into a vector equation. In addition, the numerical scheme is constructed with the aim of achieving a fast and accurate solver by applying (1) the central point approximation to the Jacobian and the components of the cofactor matrix in each integral of the discretized Maxwell's equation, and (2) the element-average technique to the sheath width in the discretization of the sheath boundary condition. Owing to these approximations, the expression of the global matrix in the Newton-Raphson iteration is explicitly obtained without the necessity of using any numerical integration method, and the resultant numerical scheme is robust and realizes fast computation.

Using the above numerical code, several new properties of the RF sheath-plasma interactions are discovered. In the 1D domain with a varying plasma density profile, it is found that multiple roots can be present due to the resonance of the propagating SW and its nonlinear interaction with the sheath. In a 2D slab geometry, sheath-plasma waves are identified for the first time via numerical simulation, and it is proved in conjunction with an electrostatic 2D sheath mode analysis that (1) the sheath-plasma wave only appears in the vicinity of the sheath surface if the plasma density is greater than the lower hybrid density, and (2) its wavelength mainly de-

pends on the plasma density, magnitude of the poloidal background magnetic field, and electron temperature. It is also demonstrated for the first time that the electric field distribution pattern in the plasma varies along the magnetic field lines as a consequence of the self-consistent interaction between the propagating SW and the sheath, and the corresponding sheath potential can reach the order of kV for parameters similar to those used for the ICRF operation in Alcator C-Mod. It is found that this variation smoothly occurs between the conducting-wall and quasi-insulating limits.

In the numerical analysis employing the 2D domain whose scale is equivalent to the Alcator C-Mod device, it is confirmed that the calculated sheath potential values are comparable to the experimental measurements. In addition, it is demonstrated for constant plasma density and straight magnetic field lines that the sheath potential in the close vicinity of the antenna current strap is insensitive to the direction of the background magnetic field in the RF sheath dominated regime. Furthermore, from the derivation of the nonlinear sheath boundary condition, an important scaling is discovered for the sheath potential $V_0$ having the form $V_0 \sim \left(b_{\mathrm{n}} E_\parallel\right)^4 / (n_{\mathrm{e}0}^2 T_{\mathrm{e}})$, where $b_{\mathrm{n}}$, $E_\parallel$, $n_{\mathrm{e}0}$, and $T_{\mathrm{e}}$ are the normal component (to the sheath) of the unit vector along the direction of the background magnetic field, parallel electric field strength, electron density, and electron temperature, respectively. It is found that the nonlinear self-consistent code that solves RF sheath-plasma interactions including the antenna coupling to $E_\parallel$ plays a major role in quantitative evaluation of the sheath potential, which sensitively varies depending on the electron density and electron temperature according to the above scaling.

Finally, a new finite element approach — finite element wave-packet method — is developed by enriching usual finite element interpolations with wave packets. This method settles intrinsic difficulties pertaining to conventional spectral approaches in (1) satisfying the boundary conditions accurately and (2) achieving fast computation. It is proved that the proposed method can yield much more accurate results for

18

multiscale wave problems than using the conventional finite element method under the same computational costs.

The outline of this thesis is as follows. In Chapter 2 the basic theory of plasma waves in the SOL is reviewed, and the derivation of the sheath boundary condition is demonstrated using flat and curved walls. A practically useful expression for the sheath width is established with the use of the Child-Langmuir law and the limits of the thermal and RF sheath dominated regimes. In addition, it is emphasized that introducing an artificial collision frequency is important to ensure a stable calculation for the case where the lower hybrid resonance appears in the calculation domain, and to separate the SOL region from the core plasma.

In Chapter 3 the discretization procedures of a combined form of Maxwell's equations and the sheath boundary condition are presented, and then the iteration algorithm for the resultant nonlinear system of discretized equations is described. The large-scale matrix equation obtained from this system is solved using massively parallel linear algebra routines. The developed numerical scheme is named "rfSOL," and its validity is verified by comparison with an analytical solution in the 1D closed domain and the results of the local dispersion relation.

Using the rfSOL code developed in Chapter 3, various RF sheath-plasma interaction problems in the 1D and 2D domains are solved based on the parameters for the Alcator C-Mod tokamak in Chapter 4. In the 1D analysis the sheath potential variation with an increase in the antenna current is investigated with constant and varying plasma density profiles. In the 2D analysis the numerically identified wave mode on the sheath is verified and further investigated through an electrostatic 2D sheath mode analysis. This is followed by the calculations of the most deleterious SW-sheath interactions, in which the variations in magnitude and distribution of the sheath potential are assessed by varying the magnitude of the current source, and the mechanism of the wave pattern variation is considered. Lastly, a series of numerical analyses is conducted under conditions close to the Alcator C-Mod tokamak by

enlarging the calculation domain and antenna length.

The thesis research takes a new direction in Chapter 5. Here a finite element wave-packet procedure is presented to solve problems of wave propagation where multiscale behavior is important. A motivation for this research is that it is still challenging to resolve all the multiscale plasma waves in the tokamak poloidal plane due to limited computational performance. The proposed scheme combines the advantages of finite element and spectral methods. The basic formulation is presented, and the capabilities of the procedure are demonstrated through the solution of some illustrative problems, including a problem that characterizes the mode-conversion behavior in tokamak plasmas.

Finally, Chapter 6 summarizes the main results of this thesis and addresses future work.

# Chapter 2

# Theory of Plasma Waves and RF Sheath Physics

## 2.1 Prologue

This chapter describes the basic theory of plasma waves and the RF sheath physics observed in the SOL of a tokamak in the ICRF. The goal is to derive the equations that govern the behavior of plasma waves in the SOL and the interaction between the waves and the sheath on metal surfaces, which are directly employed in the present finite element numerical analyses. The geometry considered here is shown in Figure 2-1; this is a simplified schematic of the tokamak poloidal cross-section in the vicinity of the limiter, assuming that the magnetic field lines intersect with a metal surface and thereby the sheath is formed. If the effect of RF waves is negligibly small, the sheath width and potential drop inside the sheath can be evaluated using the well-known Bohm sheath theory [45]. However, if the RF waves with large electric-field strength approach the wall, the sheath width can be significantly increased to avoid further expelling the electrons from the plasma and then the ions are further accelerated inside the sheath, enhancing sputtering as a result. Therefore, it is important to establish a predictive numerical tool which quantifies the sheath potential with consideration
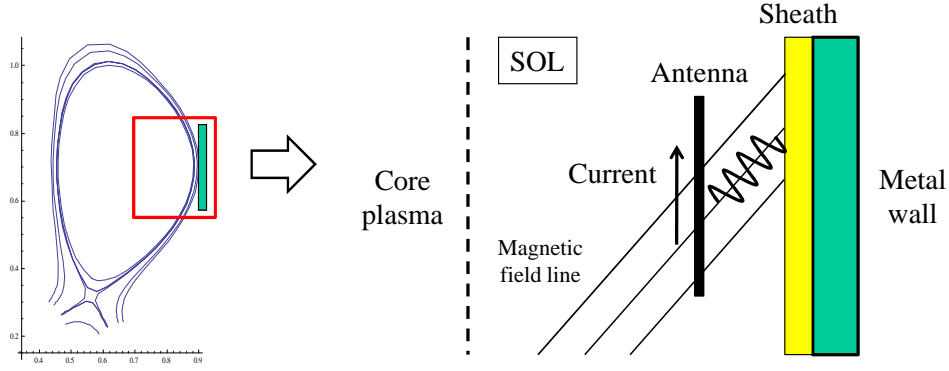
Figure 2-1: Illustration of the tokamak poloidal cross-section in the vicinity of the limiter (courtesy of J.R. Myra).

of self-consistent RF sheath-plasma interactions.

The plan in this chapter is as follows. First, a description of the electromagnetic wave propagation in a cold plasma is presented. A special attention will be given to the classification of the waves in the ICRF into fast and slow waves. Second, the necessity of introducing the collisional effect for a certain condition is described. Third, the concept of the "sheath boundary condition" is introduced and its formulation is fully described. Finally, the absorbing boundary condition is introduced to complete the present numerical model.

Unless otherwise noted, the units used in this study conform to the International System of Units (SI).

## 2.2   Validity of Using a Cold Plasma Model

All the analyses in this study will be conducted using a cold plasma model. One parameter which shows the validity of this premise is the Larmor radius factor defined as

$$b_{\mathrm{L}j} = \frac{k_\perp^2 v_{\mathrm{t}j\perp}^2}{2\omega_{\mathrm{c}j}^2} \tag{2.1}$$

22

where $k_\perp$ is the perpendicular wavenumber, $v_{tj\perp}$ is the perpendicular thermal speed, and $\omega_{cj}$ is the cyclotron frequency; the term "perpendicular" means the perpendicular direction to the background magnetic field, and the subscript $j$ indicates an ion (i) or an electron (e). Here the perpendicular thermal speed and cyclotron frequency are, respectively, defined as $v_{tj\perp} = (2T_{j\perp}/m_j)^{1/2}$ and $\omega_{cj} = |q_j|\,B/m_j$, where $T_{j\perp}$ is the temperature perpendicular to the background magnetic field, $m_j$ is the particle mass, $q_j$ is the electric charge, and $B$ is the magnitude of the background magnetic field. When the condition $b_{Lj} \ll 1$ is satisfied, it can be seen that the hot plasma equations naturally reduce to the corresponding cold plasma equations [46]. In the ICRF the perpendicular wavenumber can be expressed as $k_\perp \simeq \omega/v_A$ [46], where $\omega$ is the applied angular velocity, and $v_A$ is the Alfvén speed defined as $v_A = (B^2/\mu_0 m_i n_i)^{1/2}$. Here $\mu_0$ is the permeability in vacuum, and $n_i$ is the number density of ions. In the regime where $T_{i\perp} \sim T_{e\perp}$ is valid, one can only evaluate $b_{Li}$ to show that $b_{Lj} \ll 1$, since $b_{Li} \gg b_{Le}$ in this case. For a plasma with $\mu_i = 2$, $T_{i\perp} \simeq 10$ eV, and $n_i = 1.0 \times 10^{18}$ m$^{-3}$ under $B = 5.4$ T and $f = 80$ MHz, it follows that $b_{Li} = 2.6 \times 10^{-7}$.

Throughout this study, only deuterium is considered as an ion species, so that $m_i = 3.3436 \times 10^{-27}$ kg, which is consistent with the Alcator C-Mod plasma in the SOL.

## 2.3  Cold Plasma Formulation in the SOL

We start the derivation of the governing equation in a cold plasma from Maxwell's equations:

$$\nabla \times \boldsymbol{E} = -\frac{\partial \boldsymbol{B}}{\partial t} \tag{2.2}$$

$$\nabla \times \boldsymbol{B} = \mu_0 \boldsymbol{J} + \frac{1}{c^2}\frac{\partial \boldsymbol{E}}{\partial t} \tag{2.3}$$

where $c$ is the speed of light. Using the assumption of small-amplitude perturbation, the electric field $\boldsymbol{E}$, the magnetic field $\boldsymbol{B}$, and the current density $\boldsymbol{J}$ in Equations (2.2) and (2.3) can be expanded in the following way:

$$Q\left(\boldsymbol{x}, t\right) = Q_0 + Q_1\left(\boldsymbol{x}, t\right) \tag{2.4}$$

where the subscripts 0 and 1 denote the zeroth-order equilibrium quantity and the first-order perturbed quantity, respectively. Here we use a Fourier analysis in time for the quantity $Q_1$, namely

$$Q_1\left(\boldsymbol{x}, t\right) = \hat{Q}_1\left(\boldsymbol{x}\right)\exp\left(-i\omega t\right) \tag{2.5}$$

where $i$ is the imaginary unit. Then the first-order equations corresponding to Equations (2.2) and (2.3) are, respectively, written as follows:

$$\nabla \times \boldsymbol{E}_1 = i\omega \boldsymbol{B}_1 \tag{2.6}$$

$$\nabla \times \boldsymbol{B}_1 = \mu_0 \boldsymbol{J}_1 - i\frac{\omega}{c^2}\boldsymbol{E}_1 \tag{2.7}$$

The perturbed current $\boldsymbol{J}_1$ consists of the induced current $\boldsymbol{J}_{\text{ind}}$ and the external current $\boldsymbol{J}_{\text{ext}}$, i.e.,

$$\boldsymbol{J}_1 = \boldsymbol{J}_{\text{ind}} + \boldsymbol{J}_{\text{ext}} \tag{2.8}$$

Further, the induced current is related to the perturbed electric field through Ohm's law:

$$\boldsymbol{J}_{\text{ind}} = \boldsymbol{\sigma} \cdot \boldsymbol{E}_1 \tag{2.9}$$

where $\boldsymbol{\sigma}$ is the conductivity tensor. Substituting Equation (2.6) into Equation (2.7) and using the relations (2.8) and (2.9), we obtain the following equation:

$$\nabla \times \nabla \times \boldsymbol{E}_1 - \frac{\omega^2}{c^2}\boldsymbol{\varepsilon} \cdot \boldsymbol{E}_1 - i\omega\mu_0\boldsymbol{J}_{\text{ext}} = \boldsymbol{0} \tag{2.10}$$

where $\boldsymbol{\varepsilon}$ is the dielectric tensor defined as

$$\boldsymbol{\varepsilon} = \boldsymbol{I} + \frac{i}{\varepsilon_0\omega}\boldsymbol{\sigma} \tag{2.11}$$

Here $\boldsymbol{I}$ is the unit tensor, and $\varepsilon_0$ is the dielectric constant in vacuum, which is yielded from the relation $c^2 = (\varepsilon_0\mu_0)^{-1}$. Equation (2.10) is the governing equation in the SOL used in the present analysis. Hereafter, the subscript 1 in $\boldsymbol{E}_1$ will be omitted, since the equilibrium electric field ($\boldsymbol{E}_0$) is assumed to be zero.

In order to obtain the expression for the dielectric tensor, in general, we are required to conduct a long calculation by starting from the momentum equations [4, 46]. However, the following dyad notation allows us to easily obtain the expression for any coordinate system:

$$\boldsymbol{\varepsilon} = (\boldsymbol{I} - \boldsymbol{bb})\,\varepsilon_\perp + \boldsymbol{bb}\varepsilon_\parallel + i\boldsymbol{b} \times \boldsymbol{I}\varepsilon_\times \tag{2.12}$$

where $\boldsymbol{b}$ is the unit vector along the background magnetic field ($\boldsymbol{b} = \boldsymbol{B}_0/|\boldsymbol{B}_0|$). Here the coefficients $\varepsilon_\perp$, $\varepsilon_\parallel$, and $\varepsilon_\times$ are expressed as follows:

$$\begin{aligned}
\varepsilon_\perp &= 1 - \sum_j \frac{\omega_{\text{p}j}^2}{\omega^2 - \Omega_j^2} \\
\varepsilon_\parallel &= 1 - \sum_j \frac{\omega_{\text{p}j}^2}{\omega^2} \\
\varepsilon_\times &= \sum_j \frac{\omega_{\text{p}j}^2\Omega_j}{\omega\left(\omega^2 - \Omega_j^2\right)}
\end{aligned} \tag{2.13}$$

25

where $\omega_{\mathrm{p}j}$ is the plasma frequency defined as $\omega_{\mathrm{p}j} = (n_{j0}e^2/\varepsilon_0 m_j)^{1/2}$, and $\Omega_j = q_j B_0/m_j$; the subscript $j$ indicates two-species particles, i.e., an ion (i) or an electron (e). In the Cartesian coordinate system, the dielectric tensor components are calculated as follows:

$$\boldsymbol{\varepsilon} = \begin{pmatrix} \left(1 - b_x^2\right)\varepsilon_\perp + b_x^2 \varepsilon_\parallel & -b_x b_y \left(\varepsilon_\perp - \varepsilon_\parallel\right) - ib_z \varepsilon_\times & -b_x b_z \left(\varepsilon_\perp - \varepsilon_\parallel\right) + ib_y \varepsilon_\times \\ -b_x b_y \left(\varepsilon_\perp - \varepsilon_\parallel\right) + ib_z \varepsilon_\times & \left(1 - b_y^2\right)\varepsilon_\perp + b_y^2 \varepsilon_\parallel & -b_y b_z \left(\varepsilon_\perp - \varepsilon_\parallel\right) - ib_x \varepsilon_\times \\ -b_x b_z \left(\varepsilon_\perp - \varepsilon_\parallel\right) - ib_y \varepsilon_\times & -b_y b_z \left(\varepsilon_\perp - \varepsilon_\parallel\right) + ib_x \varepsilon_\times & \left(1 - b_z^2\right)\varepsilon_\perp + b_z^2 \varepsilon_\parallel \end{pmatrix}$$

$$(2.14)$$

where $b_x$, $b_y$, and $b_z$ are the components of $\boldsymbol{b}$ in the $x$, $y$, and $z$ directions, respectively. Throughout this study, we assume that charge ambipolarity in the plasma is retained, i.e., $n_{\mathrm{e}0} = n_{\mathrm{i}0} = n_0$.

## 2.4 Fast and Slow Waves in the ICRF

Further assuming the Fourier mode in space in Equation (2.5), we can convert $\nabla$ to $i\boldsymbol{k}$ in Maxwell's equations, where $\boldsymbol{k}$ is the wavenumber vector. This implies that we consider a homogeneous plasma with constant plasma density and a constant magnetic field in space at the equilibrium state (in a strict sense). Then Equation (2.10) reduces to

$$\boldsymbol{n} \times \left(\boldsymbol{n} \times \boldsymbol{E}\right) + \boldsymbol{\varepsilon} \cdot \boldsymbol{E} + \frac{i}{\varepsilon_0 \omega} \boldsymbol{J}_{\mathrm{ext}} = \boldsymbol{0} \qquad (2.15)$$

where $\boldsymbol{n}$ is the index of refraction defined as $\boldsymbol{n} = c\boldsymbol{k}/\omega$. Now let us focus on the region where $\boldsymbol{J}_{\mathrm{ext}} = \boldsymbol{0}$. Using the vector identity

$$\boldsymbol{n} \times \left(\boldsymbol{n} \times \boldsymbol{E}\right) = \left(\boldsymbol{n} \cdot \boldsymbol{E}\right)\boldsymbol{n} - n^2 \boldsymbol{E}$$

26

(here $n^2 = \boldsymbol{n} \cdot \boldsymbol{n}$), Equation (2.15) can be rewritten as follows:

$$\left(\boldsymbol{n}\boldsymbol{n} - n^2\boldsymbol{I} + \boldsymbol{\varepsilon}\right) \cdot \boldsymbol{E} = \boldsymbol{0} \tag{2.16}$$

Equation (2.16) readily yields the following dispersion relation:

$$\left|\boldsymbol{n}\boldsymbol{n} - n^2\boldsymbol{I} + \boldsymbol{\varepsilon}\right| = 0 \tag{2.17}$$

In the coordinate system defined as

$$\boldsymbol{\varsigma} = \frac{\boldsymbol{k}_\perp}{|\boldsymbol{k}_\perp|}, \quad \boldsymbol{\varpi} = \frac{\boldsymbol{b} \times \boldsymbol{k}_\perp}{|\boldsymbol{k}_\perp|}, \quad \boldsymbol{b} = \frac{\boldsymbol{B}_0}{|\boldsymbol{B}_0|} \tag{2.18}$$

the components of the dielectric tensor are given as follows:

$$\boldsymbol{\varepsilon} = \begin{pmatrix} \varepsilon_\perp & -i\varepsilon_\times & 0 \\ i\varepsilon_\times & \varepsilon_\perp & 0 \\ 0 & 0 & \varepsilon_\| \end{pmatrix} \tag{2.19}$$

Substituting Equation (2.19) into Equation (2.17) and noting that $\boldsymbol{n} = n_\perp \boldsymbol{\varsigma} + n_\| \boldsymbol{b}$, one gets

$$\begin{vmatrix} \varepsilon_\perp - n_\|^2 & -i\varepsilon_\times & n_\perp n_\| \\ i\varepsilon_\times & \varepsilon_\perp - n^2 & 0 \\ n_\perp n_\| & 0 & \varepsilon_\| - n_\perp^2 \end{vmatrix} = 0 \tag{2.20}$$

Evaluating Equation (2.20) yields the fourth order dispersion relation

$$\left(n_\perp^2 - \varepsilon_\|\right)\left(n_\|^2 - \varepsilon_\perp\right)\left(n^2 - \varepsilon_\perp\right) - n_\perp^2 n_\|^2 \left(n^2 - \varepsilon_\perp\right) - \varepsilon_\times^2 \left(n_\perp^2 - \varepsilon_\|\right) = 0 \tag{2.21}$$

in which both fast and slow waves are coupled.

### 2.4.1 FW and SW Dispersion Relations

Equation (2.21) can be reduced to the second order dispersion relations by taking two limiting cases [27]. First, the FW obeys the ordering $n_\perp^2 \sim n_\parallel^2 \sim \varepsilon_\perp, \varepsilon_\times \ll \varepsilon_\parallel$. Then the second term in Equation (2.21) is smaller than the other terms by $\mathcal{O}\left(\varepsilon_\perp/\varepsilon_\parallel\right)$, and thus it can be omitted. As a result, we obtain the FW dispersion relation as follows:

$$\left(n_\parallel^2 - \varepsilon_\perp\right)^2 + n_\perp^2 \left(n_\parallel^2 - \varepsilon_\perp\right) - \varepsilon_\times^2 = 0 \tag{2.22}$$

On the other hand, the SW obeys the ordering $n_\perp^2 \sim \varepsilon_\parallel \gg \varepsilon_\perp, \varepsilon_\times \sim n_\parallel^2$. Then the third term in Equation (2.21) is smaller than the other terms by $\mathcal{O}\left(\varepsilon_\perp/\varepsilon_\parallel\right)$, and thus it can be omitted. Consequently, we obtain the SW dispersion relation as follows:

$$n_\parallel^2 \varepsilon_\parallel + \varepsilon_\perp \left(n_\perp^2 - \varepsilon_\parallel\right) = 0 \tag{2.23}$$

Note that the same results are obtained in Stix's notation [46] by considering that $|\sin\theta/\cos\theta| \sim 1$ for the FW and $|\sin\theta/\cos\theta| \gg 1$ for the SW, where $\sin\theta = n_\perp/n$ and $\cos\theta = n_\parallel/n$.

### 2.4.2 Electrostatic Dispersion Relation

Forming the inner product of Equation (2.15) with $\boldsymbol{k}$ while keeping $\boldsymbol{J}_{\text{ext}} = \boldsymbol{0}$, we obtain

$$\boldsymbol{k} \cdot (\boldsymbol{\varepsilon} \cdot \boldsymbol{E}) = 0 \tag{2.24}$$

When the electrostatic approximation is valid, the electric field is expressed as $\boldsymbol{E} = -\nabla\Phi = -i\boldsymbol{k}\Phi$. In this case, Equation(2.24) yields

$$\boldsymbol{k} \cdot \boldsymbol{\varepsilon} \cdot \boldsymbol{k} = 0 \tag{2.25}$$

for a nontrivial solution ($\boldsymbol{E} \neq \boldsymbol{0}$). Then using Equation (2.19) and noting that $\boldsymbol{k} = k_\perp \boldsymbol{\varsigma} + k_\parallel \boldsymbol{b}$, we obtain the following relation from Equation (2.25):

$$k_\perp^2 \varepsilon_\perp + k_\parallel^2 \varepsilon_\parallel = 0 \tag{2.26}$$

This is the electrostatic dispersion relation. Alternatively, we can rewrite Equation (2.26) as

$$n_\perp^2 \varepsilon_\perp + n_\parallel^2 \varepsilon_\parallel = 0 \tag{2.27}$$

Here note that Equation (2.27) is obtained from the SW dispersion relation (2.23) when the condition $n_\parallel^2 \gg \varepsilon_\perp$ is satisfied.

### 2.4.3 FW and SW Polarizations

Based on the coordinate system of Equation (2.18), Equation (2.16) is rewritten in a matrix form as follows:

$$\begin{pmatrix} \varepsilon_\perp - n_\parallel^2 & -i\varepsilon_\times & n_\perp n_\parallel \\ i\varepsilon_\times & \varepsilon_\perp - n^2 & 0 \\ n_\perp n_\parallel & 0 & \varepsilon_\parallel - n_\perp^2 \end{pmatrix} \begin{pmatrix} E_\varsigma \\ E_\varpi \\ E_\parallel \end{pmatrix} = \begin{pmatrix} 0 \\ 0 \\ 0 \end{pmatrix} \tag{2.28}$$

The polarizations for the fast and slow waves are determined from the appropriate submatrices of Equation (2.28). In the FW ordering, we notice that $|E_\varsigma| \sim |E_\varpi| \gg |E_\parallel|$ ($|E_\parallel| / |E_\varsigma| \sim \mathcal{O}\left(\varepsilon_\perp/\varepsilon_\parallel\right)$), so that Equation (2.28) reduces to

$$\begin{pmatrix} \varepsilon_\perp - n_\parallel^2 & -i\varepsilon_\times \\ i\varepsilon_\times & \varepsilon_\perp - n^2 \end{pmatrix} \begin{pmatrix} E_\varsigma \\ E_\varpi \end{pmatrix} \simeq \begin{pmatrix} 0 \\ 0 \end{pmatrix} \tag{2.29}$$

It is confirmed that the dispersion relation (2.22) is directly obtained from Equation (2.29). The FW polarization is then expressed as follows:

$$\frac{E_\varsigma}{E_\varpi} = -i \frac{\varepsilon_\times}{n_\parallel^2 - \varepsilon_\perp} \tag{2.30}$$

Similarly, in the SW ordering, we find that $|E_\varsigma| \sim |E_\parallel| \gg |E_\varpi|$ ($|E_\varpi|/|E_\varsigma| \sim \mathcal{O}\left(\varepsilon_\perp/\varepsilon_\parallel\right)$). As a result, Equation (2.28) reduces to the following equation:

$$\begin{pmatrix} \varepsilon_\perp - n_\parallel^2 & n_\perp n_\parallel \\ n_\perp n_\parallel & \varepsilon_\parallel - n_\perp^2 \end{pmatrix} \begin{pmatrix} E_\varsigma \\ E_\parallel \end{pmatrix} \simeq \begin{pmatrix} 0 \\ 0 \end{pmatrix} \tag{2.31}$$

Again, we notice that Equation (2.23) is directly obtained from Equation (2.31). The SW polarization is thus written as

$$\frac{E_\varsigma}{E_\parallel} = \frac{n_\parallel n_\perp}{n_\parallel^2 - \varepsilon_\perp} \tag{2.32}$$

From the results in Equations (2.30) and (2.32), we can straightforwardly obtain the unit polarization vectors used in Reference [27].

### 2.4.4   FW and SW Resonances and Cut-Offs

The fast and slow wave dispersion relations in Equations (2.22) and (2.23) are, respectively, rewritten in terms of $n_\perp^2$ as follows:

$$n_\perp^2 = \frac{\left(n_\parallel^2 - \varepsilon_R\right)\left(n_\parallel^2 - \varepsilon_L\right)}{\varepsilon_\perp - n_\parallel^2} \qquad \text{(FW)} \tag{2.33}$$

$$n_\perp^2 = \frac{\varepsilon_\parallel}{\varepsilon_\perp}\left(\varepsilon_\perp - n_\parallel^2\right) \qquad \text{(SW)} \tag{2.34}$$

where

$$\varepsilon_R = \varepsilon_\perp + \varepsilon_\times, \quad \varepsilon_L = \varepsilon_\perp - \varepsilon_\times \tag{2.35}$$

Here $k_\parallel$ is assumed to be determined by the antenna. Then from Equation (2.33), we find that the resonance for the FW occurs at $n_\parallel^2 = \varepsilon_\perp$, which corresponds to the Alfvén resonance. Also, we see from Equation (2.34) that the resonance for the SW occurs at $\varepsilon_\perp = 0$, which corresponds to the lower hybrid resonance. On the other hand, the FW cutoff occurs at $n_\parallel^2 = \varepsilon_R, \varepsilon_L$, while the SW is cutoff at $n_\parallel^2 = \varepsilon_\perp$.

When $n_\parallel^2 \simeq \varepsilon_\perp$, the value of $n_\perp^2$ for the FW becomes very large, while its value becomes very small for the SW. In this case the orderings that were used to originally separate the fast and slow waves (see Section 2.4.1) are no longer valid.

## 2.5   Necessity of Introducing the Collisional Effect

When a resonance appears in the calculation domain in a numerical analysis, the numerical result becomes unstable, and we often see grid-scale oscillation. This is due to the fact that there exists a region where the grid resolution is not enough to capture very small wavelengths of the wave in the vicinity of (and at) the resonance point, no matter how fine the grids are (recall that the resonance corresponds to an infinite value of $k_\perp$, which yields an infinitesimal wavelength). This is a difficulty of employing the cold plasma formulation, which arises unavoidably for a certain condition (e.g., by spatially varying density or background magnetic field). However, we can avoid this problem by introducing the collisional effect, which will be described in this section.

First, for a low-temperature plasma, the macroscopic fluid equations describing conservation of momentum for electrons and ions are written as follows:

$$
\begin{aligned}
m_e n_e \left( \frac{\partial}{\partial t} + \boldsymbol{u}_e \cdot \nabla \right) \boldsymbol{u}_e &\simeq -e n_e \left( \boldsymbol{E} + \boldsymbol{u}_e \times \boldsymbol{B} \right) - m_e n_e \bar{\nu}_{ei} \left( \boldsymbol{u}_e - \boldsymbol{u}_i \right) \\
m_i n_i \left( \frac{\partial}{\partial t} + \boldsymbol{u}_i \cdot \nabla \right) \boldsymbol{u}_i &\simeq e n_i \left( \boldsymbol{E} + \boldsymbol{u}_i \times \boldsymbol{B} \right) - m_e n_e \bar{\nu}_{ei} \left( \boldsymbol{u}_i - \boldsymbol{u}_e \right)
\end{aligned}
\tag{2.36}
$$

where $\boldsymbol{u}_{e,i}$ are, respectively, the macroscopic electron and ion velocities, and $\bar{\nu}_{ei}$ is the

electron-ion momentum exchange collision frequency defined as

$$\bar{\nu}_{\mathrm{ei}} = \frac{\sqrt{2}}{12\pi^{3/2}} \frac{e^4 n_{\mathrm{i}}}{\varepsilon_0^2 m_{\mathrm{e}}^{1/2} T^{3/2}} \ln \Lambda \simeq 1.8 \times 10^5 \frac{n_{20}}{T_{\mathrm{k}}^{3/2}} \quad \left[\mathrm{s}^{-1}\right] \qquad (2.37)$$

for $\ln \Lambda = 20$ [4]; here $n_{20} = n_{\mathrm{i}}\left[\mathrm{m}^{-3}\right]/10^{20}\left[\mathrm{m}^{-3}\right]$ and $T_{\mathrm{k}} = T\left[\mathrm{eV}\right]/10^3\left[\mathrm{eV}\right]$. In Equation (2.36) the pressure gradient terms are omitted as being small. Now let us assume a homogeneous plasma at the equilibrium state, which is described as

$$n_{\mathrm{e}} = n_{\mathrm{i}} = n_0, \quad \boldsymbol{u}_{\mathrm{e}} = \boldsymbol{u}_{\mathrm{i}} = \boldsymbol{0}$$

$$\boldsymbol{B} = \boldsymbol{B}_0, \quad \boldsymbol{E} = \boldsymbol{0}$$

and use a Fourier analysis in time for the first-order quantities. Then the electron and ion equations in Equation (2.36) are, respectively, rewritten as follows:

$$-i\omega m_{\mathrm{e}} n_{\mathrm{e}} \boldsymbol{u}_{\mathrm{e}1} = -e n_{\mathrm{e}} \left(\boldsymbol{E}_1 + \boldsymbol{u}_{\mathrm{e}1} \times \boldsymbol{B}_0\right) - m_{\mathrm{e}} n_{\mathrm{e}} \bar{\nu}_{\mathrm{ei}} \left(\boldsymbol{u}_{\mathrm{e}1} - \boldsymbol{u}_{\mathrm{i}1}\right)$$
$$-i\omega m_{\mathrm{i}} n_{\mathrm{i}} \boldsymbol{u}_{\mathrm{i}1} = e n_{\mathrm{i}} \left(\boldsymbol{E}_1 + \boldsymbol{u}_{\mathrm{i}1} \times \boldsymbol{B}_0\right) - m_{\mathrm{e}} n_{\mathrm{e}} \bar{\nu}_{\mathrm{ei}} \left(\boldsymbol{u}_{\mathrm{i}1} - \boldsymbol{u}_{\mathrm{e}1}\right) \qquad (2.38)$$

As an example, for a plasma with $n_0 = 1.0 \times 10^{18}$ m$^{-3}$ and $T_{\mathrm{e}} = T_{\mathrm{i}} = 10$ eV, the electron-ion momentum exchange collision frequency is calculated at $\bar{\nu}_{\mathrm{ei}} \simeq 1.8 \times 10^6$ s$^{-1}$, which is much smaller compared to the applied frequency in ICRF ($f = 80$ MHz). Thus, the macroscopic electron and ion velocities can be evaluated by neglecting the collision terms in Equation (2.38). As a result, one gets

$$\boldsymbol{u}_{\mathrm{e}1\perp} \sim \boldsymbol{u}_{\mathrm{i}1\perp}, \quad \frac{u_{\mathrm{e}1\parallel}}{u_{\mathrm{i}1\parallel}} \sim \mathcal{O}\left(\frac{m_{\mathrm{i}}}{m_{\mathrm{e}}}\right) \qquad (2.39)$$

where the subscripts $\perp$ and $\parallel$ denote the quantities in the perpendicular and parallel directions to the background magnetic field, respectively. Therefore, we can estimate

$\boldsymbol{u}_{\text{e1}} - \boldsymbol{u}_{\text{i1}} \sim \boldsymbol{u}_{\text{e1}}$ in order of magnitude, and rewrite Equation (2.38) as

$$
\begin{aligned}
-i\omega m_{\text{e}} n_{\text{e}} \boldsymbol{u}_{\text{e1}} &= -e n_{\text{e}} \left( \boldsymbol{E}_1 + \boldsymbol{u}_{\text{e1}} \times \boldsymbol{B}_0 \right) - m_{\text{e}} n_{\text{e}} \bar{\nu}_{\text{ei}} \boldsymbol{u}_{\text{e1}} \\
-i\omega m_{\text{i}} n_{\text{i}} \boldsymbol{u}_{\text{i1}} &= e n_{\text{i}} \left( \boldsymbol{E}_1 + \boldsymbol{u}_{\text{i1}} \times \boldsymbol{B}_0 \right) + m_{\text{e}} n_{\text{e}} \bar{\nu}_{\text{ei}} \boldsymbol{u}_{\text{e1}}
\end{aligned}
\tag{2.40}
$$

Further, we find in the perpendicular component of the ion equation that even for $\omega \sim \bar{\nu}_{\text{ei}}$ the collision term is much smaller than the inertial term by $\mathcal{O}\left( m_{\text{e}}/m_{\text{i}} \right)$. Consequently, we could neglect the collision term in the ion equation and consider the collisional effect only in the electron equation. The end result is that the electron mass $m_{\text{e}}$ is simply replaced by the quantity $m_{\text{e}} \left( 1 + i\bar{\nu}_{\text{ei}}/\omega \right)$, which is the same conclusion given by Stix [46]. Using this newly-defined "electron mass," the resonances described in Section 2.4.4 do not occur, since the quantity $\varepsilon_\perp$ now has a nonzero imaginary part so that $\varepsilon_\perp \neq 0$ or $n_\parallel^2 - \varepsilon_\perp \neq 0$ at every point in the calculation domain for any density variation. The wavenumber is then kept finite in the resonance region, and the corresponding wave can be well resolved with sufficiently fine grids. Of course, we do not need to consider the collisional effect if it is assured that no resonance occurs in the calculation domain.

## 2.6   A Condition for Sheath Formation

The previous sections have provided an overview of the wave phenomena observed in the edge plasma. The rest of this chapter will mainly be devoted to the descriptions of the sheath physics, which is the central theme in this study.

First, let us consider a condition for the thermal sheath to be formed on a metal wall when the magnetic field line intersects with the wall at a sufficiently large angle $\vartheta$. The origin of the sheath formation is the difference in thermal velocity between the electrons and ions at a conductor surface, where both species try to leave plasma. Since the electrons always move along the field lines faster than the ions due to their smaller mass, it would be natural to gather that the electrons become scarcer than the

ions in the close vicinity of the metal wall. When this really happens, the potential barrier inside the sheath plays a role to confine the electrons and restore charge ambipolarity in the plasma; in fact, the potential drop and sheath width $\Delta_{\mathrm{sh}}$ (defined later) are determined such that the net flux to the wall vanishes in steady state. For electrons and ions having the velocity components $v_{\mathrm{en}}$ and $v_{\mathrm{in}}$ perpendicular to the wall, the following relation is required to be satisfied for the thermal sheath to be retained at the wall:

$$\frac{\Delta_{\mathrm{sh}}}{v_{\mathrm{en}}} < \frac{\Delta_{\mathrm{sh}}}{v_{\mathrm{in}}} \tag{2.41}$$

Equation (2.41) indicates that the electron transit time across the sheath needs to be smaller compared to the ion transit time. Here the velocity components $v_{\mathrm{en}}$ and $v_{\mathrm{in}}$ are, respectively, evaluated as follows:

$$v_{\mathrm{en}} \sim v_{\mathrm{te}} \sin \vartheta \tag{2.42}$$

$$v_{\mathrm{in}} \sim c_{\mathrm{s}} \tag{2.43}$$

where $v_{\mathrm{te}}$ is the electron thermal speed defined as $v_{\mathrm{te}} = (2T_{\mathrm{e}}/m_{\mathrm{e}})^{1/2}$, $c_{\mathrm{s}}$ is the acoustic velocity defined as $c_{\mathrm{s}} = (T_{\mathrm{e}}/m_{\mathrm{i}})^{1/2}$, and $\sin \vartheta = |B_{\mathrm{n}}/B|$, where $B_{\mathrm{n}}$ is the perpendicular component of the background magnetic field to the wall. Note that Equation (2.43) comes from the Bohm sheath criterion [45]. Then, substituting Equations (2.42) and (2.43) into Equation (2.41) yields

$$\vartheta \gtrsim \left(\frac{m_{\mathrm{e}}}{m_{\mathrm{i}}}\right)^{1/2} \tag{2.44}$$

This is the required angle for the sheath formation. If the magnetic field line is close to be parallel to the metal wall, the electron loss would be negligibly small due to the gyro motion. Therefore, having a lower limit of the contact angle as described in Equation (2.44) is physically reasonable.

Most situations of practical interest for sheaths in a tokamak obey the condition shown in Equation (2.44). This type of sheath is sometimes called an ion-rich sheath (since the electrons are mostly excluded from the sheath region). For smaller angles, the ions can actually be lost to the wall faster than the electrons, resulting in an entirely different sheath structure (i.e., electron-rich sheath; see Reference [47]). However, this situation will not be considered in this thesis.

The discussion in this section assumes that RF electric fields are not present. If they exist, the electrons are further accelerated along the field lines, so that the RF driven sheaths can have higher voltage than the thermal (Bohm) sheaths considered here. The details of the Bohm and RF sheath potentials will be discussed in more depth in Section 2.8.

## 2.7    Derivation of the Sheath Boundary Condition

In the previous subsection we find that an ion-rich sheath can be formed on the metal wall when the magnetic field line intersects with the wall at an angle larger than $(m_e/m_i)^{1/2}$. The next question is how we should take into account the sheath region in the present numerical analysis. Recall that our interest includes the physics of plasma in the SOL, whose characteristic length is several orders of magnitude greater than a typical sheath width (the order of the Debye length). Then it would be virtually impossible to calculate detailed wave phenomena in the SOL and sheath simultaneously, since these two spatial scales are so different that a prohibitively large number of grids would be required in numerical simulation if the grid size is adjusted to the size which is sufficient to resolve the physics in the sheath region (it is true even if we use a nonuniform mesh, since the adjacent grid sizes should not be vastly different for a stable calculation). Furthermore, kinetic effects must be considered if we aim to investigate the correct physics inside the sheath, which raises a question of how to naturally connect with the cold plasma formulation in the SOL (of course,
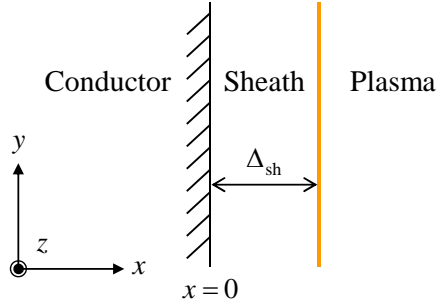
Figure 2-2: Slab model with a flat wall for the derivation of the sheath boundary conditions.

we can apply the kinetic equations even in the SOL, but it will make computational cost truly enormous since in general the integrals have to be evaluated numerically).

The above-mentioned difficulties, however, can be solved if we make some reasonable approximations for the sheath. Surprisingly, the sheath effect can then be taken into account without resolving the sheath region; in fact, by means of a boundary condition. This is the "sheath boundary condition," which was first derived by Myra et al. for the full electromagnetic case [27] and later improved to a self-consistent form by D'Ippolito and Myra [33]. The purpose of this section is to review the derivation of the sheath boundary condition by reference to their previous work and recent supplements [48, 49]. First, the analysis is conducted for the case of an electromagnetic wave incident on a flat wall. Then, the derived sheath boundary condition is verified with a curved wall based on a general curvilinear coordinate system.

## 2.7.1  Sheath Boundary Condition for a Flat Wall

The geometry considered here is shown in Figure 2-2. The sheath is assumed to be planar with the time-averaged characteristic width $\Delta_{\rm sh}$ and sandwiched between the conductor (left) and the plasma (right). The Cartesian coordinate system is employed for the subsequent calculation; the $y$-$z$ plane is set parallel to the conductor, and $x = 0$ is positioned at the left edge of the sheath.

In the sheath region electrons are excluded due to the potential barrier so that

36

the electron density there is much smaller compared to that in the plasma away from the sheath. Thus, the coefficients $\varepsilon_\perp$, $\varepsilon_\parallel$, and $\varepsilon_\times$ in the dielectric tensor can be approximated as $\varepsilon_\perp \simeq \varepsilon_\parallel \simeq 1$ and $\varepsilon_\times \simeq 0$ (see Equation (2.13)). As a result, the dielectric tensor is reduced to $\boldsymbol{\varepsilon} \simeq \boldsymbol{I}$ as is evident from Equation (2.12), and we see that $\boldsymbol{\sigma} \simeq \boldsymbol{0}$ (in Equation (2.11)) and then $\boldsymbol{J}_{\mathrm{ind}} \simeq \boldsymbol{0}$ (in Equation (2.9)). In addition, we notice that $\boldsymbol{n} \cdot \boldsymbol{E} = 0$ from Equation (2.15). Consequently, Equation (2.16) is simplified as

$$\left(n^2 - 1\right) \boldsymbol{E} = \boldsymbol{0}$$

which yields the following dispersion relation:

$$n^2 = 1 \tag{2.45}$$

This is identical with the dispersion relation in vacuum. The results shown here indicate that the sheath is reasonably modeled as a vacuum layer of the same width.

Next, let us consider that the electric field in the sheath (vacuum) region, $\boldsymbol{E}^{(\mathrm{sh})}$, is expressed by the two linearly independent vectors, namely, the transverse electric (TE) and transverse magnetic (TM) modes:

$$\boldsymbol{E}^{(\mathrm{sh})} = C_{\mathrm{e}} \boldsymbol{E}_{\mathrm{TE}} + C_{\mathrm{m}} \boldsymbol{E}_{\mathrm{TM}} \tag{2.46}$$

where $C_{\mathrm{e}}$ and $C_{\mathrm{m}}$ are arbitrary constants. The TE mode of the electric field, $\boldsymbol{E}_{\mathrm{TE}}$, is defined such that $E_{\mathrm{TE}x} = 0$, while the TM mode of the electric field, $\boldsymbol{E}_{\mathrm{TM}}$, is defined such that $B_{\mathrm{TM}x} = 0$. Assuming a wave of the form $\exp\left(ik_y y + ik_z z\right)$ in the $y$-$z$ plane and a standing wave $\sin\left(k_x x\right)$ in the $x$ direction, and noting that the boundary condition $\boldsymbol{E}_{\mathrm{t}}^{(\mathrm{sh})} = \boldsymbol{0}$ (vanishing tangential components) must be satisfied at $x = 0$,

the electric fields $\boldsymbol{E}_{\mathrm{TE}}$ and $\boldsymbol{E}_{\mathrm{TM}}$ are expressed in the following form:

$$\boldsymbol{E}_{\mathrm{TE}} = \mathrm{e}^{i(k_y y + k_z z - \omega t)} \left[ 0, \, a_1 \sin(k_x x), \, a_2 \sin(k_x x) \right] \tag{2.47}$$

$$\boldsymbol{E}_{\mathrm{TM}} = \mathrm{e}^{i(k_y y + k_z z - \omega t)} \left[ b_1 \cos(k_x x), \, b_2 \sin(k_x x), \, b_3 \sin(k_x x) \right] \tag{2.48}$$

The procedure to determine the coefficients $a_1$, $a_2$, $b_1$, $b_2$, and $b_3$ is as follows. First, since we assume that $\boldsymbol{J}_{\mathrm{ind}} = \boldsymbol{0}$ in the sheath, it is required that $\nabla \cdot \boldsymbol{E}^{(\mathrm{sh})} = 0$, which in turn $\nabla \cdot \boldsymbol{E}_{\mathrm{TE}} = 0$ and $\nabla \cdot \boldsymbol{E}_{\mathrm{TM}} = 0$. The divergence-free condition of $\boldsymbol{E}_{\mathrm{TE}}$ leads to

$$ik_y a_1 + ik_z a_2 = 0$$

Then we can choose $a_1 = -n_z \; (= -ck_z/\omega)$ and $a_2 = n_y$, and get

$$\boldsymbol{E}_{\mathrm{TE}} = \mathrm{e}^{i(k_y y + k_z z - \omega t)} \left[ 0, \, -n_z \sin(k_x x), \, n_y \sin(k_x x) \right] \tag{2.49}$$

Similarly, the divergence-free condition of $\boldsymbol{E}_{\mathrm{TM}}$ yields

$$-k_x b_1 + ik_y b_2 + ik_z b_3 = 0$$

Also, the definition of the TM mode requires that $\nabla \times \boldsymbol{E}_{\mathrm{TM}}|_x = 0$, leading to

$$-k_z b_2 + k_y b_3 = 0$$

Thus, we can choose $b_1 = n_y^2 + n_z^2$, $b_2 = -in_x n_y$, and $b_3 = -in_x n_z$. Consequently, Equation (2.48) is rewritten as

$$\boldsymbol{E}_{\mathrm{TM}} = \mathrm{e}^{i(k_y y + k_z z - \omega t)} \left[ \left( n_y^2 + n_z^2 \right) \cos(k_x x), \, -in_x n_y \sin(k_x x), \, -in_x n_z \sin(k_x x) \right] \tag{2.50}$$

It is easily confirmed from Equations (2.49) and (2.50) that $\boldsymbol{E}_{\mathrm{TE}} \cdot \boldsymbol{E}_{\mathrm{TM}} = 0$.

Without loss of generality, the tangential component of the wavevector can be

aligned parallel to the $z$ axis. Then we can set $k_y = 0$, and the electric field in the sheath is written as

$$
\boldsymbol{E}^{(\text{sh})} = \left[ C_{\text{e}} \begin{pmatrix} 0 \\ -n_z \sin\left(k_x x\right) \\ 0 \end{pmatrix} + C_{\text{m}} \begin{pmatrix} n_z^2 \cos\left(k_x x\right) \\ 0 \\ -i n_x n_z \sin\left(k_x x\right) \end{pmatrix} \right] \mathrm{e}^{i(k_z z - \omega t)} \tag{2.51}
$$

The corresponding magnetic field, $\boldsymbol{B}^{(\text{sh})}$, is obtained using Faraday's law as follows:

$$
\boldsymbol{B}^{(\text{sh})} = \left[ C_{\text{e}} \begin{pmatrix} n_z^2 \sin\left(k_x x\right) \\ 0 \\ i n_x n_z \cos\left(k_x x\right) \end{pmatrix} + C_{\text{m}} \begin{pmatrix} 0 \\ n_z \cos\left(k_x x\right) \\ 0 \end{pmatrix} \right] \mathrm{e}^{i(k_z z - \omega t)}/c \tag{2.52}
$$

Here the vacuum dispersion relation (2.45) is employed.

Since the transition between the sheath and plasma regions is smooth, the following conditions of continuity must be satisfied at the sheath-plasma boundary:

$$
\boldsymbol{E}_{\text{t}}^{(\text{sh})} = \boldsymbol{E}_{\text{t}}^{(\text{pl})} = \tilde{\boldsymbol{E}}_{\text{t}}^{(\text{pl})} \mathrm{e}^{i(k_z z - \omega t)} \tag{2.53}
$$

$$
D_{\text{n}}^{(\text{sh})} = \varepsilon_{\text{sh}} E_{\text{n}}^{(\text{sh})} = D_{\text{n}}^{(\text{pl})} = \tilde{D}_{\text{n}}^{(\text{pl})} \mathrm{e}^{i(k_z z - \omega t)} \tag{2.54}
$$

where the superscript pl denotes the quantities on the plasma side, and the subscripts t and n denote the tangential and normal components to the boundary, respectively. In Equation (2.54) $D_{\text{n}}$ is the normal component of the electric displacement, and $\varepsilon_{\text{sh}}$ is the dielectric constant in the sheath, which is assumed to be equal to $\varepsilon_0$ in vacuum. Substituting Equation (2.51) into Equations (2.53) and (2.54) yields

$$
\tilde{E}_y^{(\text{pl})} = -C_{\text{e}} n_z \sin\left(k_x \Delta_{\text{sh}}\right) \tag{2.55}
$$

$$
\tilde{E}_z^{(\text{pl})} = -i C_{\text{m}} n_x n_z \sin\left(k_x \Delta_{\text{sh}}\right) \tag{2.56}
$$

$$
\tilde{D}_x^{(\text{pl})} = \varepsilon_{\text{sh}} C_{\text{m}} n_z^2 \cos\left(k_x \Delta_{\text{sh}}\right) \tag{2.57}
$$

In addition, Ampere's law and Gauss's law for magnetism give the following conditions of continuity:

$$\boldsymbol{B}_{\mathrm{t}}^{(\mathrm{sh})} = \boldsymbol{B}_{\mathrm{t}}^{(\mathrm{pl})} = \tilde{\boldsymbol{B}}_{\mathrm{t}}^{(\mathrm{pl})}\mathrm{e}^{i(k_z z - \omega t)} \tag{2.58}$$

$$B_{\mathrm{n}}^{(\mathrm{sh})} = B_{\mathrm{n}}^{(\mathrm{pl})} = \tilde{B}_{\mathrm{n}}^{(\mathrm{pl})}\mathrm{e}^{i(k_z z - \omega t)} \tag{2.59}$$

Substituting Equation (2.52) into Equations (2.58) and (2.59), one gets

$$\tilde{B}_y^{(\mathrm{pl})} = C_{\mathrm{m}} n_z \cos\left(k_x \Delta_{\mathrm{sh}}\right)/c \tag{2.60}$$

$$\tilde{B}_z^{(\mathrm{pl})} = i C_{\mathrm{e}} n_x n_z \cos\left(k_x \Delta_{\mathrm{sh}}\right)/c \tag{2.61}$$

$$\tilde{B}_x^{(\mathrm{pl})} = C_{\mathrm{e}} n_z^2 \sin\left(k_x \Delta_{\mathrm{sh}}\right)/c \tag{2.62}$$

We have so far six relations in Equations (2.55)–(2.57) and Equations (2.60)–(2.62). However, two of them are redundant. This is confirmed by Faraday's law and Ampere's law on the plasma side. First, Faraday's law

$$\nabla \times \boldsymbol{E}^{(\mathrm{pl})} = -\frac{\partial \boldsymbol{B}^{(\mathrm{pl})}}{\partial t} = i\omega \boldsymbol{B}^{(\mathrm{pl})}$$

yields

$$B_x^{(\mathrm{pl})} = -\frac{k_z}{\omega} E_y^{(\mathrm{pl})}$$

which proves that Equation (2.55) is identical with Equation (2.62). Second, Ampere's law

$$\nabla \times \boldsymbol{B}^{(\mathrm{pl})} = \mu_0 \frac{\partial \boldsymbol{D}^{(\mathrm{pl})}}{\partial t} = -i\omega \mu_0 \boldsymbol{D}^{(\mathrm{pl})}$$

gives

$$D_x^{(\mathrm{pl})} = \frac{k_z}{\omega\mu_0} B_y^{(\mathrm{pl})}$$

which shows that Equations (2.57) and (2.60) are redundant. Therefore, the independent equations are

$$\tilde{E}_z^{(\mathrm{pl})} = -iC_{\mathrm{m}}n_xn_z \sin\left(k_x\Delta_{\mathrm{sh}}\right)$$

$$\tilde{D}_x^{(\mathrm{pl})} = \varepsilon_{\mathrm{sh}}C_{\mathrm{m}}n_z^2 \cos\left(k_x\Delta_{\mathrm{sh}}\right)$$

$$\tilde{B}_z^{(\mathrm{pl})} = iC_{\mathrm{e}}n_xn_z \cos\left(k_x\Delta_{\mathrm{sh}}\right)/c$$

$$\tilde{B}_x^{(\mathrm{pl})} = C_{\mathrm{e}}n_z^2 \sin\left(k_x\Delta_{\mathrm{sh}}\right)/c$$

From these four equations we can obtain two relations by eliminating the coefficients $C_{\mathrm{e}}$ and $C_{\mathrm{m}}$. Using Equations (2.56) and (2.57), one gets

$$n_z E_z^{(\mathrm{pl})} = -in_x \frac{D_x^{(\mathrm{pl})}}{\varepsilon_{\mathrm{sh}}} \tan\left(k_x\Delta_{\mathrm{sh}}\right) \tag{2.63}$$

Similarly, Equations (2.61) and (2.62) yield

$$n_x B_x^{(\mathrm{pl})} = -in_z B_z^{(\mathrm{pl})} \tan\left(k_x\Delta_{\mathrm{sh}}\right) \tag{2.64}$$

Equations (2.63) and (2.64) show the general boundary conditions at the sheath-plasma boundary, which are derived rigorously from Maxwell's equations, except that the sheath region is approximated as vacuum space.

In the present analysis we can reasonably take the following thin-sheath limit:

$$|k_x\Delta_{\mathrm{sh}}| \ll 1 \tag{2.65}$$

The evidence is as follows. If Equation (2.65) is correct, the following inequality must

41

also be satisfied:

$$\left(\frac{\omega}{c}\right)^2 \Delta_{\text{sh}}^2 - k_z^2 \Delta_{\text{sh}}^2 \ll 1$$

As will be shown later, the sheath width can be estimated to be in the order of the electron Debye length. Then, in ICRF ($f = 80$ MHz) we can surely confirm that $\omega \Delta_{\text{sh}}/c \ll 1$. Also, as will be evident in later numerical analyses, the condition $|k_z \Delta_{\text{sh}}| \ll 1$ is usually satisfied. The approximation (2.65) simplifies the previous results as follows:

$$ik_z E_z^{(\text{pl})} = \left(k_0^2 - k_z^2\right) \frac{\Delta_{\text{sh}}}{\varepsilon_{\text{sh}}} D_x^{(\text{pl})} \tag{2.66}$$

$$B_x^{(\text{pl})} = -ik_z \Delta_{\text{sh}} B_z^{(\text{pl})} \tag{2.67}$$

where $k_0 = \omega/c$. Due to Faraday's law, we notice that $B_x^{(\text{pl})} = -k_z E_y^{(\text{pl})}/\omega$ and $B_z^{(\text{pl})} \simeq k_{x,\text{p}} E_y^{(\text{pl})}/\omega$, where $k_{x,\text{p}}$ is the characteristic wavenumber in the $x$ direction on the plasma side. Then Equation (2.67) is rewritten as

$$\left(1 - ik_{x,\text{p}} \Delta_{\text{sh}}\right) B_x^{(\text{pl})} \simeq 0 \tag{2.68}$$

Since the condition $|k_{x,\text{p}} \Delta_{\text{sh}}| \ll 1$ is usually satisfied, Equation (2.68) can be simply approximated as

$$B_x^{(\text{pl})} \simeq 0 \tag{2.69}$$

On the other hand, the right-hand side of Equation (2.66) cannot be neglected in general since the coefficient $\varepsilon_\parallel$ is large.

If the conductor and plasma are located in the opposite way with respect to the sheath, we can still follow the same procedure as above, but notice the following change: $\tan\left(k_x \Delta_{\text{sh}}\right) \to -\tan\left(k_x \Delta_{\text{sh}}\right)$. Thus, the result corresponding to Equation

(2.66) becomes

$$ik_z E_z^{(pl)} = - \left( k_0^2 - k_z^2 \right) \frac{\Delta_{sh}}{\varepsilon_{sh}} D_x^{(pl)} \tag{2.70}$$

at the sheath-plasma boundary.

Consequently, in the thin-sheath limit we can write the sheath boundary conditions in differential form as follows:

$$\nabla_t \cdot \boldsymbol{E}_t^{(pl)} = \left( k_0^2 + \nabla_t^2 \right) \left( \frac{\Delta_{sh}}{\varepsilon_{sh}} D_n^{(pl)} \right) \tag{2.71}$$

$$B_n^{(pl)} = 0 \tag{2.72}$$

where the subscript n denotes the perpendicular direction to the sheath pointing to the plasma side, and the subscript t denotes the plane tangential to the sheath. It should be emphasized here that the above boundary conditions are described only with the fields on the plasma side, which makes it unnecessary to resolve the narrow sheath region in numerical analysis.

## 2.7.2 Electrostatic Approximation

In ICRF the value of $k_0$ is usually much smaller compared to that of $k_t$ (or $k_z$ here). Then Equation (2.66) can be approximated as

$$E_z^{(pl)} = ik_z \frac{\Delta_{sh}}{\varepsilon_{sh}} D_x^{(pl)} \tag{2.73}$$

which leads to the following sheath boundary condition in differential form:

$$\boldsymbol{E}_t^{(pl)} = \nabla_t \left( \frac{\Delta_{sh}}{\varepsilon_{sh}} D_n^{(pl)} \right) \tag{2.74}$$

In fact, neglecting $k_0$ (or assuming that $n^2 \simeq 0$) in Equation (2.66) corresponds to the electrostatic approximation in vacuum. This is easily confirmed by approximating

$\varepsilon \simeq \boldsymbol{I}$ in Equation (2.25).

In the electrostatic limit, the electric field in the sheath must be expressed using the electric potential $\Phi^{(\mathrm{sh})}$ as follows:

$$\boldsymbol{E}^{(\mathrm{sh})} = -\nabla \Phi^{(\mathrm{sh})} \tag{2.75}$$

In this case the corresponding magnetic field is zero due to Faraday's law so that Equation (2.72) is automatically satisfied (and thus redundant). In order for Equation (2.46) to be consistent with Equation (2.75), we require that $C_{\mathrm{e}} \to 0$. Then the electric potential $\Phi^{(\mathrm{sh})}$ is explicitly expressed as

$$\Phi^{(\mathrm{sh})} = -C_{\mathrm{m}} \frac{c}{\omega} n_x \sin\left(k_x x\right) \mathrm{e}^{i(k_z z - \omega t)} \tag{2.76}$$

Notice again that we employ $n^2 \simeq 0$. In the thin-sheath limit Equation (2.76) is approximated as

$$\Phi^{(\mathrm{sh})} \simeq -C_{\mathrm{m}} n_x^2 x \mathrm{e}^{i(k_z z - \omega t)} \tag{2.77}$$

The important fact here is that the electric potential is linearly varied in the perpendicular direction to the metal (or sheath) surface.

### 2.7.3 Verification with a Curved Wall

The sheath boundary condition (2.74) in the previous subsection was calculated based on the assumption of a flat wall, in which the sheath width $\Delta_{\mathrm{sh}}$ is constant. In order to verify the obtained result, let us consider next the curved geometry shown in Figure 2-3. Here, it is assumed that in a general curvilinear coordinate system $(\tau, \upsilon, z)$ the metal-sheath and sheath-plasma boundaries are located at $\upsilon = 0$ and $\upsilon = \delta$, respectively, and the wave has a variation of $\exp\left(i k_z z\right)$ in space.

In the electrostatic limit, the electric field in the sheath is expressed as shown in

44
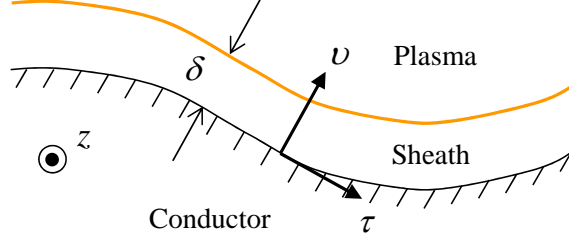
Figure 2-3: Geometry showing a curved sheath in curvilinear coordinates.

Equation (2.75). The expression for the electric potential $\Phi^{(\mathrm{sh})}$ should be in principle obtained by solving Laplace's equation subject to the boundary conditions at the two surfaces, namely, $\Phi^{(\mathrm{sh})}(\tau, 0) = 0$ and $\Phi^{(\mathrm{sh})}(\tau, \delta) = \Phi_{\mathrm{s}}(\tau)$. However, in the thin-sheath limit, it would be a reasonable ansatz to have the electric potential of the form

$$\Phi^{(\mathrm{sh})} = \Phi_{\mathrm{s}}(\tau)\frac{\upsilon}{\delta} = \tilde{\Phi}_{\mathrm{s}}(\tau)\frac{\upsilon}{\delta}\mathrm{e}^{i(k_z z - \omega t)} \tag{2.78}$$

from the result in Equation (2.77).

In the curvilinear coordinates considered here, the covariant base vectors $\boldsymbol{g}_i$ ($i = 1, 2, 3$) are defined as follows:

$$\begin{aligned}
\frac{\partial \boldsymbol{r}}{\partial x^1} &= \frac{\partial \boldsymbol{r}}{\partial \tau} = \boldsymbol{g}_1 = h\boldsymbol{e}_\tau \\
\frac{\partial \boldsymbol{r}}{\partial x^2} &= \frac{\partial \boldsymbol{r}}{\partial \upsilon} = \boldsymbol{g}_2 = q\boldsymbol{e}_\upsilon \\
\frac{\partial \boldsymbol{r}}{\partial x^3} &= \frac{\partial \boldsymbol{r}}{\partial z} = \boldsymbol{g}_3 = \boldsymbol{e}_z
\end{aligned} \tag{2.79}$$

where $\boldsymbol{r}$ is the position vector, and $x^1 = \tau$, $x^2 = \upsilon$, $x^3 = z$; $\boldsymbol{e}_\tau$, $\boldsymbol{e}_\upsilon$, and $\boldsymbol{e}_z$ are the unit vectors in the $\tau$, $\upsilon$, and $z$ directions, respectively. In general $h$ and $q$ are the functions of $\tau$ and $\upsilon$. Since the relation between the covariant base vectors and the corresponding contravariant base vectors $\boldsymbol{g}^j$ is

$$\boldsymbol{g}_i \cdot \boldsymbol{g}^j = \delta_i^j \tag{2.80}$$

($\delta_i^j$ is the Kronecker delta), the contravariant base vectors for these coordinates are

$$\boldsymbol{g}^1 = \frac{1}{h}\boldsymbol{e}_\tau, \quad \boldsymbol{g}^2 = \frac{1}{q}\boldsymbol{e}_v, \quad \boldsymbol{g}^3 = \boldsymbol{e}_z \tag{2.81}$$

Then the gradient of $\Phi^{(\mathrm{sh})}$ is written as follows:

$$\begin{aligned}
\nabla\Phi^{(\mathrm{sh})} &= \frac{\partial\Phi^{(\mathrm{sh})}}{\partial x^i}\boldsymbol{g}^i \\
&= \frac{1}{h}\frac{\partial\Phi^{(\mathrm{sh})}}{\partial\tau}\boldsymbol{e}_\tau + \frac{1}{q}\frac{\partial\Phi^{(\mathrm{sh})}}{\partial v}\boldsymbol{e}_v + ik_z\Phi^{(\mathrm{sh})}\boldsymbol{e}_z
\end{aligned} \tag{2.82}$$

where the summation convention applies to the superscript $i$. Substituting Equation (2.78) into Equation (2.82), and using Equation (2.75) yields the following expression for the electric field in the sheath:

$$\boldsymbol{E}^{(\mathrm{sh})} = -\frac{v}{h\delta}\frac{d\Phi_{\mathrm{s}}}{d\tau}\boldsymbol{e}_\tau - \frac{\Phi_{\mathrm{s}}}{q\delta}\boldsymbol{e}_v - ik_z\Phi_{\mathrm{s}}\frac{v}{\delta}\boldsymbol{e}_z \tag{2.83}$$

Then at $v = \delta$ one gets

$$\begin{aligned}
\boldsymbol{E}_{\mathrm{t}}^{(\mathrm{sh})} &= -\frac{1}{h}\frac{d\Phi_{\mathrm{s}}}{d\tau}\boldsymbol{e}_\tau - ik_z\Phi_{\mathrm{s}}\boldsymbol{e}_z \\
E_{\mathrm{n}}^{(\mathrm{sh})} &= -\frac{\Phi_{\mathrm{s}}}{q\delta}
\end{aligned} \tag{2.84}$$

Now recall that we can employ two conditions of continuity in terms of the electric field at the sheath-plasma boundary, which are shown in Equations (2.53) and (2.54). First, continuity of the tangential electric field components simply gives the following relation at the surface $v = \delta$:

$$\boldsymbol{E}_{\mathrm{t}}^{(\mathrm{sh})} = \boldsymbol{E}_{\mathrm{t}}^{(\mathrm{pl})} = -\nabla_{\mathrm{t}}\Phi_{\mathrm{s}} \tag{2.85}$$

Second, continuity of the normal electric displacement together with Equation (2.84)

46

yields the expression for the electric potential $\Phi_s$ as follows:

$$\Phi_s = -\frac{q\delta}{\varepsilon_{sh}} D_n^{(pl)} \tag{2.86}$$

Notice that $\Delta_{sh} \simeq q\delta$ in the thin-sheath limit where $q \simeq q(\tau)$. Consequently, substituting Equation (2.86) into Equation (2.85), we obtain the sheath boundary condition of the form

$$\boldsymbol{E}_t^{(pl)} = \nabla_t \left( \frac{\Delta_{sh}}{\varepsilon_{sh}} D_n^{(pl)} \right) \tag{2.87}$$

which is identical with Equation (2.74). Therefore, at least in the lowest order, we could conclude that the sheath boundary condition (2.87) is valid for any curved (but reasonably smoothed) geometry with the assumption that the sheath is vacuum, thin, and electrostatic. Here note that the sheath width $\Delta_{sh}$ should appear inside the nabla operator. An important physical observation is that for $\Delta_{sh} \to 0$ the sheath boundary condition naturally reduces to the conducting-wall boundary condition, where the tangential electric field components are zero at the boundary.

## 2.8 Evaluation of Sheath Width

The next step which is necessary to employ the sheath boundary condition (2.87) is to determine the sheath width $\Delta_{sh}$. In this study the sheath width is assumed to satisfy the Child-Langmuir law [50, 51]

$$\Delta_{sh} = \lambda_{De} \left( \frac{eV_0}{T_e} \right)^{3/4} \tag{2.88}$$

where $\lambda_{De}$ is the electron Debye length defined as $\lambda_{De} = (\varepsilon_0 T_e / n_{e0} e^2)^{1/2}$, and $V_0$ is the rectified (DC) sheath potential. The choice of $V_0$ depends on the magnitude of $eV_{sh}/T_e$, which will be described in the following subsections (including the definition

of $V_{\mathrm{sh}}$).

This Child-Langmuir law should be valid when $\boldsymbol{E} \times \boldsymbol{B}$ drifts and finite ion Larmor radius can be neglected. These conditions may break down in some cases, such as when the background magnetic field intersects at a very small angle with the surface. However, as mentioned in Section 2.6, this is beyond the scope of this thesis research.

## 2.8.1 Sheath Width for $V_0 \sim V_{\mathrm{B}}$

First, let us recall the derivation of the Bohm sheath criterion [45]. With the assumption that $T_{\mathrm{i}} \ll T_{\mathrm{e}}$ and the electrostatic approximation, the ion and electron densities are, respectively, expressed as follows:

$$n_{\mathrm{i0}} = n_0 \left( 1 - \frac{2e\phi}{m_{\mathrm{i}} u_0^2} \right)^{-1/2} \tag{2.89}$$

$$n_{\mathrm{e0}} = n_0 \exp \left( \frac{e\phi}{T_{\mathrm{e}}} \right) \tag{2.90}$$

where $\phi$ is the negative electric potential which approaches zero with increasing distance from the sheath, and $u_0$ is the ion velocity, which is perpendicular to the sheath, at the point where $\phi = 0$ (see Figure 2-4). Here assume that $u_0 \gtrsim c_{\mathrm{s}}$ for the sheath formation (see Section 2.6), which is equivalent to

$$\frac{m_{\mathrm{i}} u_0^2}{T_{\mathrm{e}}} \sim 1 \tag{2.91}$$

Then, from Equations (2.89) and (2.91) we notice that $n_{\mathrm{i0}} \simeq n_0$ for $|e\phi/T_{\mathrm{e}}| \ll 1$.

Due to the formation of the sheath, the ions are accelerated inside the sheath, while most of the electrons are reflected by the potential barrier; i.e., the role of the sheath is to preserve charge ambipolarity in the plasma in such a way as briefly described in Section 2.6. Based on this standpoint, the Bohm sheath potential $V_{\mathrm{B}}$ ($> 0$) is defined such that the electron flux becomes equal to the ion flux at the wall.
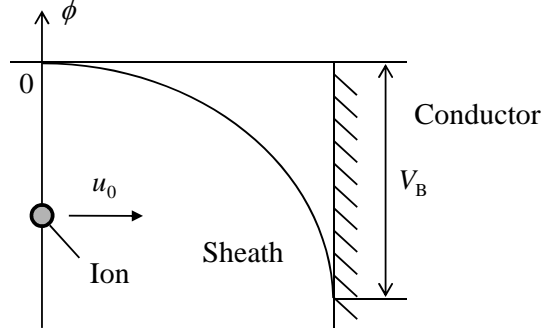
Figure 2-4: A profile of the electric potential in a planar sheath and a ballistic ion entering with the velocity $u_0$.

Namely, for $n_{i0} \simeq n_0$ we obtain

$$n_0 e v_{in} - n_0 e^{-eV_B/T_e} e v_{en} = 0$$

which yields

$$\frac{v_{en}}{v_{in}} = e^{eV_B/T_e} \tag{2.92}$$

Substituting Equations (2.42) and (2.43) into Equation (2.92) leads to the following approximate expression for $V_B$:

$$V_B \simeq \frac{T_e}{e} \ln\left[\left(\frac{m_i}{m_e}\right)^{1/2} \sin\vartheta\right] \tag{2.93}$$

When the rectified sheath potential is the same order as the Bohm sheath potential $(V_0 \sim V_B)$, the corresponding sheath width is evaluated as

$$\Delta_{sh} = C_{th}\lambda_{De} \tag{2.94}$$

49

where

$$C_{\mathrm{th}} = \left\{ \ln \left[ \left( \frac{m_{\mathrm{i}}}{m_{\mathrm{e}}} \right)^{1/2} \sin \vartheta \right] \right\}^{3/4} \tag{2.95}$$

Notice that the sheath width is a function of the contact angle. At this point it is important to keep in mind that Equation (2.95) is not valid when $\vartheta < (m_{\mathrm{e}}/m_{\mathrm{i}})^{1/2}$ due to the criterion (2.44) derived in Section 2.6. If the calculated contact angle at some point on the wall becomes less than $(m_{\mathrm{e}}/m_{\mathrm{i}})^{1/2}$ in numerical analysis, a useful remedy would be to switch the value of $C_{\mathrm{th}}$ to zero, i.e.,

$$C_{\mathrm{th}} = \begin{cases} 0 & \text{for } \vartheta \le (m_{\mathrm{e}}/m_{\mathrm{i}})^{1/2} \\[2ex] \left\{ \ln \left[ \left( \frac{m_{\mathrm{i}}}{m_{\mathrm{e}}} \right)^{1/2} \sin \vartheta \right] \right\}^{3/4} & \text{for } \vartheta > (m_{\mathrm{e}}/m_{\mathrm{i}})^{1/2} \end{cases} \tag{2.96}$$

The transition between the two cases is smooth since $C_{\mathrm{th}} = 0$ for $\sin \vartheta = (m_{\mathrm{e}}/m_{\mathrm{i}})^{1/2}$.

## 2.8.2 Sheath Width for $V_0 \sim V_{\mathrm{sh}}$

Next, consider the case where the rectified sheath potential is the same order as the instantaneous sheath voltage $V_{\mathrm{sh}}$ defined by

$$V_{\mathrm{sh}} \equiv \left| \int E_{\mathrm{n}}^{(\mathrm{sh})} dn \right| \simeq \Delta_{\mathrm{sh}} \left| E_{\mathrm{n}}^{(\mathrm{sh})} \right| \tag{2.97}$$

The integral in Equation (2.97) is taken across the sheath in the direction normal to the wall. Using the expression that $V_0 = C_{\mathrm{sh}} V_{\mathrm{sh}}$ where $C_{\mathrm{sh}}$ is an order-unity constant giving the rectification factor [11], Equation (2.88) becomes

$$\Delta_{\mathrm{sh}} = \lambda_{\mathrm{De}} \left( \frac{e C_{\mathrm{sh}} V_{\mathrm{sh}}}{T_{\mathrm{e}}} \right)^{3/4} \tag{2.98}$$

Substituting Equation (2.97) into Equation (2.98) yields

$$\Delta_{\text{sh}} = \left( \frac{eC_{\text{sh}}}{T_{\text{e}}} \left| E_{\text{n}}^{(\text{sh})} \right| \right)^3 \lambda_{\text{De}}^4 \tag{2.99}$$

Due to the continuity of the normal electric displacement at the sheath surface (see Equation (2.54)), Equation (2.99) can be further rewritten as follows:

$$\Delta_{\text{sh}} = \left( \frac{eC_{\text{sh}}}{\varepsilon_{\text{sh}} T_{\text{e}}} \left| D_{\text{n}}^{(\text{pl})} \right| \right)^3 \lambda_{\text{De}}^4 \tag{2.100}$$

Notice that the sheath boundary condition becomes nonlinear for this case. From Equation (2.100) we find that the sheath width can be largely increased by the RF waves with high electric-field strength.

### 2.8.3   Approximate Expression for the Sheath Width

Based on the results obtained in the previous subsections, a useful approximate expression for the sheath width would be written as follows:

$$\Delta_{\text{sh}} = \left( \frac{eC_{\text{sh}}}{\varepsilon_{\text{sh}} T_{\text{e}}} \left| D_{\text{n}}^{(\text{pl})} \right| \right)^3 \lambda_{\text{De}}^4 + C_{\text{th}} \lambda_{\text{De}} \tag{2.101}$$

The accuracy of this expression is valid for $eV_{\text{sh}}/T_{\text{e}} \gg 1$ and $eV_{\text{sh}}/T_{\text{e}} \ll 1$. In the intermediate region ($eV_{\text{sh}}/T_{\text{e}} \sim 1$) the proposed form may not be so accurate, but provides a smooth interpolation between the two limits. The corresponding rectified sheath potential can be obtained from Equation (2.88) as follows:

$$V_0 = \frac{T_{\text{e}}}{e} \left( \frac{\Delta_{\text{sh}}}{\lambda_{\text{De}}} \right)^{4/3} \tag{2.102}$$

which approaches $C_{\text{sh}} V_{\text{sh}}$ for $eV_{\text{sh}}/T_{\text{e}} \gg 1$ and $V_{\text{B}}$ for $eV_{\text{sh}}/T_{\text{e}} \ll 1$.

## 2.9 Absorbing Boundary Condition

The last topic in this chapter is the boundary condition between the hot core plasma and the cold plasma in the SOL. Although there is no clear boundary between the two regions, the core plasma needs to be excluded from the calculation domain since obviously the cold plasma formulation cannot be applied to this high temperature plasma. On the other hand, one has to avoid having reflected waves from the fictitious core-edge plasma boundary since these waves are not physical. Therefore, the task here is to establish a boundary condition which enables to cut out the hot plasma region without affecting an important sheath-plasma interaction observed in the SOL.

In cases of practical interest for tokamak heating, most of the RF waves that enter the core plasma are absorbed there. As far as studying the RF sheath-plasma interactions in the SOL is concerned, it does not matter how this absorption occurs, so we can use an artificial absorption condition at the boundary of the edge and core regions. The easiest way would be to introduce a damping layer in the vicinity of the core-edge plasma boundary. Specifically, the electron-ion momentum exchange collision frequency introduced into the electron mass in Section 2.5 is replaced with

$$\nu = \nu_0 e^{-(x-x_{\mathrm{abs}})/\lambda_\nu} + C_{\mathrm{R}}\bar{\nu}_{\mathrm{ei}} \tag{2.103}$$

where $\nu_0$ is the artificial frequency, $x_{\mathrm{abs}}$ is the position of the core-side boundary of the plasma, and $\lambda_\nu$ represents the length of the damping layer. The choice of the values for $\nu_0$ and $\lambda_\nu$ depends on the calculation condition and requires some numerical experimentation. However, it is important to point out that $\nu_0$ must be much larger than the applied frequency $\omega$ to assure an appropriate damping on the core side, and the length $\lambda_\nu$ should correspond to several wavelengths of a propagating wave. The coefficient $C_{\mathrm{R}}$ in Equation (2.103) is a positive rectification factor adjusted to assure the numerical stability for a given grid resolution in the resonance region. According to the above procedure, the actual boundary condition on the core side is

not important (since $\boldsymbol{E} \to \boldsymbol{0}$ for complete absorption) so that we can impose that $\boldsymbol{E}_\mathrm{t} = \boldsymbol{0}$, for example. This condition identical with the boundary condition for a conducting wall, together with the damping layer, is called the "absorbing boundary condition" in later numerical analyses.

# Chapter 3

# Development of the rfSOL Code

## 3.1 Prologue

The goal in this chapter is to develop a numerical scheme based on the governing equations, which were derived in Chapter 2, in the 2D space, and verify its accuracy using the analytical solution and theories. For the discretization of the governing equations, a conventional finite element technique with piecewise (bi)quadratic interpolation functions [52] is employed. One of the most important advantages of the finite element method is that it can easily deal with the problems with complicated boundary shapes. Considering that an ultimate goal is to apply the developed numerical scheme to a realistic tokamak divertor geometry, this feature is indeed essential. Other important features include ease in incorporating various boundary conditions into the scheme and formation of a sparse global matrix, which makes it possible to achieve fast computation with use of state-of-art matrix solvers. In addition, the extension of the code to solve a problem in the 3D space can be conducted in a straightforward manner. Due to these favorable features, many researchers have adopted the finite element method to calculate various problems in tokamak plasmas (e.g., see References [53–56]).

The present finite element scheme is developed with the aim of achieving a fast

and accurate solver for RF sheath-plasma interaction problems. For this purpose, two special techniques are adopted in the scheme. First, the central point approximation is applied to the Jacobian and the components of the cofactor matrix in each integral of the discretized Maxwell's equation (more precisely, a combined form of Maxwell's equations). This enables the integrals to be calculated analytically without the necessity of using any numerical integration method, leading to a large increase in speed of computation, especially for plasma wave problems that require a huge number of grid points for accurate predictions. In fact, this approximation is also desirable from a stability point of view, since a high-order numerical integration method can yield unwanted numerical oscillation when the grid size becomes smaller. Second, the element average employing piecewise quadratic interpolation functions is effectively applied to the discretized equation corresponding to the sheath boundary condition. Recall that $\Delta_{\mathrm{sh}} D_{\mathrm{n}}^{(\mathrm{pl})} \propto \left| D_{\mathrm{n}}^{(\mathrm{pl})} \right|^3 D_{\mathrm{n}}^{(\mathrm{pl})}$ on the right-hand side of the sheath boundary condition for the RF sheath dominated regime. Applying the element average to the sheath width and its derivative not only achieves further speed-up of the code but also largely simplifies calculations to obtain explicit values of the global matrix components, compared to the case where every electric field component in the polynomial is naively interpolated with quadratic interpolation. In general, the techniques mentioned here are not automatically adopted in commercial finite element solvers, so that a careful derivation of the system of discretized equations is necessary.

Chapter 3 begins with the finite element discretization of Maxwell's equation (with special attention to the treatment of the antenna current) and the sheath boundary condition. For ease of understanding, the discretization procedure for the sheath boundary condition is demonstrated for a flat wall at the beginning, and then it is generalized so as to be applied to an arbitrarily-shaped curved wall. The obtained nonlinear system of discretized equations is then iteratively solved by means of a Newton-Raphson method. Here, focusing on the sparsity of the global matrix, MUMPS (MUltifrontal Massively Parallel Solver) is effectively employed for the

large-scale computation. The validity of the established numerical scheme is verified with several test problems in a 1D domain, and the performance of calculations is investigated through a scaling test at the end of this chapter.

The developed finite element code is named "rfSOL (integrated code for RF sheath-plasma interactions with a realistic SOL geometry)," and will be extensively used in the next chapter to analyze various sheath-plasma interaction problems.

## 3.2   Finite Element Discretizations

The first half of this chapter will be devoted to the description of how the new finite element code is constructed. In this section the discretization procedure for the governing equations is described with the assumption that the calculation domain is bounded by the sheath and absorbing boundary conditions. The brief overview of the present finite element formulation is as follows. First, a combined form of Maxwell's equations is multiplied by an arbitrary function (weight function) and integrated over the volume (including its surface) defining the domain, according to the standard finite element procedure. Here the arbitrary function $\boldsymbol{W}$ is chosen for convenience such that its tangential components are zero on the boundary surface. This allows the sheath boundary condition to be introduced as a Dirichlet boundary condition of the problem. Since the sheath boundary condition is expressed as a partial differential equation, it is also necessary to discretize this boundary condition using an appropriate technique. Although the choice of the discretization method for the sheath boundary condition can be arbitrary, a straightforward and efficient way is to apply the 1D finite element approach by employing a different weight function $\boldsymbol{W}^{\mathrm{S}}$ defined on the boundary. The weight functions and unknown electric field are represented on grid elements with use of piecewise-defined interpolation functions. The goal of this section is to obtain a set of coupled equations for the unknown nodal values of the electric field components in the Cartesian coordinate system.

### 3.2.1 Discretization of Maxwell's Equation

The present numerical scheme is constructed based on the weighted residual method. First, forming the inner product of Equation (2.10) with the weight function $\boldsymbol{W}$, and then integrating it over the calculation domain $\Omega$ yields

$$\int_\Omega \boldsymbol{W} \cdot \left( \nabla \times \nabla \times \boldsymbol{E} - \frac{\omega^2}{c^2} \boldsymbol{\varepsilon} \cdot \boldsymbol{E} - i\omega\mu_0 \boldsymbol{J}_{\text{ext}} \right) d\Omega = 0 \tag{3.1}$$

Due to the identity

$$\boldsymbol{W} \cdot (\nabla \times \nabla \times \boldsymbol{E}) = \nabla \times \boldsymbol{W} \cdot \nabla \times \boldsymbol{E} - \nabla \cdot [\boldsymbol{W} \times (\nabla \times \boldsymbol{E})]$$

the first term on the left-hand side of Equation (3.1) is rewritten as follows:

$$\begin{aligned}
T_1 &= \int_\Omega \boldsymbol{W} \cdot (\nabla \times \nabla \times \boldsymbol{E}) \, d\Omega \\
&= \int_\Omega \nabla \times \boldsymbol{W} \cdot \nabla \times \boldsymbol{E} \, d\Omega - \int_\Gamma \hat{\boldsymbol{n}} \cdot [\boldsymbol{W} \times (\nabla \times \boldsymbol{E})] \, d\Gamma \\
&= \int_\Omega \nabla \times \boldsymbol{W} \cdot \nabla \times \boldsymbol{E} \, d\Omega - \int_\Gamma \hat{\boldsymbol{n}} \times \boldsymbol{W} \cdot \nabla \times \boldsymbol{E} \, d\Gamma
\end{aligned}$$

where $\Gamma$ represents the boundary of the domain $\Omega$, and $\hat{\boldsymbol{n}}$ is the outward-pointing unit normal vector on $\Gamma$. Here Gauss theorem is employed to obtain the boundary integral term. Then, substituting this expression into Equation (3.1) gives

$$\begin{aligned}
&\int_\Omega \left( \nabla \times \boldsymbol{W} \cdot \nabla \times \boldsymbol{E} - \frac{\omega^2}{c^2} \boldsymbol{W} \cdot \boldsymbol{\varepsilon} \cdot \boldsymbol{E} - i\omega\mu_0 \boldsymbol{W} \cdot \boldsymbol{J}_{\text{ext}} \right) d\Omega \\
&= \int_\Gamma \hat{\boldsymbol{n}} \times \boldsymbol{W} \cdot \nabla \times \boldsymbol{E} \, d\Gamma
\end{aligned} \tag{3.2}$$

Since the sheath and absorbing boundary conditions are regarded as Dirichlet boundary conditions and imposed on the tangential components of the electric field at the boundary, the weight function at the boundary is required that $\boldsymbol{W}_{\text{t}} = \boldsymbol{0}$; here the subscript t denotes the component in the tangential plane to the boundary. Thus, the

boundary integral term in Equation (3.2) is omitted due to the fact that $\hat{\boldsymbol{n}} \times \boldsymbol{W} = \boldsymbol{0}$. Consequently, the weak form of Maxwell's equation for this analysis is given by

$$\int_{\Omega} \left( \nabla \times \boldsymbol{W} \cdot \nabla \times \boldsymbol{E} - \frac{\omega^2}{c^2} \boldsymbol{W} \cdot \boldsymbol{\varepsilon} \cdot \boldsymbol{E} - i\omega\mu_0 \boldsymbol{W} \cdot \boldsymbol{J}_{\text{ext}} \right) d\Omega = 0 \tag{3.3}$$

In order to spatially discretize Equation (3.3) in the $x$-$y$ plane, the calculation domain is divided into nine-node grid elements, and then the weight function and electric field are defined based on the standard Galerkin approach as follows:

$$\boldsymbol{W} = \hat{\boldsymbol{W}}_i N_i (x, y) \, \mathrm{e}^{-ik_z z} = \tilde{N}_i \hat{\boldsymbol{W}}_i \tag{3.4}$$

$$\boldsymbol{E} = \hat{\boldsymbol{E}}_j N_j (x, y) \, \mathrm{e}^{i(k_z z - \omega t)} \tag{3.5}$$

where $N_i$ and $N_j$ are the piecewise biquadratic interpolation functions, $\hat{\boldsymbol{W}}_i$ and $\hat{\boldsymbol{E}}_j$ are the nodal vectors, and the subscripts $i$ and $j$ denote the global node number. Here the summation convention applies to the subscripts $i$ and $j$. Since the shape function $N_i$ is nonzero only in the grid elements which include the node $i$, it can be defined in a grid element using the local coordinate variables $\xi$ and $\eta$ as follows:

$$N_\alpha (\xi, \eta) = \left[ \frac{\xi_\alpha \xi}{2} (1 + \xi_\alpha \xi) + \left(1 - \xi_\alpha^2\right) \left(1 - \xi^2\right) \right]$$
$$\cdot \left[ \frac{\eta_\alpha \eta}{2} (1 + \eta_\alpha \eta) + \left(1 - \eta_\alpha^2\right) \left(1 - \eta^2\right) \right] \tag{3.6}$$

where $-1 \leq \xi, \eta \leq 1$, and the subscript $\alpha$ denotes the local node number ($\alpha = 1, \ldots, 9$). Here

$$\xi_\alpha = (\xi_1, \ldots, \xi_9) = (-1, 1, 1, -1, 0, 1, 0, -1, 0)$$

$$\eta_\alpha = (\eta_1, \ldots, \eta_9) = (-1, -1, 1, 1, -1, 0, 1, 0, 0)$$

Figure 3-1 shows a nine-node element defined in the physical space based on the Cartesian coordinate system ($\boldsymbol{x} = (x, y)$) and in the mapping space based on a normalized

59
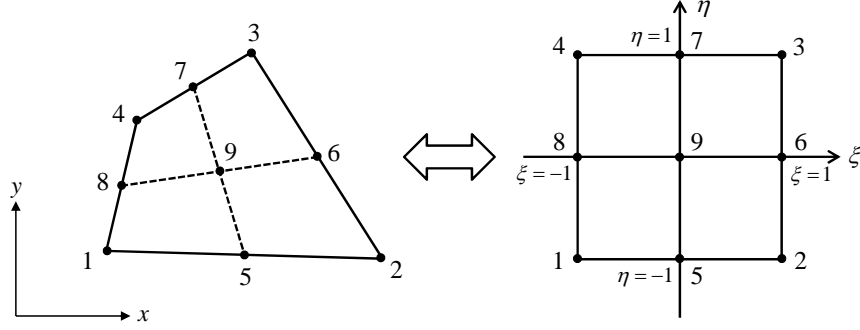
Figure 3-1: A nine-node element in the physical and mapping spaces.

coordinate system ($\boldsymbol{\xi} = (\xi, \eta)$).

Substituting Equation (3.4) into the first term in Equation (3.3) and using the identity

$$\nabla \times \boldsymbol{W} \cdot \nabla \times \boldsymbol{E} = \nabla \times \left( \tilde{N}_i \hat{\boldsymbol{W}}_i \right) \cdot \nabla \times \boldsymbol{E}$$

$$= \left( \nabla \tilde{N}_i \times \hat{\boldsymbol{W}}_i + \tilde{N}_i \nabla \times \hat{\boldsymbol{W}}_i \right) \cdot \nabla \times \boldsymbol{E}$$

$$= \left[ (\nabla \times \boldsymbol{E}) \times \nabla \tilde{N}_i \right] \cdot \hat{\boldsymbol{W}}_i$$

(here $\nabla \times \hat{\boldsymbol{W}}_i = \boldsymbol{0}$ in the Cartesian coordinate system) we obtain

$$\hat{\boldsymbol{W}}_i \cdot \int_\Omega \left( \nabla \times \boldsymbol{E} \times \nabla \tilde{N}_i - \frac{\omega^2}{c^2} \tilde{N}_i \boldsymbol{\varepsilon} \cdot \boldsymbol{E} - i\omega\mu_0 \tilde{N}_i \boldsymbol{J}_{\text{ext}} \right) d\Omega = 0 \tag{3.7}$$

The requirement that Equation (3.7) needs to be satisfied for arbitrary weight functions in the domain $\Omega$ (excluding the boundary $\Gamma$) leads to the following equation:

$$\int_\Omega \left( \nabla \times \boldsymbol{E} \times \nabla \tilde{N}_i - \frac{\omega^2}{c^2} \tilde{N}_i \boldsymbol{\varepsilon} \cdot \boldsymbol{E} - i\omega\mu_0 \tilde{N}_i \boldsymbol{J}_{\text{ext}} \right) d\Omega = \boldsymbol{0} \qquad \text{in } \Omega \tag{3.8}$$

On the boundary $\Gamma$ we impose the condition $\boldsymbol{W}_{\text{t}} = \boldsymbol{0}$, so that

$$\boldsymbol{s}_i \cdot \int_\Omega \left( \nabla \times \boldsymbol{E} \times \nabla \tilde{N}_i - \frac{\omega^2}{c^2} \tilde{N}_i \boldsymbol{\varepsilon} \cdot \boldsymbol{E} - i\omega\mu_0 \tilde{N}_i \boldsymbol{J}_{\text{ext}} \right) d\Omega = 0 \qquad \text{on } \Gamma \tag{3.9}$$

60
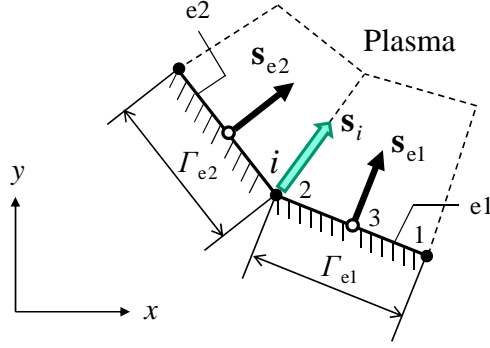
Figure 3-2: Normal vectors at the boundary nodes.

where $\boldsymbol{s}_i$ is the unit normal vector at the node $i$ to the boundary $\Gamma$. In Equation (3.9) we note that the summation convention is not applied to the subscript $i$. Since the interpolation function $\tilde{N}_i$ possesses nonzero values only in the grid elements which include the node $i$, the integration range in Equations (3.8) and (3.9) is restricted within these grid elements.

Although $\boldsymbol{s}_i$ can be directed either outward or inward, we define it as the unit normal vector pointing to the plasma side so that it can also be used to determine $D_\mathrm{n}$ conveniently in the sheath boundary condition. If the local node number (1,2,3) of the nodes in a grid edge that constitutes a part of the boundary is defined as shown in Figure 3-2, the unit normal vector at the local node number 3 is easily obtained as follows:

$$\boldsymbol{s}_\mathrm{e} = \frac{y_2 - y_1}{\Gamma_\mathrm{e}} \boldsymbol{e}_x - \frac{x_2 - x_1}{\Gamma_\mathrm{e}} \boldsymbol{e}_y \tag{3.10}$$

where $x_{1,2}$, $y_{1,2}$ are the coordinate values corresponding to the local node number shown in their subscripts, $\Gamma_\mathrm{e}$ is the length of the grid edge, and $\boldsymbol{e}_x$, $\boldsymbol{e}_y$ are the unit vectors in the $x$, $y$ directions, respectively (the same shall apply to $\boldsymbol{e}_z$). The unit normal vector at the local node number 1 or 2 (the node $i$ in Figure 3-2) is then calculated by applying the nodal-average method to the 1D grid elements on the

boundary as follows:

$$s_i' = \frac{s_{e1}\Gamma_{e1} + s_{e2}\Gamma_{e2}}{\Gamma_{e1} + \Gamma_{e2}} \tag{3.11}$$

where the subscripts e1 and e2 denote the grid elements that possess the node $i$, and $s_{e1}$, $s_{e2}$ are the unit normal vectors at the local node number 3 in the elements e1 and e2, respectively. To assure that its magnitude is 1, the vector $s_i'$ is normalized by

$$s_i = \frac{s_{xi}'}{\left((s_{xi}')^2 + (s_{yi}')^2\right)^{1/2}}e_x + \frac{s_{yi}'}{\left((s_{xi}')^2 + (s_{yi}')^2\right)^{1/2}}e_y \tag{3.12}$$

Assuming that the external current is expressed as

$$J_{ext} = J_{ant}e^{i(k_z z - \omega t)}e_y \tag{3.13}$$

and the dielectric tensor is also interpolated as $\varepsilon = N_k \varepsilon_k$ using its nodal values $\varepsilon_k$, the components of Equation (3.8) are written as follows:

- $x$ component

$$F_{xi} \equiv \int_\Omega \left[ k_z^2 N_i N_j \hat{E}_{xj} + ik_z N_i \frac{\partial N_j}{\partial x}\hat{E}_{zj} - \frac{\partial N_i}{\partial y}\frac{\partial N_j}{\partial x}\hat{E}_{yj} + \frac{\partial N_i}{\partial y}\frac{\partial N_j}{\partial y}\hat{E}_{xj} \right.$$
$$\left. - \frac{\omega^2}{c^2} N_i N_j N_k \left( \varepsilon_{xxk}\hat{E}_{xj} + \varepsilon_{xyk}\hat{E}_{yj} + \varepsilon_{xzk}\hat{E}_{zj} \right) \right] d\Omega = 0 \tag{3.14}$$

- $y$ component

$$F_{yi} \equiv \int_\Omega \left[ \frac{\partial N_i}{\partial x}\frac{\partial N_j}{\partial x}\hat{E}_{yj} - \frac{\partial N_i}{\partial x}\frac{\partial N_j}{\partial y}\hat{E}_{xj} + ik_z N_i \frac{\partial N_j}{\partial y}\hat{E}_{zj} + k_z^2 N_i N_j \hat{E}_{yj} \right.$$
$$\left. - \frac{\omega^2}{c^2} N_i N_j N_k \left( \varepsilon_{yxk}\hat{E}_{xj} + \varepsilon_{yyk}\hat{E}_{yj} + \varepsilon_{yzk}\hat{E}_{zj} \right) \right] d\Omega \tag{3.15}$$
$$= i\omega\mu_0 \int_\Omega N_i J_{ant} d\Omega \equiv R_{yi}$$

- $z$ component

$$F_{zi} \equiv \int_{\Omega} \left[ \frac{\partial N_i}{\partial y} \frac{\partial N_j}{\partial y} \hat{E}_{zj} - ik_z \frac{\partial N_i}{\partial y} N_j \hat{E}_{yj} - ik_z \frac{\partial N_i}{\partial x} N_j \hat{E}_{xj} + \frac{\partial N_i}{\partial x} \frac{\partial N_j}{\partial x} \hat{E}_{zj} \right.$$
$$\left. - \frac{\omega^2}{c^2} N_i N_j N_k \left( \varepsilon_{zxk} \hat{E}_{xj} + \varepsilon_{zyk} \hat{E}_{yj} + \varepsilon_{zzk} \hat{E}_{zj} \right) \right] d\Omega = 0 \tag{3.16}$$

The calculations of the integrals are summarized in Appendix A.1. Here the Jacobian and the components of the cofactor matrix in each grid element are evaluated at the centroid of the element (i.e., at $\xi = \eta = 0$ in the mapping space). Owing to this approximation, all the integrals are calculated analytically, which leads to significant speed-up of the scheme (since in general, a numerical integration method requires iterative calculations). Using Equations (3.12), (3.14), and (3.15), Equation (3.9) is rewritten as follows:

$$s_{xi} F_{xi} + s_{yi} F_{yi} = 0 \qquad \text{on } \Gamma \tag{3.17}$$

Here we assume that $R_{yi} = 0$ at the boundary. The discretization of the term including the external current in Equation (3.15) will be described in the next subsection.

## 3.2.2 Discretization of the Antenna Current

In this study, the external current, which corresponds to the antenna current, is modeled with a delta function in such a way that $J_{\text{ant}} = K(y) \delta(x - x_{\text{ant}})$ for simplicity; here we assume that the current strap is located at $x = x_{\text{ant}}$. Then the integral on the right-hand side of Equation (3.15) is calculated as follows:

$$\int_{\Omega} N_i J_{\text{ant}} d\Omega = \int_l N_i^{\text{A}} N_j^{\text{A}} K_j dl \tag{3.18}$$

where $l$ represents the 1D coordinate along the direction of the antenna current, and the subscripts $i$ and $j$ denote the global node number of the nodes located on

63
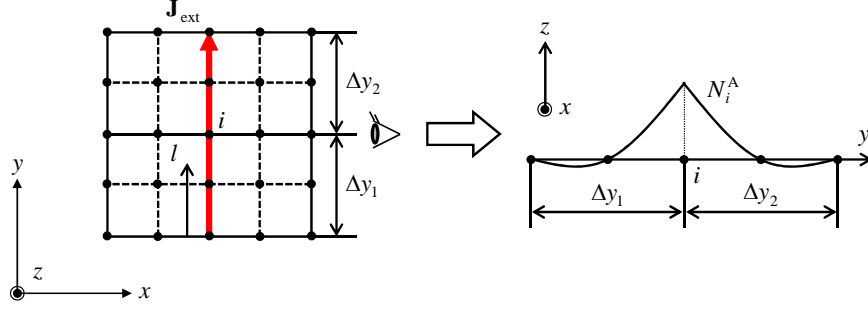
Figure 3-3: The interpolation function $N_i^{\mathrm{A}}$ defined along the antenna current.

the current strap (see Figure 3-3). Here the surface current $K$ is interpolated as $K = N_j^{\mathrm{A}} K_j$ using its nodal values $K_j$. The shape function $N_j^{\mathrm{A}}$ is the piecewise quadratic interpolation function which can be defined in a 1D grid element on the current strap as follows:

$$N_\alpha^{\mathrm{A}} (\xi) = \frac{\xi_\alpha \xi}{2} \left(1 + \xi_\alpha \xi\right) + \left(1 - \xi_\alpha^2\right) \left(1 - \xi^2\right) \tag{3.19}$$

where $-1 \leq \xi \leq 1$, and the subscript $\alpha$ denotes the local node number ($\alpha = 1, 2, 3$); $\xi_{1,2,3} = -1, 1, 0$.

### 3.2.3 Discretization of the Sheath Boundary Condition Imposed on a Flat Wall

The sheath boundary condition described in Equation (2.87) can be discretized by employing the 1D finite element method when we consider the problem in the 2D space. At the beginning, this procedure is demonstrated with a flat wall that lies in the $y$-$z$ plane as shown in Figure 2-2; that is, we only consider a 2D slab geometry here. The discretization procedure will be generalized so as to be applied to a general curved geometry in the next subsection.

First, forming the inner product of Equation (2.87) with the weight function $\boldsymbol{W}^{\mathrm{S}}$,

and then integrating it over the sheath region $\Gamma^{\mathrm{S}}$ yields

$$\int_{\Gamma^{\mathrm{S}}} \boldsymbol{W}^{\mathrm{S}} \cdot \left[ \boldsymbol{E}_{\mathrm{t}} - \nabla_{\mathrm{t}} \left( \frac{\Delta_{\mathrm{sh}}}{\varepsilon_{\mathrm{sh}}} D_{\mathrm{n}} \right) \right] d\Gamma^{\mathrm{S}} = 0 \tag{3.20}$$

where the superscript pl is omitted. Let us next define the weight function and electric field as

$$\boldsymbol{W}^{\mathrm{S}} = \hat{\boldsymbol{W}}_i^{\mathrm{S}} N_i^{\mathrm{S}} \left( \tau \right) \mathrm{e}^{-ik_z z} = \tilde{N}_i^{\mathrm{S}} \hat{\boldsymbol{W}}_i^{\mathrm{S}} \tag{3.21}$$

$$\boldsymbol{E} = \hat{\boldsymbol{E}}_j^{\mathrm{S}} N_j^{\mathrm{S}} \left( \tau \right) \mathrm{e}^{i(k_z z - \omega t)} \tag{3.22}$$

where $N_i^{\mathrm{S}}$ and $N_j^{\mathrm{S}}$ are the piecewise quadratic interpolation functions with respect to $\tau$ (see Figure 2-3), and the subscripts $i$ and $j$ denote the global node number on $\Gamma^{\mathrm{S}}$. Here the summation convention applies to the subscripts $i$ and $j$, and the superscript S is attached to explicitly show that the quantity is positioned on $\Gamma^{\mathrm{S}}$. The shape function $N_i^{\mathrm{S}}$ or $N_j^{\mathrm{S}}$ can be locally defined in a 1D grid element on the sheath as shown in Equation (3.19).

When we assume that the sheath is planar and its surface lies in the $y$-$z$ plane, the sheath boundary condition is expressed as

$$\boldsymbol{E}_{\mathrm{t}} = \pm \nabla_{\mathrm{t}} \left( \Delta_{\mathrm{sh}} \kappa \right) \tag{3.23}$$

where

$$\Delta_{\mathrm{sh}} = \left( \frac{eC_{\mathrm{sh}}}{T_{\mathrm{e}}} \right)^3 \lambda_{\mathrm{De}}^4 \left| \kappa \right|^3 + C_{\mathrm{th}} \lambda_{\mathrm{De}}$$
$$\kappa = \varepsilon_{xx} E_x + \varepsilon_{xy} E_y + \varepsilon_{xz} E_z \tag{3.24}$$

The positive and negative signs in front of the nabla operator on the right-hand side of Equation (3.23) correspond to the cases where the conductor is located on the left and right sides of the sheath, respectively.

For the left planar sheath whose boundary with the plasma is located at $x = x_{\mathrm{L}}$, Equation (3.20) reduces to

$$\int_{\Gamma^{\mathrm{S}}} N_i^{\mathrm{S}}(y) \left[ \boldsymbol{E}_{\mathrm{t}} - \nabla_{\mathrm{t}} (\Delta_{\mathrm{sh}} \kappa) \right] d\Gamma^{\mathrm{S}} \bigg|_{x=x_{\mathrm{L}}} = \boldsymbol{0} \tag{3.25}$$

considering that Equation (3.20) needs to be satisfied for arbitrary weight functions (recall that the calculation domain is defined in the $x$-$y$ plane). The $y$ component of Equation (3.25) is then simply written as

$$\int_{\Gamma^{\mathrm{S}}} N_i^{\mathrm{S}} \left[ E_y - \frac{d}{dy} (\Delta_{\mathrm{sh}} \kappa) \right] d\Gamma^{\mathrm{S}} \bigg|_{x=x_{\mathrm{L}}} = 0 \tag{3.26}$$

Now, let us make the following approximation for the derivative of $\Delta_{\mathrm{sh}} \kappa$:

$$\frac{d}{dy} (\Delta_{\mathrm{sh}} \kappa) \simeq \left\langle \frac{d\Delta_{\mathrm{sh}}}{dy} \right\rangle_{\mathrm{e}} \kappa + \langle \Delta_{\mathrm{sh}} \rangle_{\mathrm{e}} \frac{d\kappa}{dy} \tag{3.27}$$

Here the variables surrounded by angle brackets with the subscript e represent the element-averaged quantities defined by

$$\langle \Delta_{\mathrm{sh}} \rangle_{\mathrm{e}} \equiv \frac{1}{\Gamma_{\mathrm{e}}^{\mathrm{S}}} \int_{\Gamma_{\mathrm{e}}^{\mathrm{S}}} \Delta_{\mathrm{sh}} d\Gamma^{\mathrm{S}} = \left( \frac{1}{\Gamma_{\mathrm{e}}^{\mathrm{S}}} \int_{\Gamma_{\mathrm{e}}^{\mathrm{S}}} N_\alpha^{\mathrm{S}} d\Gamma^{\mathrm{S}} \right) (\Delta_{\mathrm{sh}})_\alpha \tag{3.28}$$

$$\left\langle \frac{d\Delta_{\mathrm{sh}}}{dy} \right\rangle_{\mathrm{e}} \equiv \frac{1}{\Gamma_{\mathrm{e}}^{\mathrm{S}}} \int_{\Gamma_{\mathrm{e}}^{\mathrm{S}}} \frac{d\Delta_{\mathrm{sh}}}{dy} d\Gamma^{\mathrm{S}} = \left( \frac{1}{\Gamma_{\mathrm{e}}^{\mathrm{S}}} \int_{\Gamma_{\mathrm{e}}^{\mathrm{S}}} \frac{dN_\alpha^{\mathrm{S}}}{dy} d\Gamma^{\mathrm{S}} \right) (\Delta_{\mathrm{sh}})_\alpha \tag{3.29}$$

where $N_\alpha^{\mathrm{S}}$ is the local quadratic functions defined in a three-node element (see Appendix A.2 for further calculations). Equation (3.27) is the key approximation which makes the discretization tractable (recall that $\Delta_{\mathrm{sh}} \propto |D_{\mathrm{n}}|^3$). Assuming that the dielectric tensor on $\Gamma^{\mathrm{S}}$ is interpolated as $\boldsymbol{\varepsilon} = N_k^{\mathrm{S}} \boldsymbol{\varepsilon}_k^{\mathrm{S}}$ using its nodal values $\boldsymbol{\varepsilon}_k^{\mathrm{S}}$, and substituting Equations (3.22), (3.24) (for $\kappa$), and (3.27) into Equation (3.26), one

gets

$$
\sum_m \left\{ \int_{\Gamma^{\rm S}_{{\rm e}(m)}} N_i^{\rm S} N_j^{\rm S} \hat{E}_{yj}^{\rm S} d\Gamma^{\rm S} \right.
$$

$$
- \left\langle \frac{d\Delta_{\rm sh}}{dy} \right\rangle_{{\rm e}(m)} \int_{\Gamma^{\rm S}_{{\rm e}(m)}} N_i^{\rm S} \left[ \left( N_k^{\rm S} \varepsilon_{xxk}^{\rm S} \right) \left( N_j^{\rm S} \hat{E}_{xj}^{\rm S} \right) + \cdots \right] d\Gamma^{\rm S} \tag{3.30}
$$

$$
\left. - \left\langle \Delta_{\rm sh} \right\rangle_{{\rm e}(m)} \int_{\Gamma^{\rm S}_{{\rm e}(m)}} N_i^{\rm S} \left[ \frac{d \left( N_k^{\rm S} \varepsilon_{xxk}^{\rm S} \right)}{dy} \left( N_j^{\rm S} \hat{E}_{xj}^{\rm S} \right) + \cdots \right] d\Gamma^{\rm S} \right\} \Bigg|_{x=x_{\rm L}} = 0
$$

where $m$ represents 1D grid elements (or a grid element) which include(s) the node $i$. Equation (3.30) can be further simplified in the following form:

$$
G_{yi}|_{x=x_{\rm L}} \equiv \sum_m \left[ \left[ N_i^{\rm S} N_j^{\rm S} \right] \hat{E}_{yj}^{\rm S} - \left( \left\langle \frac{d\Delta_{\rm sh}}{dy} \right\rangle_{{\rm e}(m)} \left[ N_i^{\rm S} N_j^{\rm S} N_k^{\rm S} \right] + \left\langle \Delta_{\rm sh} \right\rangle_{{\rm e}(m)} \left[ N_i^{\rm S} \tilde{N}_j^{\rm S} \tilde{N}_k^{\rm S} \right] \right) \right.
$$

$$
\left. \cdot \left( \varepsilon_{xxk}^{\rm S} \hat{E}_{xj}^{\rm S} + \varepsilon_{xyk}^{\rm S} \hat{E}_{yj}^{\rm S} + \varepsilon_{xzk}^{\rm S} \hat{E}_{zj}^{\rm S} \right) \right] \Bigg|_{x=x_{\rm L}} = 0
$$

$$
\tag{3.31}
$$

with

$$
\left[ N_i^{\rm S} N_j^{\rm S} \right] \equiv \int_{\Gamma^{\rm S}_{{\rm e}(m)}} N_i^{\rm S} N_j^{\rm S} d\Gamma^{\rm S}, \quad \left[ N_i^{\rm S} N_j^{\rm S} N_k^{\rm S} \right] \equiv \int_{\Gamma^{\rm S}_{{\rm e}(m)}} N_i^{\rm S} N_j^{\rm S} N_k^{\rm S} d\Gamma^{\rm S}
$$

$$
\left[ N_i^{\rm S} \tilde{N}_j^{\rm S} \tilde{N}_k^{\rm S} \right] \equiv \left[ N_i^{\rm S} \left( N_j^{\rm S} \right)' N_k^{\rm S} \right] + \left[ N_i^{\rm S} N_j^{\rm S} \left( N_k^{\rm S} \right)' \right]
$$

$$
\left[ N_i^{\rm S} \left( N_j^{\rm S} \right)' N_k^{\rm S} \right] \equiv \int_{\Gamma^{\rm S}_{{\rm e}(m)}} N_i^{\rm S} \frac{dN_j^{\rm S}}{dy} N_k^{\rm S} d\Gamma^{\rm S} \tag{3.32}
$$

$$
\left[ N_i^{\rm S} N_j^{\rm S} \left( N_k^{\rm S} \right)' \right] \equiv \int_{\Gamma^{\rm S}_{{\rm e}(m)}} N_i^{\rm S} N_j^{\rm S} \frac{dN_k^{\rm S}}{dy} d\Gamma^{\rm S}
$$

The calculations of the integrals in Equation (3.32) are summarized in Appendix A.2.

The $z$ component of Equation (3.25) is written as

$$
\int_{\Gamma^{\rm S}} N_i^{\rm S} \left( E_z - ik_z \Delta_{\rm sh} \kappa \right) d\Gamma^{\rm S} \Bigg|_{x=x_{\rm L}} = 0 \tag{3.33}
$$

67

considering that $\kappa \propto \mathrm{e}^{ik_z z}$. Then the corresponding discretized equation is given by

$$G_{zi}|_{x=x_{\mathrm{L}}} \equiv \sum_m \left[ \left[ N_i^{\mathrm{S}} N_j^{\mathrm{S}} \right] \hat{E}_{zj}^{\mathrm{S}} - ik_z \langle \Delta_{\mathrm{sh}} \rangle_{\mathrm{e}(m)} \left[ N_i^{\mathrm{S}} N_j^{\mathrm{S}} N_k^{\mathrm{S}} \right] \right.$$
$$\left. \cdot \left( \varepsilon_{xxk}^{\mathrm{S}} \hat{E}_{xj}^{\mathrm{S}} + \varepsilon_{xyk}^{\mathrm{S}} \hat{E}_{yj}^{\mathrm{S}} + \varepsilon_{xzk}^{\mathrm{S}} \hat{E}_{zj}^{\mathrm{S}} \right) \right] \Big|_{x=x_{\mathrm{L}}} = 0 \tag{3.34}$$

using the approximation that $\Delta_{\mathrm{sh}} \simeq \langle \Delta_{\mathrm{sh}} \rangle_{\mathrm{e}(m)}$.

In the same way, the discretized equations on the right planar sheath surface, which is located at $x = x_{\mathrm{R}}$, are obtained as follows:

$$G_{yi}|_{x=x_{\mathrm{R}}} \equiv \sum_m \left[ \left[ N_i^{\mathrm{S}} N_j^{\mathrm{S}} \right] \hat{E}_{yj}^{\mathrm{S}} + \left( \left\langle \frac{d\Delta_{\mathrm{sh}}}{dy} \right\rangle_{\mathrm{e}(m)} \left[ N_i^{\mathrm{S}} N_j^{\mathrm{S}} N_k^{\mathrm{S}} \right] + \langle \Delta_{\mathrm{sh}} \rangle_{\mathrm{e}(m)} \left[ N_i^{\mathrm{S}} \tilde{N}_j^{\mathrm{S}} \tilde{N}_k^{\mathrm{S}} \right] \right) \right.$$
$$\left. \cdot \left( \varepsilon_{xxk}^{\mathrm{S}} \hat{E}_{xj}^{\mathrm{S}} + \varepsilon_{xyk}^{\mathrm{S}} \hat{E}_{yj}^{\mathrm{S}} + \varepsilon_{xzk}^{\mathrm{S}} \hat{E}_{zj}^{\mathrm{S}} \right) \right] \Big|_{x=x_{\mathrm{R}}} = 0$$
$$\tag{3.35}$$

$$G_{zi}|_{x=x_{\mathrm{R}}} \equiv \sum_m \left[ \left[ N_i^{\mathrm{S}} N_j^{\mathrm{S}} \right] \hat{E}_{zj}^{\mathrm{S}} + ik_z \langle \Delta_{\mathrm{sh}} \rangle_{\mathrm{e}(m)} \left[ N_i^{\mathrm{S}} N_j^{\mathrm{S}} N_k^{\mathrm{S}} \right] \right.$$
$$\left. \cdot \left( \varepsilon_{xxk}^{\mathrm{S}} \hat{E}_{xj}^{\mathrm{S}} + \varepsilon_{xyk}^{\mathrm{S}} \hat{E}_{yj}^{\mathrm{S}} + \varepsilon_{xzk}^{\mathrm{S}} \hat{E}_{zj}^{\mathrm{S}} \right) \right] \Big|_{x=x_{\mathrm{R}}} = 0 \tag{3.36}$$

Notice that the sign in front of the derivatives of $\Delta_{\mathrm{sh}}\kappa$ is reversed (see Equation (3.23)).

## 3.2.4  Discretization of the Sheath Boundary Condition Imposed on a Curved Wall

The discretization of the sheath boundary condition can be straightforwardly extended to deal with the problem including a curved wall. When we assume that the sheath surface lies in the $\tau$-$z$ plane, the sheath boundary condition is expressed as

$$\boldsymbol{E}_{\mathrm{t}} = \nabla_{\mathrm{t}} \left( \Delta_{\mathrm{sh}}\kappa \right) \tag{3.37}$$

where

$$\Delta_{\mathrm{sh}} = \left(\frac{eC_{\mathrm{sh}}}{T_{\mathrm{e}}}\right)^3 \lambda_{\mathrm{De}}^4 |\kappa|^3 + C_{\mathrm{th}}\lambda_{\mathrm{De}} \tag{3.38}$$

$$\kappa = \boldsymbol{s} \cdot (\boldsymbol{\varepsilon} \cdot \boldsymbol{E})$$

The $\tau$ component of the integral equation is written as

$$\int_{\Gamma^{\mathrm{S}}} N_i^{\mathrm{S}}(\tau) \left[E_\tau - \frac{d}{d\tau}\left(\Delta_{\mathrm{sh}}\kappa\right)\right] d\Gamma^{\mathrm{S}} = 0 \tag{3.39}$$

Here, consider the following approximation for the derivative of $\Delta_{\mathrm{sh}}\kappa$:

$$\frac{d}{d\tau}\left(\Delta_{\mathrm{sh}}\kappa\right) \simeq \left\langle\frac{d\Delta_{\mathrm{sh}}}{d\tau}\right\rangle_{\mathrm{e}} \kappa + \langle\Delta_{\mathrm{sh}}\rangle_{\mathrm{e}}\frac{d\kappa}{d\tau}$$

$$\simeq \left[\left\langle\frac{d\Delta_{\mathrm{sh}}}{d\tau}\right\rangle_{\mathrm{e}}\langle\boldsymbol{s}\rangle_{\mathrm{e}} + \langle\Delta_{\mathrm{sh}}\rangle_{\mathrm{e}}\left\langle\frac{d\boldsymbol{s}}{d\tau}\right\rangle_{\mathrm{e}}\right]\cdot(\boldsymbol{\varepsilon}\cdot\boldsymbol{E}) + \langle\Delta_{\mathrm{sh}}\rangle_{\mathrm{e}}\langle\boldsymbol{s}\rangle_{\mathrm{e}}\cdot\frac{d}{d\tau}(\boldsymbol{\varepsilon}\cdot\boldsymbol{E}) \tag{3.40}$$

As before, the variables surrounded by angle brackets with the subscript e represent the element-averaged quantities. Following the same procedure shown in Equations (3.30) and (3.31), one gets

$$
\begin{aligned}
G_{\tau i} \equiv \sum_m \Bigg\{ & \left[N_i^{\mathrm{S}}N_j^{\mathrm{S}}\right]\hat{E}_{\tau j}^{\mathrm{S}} \\
& - \left[\left(\left\langle\frac{d\Delta_{\mathrm{sh}}}{d\tau}\right\rangle_{\mathrm{e}(m)}\langle s_x\rangle_{\mathrm{e}(m)} + \langle\Delta_{\mathrm{sh}}\rangle_{\mathrm{e}(m)}\left\langle\frac{ds_x}{d\tau}\right\rangle_{\mathrm{e}(m)}\right)\left[N_i^{\mathrm{S}}N_j^{\mathrm{S}}N_k^{\mathrm{S}}\right] \right. \\
& \left. + \langle\Delta_{\mathrm{sh}}\rangle_{\mathrm{e}(m)}\langle s_x\rangle_{\mathrm{e}(m)}\left[N_i^{\mathrm{S}}\tilde{N}_j^{\mathrm{S}}\tilde{N}_k^{\mathrm{S}}\right]\right]\left(\varepsilon_{xxk}^{\mathrm{S}}\hat{E}_{xj}^{\mathrm{S}} + \varepsilon_{xyk}^{\mathrm{S}}\hat{E}_{yj}^{\mathrm{S}} + \varepsilon_{xzk}^{\mathrm{S}}\hat{E}_{zj}^{\mathrm{S}}\right) \\
& - \left[\left(\left\langle\frac{d\Delta_{\mathrm{sh}}}{d\tau}\right\rangle_{\mathrm{e}(m)}\langle s_y\rangle_{\mathrm{e}(m)} + \langle\Delta_{\mathrm{sh}}\rangle_{\mathrm{e}(m)}\left\langle\frac{ds_y}{d\tau}\right\rangle_{\mathrm{e}(m)}\right)\left[N_i^{\mathrm{S}}N_j^{\mathrm{S}}N_k^{\mathrm{S}}\right] \right. \\
& \left. + \langle\Delta_{\mathrm{sh}}\rangle_{\mathrm{e}(m)}\langle s_y\rangle_{\mathrm{e}(m)}\left[N_i^{\mathrm{S}}\tilde{N}_j^{\mathrm{S}}\tilde{N}_k^{\mathrm{S}}\right]\right]\left(\varepsilon_{yxk}^{\mathrm{S}}\hat{E}_{xj}^{\mathrm{S}} + \varepsilon_{yyk}^{\mathrm{S}}\hat{E}_{yj}^{\mathrm{S}} + \varepsilon_{yzk}^{\mathrm{S}}\hat{E}_{zj}^{\mathrm{S}}\right)\Bigg\} = 0
\end{aligned}
\tag{3.41}
$$

The quantity $\hat{E}^S_{\tau j}$ needs to be expressed using $\hat{E}^S_{xj}$ and $\hat{E}^S_{yj}$ with use of the following relation:

$$\hat{E}^S_{\tau j} = \boldsymbol{e}_x \cdot \boldsymbol{e}_{\tau j} \hat{E}^S_{xj} + \boldsymbol{e}_y \cdot \boldsymbol{e}_{\tau j} \hat{E}^S_{yj} \tag{3.42}$$

where $\boldsymbol{e}_{\tau j}$ is the unit normal vector in the $\tau$ direction at the node $j$, which can be obtained in a similar way to $\boldsymbol{s}_i$ (see Section 3.2.1).

Next, the $z$ component of the integral equation is given by

$$\int_{\Gamma^S} N^S_i \left( E_z - ik_z \Delta_{\mathrm{sh}} \kappa \right) d\Gamma^S = 0 \tag{3.43}$$

Then the corresponding discretized equation is

$$
\begin{aligned}
G_{zi} \equiv \sum_m \Big[ & \left[ N^S_i N^S_j \right] \hat{E}^S_{zj} \\
& - ik_z \langle \Delta_{\mathrm{sh}} \rangle_{\mathrm{e}(m)} \langle s_x \rangle_{\mathrm{e}(m)} \left[ N^S_i N^S_j N^S_k \right] \cdot \left( \varepsilon^S_{xxk} \hat{E}^S_{xj} + \varepsilon^S_{xyk} \hat{E}^S_{yj} + \varepsilon^S_{xzk} \hat{E}^S_{zj} \right) \\
& - ik_z \langle \Delta_{\mathrm{sh}} \rangle_{\mathrm{e}(m)} \langle s_y \rangle_{\mathrm{e}(m)} \left[ N^S_i N^S_j N^S_k \right] \cdot \left( \varepsilon^S_{yxk} \hat{E}^S_{xj} + \varepsilon^S_{yyk} \hat{E}^S_{yj} + \varepsilon^S_{yzk} \hat{E}^S_{zj} \right) \Big] = 0
\end{aligned}
\tag{3.44}
$$

using the approximations that $\Delta_{\mathrm{sh}} \simeq \langle \Delta_{\mathrm{sh}} \rangle_{\mathrm{e}(m)}$ and $\boldsymbol{s} \simeq \langle \boldsymbol{s} \rangle_{\mathrm{e}(m)}$.

## 3.3  Newton-Raphson Method

The nonlinear system of discretized equations derived in the previous section can be solved by employing the Newton-Raphson method, which is one of the most frequently used iteration schemes (a number of related methods can be seen in Reference [57]). The procedure will be described here in detail.

First of all, the present finite element equations are simply written as follows:

$$\boldsymbol{F} = \boldsymbol{R} \tag{3.45}$$

with

$$\boldsymbol{F}^{\mathrm{T}} = \begin{pmatrix} F_{x(1)} \cdots F_{x(\mathrm{NP})} & F_{y(1)} \cdots F_{y(\mathrm{NP})} & F_{z(1)} \cdots F_{z(\mathrm{NP})} & F_{v(1)} \cdots F_{v(\mathrm{NS+NA})} \\ G_{\tau(1)} \cdots G_{\tau(\mathrm{NS})} & G_{z(1)} \cdots G_{z(\mathrm{NS})} & H_{\tau(1)} \cdots H_{\tau(\mathrm{NA})} & H_{z(1)} \cdots H_{z(\mathrm{NA})} \end{pmatrix} \tag{3.46}$$

$$\boldsymbol{R}^{\mathrm{T}} = \begin{pmatrix} 0 \cdots 0 & R_{y(1)} \cdots R_{y(\mathrm{NP})} & 0 \cdots 0 \end{pmatrix} \tag{3.47}$$

where NP, NS, and NA are the numbers of nodes in the plasma, on the sheath surface, and on the core-edge plasma boundary, respectively, and the total number of nodes is expressed as NT (= NP+NS+NA); $H_{\tau i}$ and $H_{zi}$ correspond to the boundary condition on the core side, i.e., $\boldsymbol{E}_{\mathrm{t}} = \boldsymbol{0}$, and $v$ corresponds to the direction perpendicular to the sheath surface. Note that each number in the parenthesis in Equations (3.46) and (3.47) does not correspond to the global node number; instead it represents an independent equation. The task here is to find the solution $\hat{\boldsymbol{E}}^*$ of the equation

$$\boldsymbol{f}\left(\hat{\boldsymbol{E}}^*\right) = \boldsymbol{F} - \boldsymbol{R} = \boldsymbol{0} \tag{3.48}$$

In the present numerical analysis $\boldsymbol{f}$ is treated as being a real vector by splitting the components of $\boldsymbol{F}$ and $\boldsymbol{R}$ into real and imaginary parts. Then the solution is expressed as

$$\left(\hat{\boldsymbol{E}}^*\right)^{\mathrm{T}} = \begin{pmatrix} \hat{E}_{x1}^{(\mathrm{R,I})*} \cdots \hat{E}_{x\mathrm{NT}}^{(\mathrm{R,I})*} & \hat{E}_{y1}^{(\mathrm{R,I})*} \cdots \hat{E}_{y\mathrm{NT}}^{(\mathrm{R,I})*} & \hat{E}_{z1}^{(\mathrm{R,I})*} \cdots \hat{E}_{z\mathrm{NT}}^{(\mathrm{R,I})*} \end{pmatrix} \tag{3.49}$$

where the superscripts R and I denote the real and imaginary parts of the quantities, respectively.

Let us assume that an intermediate solution $\hat{\boldsymbol{E}}^{(n)}$ is evaluated in the $n$-th iteration. Then a Taylor series expansion gives

$$f_i\left(\hat{\boldsymbol{E}}^{(n)} + \delta\hat{\boldsymbol{E}}\right) = f_i\left(\hat{\boldsymbol{E}}^{(n)}\right) + \sum_{j=1}^{\mathrm{NT}} \left.\frac{\partial f_i}{\partial \hat{E}_{x,y,zj}^{(\mathrm{R,I})}}\right|_{\hat{\boldsymbol{E}}^{(n)}} \delta\hat{E}_{x,y,zj}^{(\mathrm{R,I})} + \mathcal{O}\left(\delta\hat{\boldsymbol{E}}^2\right) \tag{3.50}$$

for $i = 1, \ldots, 6NT$. In matrix notation Equation (3.50) is

$$\boldsymbol{f}\left(\hat{\boldsymbol{E}}^{(n)} + \delta\hat{\boldsymbol{E}}\right) = \boldsymbol{f}\left(\hat{\boldsymbol{E}}^{(n)}\right) + \boldsymbol{K}^{(n)} \cdot \delta\hat{\boldsymbol{E}} + \mathcal{O}\left(\delta\hat{\boldsymbol{E}}^2\right) \tag{3.51}$$

where

$$\boldsymbol{K}^{(n)} = \left.\frac{\partial f_i}{\partial \hat{E}_{x,y,zj}^{(\mathrm{R,I})}}\right|_{\hat{\boldsymbol{E}}^{(n)}} \boldsymbol{e}_i\boldsymbol{e}_j \tag{3.52}$$

Notice that the expression of $\boldsymbol{K}^{(n)}$ is explicitly obtained using the discretized equations (3.14)–(3.16), (3.41), and (3.44). A procedure to obtain the derivative expressions of the discretized sheath boundary condition is demonstrated in Appendix B for a flat wall. Neglecting the high-order terms in Equation (3.51) and setting $\boldsymbol{f}\left(\hat{\boldsymbol{E}}^{(n)} + \delta\hat{\boldsymbol{E}}\right) = \boldsymbol{0}$, we obtain a set of linear equations for the correction $\delta\hat{\boldsymbol{E}}$, namely

$$\boldsymbol{K}^{(n)} \cdot \delta\hat{\boldsymbol{E}} = -\boldsymbol{f}\left(\hat{\boldsymbol{E}}^{(n)}\right) \tag{3.53}$$

In this study the matrix equation (3.53) is solved by MUMPS, which will be described in the next section. The solution is then improved by adding the correction:

$$\hat{\boldsymbol{E}}^{(n+1)} = \hat{\boldsymbol{E}}^{(n)} + \delta\hat{\boldsymbol{E}} \tag{3.54}$$

The process is iteratively conducted until the solution is fully converged. The present scheme adopts the following convergence criterion:

$$\left.\frac{\left|\delta\hat{E}_x\right|}{\left|\hat{E}_x^{(n+1)}\right|}, \quad \frac{\left|\delta\hat{E}_y\right|}{\left|\hat{E}_y^{(n+1)}\right|}, \quad \frac{\left|\delta\hat{E}_z\right|}{\left|\hat{E}_z^{(n+1)}\right|}\right|_{\mathrm{max}} < \varepsilon_{\mathrm{err}} \tag{3.55}$$

where $\varepsilon_{\mathrm{err}}$ is a parameter which may be adjusted depending on the problems; in general, the condition where $\varepsilon_{\mathrm{err}} \leq 10^{-3}$ yields an accurate solution.

If the nonlinear part of the sheath boundary condition, specifically, the first term

of Equation (2.101) can be neglected (due to low electric field strength), the finite element equations (3.45) reduce to the following linear form:

$$\boldsymbol{F} = \boldsymbol{G} \cdot \hat{\boldsymbol{E}} = \boldsymbol{R} \tag{3.56}$$

In this case the solution $\hat{\boldsymbol{E}}$ is directly calculated by inverting the matrix $\boldsymbol{G}$, namely

$$\hat{\boldsymbol{E}} = \boldsymbol{G}^{-1} \cdot \boldsymbol{R} \tag{3.57}$$

Notice that the solution then becomes proportional to $J_{\mathrm{ant}}$ in Equation (3.13).

## 3.4 Parallel Computation Using MUMPS

### 3.4.1 General Information on MUMPS and Code Implementation

As described in the previous section, the present numerical scheme is required to calculate the system of linear equations with 6NT unknowns at each Newton-Raphson iteration. Considering that our interest is the physics of plasma waves in the 2D domain and SWs often yield small wavelengths, it is not hard to anticipate that the computational cost becomes indeed huge when satisfactory grid resolution is provided for an accurate numerical solution. However, at the same time, it is important to keep in mind that the unsymmetric matrix $\boldsymbol{K}^{(n)}$ defined in Equation (3.52) is sparse owing to the finite element discretization. For this reason, the present numerical simulation can be effectively conducted by employing MUMPS (ver.4.9.2), which is briefly described below.

MUMPS is a software package for solving large sparse systems of linear equations of the form $\boldsymbol{A} \cdot \boldsymbol{x} = \boldsymbol{b}$, where $\boldsymbol{A}$ can be an unsymmetric matrix, on distributed memory parallel computers. MUMPS is a direct method based on a multifrontal approach
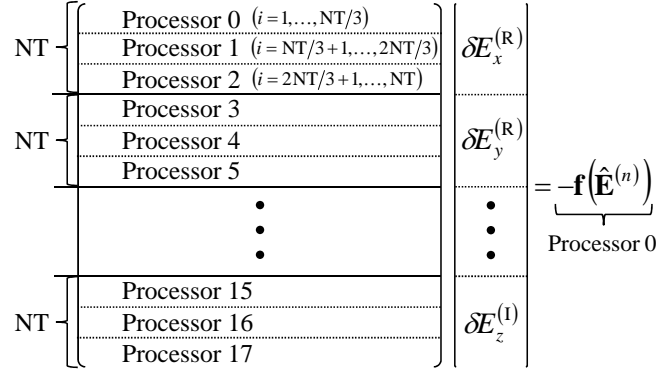
73

$$
\mathrm{NT} \left\{
\begin{array}{|l|}
\hline
\text{Processor 0} \quad (i = 1, \ldots, \mathrm{NT}/3) \\
\hline
\text{Processor 1} \quad (i = \mathrm{NT}/3+1, \ldots, 2\mathrm{NT}/3) \\
\hline
\text{Processor 2} \quad (i = 2\mathrm{NT}/3+1, \ldots, \mathrm{NT}) \\
\hline
\end{array}
\right.
\; \delta E_x^{(\mathrm{R})}
$$

Figure 3-4: An example of the matrix partitioning for a parallel computation.

which performs a direct factorization $\boldsymbol{A} = \boldsymbol{L} \cdot \boldsymbol{U}$ or $\boldsymbol{A} = \boldsymbol{L} \cdot \boldsymbol{D} \cdot \boldsymbol{L}^{\mathrm{T}}$ depending on the symmetry of the matrix. The software is written in Fortran 90 and requires MPI for message passing. More detailed descriptions can be found in Reference [58].

Figure 3-4 shows an example of the matrix partitioning used in the present finite element code for parallel computation with MUMPS. As a matter of convenience in programming, the total number of processors, NPROC, is determined such that it is in multiples of 6, and the matrix $\boldsymbol{K}^{(n)}$ is divided into NPROC groups of rows. In each group of rows only nonzero matrix elements are extracted, and their row and column numbers together with their values are stored into the corresponding processor. On the other hand, the entire column vector $\boldsymbol{f}\left(\hat{\boldsymbol{E}}^{(n)}\right)$ on the right-hand side of Equation (3.53) is stored into only processor 0. To enable high-resolution computation with a large size sparse matrix, ParMETIS is employed at the analysis step in the execution of MUMPS. The calculations are performed on the Franklin Cray-XT4 computer system at NERSC (National Energy Research Scientific Computing Center).

### 3.4.2 Precautions for Use

When the problem size, or the number of unknowns is increased, it is more likely to encounter several errors which are mostly related to the amount of memory. The

following are the list showing some of the most frequently seen error messages in the present calculations and the possible solutions to these errors.

(1) "MPICH has run out of unexpected buffer space. Try increasing the value of env var MPICH_UNEX_BUFFER_SIZE (cur value is 62914560), and/or reducing the size of MPICH_MAX_SHORT_MSG_SIZE (cur value is 128000)."

The problem can be solved by adding the following sentences into the batch script:

setenv MPICH_UNEX_BUFFER_SIZE 130000000

setenv MPICH_MAX_SHORT_MSG_SIZE 64000

(2) "OOM killer terminated this process."

The application used more memory than available on a Franklin node ~8 GB. The problem can be avoided by running with only 1 core per node by adding the following sentence into the batch script:

#PBS -l mppnppn=1

The corresponding command to launch a parallel job is written as

aprun -n NPROC -N 1 ./(executable file name)

(3) "On return from DMUMPS, INFOG(1)= -17"

The internal send buffer that was allocated dynamically by MUMPS on the processor is too small. The problem can be solved by increasing the value of ICNTL(14) in the main file.

(4) "PtlMEInsert failed with error : PTL_NO_SPACE"

75

The internal send buffer allocated is so large that the buffer space was run out. The problem can be solved by decreasing the value of ICNTL(14).

Among these errors, setting the appropriate buffer sizes can be tricky. The main reason is that every application has a different communication pattern. In principle, if an application sends and receives many messages, it will likely need more MPI buffer spaces. Therefore, errors occur if the communication buffers are exhausted when processors need to communicate with each other. Currently, the most effective way to avoid the error pertaining the buffer size would be to adjust the value of ICNTL(14). However, this approach requires us to struggle between errors (3) and (4) above through trial and error.

Empirically, it is found that the buffer size error is less frequently occurred when the total number of processors is set at the smallest value for a given problem size, which is equivalent to maximize the computation/communication ratio. This may be explained by the following reasons. First, spending more time in computing allows the buffers to be cleared and reused for message communication. Or secondly, increasing the ratio of computation to communication may decrease the necessity of communication since more data is available locally on each processor. However, it should be pointed out that even with this approach, the calculation becomes frequently failed by errors (3) and (4) when the total number of processors gets large (more than approximately 100 for the present finite element code). Although it is possible to increase the number of processors without limit when the code is run on Franklin, the present MUMPS algorithm virtually imposes a limitation on a problem size due to limited buffer space.
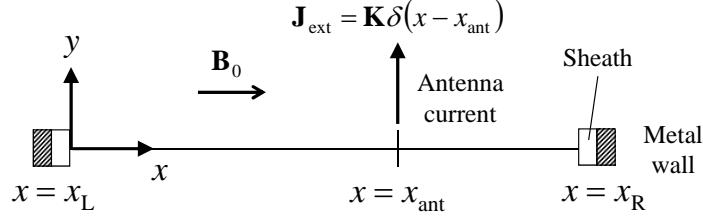
Figure 3-5: 1D calculation model for the derivation of the analytical solution.

## 3.5 Code Verification in 1D Geometry

### 3.5.1 Analytical Solution for Constant $n_0$ and $B_0$ in a 1D Domain

In order to verify the developed numerical scheme named "rfSOL," this section attempts to derive an analytical solution for the plasma wave driven by the antenna current in the 1D geometry subject to the sheath boundary condition at both ends, and compare the numerical results with the corresponding analytical results. The calculation domain considered here is shown in Figure 3-5; a constant-density plasma is filled in a waveguide which is assumed to be infinitely long in the $y$ and $z$ directions. The background magnetic field is also assumed to be constant in magnitude and pointed purely in the $x$ direction. The wavenumber components $k_y$ and $k_z$ are fixed (imposed), and the antenna current density is given by

$$\boldsymbol{J}_{\text{ext}} = K\delta\left(x - x_{\text{ant}}\right) \mathrm{e}^{i\left(k_y y + k_z z - \omega t\right)} \boldsymbol{e}_y = \boldsymbol{K}\delta\left(x - x_{\text{ant}}\right)$$

where $K$ is constant.

The derivation starts from a single vector equation for $\boldsymbol{E}$ derived in Chapter 2, which is repeated here for convenience:

$$\nabla \times \nabla \times \boldsymbol{E} - \frac{\omega^2}{c^2}\boldsymbol{\varepsilon} \cdot \boldsymbol{E} - i\omega\mu_0 \boldsymbol{J}_{\text{ext}} = \boldsymbol{0} \tag{3.58}$$

77

From Equation (2.14) one can write the dielectric tensor components as

$$
\varepsilon = \begin{pmatrix} \varepsilon_{xx} & 0 & 0 \\ 0 & \varepsilon_{yy} & \varepsilon_{yz} \\ 0 & \varepsilon_{zy} & \varepsilon_{zz} \end{pmatrix}
\tag{3.59}
$$

due to the assumption that $b_y = b_z = 0$. Now, let us look for a solution to Equation (3.58) in the following form:

$$
\boldsymbol{E} = \hat{\boldsymbol{E}} e^{i(k_x x + k_y y + k_z z - \omega t)}
\tag{3.60}
$$

Then, substituting Equation (3.60) into Equation (3.58), and focusing on the region where $\boldsymbol{J}_{\text{ext}} = \boldsymbol{0}$ yields

$$
\begin{pmatrix} \mathcal{D}_{11} & \mathcal{D}_{12} & \mathcal{D}_{13} \\ \mathcal{D}_{21} & \mathcal{D}_{22} & \mathcal{D}_{23} \\ \mathcal{D}_{31} & \mathcal{D}_{32} & \mathcal{D}_{33} \end{pmatrix} \begin{pmatrix} E_x \\ E_y \\ E_z \end{pmatrix} = \begin{pmatrix} 0 \\ 0 \\ 0 \end{pmatrix}
\tag{3.61}
$$

where

$$
\begin{aligned}
\mathcal{D}_{11} &= k_y^2 + k_z^2 - \frac{\omega^2}{c^2}\varepsilon_{xx}, \quad \mathcal{D}_{12} = -k_x k_y, \quad \mathcal{D}_{13} = -k_x k_z \\
\mathcal{D}_{21} &= -k_x k_y, \quad \mathcal{D}_{22} = k_x^2 + k_z^2 - \frac{\omega^2}{c^2}\varepsilon_{yy}, \quad \mathcal{D}_{23} = -k_y k_z - \frac{\omega^2}{c^2}\varepsilon_{yz} \\
\mathcal{D}_{31} &= -k_x k_z, \quad \mathcal{D}_{32} = -k_y k_z - \frac{\omega^2}{c^2}\varepsilon_{zy}, \quad \mathcal{D}_{33} = k_x^2 + k_y^2 - \frac{\omega^2}{c^2}\varepsilon_{zz}
\end{aligned}
\tag{3.62}
$$

A straightforward calculation shows that the dispersion relation derived from Equation (3.61) forms a quadratic equation in terms of $k_x^2$:

$$
\mathcal{A}_1 k_x^4 + \mathcal{A}_2 k_x^2 + \mathcal{A}_3 = 0
\tag{3.63}
$$

78

where

$$\mathcal{A}_1 = \varepsilon_{xx}$$

$$\mathcal{A}_2 = k_y^2 (\varepsilon_{xx} + \varepsilon_{yy}) + k_z^2 (\varepsilon_{xx} + \varepsilon_{zz}) - \frac{\omega^2}{c^2}\varepsilon_{xx}(\varepsilon_{yy} + \varepsilon_{zz})$$

$$\mathcal{A}_3 = (k_y^2 + k_z^2)(k_y^2\varepsilon_{yy} + k_z^2\varepsilon_{zz}) - \frac{\omega^2}{c^2}\left[k_y^2\varepsilon_{yy}(\varepsilon_{xx} + \varepsilon_{zz}) + k_z^2\varepsilon_{zz}(\varepsilon_{xx} + \varepsilon_{yy})\right.$$
$$\left. +\varepsilon_{yz}^2\left(k_y^2 + k_z^2 - \frac{\omega^2}{c^2}\varepsilon_{xx}\right) - \frac{\omega^2}{c^2}\varepsilon_{xx}\varepsilon_{yy}\varepsilon_{zz}\right]$$

(3.64)

The expression for $k_x^2$ is then easily obtained as follows:

$$k_x^2 = \frac{-\mathcal{A}_2 \pm (\mathcal{A}_2^2 - 4\mathcal{A}_1\mathcal{A}_3)^{1/2}}{2\mathcal{A}_1}$$

(3.65)

Notice that the coefficients $\mathcal{A}_1$, $\mathcal{A}_2$, and $\mathcal{A}_3$ in Equation (3.64) are all real values. If the background magnetic field has the $z$ component, the corresponding dispersion relation yields a general 4th-degree equation in terms of $k_x$, which is difficult to solve.

In general, Equation (3.65) gives two possible values for $k_x^2$, which results in four different roots for $k_x$. Since the domain is bounded in the $x$ direction, all the roots are physically acceptable, so that the general solution to Equation (3.58) is written as

$$\boldsymbol{E} = \left(\sum_{j=1}^{4} C_j \tilde{\boldsymbol{E}}_j e^{ik_{xj}x}\right) e^{i(k_y y + k_z z - \omega t)}$$

(3.66)

where $C_{1,...,4}$ are arbitrary constants, and $\tilde{\boldsymbol{E}}_j$ is the polarization eigenvector corresponding to $k_{xj}$.

In order to facilitate the derivation of the eigenvector $\tilde{\boldsymbol{E}}_j$, let us rewrite the matrix equation (3.61) in the following form:

$$\boldsymbol{\mathcal{D}}_i \cdot \tilde{\boldsymbol{E}}_i = \boldsymbol{0}$$

(3.67)

where the subscript $i$ indicates the number $1, \ldots, 4$ corresponding to $k_x = k_{x1}, \ldots, k_{x4}$, respectively. Since we know that $\det(\boldsymbol{\mathcal{D}}_i) = 0$, this implies only two of the three equations in Equation (3.61) are independent (in other words, for example, the third row equation must be obtained by the linear combination of the first and second row equations). In fact, by observing the matrix elements, we notice that one can pick up any two equations to obtain the eigenvectors. Here, let us specify that $\tilde{E}_{zi} = 1$. Then the resulting polarization eigenvectors are calculated using the first and second row equations of Equation (3.61) as follows:

$$
\begin{aligned}
\tilde{E}_{xi} &= \frac{1}{\mathcal{D}_{21}} \left( \mathcal{D}_{22} \frac{\mathcal{D}_{31}\mathcal{D}_{23} - \mathcal{D}_{21}\mathcal{D}_{33}}{\mathcal{D}_{31}\mathcal{D}_{22} - \mathcal{D}_{21}\mathcal{D}_{32}} - \mathcal{D}_{23} \right) \\
\tilde{E}_{yi} &= -\frac{\mathcal{D}_{31}\mathcal{D}_{23} - \mathcal{D}_{21}\mathcal{D}_{33}}{\mathcal{D}_{31}\mathcal{D}_{22} - \mathcal{D}_{21}\mathcal{D}_{32}} \\
\tilde{E}_{zi} &= 1
\end{aligned}
\tag{3.68}
$$

When the domain is divided by the presence of the external surface current, the general solutions for the electric field in region A and region B in Figure 3-5 are, respectively, written as

$$
\boldsymbol{E}_{\mathrm{A}} = \left( \sum_{j=1}^{4} C_{\mathrm{A}j} \tilde{\boldsymbol{E}}_j e^{ik_{xj}x} \right) e^{i(k_y y + k_z z - \omega t)}
\tag{3.69}
$$

$$
\boldsymbol{E}_{\mathrm{B}} = \left( \sum_{j=1}^{4} C_{\mathrm{B}j} \tilde{\boldsymbol{E}}_j e^{ik_{xj}x} \right) e^{i(k_y y + k_z z - \omega t)}
\tag{3.70}
$$

where $C_{\mathrm{A}1}, \ldots, C_{\mathrm{A}4}$ and $C_{\mathrm{B}1}, \ldots, C_{\mathrm{B}4}$ are constants to be determined. The corresponding expressions for the magnetic field are calculated by Faraday's law (see Equation (2.6)). The results are as follows:

$$
\begin{aligned}
\boldsymbol{B}_{\mathrm{A}} = -\frac{i}{\omega} e^{i(k_y y + k_z z - \omega t)} \sum_{j=1}^{4} i C_{\mathrm{A}j} e^{ik_{xj}x} \\
\cdot \left[ \left( k_y \tilde{E}_{zj} - k_z \tilde{E}_{yj} \right) \boldsymbol{e}_x + \left( k_z \tilde{E}_{xj} - k_{xj} \tilde{E}_{zj} \right) \boldsymbol{e}_y + \left( k_{xj} \tilde{E}_{yj} - k_y \tilde{E}_{xj} \right) \boldsymbol{e}_z \right]
\end{aligned}
\tag{3.71}
$$

$$\boldsymbol{B}_{\mathrm{B}} = -\frac{i}{\omega} \mathrm{e}^{i(k_y y + k_z z - \omega t)} \sum_{j=1}^{4} i C_{\mathrm{B}j} \mathrm{e}^{i k_{xj} x}$$

$$\cdot \left[ \left( k_y \tilde{E}_{zj} - k_z \tilde{E}_{yj} \right) \boldsymbol{e}_x + \left( k_z \tilde{E}_{xj} - k_{xj} \tilde{E}_{zj} \right) \boldsymbol{e}_y + \left( k_{xj} \tilde{E}_{yj} - k_y \tilde{E}_{xj} \right) \boldsymbol{e}_z \right] \qquad (3.72)$$

where the subscripts A and B denote the quantities in region A and region B, respectively, in the same way as for the electric field.

Since the magnetic field line intersects at a right angle with the walls, the sheath must be present at both ends, which yields the following four conditions:

$$\boldsymbol{E}_{\mathrm{At}}\big|_{x=x_{\mathrm{L}}} = i\boldsymbol{k}_{\mathrm{t}} \left[ \left( \alpha_{\mathrm{sh}} \left| \varepsilon_{xx} E_x \right|^3 + \beta_{\mathrm{sh}} \right) \varepsilon_{xx} E_x \right] \Big|_{x=x_{\mathrm{L}}}$$

$$\boldsymbol{E}_{\mathrm{Bt}}\big|_{x=x_{\mathrm{R}}} = -i\boldsymbol{k}_{\mathrm{t}} \left[ \left( \alpha_{\mathrm{sh}} \left| \varepsilon_{xx} E_x \right|^3 + \beta_{\mathrm{sh}} \right) \varepsilon_{xx} E_x \right] \Big|_{x=x_{\mathrm{R}}} \qquad (3.73)$$

where

$$\alpha_{\mathrm{sh}} = \left( \frac{e C_{\mathrm{sh}}}{T_{\mathrm{e}}} \right)^3 \lambda_{\mathrm{De}}^4, \quad \beta_{\mathrm{sh}} = C_{\mathrm{th}} \lambda_{\mathrm{De}}$$

$$\boldsymbol{k}_{\mathrm{t}} = k_y \boldsymbol{e}_y + k_z \boldsymbol{e}_z \qquad (3.74)$$

At the position where the surface current is present ($x = x_{\mathrm{ant}}$), one has to consider the jump conditions in both the electric and magnetic fields, which are given by

$$E_{\mathrm{A}y}\big|_{x=x_{\mathrm{ant}}} = E_{\mathrm{B}y}\big|_{x=x_{\mathrm{ant}}}, \quad E_{\mathrm{A}z}\big|_{x=x_{\mathrm{ant}}} = E_{\mathrm{B}z}\big|_{x=x_{\mathrm{ant}}}$$

$$B_{\mathrm{A}y}\big|_{x=x_{\mathrm{ant}}} = B_{\mathrm{B}y}\big|_{x=x_{\mathrm{ant}}}, \quad B_{\mathrm{A}z} - B_{\mathrm{B}z}\big|_{x=x_{\mathrm{ant}}} = \mu_0 K \mathrm{e}^{i(k_y y + k_z z - \omega t)} \qquad (3.75)$$

Consequently, one finds that the problem can be analytically solved since eight unknowns are calculated with the same number of equations.

If the nonlinear part of the sheath boundary condition can be neglected based on the amplitude of the RF fields, the linear system of equations is written as

$$\mathcal{G} \cdot C = \mathcal{R} \qquad (3.76)$$

where

$$\boldsymbol{C}^{\mathrm{T}} = \left( C_{\mathrm{A1}}^{\mathrm{(R,I)}} \cdots C_{\mathrm{A4}}^{\mathrm{(R,I)}} \quad C_{\mathrm{B1}}^{\mathrm{(R,I)}} \cdots C_{\mathrm{B4}}^{\mathrm{(R,I)}} \right) \tag{3.77}$$

The constant vector $\boldsymbol{C}$ is then immediately obtained by applying the Gaussian elimination, for example. However, in general the nonlinearity in the sheath boundary condition needs to be taken into account. In that case one has to iteratively calculate the vector $\boldsymbol{C}$, for example, using the Newton-Raphson method described in Section 3.3. The corresponding equation is written in the following form:

$$\boldsymbol{\mathcal{K}}^{(n)} \cdot \delta \boldsymbol{C} = -\boldsymbol{f}\left(\boldsymbol{C}^{(n)}\right) \tag{3.78}$$

where the superscript $n$ indicates the number of iteration, and

$$\begin{aligned}
\boldsymbol{\mathcal{K}}^{(n)} &= \left. \frac{\partial f_i}{\partial C_{\mathrm{A,B}j}^{\mathrm{(R,I)}}} \right|_{\boldsymbol{C}^{(n)}} \boldsymbol{e}_i \boldsymbol{e}_j \\
\delta \boldsymbol{C} &= \boldsymbol{C}^{(n+1)} - \boldsymbol{C}^{(n)}
\end{aligned} \tag{3.79}$$

Here $\boldsymbol{\mathcal{K}}^{(n)}$ is a second order tensor with $i = 1, \ldots, 16$ and $j = 1, \ldots, 4$.

### 3.5.2 Comparison between the Analytical and Numerical Solutions

First of all, the numerical results obtained with the 1D rfSOL code, which is straightforwardly constructed by converting $\partial/\partial y$ to $ik_y$ in Section 3.2, are compared with the results given by the analytical solution both for the linear and nonlinear cases. Based on Figure 3-5 the calculation domain is defined such that $x_{\mathrm{L}} = 0$ m, $x_{\mathrm{ant}} = 3.5$ m, and $x_{\mathrm{R}} = 5$ m. The plasma density and background magnetic field are assumed to be constant; $n_0 = 2.0 \times 10^{17}$ m$^{-3}$ and $B_0 = 5.4$ T. The other common parameters fixed in this analysis are $f = 80$ MHz, $T_{\mathrm{e}} = 10$ eV, $k_y = 0$ m$^{-1}$, and $k_z = 10.8$ m$^{-1}$.

For these parameters a SW propagates in the $x$ direction, which can be confirmed by rewriting Equation (2.23) in terms of $n_\parallel^2$. The surface current $K$ is set at 1 A/m for the linear case, while it is increased to 5 kA/m for the nonlinear case. In this numerical analysis a uniform mesh which includes 201 grid points (100 three-node elements) is used for the finite element discretization.

Figure 3-6 shows the comparison between the analytical and numerical solutions for the linear case, which are obtained by approximating the sheath boundary condition as

$$\boldsymbol{E}_{\mathrm{t}} = i\boldsymbol{k}_{\mathrm{t}} \left( \frac{\beta_{\mathrm{sh}}}{\varepsilon_{\mathrm{sh}}} D_{\mathrm{n}} \right) = i\boldsymbol{k}_{\mathrm{t}} \frac{\lambda_{\mathrm{De}}}{\varepsilon_{\mathrm{sh}}} \left\{ \ln \left[ \left( \frac{m_{\mathrm{i}}}{m_{\mathrm{e}}} \right)^{1/2} \right] \right\}^{3/4} D_{\mathrm{n}} \tag{3.80}$$

(see Equation (2.96)). Here "BC" in the legend stands for "boundary condition," and the dashed line indicates the antenna position. It is confirmed that the profiles of $\mathrm{Im}(E_x)$ and $\mathrm{Re}(E_z)$ are in good agreement. It is also found that the sheath boundary condition slightly increases the magnitude of variation in both electric field components, by comparing with the results for the conducting-wall boundary condition, i.e., $\boldsymbol{E}_{\mathrm{t}} = \boldsymbol{0}$. However, it is not always the case. As will be shown later, the electric field amplitude can be reduced with the increase of the sheath width.

Figure 3-7 shows the comparison between the analytical and numerical solutions for the nonlinear case. Here, the rectification factor $C_{\mathrm{sh}}$ and the convergence criterion $\varepsilon_{\mathrm{err}}$ are fixed at 0.6 and $1.0 \times 10^{-7}$, respectively. It is again confirmed that the profiles of $\mathrm{Im}(E_x)$ and $\mathrm{Re}(E_z)$ are in good agreement. Since the large surface current yields high electric field strength, the instantaneous sheath voltage $V_{\mathrm{sh}}$ dominates the Bohm sheath potential $V_{\mathrm{B}}$ in this problem; in fact, $C_{\mathrm{sh}} V_{\mathrm{sh}} = 8.8$ kV, while $V_{\mathrm{B}} = 41$ V at the right boundary. The resultant enlarged sheath width can modify the whole profile of the electric field corresponding to the Bohm sheath model ($C_{\mathrm{sh}} = 0$) as shown in both figures.
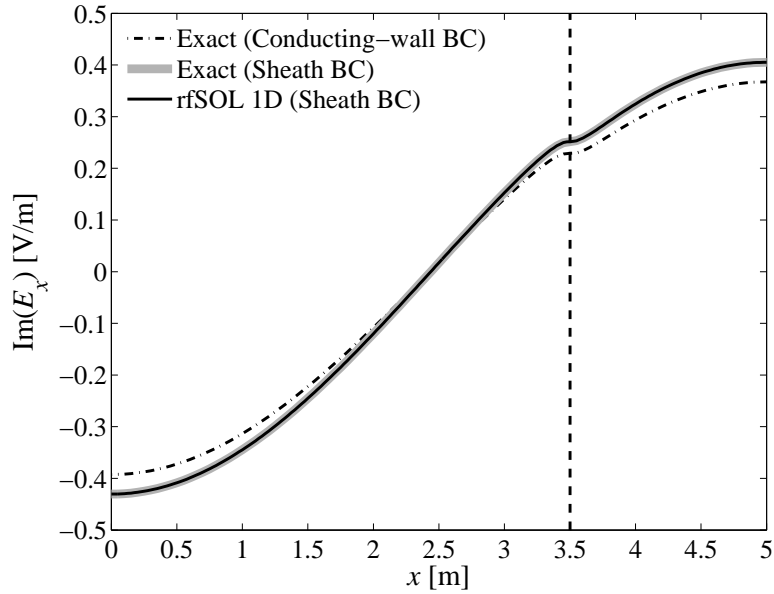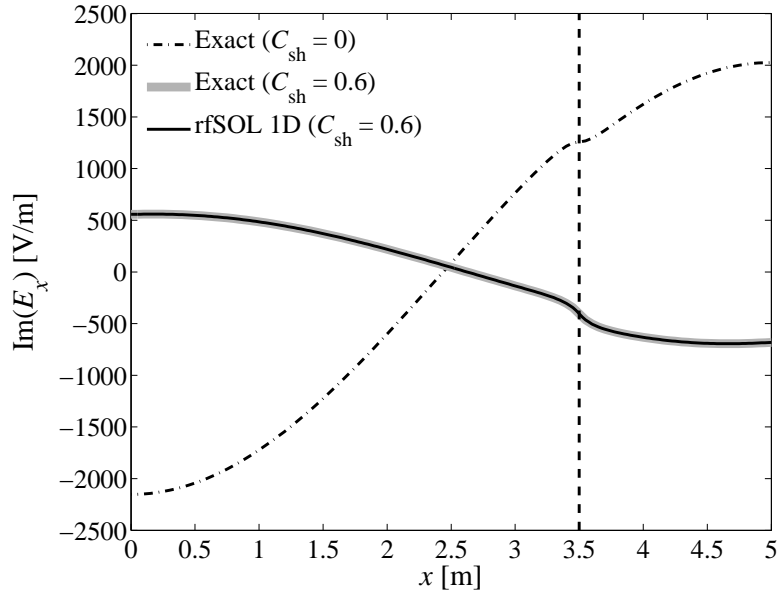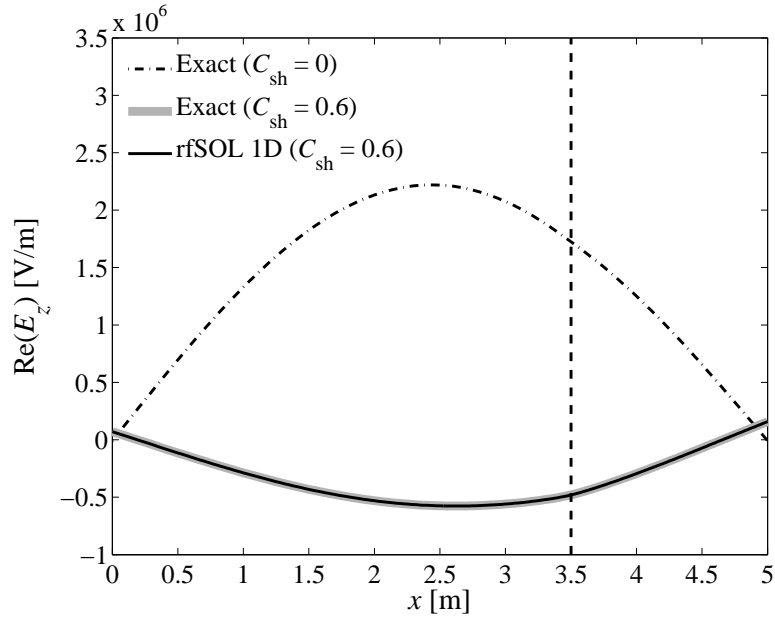
(a)
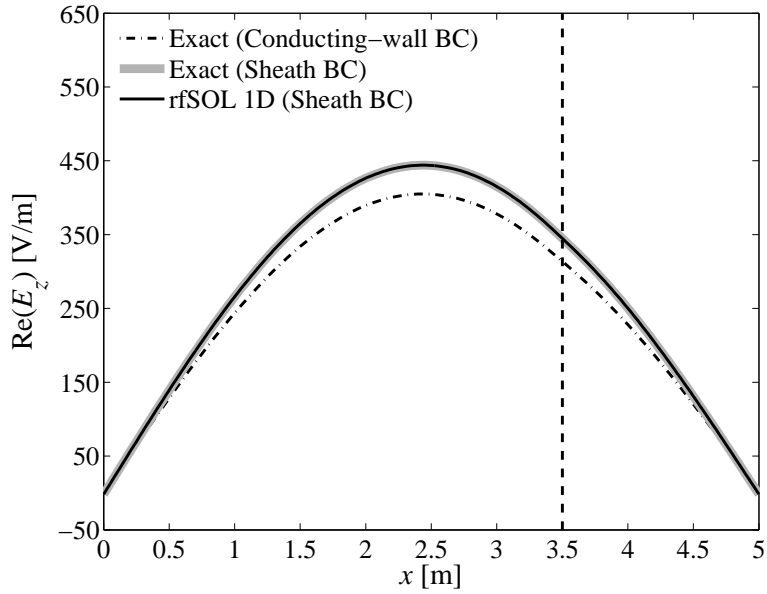


(b)

Figure 3-6: Comparison between the analytical and numerical solutions for the linearly-approximated sheath boundary condition: (a) $\mathrm{Im}(E_x)$ vs. $x$; and (b) $\mathrm{Re}(E_z)$ vs. $x$. The vertical dashed line indicates the antenna position.

84

(a)



(b)

Figure 3-7: Comparison between the analytical and numerical solutions for the non-linear sheath boundary condition: (a) $\mathrm{Im}(E_x)$ vs. $x$; and (b) $\mathrm{Re}(E_z)$ vs. $x$. The vertical dashed line indicates the antenna position.

### 3.5.3 Lower Hybrid Resonance in a Varying $n_0$ Field

Next, let us consider the case where the plasma density is varied in the $x$ direction with a constant background magnetic field parallel to the walls. The purpose of this calculation is to see whether the lower hybrid resonance correctly appeares at the right position. In this test problem the calculation domain is defined such that $x_{\mathrm{L}} = 0$ m, $x_{\mathrm{ant}} = 0.155$ m, and $x_{\mathrm{R}} = 0.23$ m. The plasma density is assumed to be varied according to the following formula:

$$n_0 = (n_{\mathrm{L}} - n_{\mathrm{R}}) \exp\left(-\frac{x - x_{\mathrm{L}}}{\lambda_n}\right) + n_{\mathrm{R}} \tag{3.81}$$

where $n_{\mathrm{L}}$ and $n_{\mathrm{R}}$ are the density values at the left and right boundaries, respectively; these values are set at $n_{\mathrm{L}} = 2.0 \times 10^{19}$ m$^{-3}$ and $n_{\mathrm{R}} = 2.0 \times 10^{16}$ m$^{-3}$. The length $\lambda_n$ is chosen such that $x_{\mathrm{R}} - x_{\mathrm{L}} \gg \lambda_n$; here, $\lambda_n = 0.02$ m. The other fixed parameters are $B_0 = 5.4$ T ($\boldsymbol{B}_0 = B_0 \boldsymbol{e}_z$), $f = 80$ MHz, $K = 1$ A/m, $k_y = 0$ m$^{-1}$, and $k_z = 10.8$ m$^{-1}$, and a piecewise uniform mesh of 3201 grid points (1600 three-node elements; 1080 elements in $x_{\mathrm{L}} \leq x \leq x_{\mathrm{ant}}$ and 520 elements in $x_{\mathrm{ant}} \leq x \leq x_{\mathrm{R}}$) is used. Since the magnetic field lines are aligned parallel to the walls, the sheath boundary condition can be approximately expressed as $\boldsymbol{E}_{\mathrm{t}} = \boldsymbol{0}$ (i.e., the nonlinear contribution is regarded as being small).

As described in Section 2.4.4, the lower hybrid resonance corresponds to $\varepsilon_\perp = 0$. For $n_0 = n_{\mathrm{e}0} = n_{\mathrm{i}0}$ the lower hybrid density $n_{\mathrm{LH}}$ is analytically calculated using Equation (2.13) as follows:

$$n_{\mathrm{LH}} = \frac{\varepsilon_0}{e^2} \left[\sum_j \frac{1}{m_j \left(\omega^2 - \Omega_j^2\right)}\right]^{-1} \tag{3.82}$$

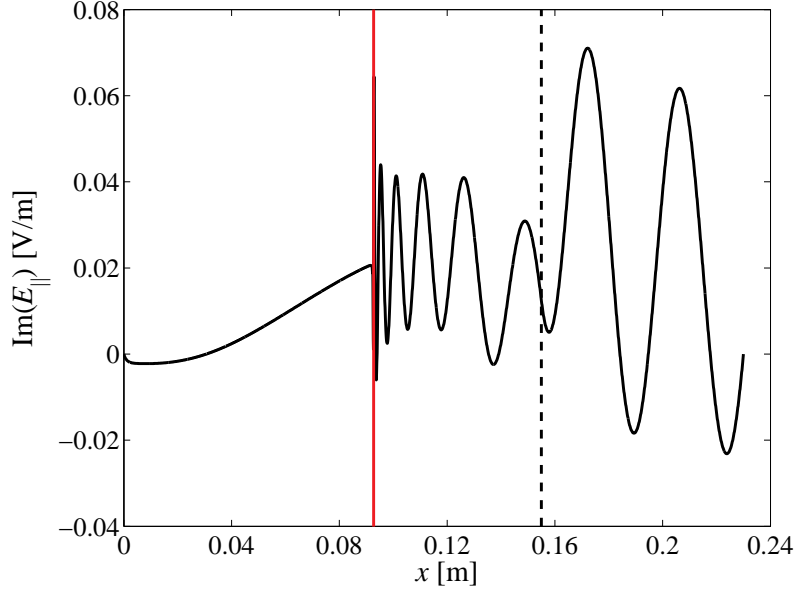Then, substituting Equation (3.82) into the left-hand side of Equation (3.81) leads to

Figure 3-8: Plot of $\mathrm{Im}\big(E_\parallel\big)$ vs. $x$ for the background magnetic field parallel to the walls. The red line shows the position of the lower hybrid resonance, and the vertical dashed line indicates the antenna position.

the expression for the position $x_{\mathrm{LH}}$ where the lower hybrid resonance appears:

$$x_{\mathrm{LH}} = -\lambda_n \ln \frac{n_{\mathrm{LH}} - n_{\mathrm{R}}}{n_{\mathrm{L}} - n_{\mathrm{R}}} \tag{3.83}$$

For the parameters given above, it follows that $x_{\mathrm{LH}} = 9.27 \times 10^{-2}$ m.

Figure 3-8 shows the variation of $\mathrm{Im}\big(E_\parallel\big)$, where $E_\parallel = \boldsymbol{E} \cdot \boldsymbol{b}$ ($\boldsymbol{b} = \boldsymbol{B}_0/|\boldsymbol{B}_0|$), along the calculation domain. Here the dashed and red lines indicate the positions at $x = x_{\mathrm{ant}}$ and $x = x_{\mathrm{LH}}$, respectively. It is confirmed that the position of the lower hybrid resonance is correctly calculated with the present numerical scheme.

The wavenumber (or the wavelength) at some particular position in the low-density region can be evaluated using the local SW dispersion relation. From Equation (2.34) one gets

$$k_\perp = k_x = \pm \frac{\omega}{c} \left[ \frac{\varepsilon_\parallel}{\varepsilon_\perp} \big(\varepsilon_\perp - n_\parallel^2\big) \right]^{1/2} \tag{3.84}$$
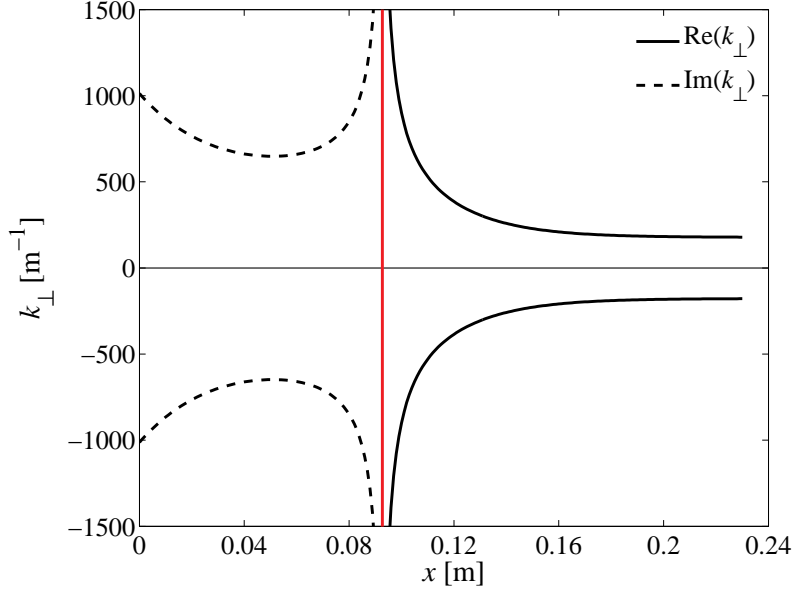
Figure 3-9: Plot of the real and imaginary parts of the perpendicular wavenumber component for the background magnetic field parallel to the walls. The red line indicates the position of the lower hybrid resonance.

The obtained perpendicular wavenumber component (i.e., the wavenumber component perpendicular to the direction of the background magnetic field) is plotted in Figure 3-9. It is observed that the SW is propagating on the right side of the lower hybrid resonance (due to the fact that $\text{Re}(k_\perp) > 0$). Using this result, for example, the wavelength at $x = 0.2$ m is calculated at $3.4 \times 10^{-2}$ m, which agrees well with the numerical result shown in Figure 3-8.

### 3.5.4 Thick-Sheath Limit

When we assume wave modes at the sheath-plasma interface, the sheath boundary condition is expressed as

$$\boldsymbol{E}_t = i\boldsymbol{k}_t \frac{\Delta_{\text{sh}}}{\varepsilon_{\text{sh}}} D_{\text{n}} \tag{3.85}$$

88

Here, let us consider the limit where $\Delta_{\text{sh}} \to \infty$. Since physically $\boldsymbol{E}_{\text{t}}$ must be finite, it is required that $D_{\text{n}} \to 0$. Consequently, the sheath becomes equivalent to an insulating layer, for which the boundary condition (3.85) reduces to

$$D_{\text{n}} = 0, \quad B_{\text{n}} = 0 \tag{3.86}$$

The purpose of the last numerical example presented below is to confirm that the developed numerical scheme surely possesses this property.

The calculation model considered here is the same as used in the previous section, except that the background magnetic field has a small $x$ component; $B_{0x} = 0.5$ T and $B_{0z} = 5.4$ T. To test the thick-sheath limit, the sheath width $\Delta_{\text{sh}}$ is expressed as

$$
\begin{aligned}
\Delta_{\text{sh}} &= \alpha_{\text{amp}} C_{\text{th}} \lambda_{\text{De}} \\
&= \alpha_{\text{amp}} \lambda_{\text{De}} \left\{ \ln \left[ \left( \frac{m_{\text{i}}}{m_{\text{e}}} \right)^{1/2} \frac{B_{0x}}{(B_{0x}^2 + B_{0z}^2)^{1/2}} \right] \right\}^{3/4}
\end{aligned} \tag{3.87}
$$

where $\alpha_{\text{amp}}$ is the artificial amplification factor. The discretized expressions corresponding to the insulating boundary condition (3.86) are, respectively, given by

$$\varepsilon_{xx} \hat{E}_{xi} + \varepsilon_{xy} \hat{E}_{yi} + \varepsilon_{xz} \hat{E}_{zi} = 0 \tag{3.88}$$

$$k_y \hat{E}_{zi} - k_z \hat{E}_{yi} = 0 \tag{3.89}$$

where the subscript i denotes the nodes at the left and right boundaries.

Figure 3-10 shows the comparison of the numerical results obtained by imposing the sheath boundary condition with $\alpha_{\text{amp}} = 1, 1000$ and the insulating boundary condition. It is observed that the wave profiles of $\text{Re}(E_{\parallel})$ and $\text{Im}(E_{\parallel})$ for $\alpha_{\text{amp}} = 1000$ are completely overlapped with the numerical results obtained using the insulating boundary condition, which demonstrates that the present code yields the correct property in the thick-sheath limit. It is also shown that the wave amplitude is sufficiently reduced when the sheath width becomes very large, although its transition

may not be monotonic (see Section 4.5 for a possible cause).

In this problem the perpendicular and parallel wavenumber components can be expressed as

$$k_\perp \simeq k_x$$
$$k_\parallel = b_x k_x + b_z k_z \tag{3.90}$$

Substituting Equation (3.90) into the SW dispersion relation (2.34) yields a quadratic equation in terms of $k_x$:

$$C_{\mathrm{SW1}} k_x^2 + C_{\mathrm{SW2}} k_x + C_{\mathrm{SW3}} = 0 \tag{3.91}$$

where

$$C_{\mathrm{SW1}} = \left(\frac{c}{\omega}\right)^2 \left(b_x^2 \varepsilon_\parallel + \varepsilon_\perp\right), \quad C_{\mathrm{SW2}} = 2\left(\frac{c}{\omega}\right)^2 b_x b_z \varepsilon_\parallel k_z$$
$$C_{\mathrm{SW3}} = \varepsilon_\parallel \left[\left(\frac{c}{\omega} b_z k_z\right)^2 - \varepsilon_\perp\right] \tag{3.92}$$

The roots of Equation (3.91) are plotted in Figure 3-11. It is confirmed that the calculated wavelength around $x = 0.2$ m, which is approximately $0.02$ m, agrees with the analytical estimate corresponding to the lower branch of $\mathrm{Re}(k_\perp)$. In addition, it is interesting to see that the lower hybrid resonance does not occur when the background magnetic field is slightly tilted to the walls. In fact, at the position where $\varepsilon_\perp = 0$, the electrostatic approximation $(n_\parallel^2 \gg \varepsilon_\perp)$ is well satisfied, yielding a finite value of $k_x$:

$$k_x\big|_{\varepsilon_\perp = 0} = -\frac{b_z}{b_x} k_z \tag{3.93}$$

For the given parameters the value of $k_x$ is calculated at $-117$ m$^{-1}$.
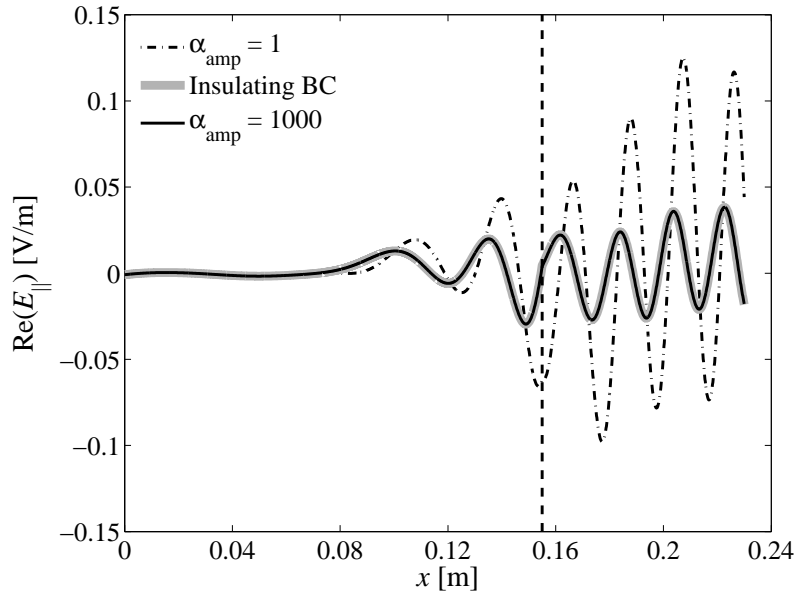
(a)
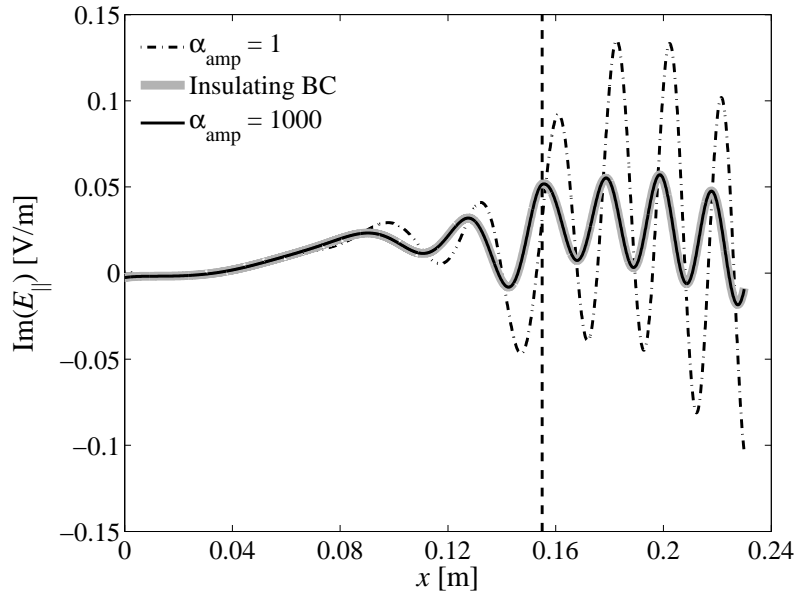


(b)

Figure 3-10: Demonstration that the sheath boundary condition reduces to the insulating boundary condition in the thick-sheath limit: (a) $\mathrm{Re}\big(E_\parallel\big)$ vs. $x$; and (b) $\mathrm{Im}\big(E_\parallel\big)$ vs. $x$. The vertical dashed line indicates the antenna position.
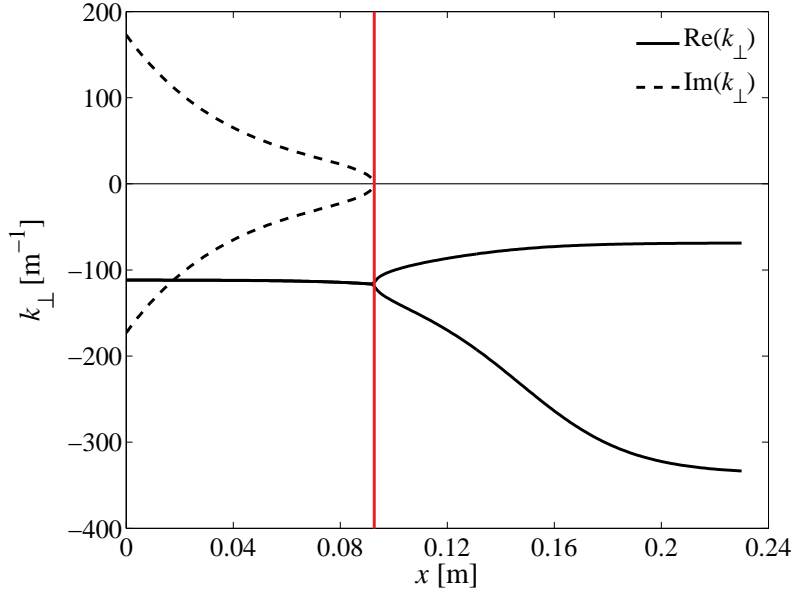
Figure 3-11: Plot of the real and imaginary parts of the perpendicular wavenumber component for the background magnetic field slightly inclined to the walls. The red line indicates the position where $\varepsilon_\perp = 0$.

## 3.6 Computational Performance

In closing this chapter the performance of calculations using the rfSOL code is briefly described in this section. Here the linear sheath-plasma interaction problem for a 2D domain is solved with two different grid resolutions: $100 \times 130$ and $200 \times 260$ nine-node elements. The detailed geometry of the 2D domain and the calculation parameters will be described in Section 4.4.1, and are thus omitted here.

Plots of wall clock time and the percentage of communication vs. number of processors are illustrated in Figure 3-12. These data were measured by the NERSC developed Integrated Performance Monitoring (IPM) Tool for MPI programs on Franklin. It is observed in both grid resolutions that the wall clock time is decreased with the increase in the number of processors when the number of processors is relatively small. However, due to the increase in communication among processors, the wall clock time eventually hovers at a certain level for both cases. It is also confirmed from Figure 3-12b that the percentage of communication in the total run time goes up to about

50 percent, but then stays almost constant.

It should be noted, however, that there is considerable variation in the estimated root size selected for Scalapack even if exactly the same run is submitted in a row; this variation of course affects the wall clock time and the percentage of communication. This may be caused by some unoptimized structure in MUMPS or ParMETIS. Therefore, the results shown in Figure 3-12 should be regarded as an example of possible trends.
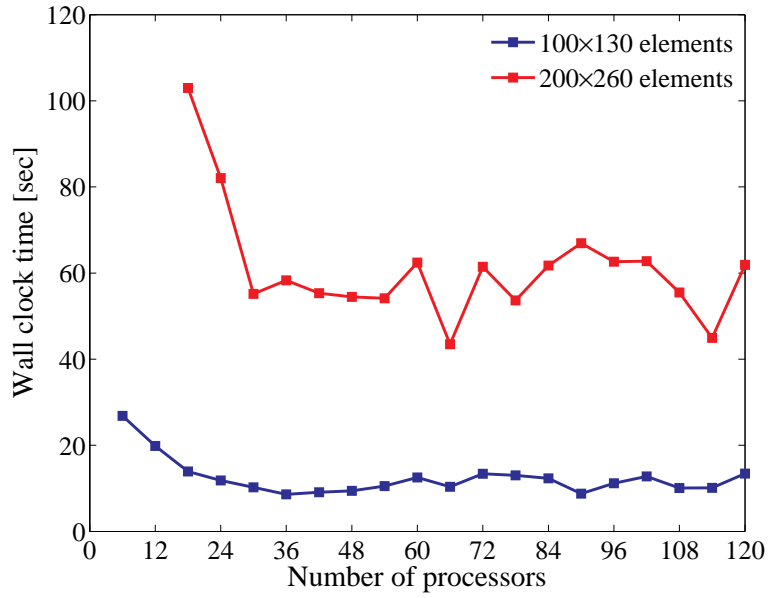
(a)
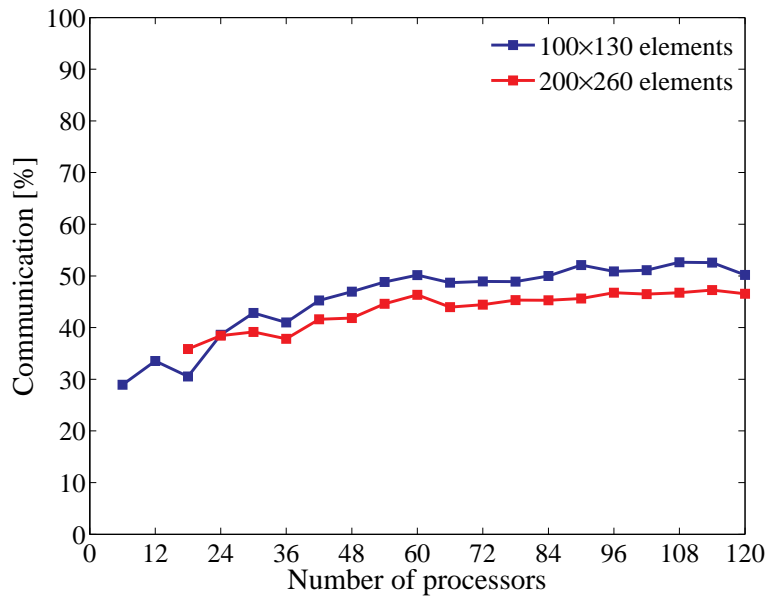


(b)

Figure 3-12: (a) Wall clock time and (b) the percentage of communication vs. number of processors with two different grid resolutions for a problem in the 2D domain.

# Chapter 4

# Numerical Simulation of RF Sheath-Plasma Interactions

## 4.1 Prologue

Using the rfSOL code described in the previous chapter, we are now ready to numerically solve various problems including RF sheath-plasma interactions. To begin, the rfSOL code is applied to two problems in the 1D domain, and the basic physics of the sheath-plasma interactions is investigated by observing the variation of the sheath potential as a function of the antenna current and the effect of sheath on waves in the edge plasma. A particular emphasis is placed on a resonance phenomenon generated by a propagating SW confined between a wall-sheath and a reflection point where $\varepsilon_\perp = 0$, and the resultant multiple roots. This is followed by the analysis in a 2D slab domain, in which both the thermal and RF sheaths are considered with various plasma density values and background magnetic fields. Here an analytical investigation is also conducted to assess the accuracy of the numerical results and elucidate the characteristics of the wave mode appeared on the sheath surface. The parameters used in the present numerical simulations come from typical ICH operating conditions in Alcator C-Mod.

## 4.2 Propagating SW and Sheath Interaction in 1D Geometry

The first application of the rfSOL code is directed to the 1D problem including the propagating SW and sheath interaction as shown in Figure 4-1. Here it is assumed that the sheath (or the metal wall) is present only on the right-hand side, while the SW is evanescent due to the absorbing layer on the left-hand side of the domain. Based on the notation in Figure 4-1 the calculation domain is defined such that $x_{\mathrm{L}} = 0$ m, $x_{\mathrm{ant}} = 2.8$ m, and $x_{\mathrm{R}} = 3.0$ m; a sufficiently long distance is provided between the left boundary and the antenna position to assure that the left-going wave amplitude is smoothly decayed to zero within the absorbing layer and thereby it is not reflected from the left boundary. The plasma density and background magnetic field are assumed to be constant; $n_0 = 1.0 \times 10^{17}$ m$^{-3}$, and $B_{0x} = 1.5$ T, $B_{0y} = 0$ T, and $B_{0z} = 4.0$ T. The value of $B_{0z}$ used here corresponds to a typical value of the toroidal background magnetic field in the edge region of the Alcator C-Mod tokamak for the hydrogen minority heating scenarios with the ICRF source frequency (in this case the toroidal background magnetic field at the major radius is adjusted to 5.4 T). The other parameters fixed in this analysis are $f = 80$ MHz, $T_{\mathrm{e}} = 10$ eV, $k_y = 0$ m$^{-1}$, $k_z = 10.8$ m$^{-1}$, $C_{\mathrm{sh}} = 0.6$, and $\varepsilon_{\mathrm{err}} = 1.0 \times 10^{-3}$; the absorbing layer is formed with $\nu_0 = 3.0 \times 10^{11}$ s$^{-1}$, $x_{\mathrm{abs}} = 0$ m, and $\lambda_\nu = 0.2$ m (see Equation (2.103)). In this numerical analysis a uniform mesh which includes 3001 grid points (1500 three-node elements) is used for the finite element discretization.

Figure 4-2 shows the variations of the real and imaginary parts of the parallel electric field component ($E_\parallel = \boldsymbol{E} \cdot \boldsymbol{b} = \boldsymbol{E} \cdot \boldsymbol{B}_0/|\boldsymbol{B}_0|$) obtained with four different antenna current values. Here the electric field is normalized by dividing it by the corresponding antenna current value; thus, the profiles of $\mathrm{Re}\left(E_\parallel\right)/K$ and $\mathrm{Im}\left(E_\parallel\right)/K$ should be unchanged if the sheath width is independent of the electric field strength. It is observed that the waves propagate with a constant wavelength until they are
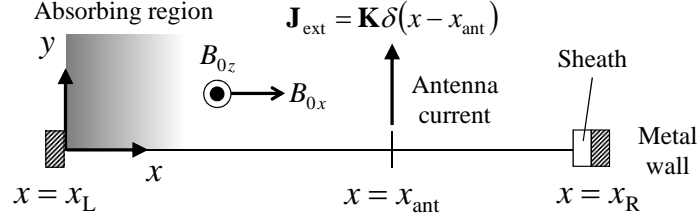
96

Figure 4-1: 1D calculation model for the propagating SW with the sheath boundary condition imposed on the right wall.

absorbed on the left-hand side. The wavelength can be analytically calculated at 0.19 m, which corresponds to one root of the SW dispersion relation (see Equations (3.91) and (3.92)) and agrees well with the numerical results. In addition, it is confirmed from Figure 4-3 that the real and imaginary parts of $E_\parallel$ are $\pi/2$ out of phase, which indicates there is no reflection from the left boundary and proves that the absorbing boundary condition is successfully introduced into the problem.

An interesting observation is that the results for $K = 5000$ kA/m are almost overlapped with the results for $K = 500$ kA/m. This may be explained in a similar fashion to the thick-sheath limit described in Section 3.5.4. From the sheath boundary condition we obtain

$$\frac{|E_z|/K}{|D_\mathrm{n}|/K} = k_z \frac{\Delta_\mathrm{sh}}{\varepsilon_\mathrm{sh}} \tag{4.1}$$

Here recall that $k_y = 0$ in this analysis. Thus, when $|E_z|/K$ is unchanged with respect to $K$ (or varied slowly compared with $\Delta_\mathrm{sh}$), $|D_\mathrm{n}|/K$ should vary inversely with $\Delta_\mathrm{sh}$. In fact, this can be seen in Figure 4-4; $|D_\mathrm{n}|/K$ decreases with an increase of $\Delta_\mathrm{sh}$ for sufficiently large values of $K$. Therefore, in the limit where $\Delta_\mathrm{sh} \to \infty$, it is expected that the sheath boundary condition will reduce to the quasi-insulating boundary condition expressed as

$$D_\mathrm{n}/K = 0, \quad B_\mathrm{n} = 0 \tag{4.2}$$
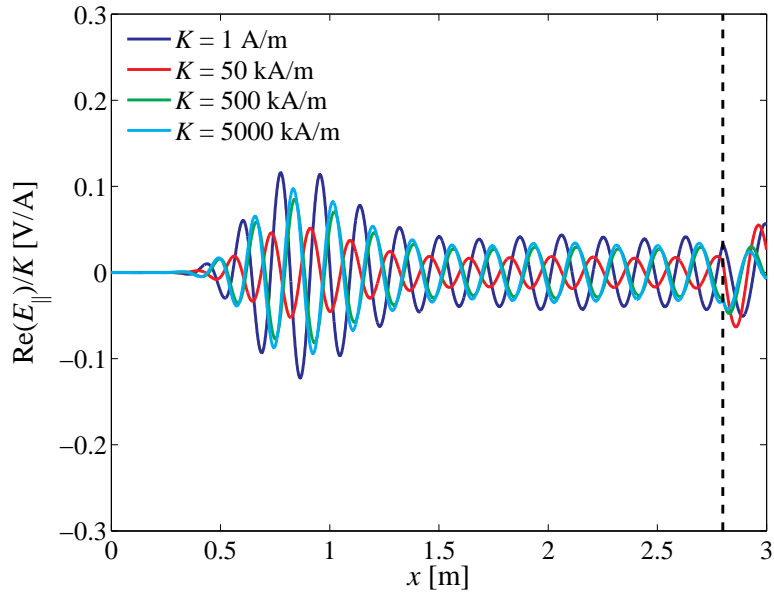
(a)
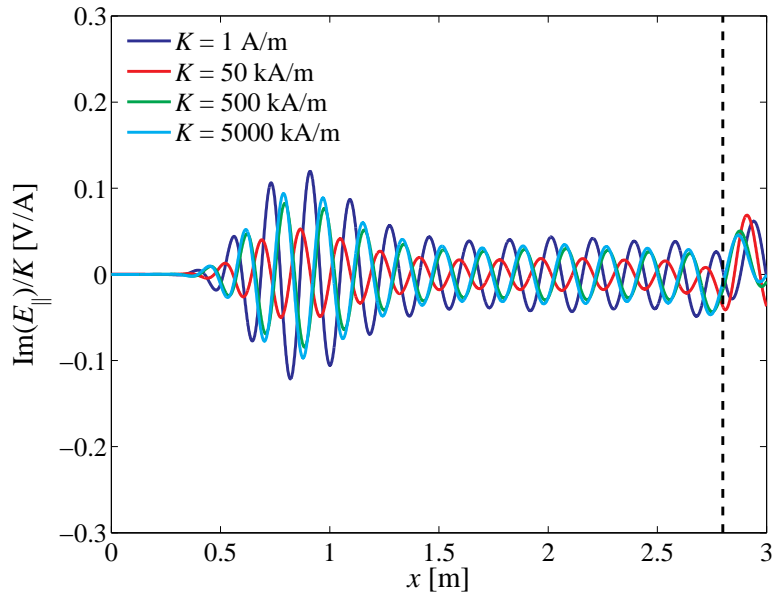


(b)

Figure 4-2: Plots of the real (a) and imaginary (b) parts of the normalized parallel electric field component along the 1D domain for four different surface current values. The vertical dashed line indicates the antenna position. These plots show the propagating SWs.
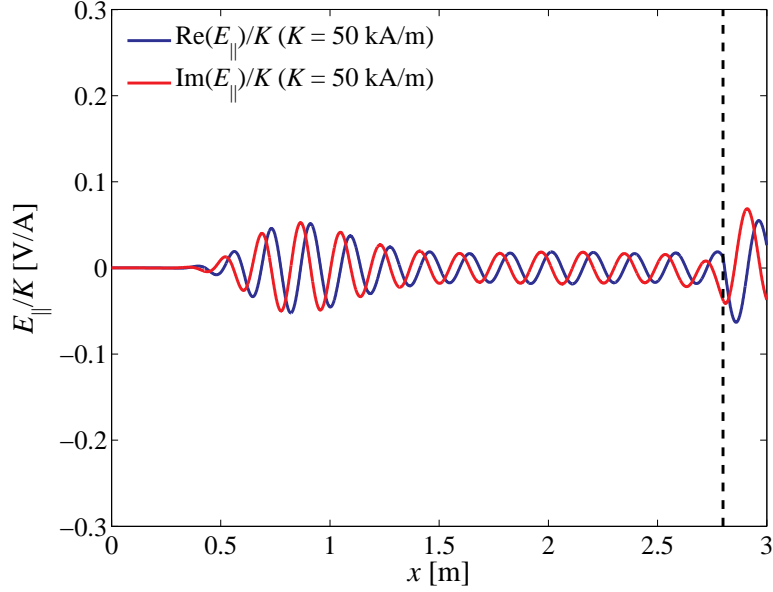
98

Figure 4-3: Plot of the real and imaginary parts of the normalized parallel electric field component for $K = 50$ kA/m. The vertical dashed line indicates the antenna position.

Figure 4-5 shows the variation of the rectified sheath potential $V_0$ as a function of $K$, including the comparison with the Bohm sheath potential $V_B$. First, it is seen from Figure 4-5a that the rectified sheath potential variation has a threshold-like turn-on characteristic, which is similar to the results obtained by the previous analytical work conducted by Myra and D'Ippolito [34, 35]. This characteristic is also observed in the variation of the sheath width (shown in Figure 4-4a) due to the relation (2.102). For the present numerical condition the sheath potential value and sheath width abruptly start increasing with the antenna current around $K = 20$ kA/m. Although the sheath potential appears to be growing almost linearly with $K$ when the antenna current exceeds this critical value, the variation is not exactly linear due to the fact that the sheath width is a function of the electric field strength. Further, it is important to realize that this threshold-like turn-on has no relation to the transition from the thermal sheath dominated regime (second term in Equation
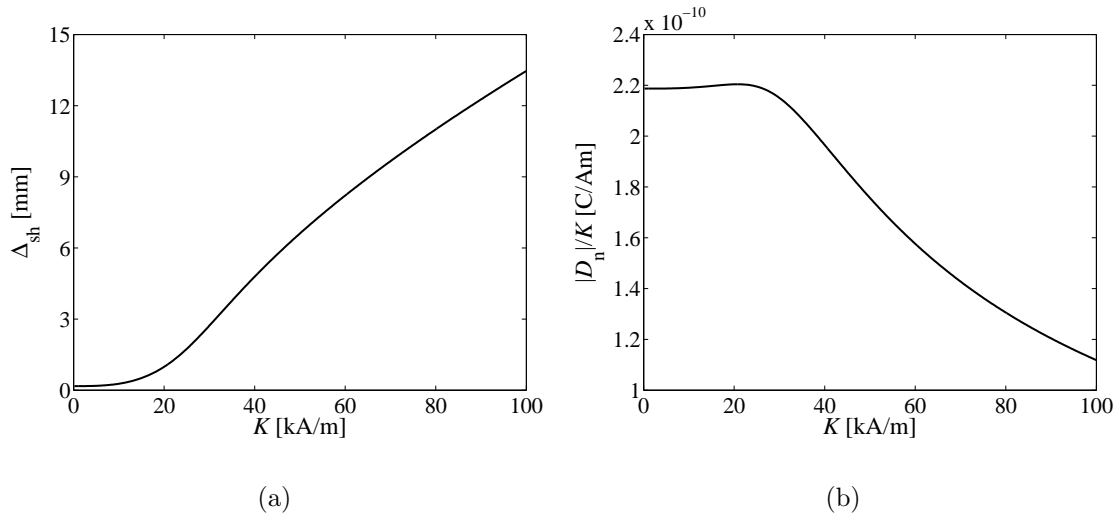
Figure 4-4: (a) The sheath width $\Delta_{\mathrm{sh}}$ and (b) normalized normal component of the electric displacement $|D_{\mathrm{n}}|/K$ on the sheath surface as functions of the antenna current $K$.
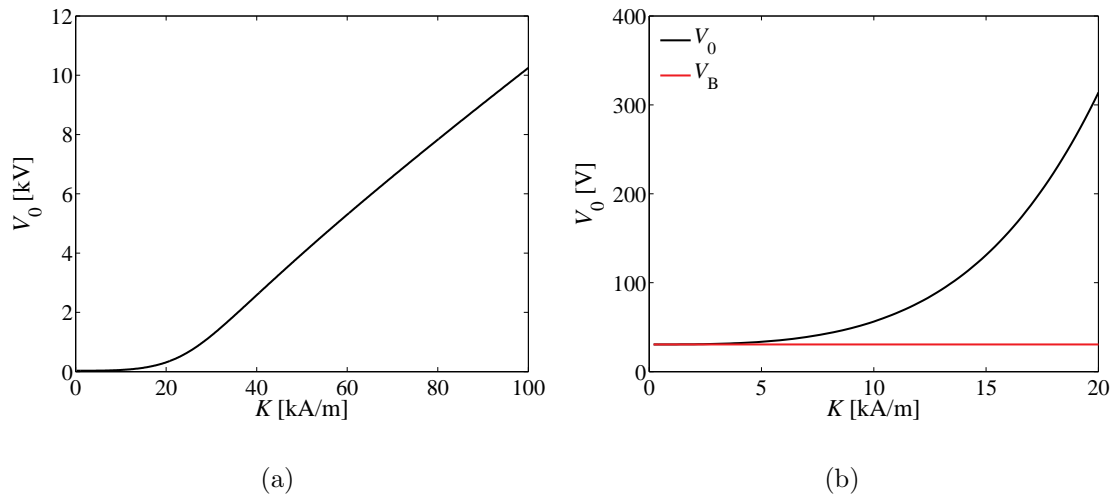


Figure 4-5: The rectified sheath potential $V_0$ as a function of the antenna current $K$: (a) entire variation; and (b) comparison with the Bohm sheath potential $V_{\mathrm{B}}$ in a restricted range of $K$.
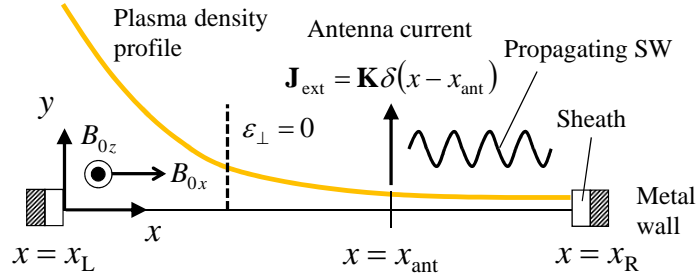
Figure 4-6: 1D calculation model for the propagating SW confined between a wall-sheath and a reflection point where $\varepsilon_\perp = 0$.

(2.101)) to the RF sheath dominated regime (first term in Equation (2.101)). As shown in Figure 4-5b, this transition occurs around $K = 5$ kA/m, below which the entire system can be approximated as being linear since the Bohm sheath potential dominates the sheath potential.

## 4.3   Multiple Roots

Consider next the sheath-plasma interaction in 1D geometry with a varying plasma density profile. The calculation model, which is shown in Figure 4-6, is mostly the same as used in the previous problem, except that the absorbing layer is replaced with the metal wall covered by a sheath, and the distribution of the plasma density is given by Equation (3.81) with $n_L = 1.0 \times 10^{19}$ m$^{-3}$, $n_R = 1.0 \times 10^{17}$ m$^{-3}$, and $\lambda_n = 0.4$ m. Here the calculation domain is defined such that $x_L = 0$ m, $x_{ant} = 0.8$ m, and $x_R = 1$ m. The background magnetic field and all other parameters (including a uniform mesh) are fixed using the same values as in the previous example. An important fact in this problem is that a SW is confined between a wall-sheath and a reflection point where $\varepsilon_\perp = 0$ due to the varying plasma density profile, which can cause resonant phenomena, as will be seen below. It is also a case of some practical importance since this situation can occur in realistic tokamak plasmas.

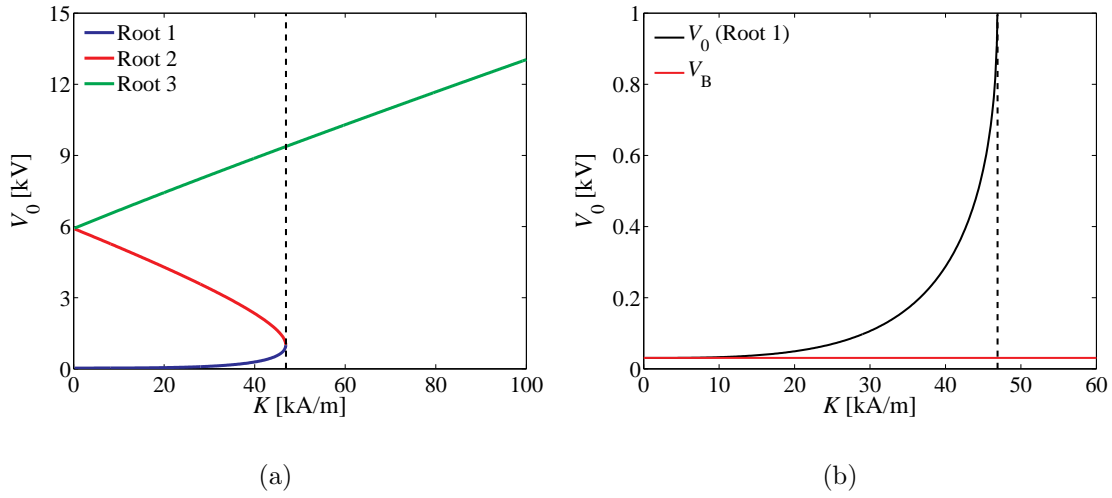Figure 4-7 shows the variation of the rectified sheath potential $V_0$ at the right

Figure 4-7: The rectified sheath potential $V_0$ at the right sheath as a function of the antenna current $K$ for the case without dissipation: (a) entire variation showing multiple roots; and (b) comparison between root 1 and the Bohm sheath potential $V_B$ in a restricted range of $K$. The vertical dashed line indicates the critical antenna current (46.9 kA/m) at which root jumping occurs.

sheath as a function of $K$. It is interesting to see in Figure 4-7a that there are three different roots for the antenna current less than 46.9 kA/m $(= K_{\text{crit}})$. As the antenna current increases, the sheath voltages in root 1 and root 2 encounter a threshold at $K = K_{\text{crit}}$ where it becomes possible for root 1 and root 2 to undergo a jump to root 3. The transition of this sharp voltage increase cannot be explained by the present assumptions, but the multiple roots we obtain are the solutions of the steady-state problem considered here. Figure 4-7b shows a magnified variation of root 1 together with the horizontal red line showing the Bohm sheath potential. It is confirmed that the RF sheath potential starts to matter around $K = 15$ kA/m in the present case.

Figure 4-8 shows the comparison of the real and imaginary parts of the normalized parallel electric field component among the three roots for $K = 40$ kA/m. It is seen that the phase and amplitude of the three roots are different from each other.

The question why we have multiple solutions in this problem can be answered by looking at the graphical solution [36] in Figure 4-9. Here the thick black curve
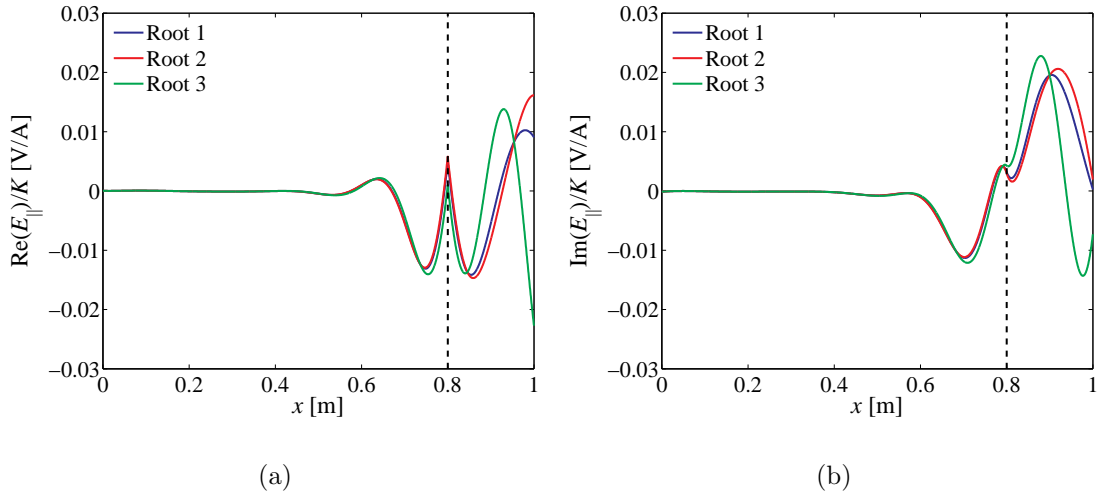
102

Figure 4-8: Comparison of the real (a) and imaginary (b) parts of the normalized parallel electric field component among the three roots for $K = 40$ kA/m. The vertical dashed line indicates the antenna position. The profiles on the right half of the plots show the propagating SWs.

corresponds to the RF sheath potential at the right sheath ($V_0 \simeq C_{\mathrm{sh}} V_{\mathrm{sh}}$), which is obtained by employing the linear 1D rfSOL code with "specified" sheath widths (the sheath width on the left-hand side is assumed to be zero). The colored curves correspond to the sheath potential $V_0$ computed from the Child-Langmuir law (see Equation (2.102)). Notice that the vertical axis of the plot shows the voltage value normalized by the antenna current; therefore, one can draw an infinite number of Child-Langmuir curves depending on the value of $K$. The intersections between the black and colored curves correspond to the self-consistent solutions (i.e., self-consistent sheath widths and potential values).

In Figure 4-9a we see a resonance behavior in the numerical solution when the sheath width approaches 3 mm. This occurs due to the phase matching of the SW confined between a wall-sheath on one side and a reflection point where $\varepsilon_\perp = 0$ on the other side. All the antenna current values shown here have three intersection points (see Figure 4-9b for a magnified local variation in the bottom left corner of Figure 4-9a). However, two intersection points approach each other with increasing
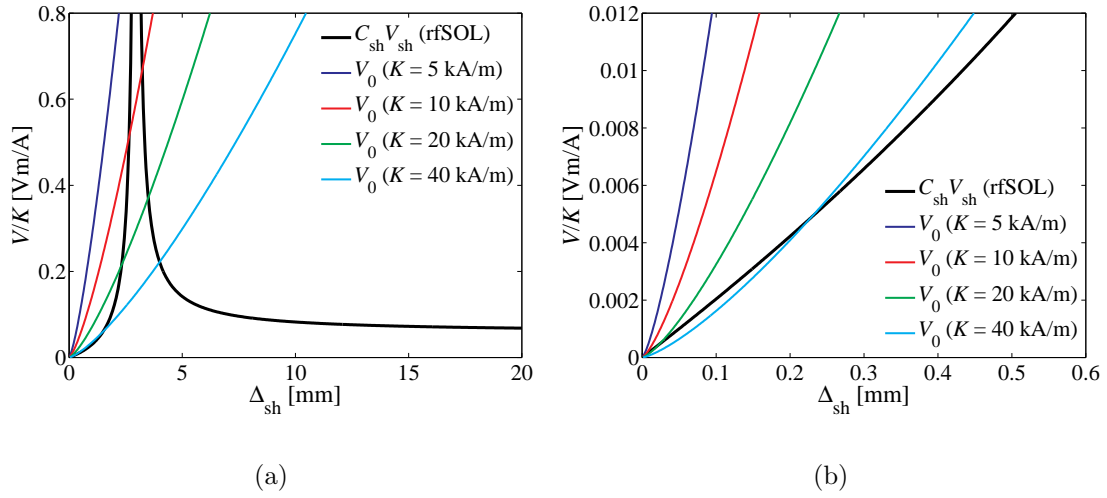
Figure 4-9: Graphical solution for the case without dissipation: (a) entire variation; and (b) local variation in a magnified area within a restricted range of $\Delta_{\mathrm{sh}}$.

antenna current; they eventually merge into one intersection point (corresponding to the tangent point to the left resonant curve) and then disappear at that point. This behavior corresponds to the root jumping observed in Figure 4-7a. It is seen that the graphical solution agrees well with the self-consistent nonlinear numerical result for a large value of $V_0$. For example, the thick black curve on the right-hand side intersects with the cyan curve ($K = 40$ kA/m) at $V/K = 0.22$ Vm/A, which gives $V = 8.9$ kV and agrees with the numerical result (root 3) in Figure 4-7a.

In the present case the lower hybrid resonance does not appear in the calculation domain, although there is a point where $\varepsilon_\perp = 0$ (see Section 3.5.4). Therefore, computation is stably conducted without introducing the collisional effect described in Section 2.5. However, this leads to a seemingly unphysical consequence where the sheath potential can be dominated by the RF contribution even for $K \to 0$ (corresponding to the intersection of root 2 and root 3 in Figure 4-7a) in connection with the fact that the resonance peak in Figure 4-9a is infinitely high. In reality, the plasma possesses small amount of dissipation, so that the resonance curve should have a finite height. The last numerical analysis in this section aims to confirm this

property by explicitly adding the dissipation into the problem.

Let us consider introducing the dissipation in the form of complex electron mass: $m_e \left( 1 + i\nu/\omega \right)$. Here, for simplicity, $\nu$ is assumed to be constant and set at $3.0 \times 10^9$ s$^{-1}$. In fact, this value is quite large (larger than the applied frequency), but it is useful to qualitatively illustrate the effects of dissipation in this problem. Figures 4-10 and 4-11 show the self-consistent numerical result obtained by the rfSOL code and the graphical solution, respectively. It is seen in Figure 4-11 that the dissipation allows the black resonance curve to have a finite height. Correspondingly, the region where the multiple roots exist becomes bounded by $K = K_{\mathrm{crit1}}$ (lower critical current) and $K = K_{\mathrm{crit2}}$ (higher critical current) as shown in Figure 4-10, and thus we obtain only root 1 in the limit where $K \to 0$, which yields the Bohm sheath potential in a desired way. The mechanism for the root jumping can involve hysteresis. For example, root 1 jumps to root 3 at $K = K_{\mathrm{crit2}}$ for increasing antenna current, while root 3 jumps to root 1 at $K = K_{\mathrm{crit1}}$ for decreasing antenna current.

## 4.4   Sheath-Plasma Waves in 2D Slab Geometry

Although we have observed several important phenomena in the 1D domain (e.g., the quasi-insulating limit and the presence of multiple roots), it is necessary to further investigate the problem in the 2D domain since we are mostly interested in the physics in finite geometry where in general one cannot assume Fourier modes in two independent spatial directions. In view of this, the rest of this chapter will be devoted to the analysis in 2D geometry using the developed 2D rfSOL code.

### 4.4.1   Numerical Analysis of the RF Sheath Interaction for Constant $n_0$ and $B_0$

Figure 4-12 shows the problem definition which corresponds to a simplified geometry of the edge plasma region including an antenna in the poloidal cross-section of a
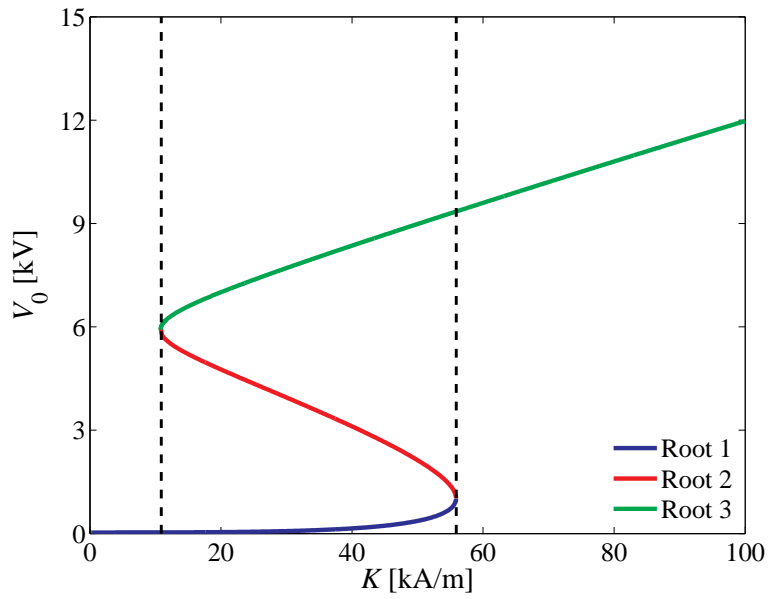
Figure 4-10: The rectified sheath potential $V_0$ at the right sheath as a function of the antenna current $K$ for the case with dissipation, showing multiple roots in a certain range of $K$. The vertical dashed lines indicate the critical antenna currents (10.9 kA/m and 55.9 kA/m) at which root jumping occurs.
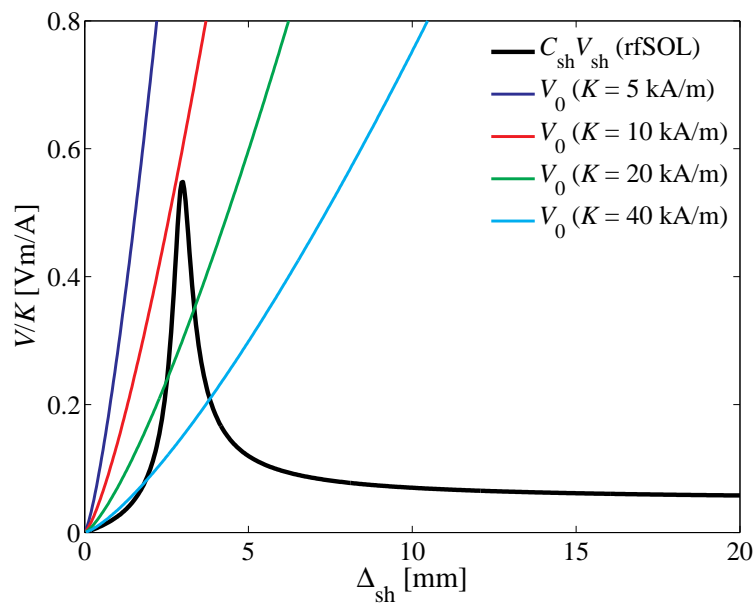


Figure 4-11: Graphical solution for the case with dissipation.
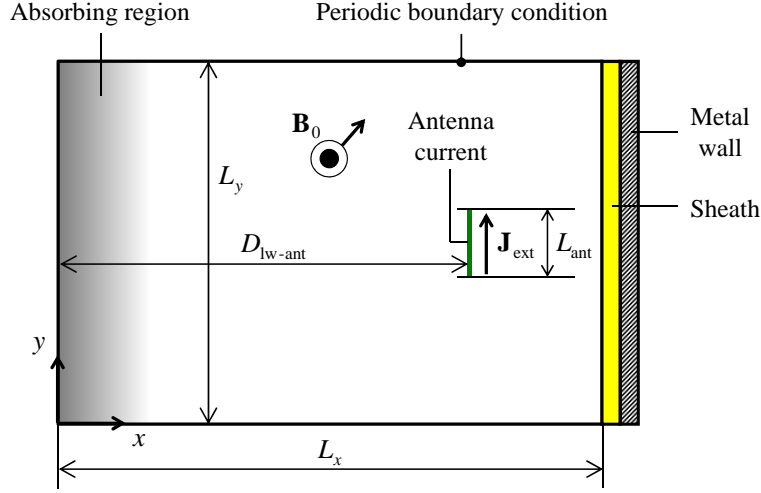
Figure 4-12: Infinitely long slab model defined on the 2D space.

tokamak (see Figure 2-1). Here the electric field in the 2D slab geometry is numerically solved subject to the sheath boundary condition on the right-hand side, the absorbing boundary condition (if necessary) on the left-hand side, and the periodic boundary condition at the top and bottom of the domain. The antenna surface current is given by a sine function in the $y$ direction in such a way that the value at both ends is zero, which is achieved using the following expression:

$$\boldsymbol{J}_{\text{ext}} = K\left(y\right) \delta\left(x - D_{\text{lw-ant}}\right) e^{i(k_z z - \omega t)} \boldsymbol{e}_y \tag{4.3}$$

where

$$K\left(y\right) = \frac{K_{\max}}{2} \left\{ \sin\left[\pi\left(\frac{2y - L_y + L_{\text{ant}}}{L_{\text{ant}}} - \frac{1}{2}\right)\right] + 1 \right\} \tag{4.4}$$

As a first step, consider the case where the plasma density and background magnetic field are assumed to be constant over the domain and only the thermal contribution in the sheath boundary condition plays a role in the sheath-plasma interaction (due to a small electric field). Although this assumption is still far from realistic

tokamak conditions, it yields many interesting features which are not observed in a simple 1D domain, as will be demonstrated below. The calculation domain and antenna position are determined such that $L_x = 0.6$ m, $L_y = 0.4$ m, $L_{\text{ant}} = 0.05$ m, and $D_{\text{lw-ant}} = 0.57$ m. Two density values, $n_0 = 2.0 \times 10^{18}$ m$^{-3}$ and $n_0 = 6.0 \times 10^{17}$ m$^{-3}$, are considered with a constant background magnetic field $B_{0x} = 1.5$ T, $B_{0y} = 0.5$ T, and $B_{0z} = 4.0$ T. For these density values both the fast and slow waves do not propagate in the cold plasma according to the results obtained by the corresponding local dispersion relations (see Figure 4-13; the red and blue lines indicate the higher and lower plasma density values considered here). Thus, it is not necessary to form an absorbing layer on the left-hand side of the domain since the electric field far away from the antenna is sufficiently damped; only the conducting-wall boundary condition, $\boldsymbol{E}_{\text{t}} = \boldsymbol{0}$, on the left boundary ($x = 0$) suffices. In this analysis the toroidal wavenumber component is fixed at 10.8 m$^{-1}$, the antenna surface current $K_{\text{max}}$ is 1 A/m, the electron temperature is 10 eV, and the applied frequency is 80 MHz. For the finite element discretization a uniform mesh which includes $801 \times 1041$ grid points ($400 \times 520$ nine-node elements; in the $x$ and $y$ directions, respectively) is used.

Figure 4-14 shows the filled contour plots of the real and imaginary parts of the parallel electric field component for $n_0 = 2.0 \times 10^{18}$ m$^{-3}$, which are obtained by imposing the conducting-wall boundary condition on the right boundary. Here the antenna and magnetic field lines are also superimposed on the plots with black lines. As expected, the large-amplitude electric field only exists in the vicinity of the current source due to the evanescent plasma waves.

However, the electric field distribution becomes significantly changed when the conducting-wall boundary condition is replaced with the thermal sheath boundary condition as seen in Figure 4-15. Clearly, a wave mode is observed along the sheath surface in both real and imaginary parts of $E_\parallel$. This particular form of wave was confirmed in previous experimental and analytical studies [28–30, 36] and called the "sheath-plasma wave (SPW)" — a particular wave generated as a consequence of
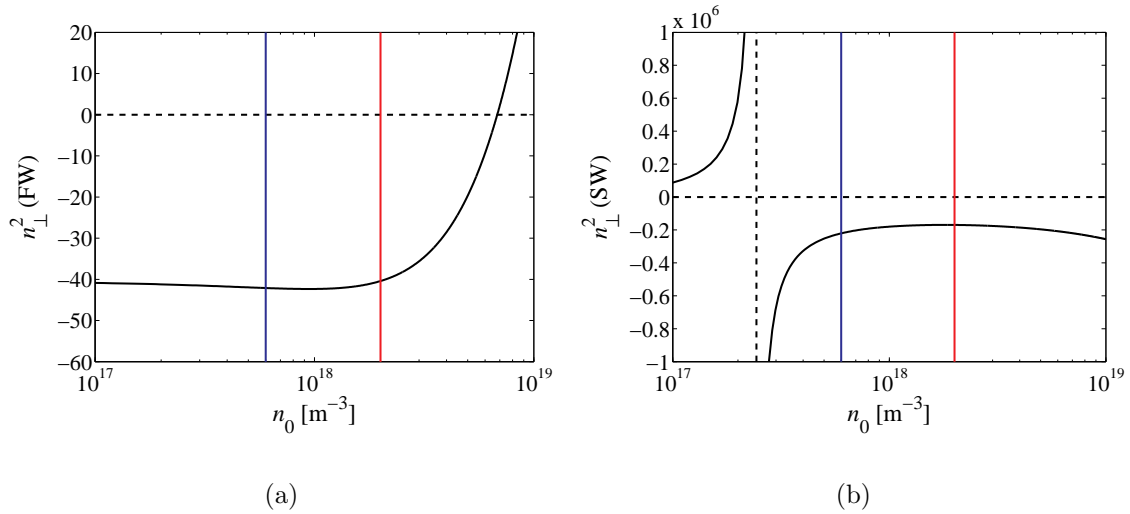
Figure 4-13: Plots of $n_\perp^2$ as a function of $n_0$ as determined by: (a) the FW dispersion relation, and (b) the SW dispersion relation. The red and blue lines indicate the higher and lower plasma density values considered here.

imposing the sheath boundary condition. The SPW observed here looks quite regular in distribution, and it is localized in the vicinity of the sheath. The source of the SPW may be attributed to the large-amplitude electric field, which is localized at the intersections between the sheath and the magnetic field lines penetrating through the antenna.

Figure 4-16 shows the variations of the parallel electric field component along the thermal sheath for the two plasma density values. It is seen for both density values that the waves are mostly sinusoidal with particular wavelengths, and the real and imaginary parts of $E_\parallel$ are $\pi/2$ out of phase, indicating that the SPWs are propagating along the sheath surface. This is indeed an interesting phenomenon since the sheath plays a role to convey the wave energy to the region far away from the current source, although the amplitude of the SPW would reduce exponentially with distance from the antenna when both the fast and slow waves are evanescent (like in the present condition). It is also confirmed that the amplitude of the electric field around the center of the sheath surface is increased when the sheath boundary condition is imposed,
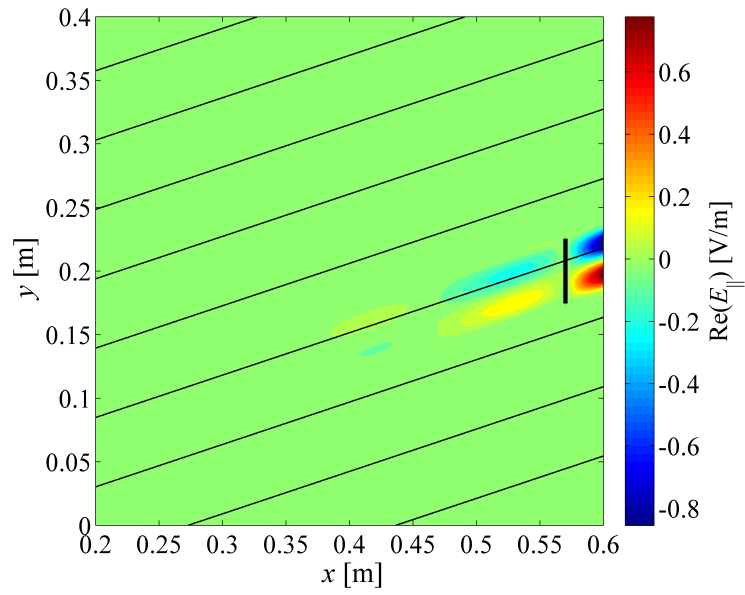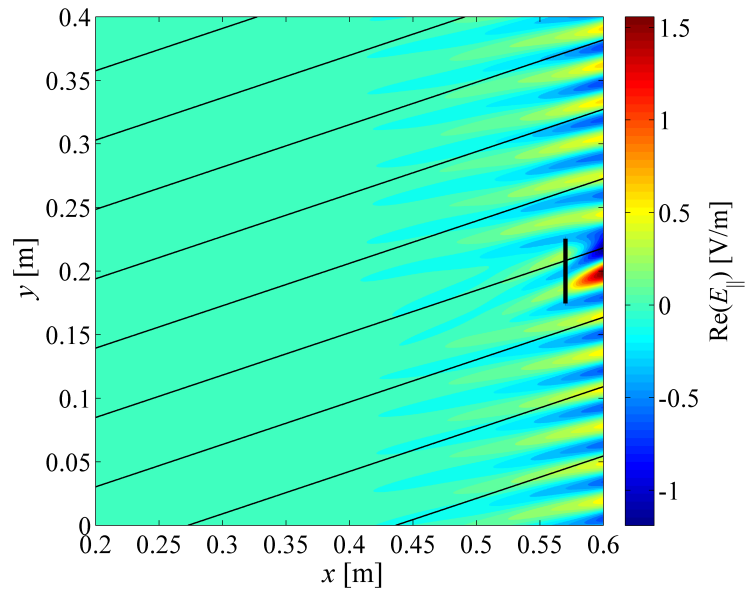
(a)
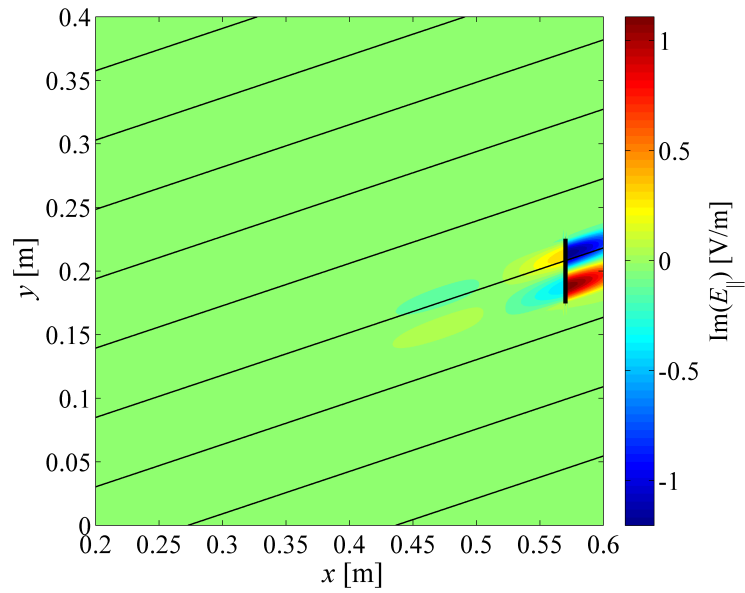


(b)

Figure 4-14: Filled contour plots of the real (a) and imaginary (b) parts of the parallel electric field component for $n_0 = 2.0 \times 10^{18}$ m$^{-3}$ under the conducting-wall boundary condition.
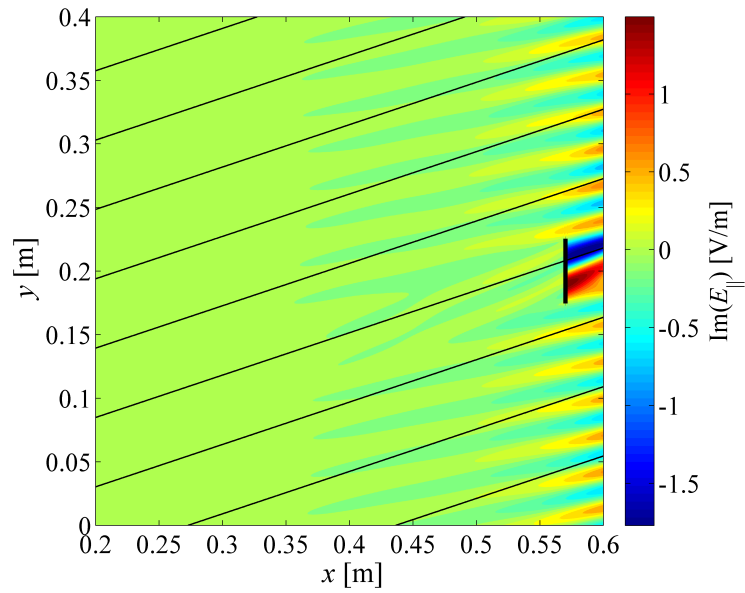
Figure 4-15: Filled contour plots of the real (a) and imaginary (b) parts of the parallel electric field component for $n_0 = 2.0 \times 10^{18}$ m$^{-3}$ under the thermal sheath boundary condition.

compared to the results for the conducting-wall boundary condition.

Figure 4-17 shows the real and imaginary parts of the parallel electric field component for $n_0 = 2.0 \times 10^{18}$ m$^{-3}$ along the cross-section at $y = 0.1$ m, corresponding to the radial variations. It is quantitatively confirmed that the SPW only exists in a narrow band adjacent to the sheath.

## 4.4.2 Electrostatic 2D Sheath Mode Analysis

In Figure 4-16 we have seen that the wavelength of the SPW varies depending on the plasma density. Then a reasonable question is what happens to the wavelength if other physical quantities, such as the plasma temperature and specified toroidal wavenumber component, are varied. In order to comprehensively understand the relations between the wavenumber of the SPW and various quantities on the sheath, one can effectively apply the theory of an electrostatic 2D sheath mode, which is summarized below.

Consider a homogeneous plasma with constant density and a uniform constant magnetic field at the equilibrium state. First, let us focus on the sheath boundary condition, which is repeated here for convenience:

$$\boldsymbol{E}_{\mathrm{t}} = \nabla_{\mathrm{t}} \left( \frac{\Delta_{\mathrm{sh}}}{\varepsilon_{\mathrm{sh}}} D_{\mathrm{n}} \right) \tag{4.5}$$

The presence of wave patterns on the sheath invokes the mode $\sim \exp\left(i\boldsymbol{k} \cdot \boldsymbol{x}\right)$. Further, assume that the electrostatic model is valid (i.e., $\boldsymbol{E} = -\nabla\Phi = -i\boldsymbol{k}\Phi$). Then for a constant sheath width, one gets

$$1 = i\Delta_{\mathrm{sh}}\boldsymbol{s} \cdot \left(\boldsymbol{\varepsilon} \cdot \boldsymbol{k}\right) \tag{4.6}$$

where $\boldsymbol{s}$ is the unit normal vector pointing to the plasma side. If the conditions $\left|\varepsilon_{\parallel}\right| \gg \left|\varepsilon_{\perp}\right|, \left|\varepsilon_{\times}\right|$ and $\left|\left(\boldsymbol{s} \cdot \boldsymbol{b}\right)\boldsymbol{s}\right| \gtrsim \left|\boldsymbol{b} - \left(\boldsymbol{s} \cdot \boldsymbol{b}\right)\boldsymbol{s}\right|$ are satisfied, one can make an approximation
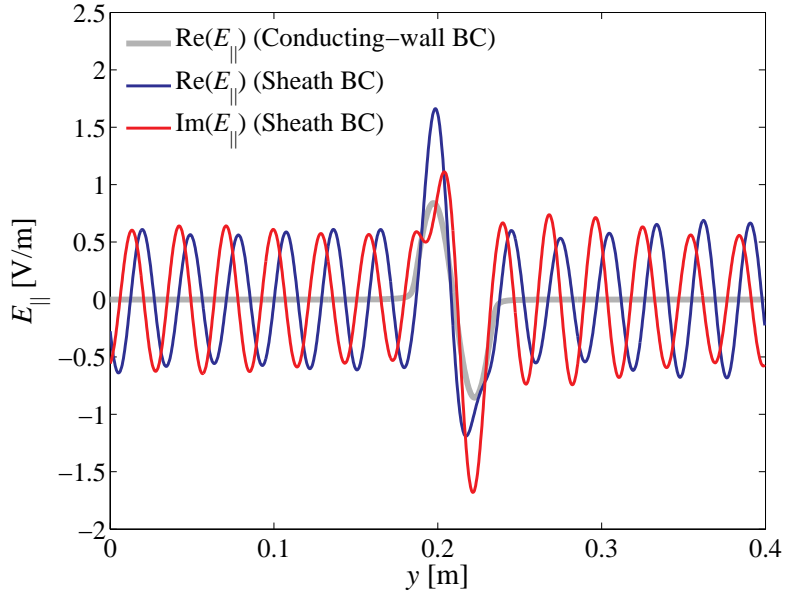
(a)
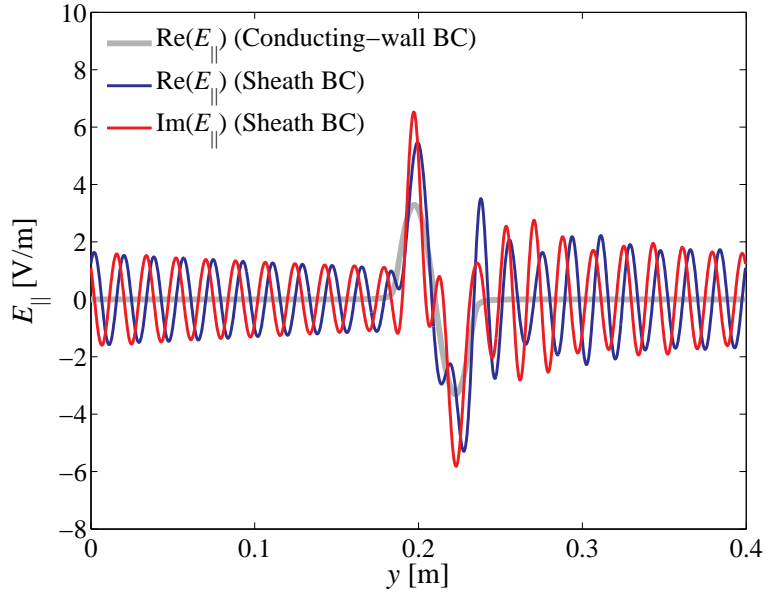


(b)

Figure 4-16: Plots of the real and imaginary parts of the parallel electric field component on the thermal sheath with a comparison to the results for the conducting-wall boundary condition for: (a) $n_0 = 2.0 \times 10^{18}$ m$^{-3}$, and (b) $n_0 = 6.0 \times 10^{17}$ m$^{-3}$.
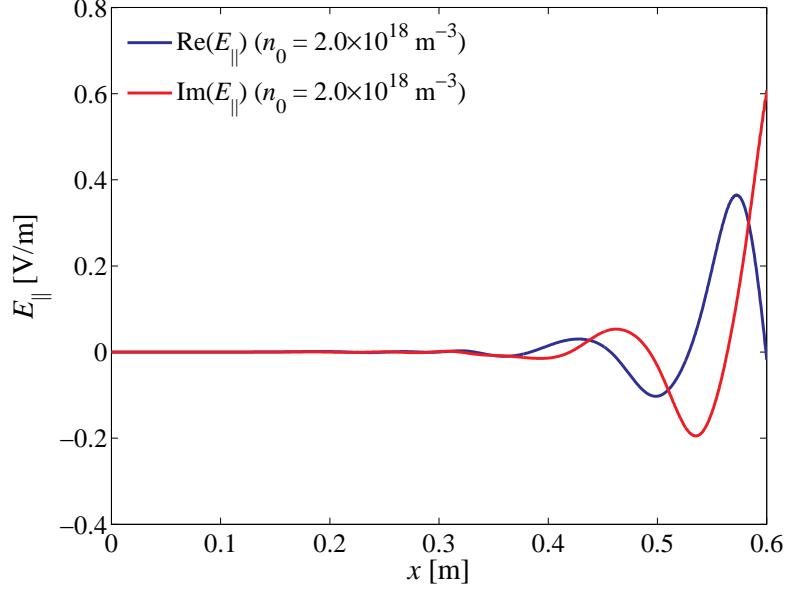
Figure 4-17: Plot of the real and imaginary parts of the parallel electric field component for $n_0 = 2.0 \times 10^{18}$ m$^{-3}$ along the cross-section at $y = 0.1$ m.

such that $\boldsymbol{\varepsilon} \cdot \boldsymbol{k} \simeq \varepsilon_\| k_\| \boldsymbol{b}$ in Equation (4.6) (see Equations (2.18) and (2.19)), yielding

$$1 = -i\Delta_{\text{sh}} b_x \varepsilon_\| k_\| \tag{4.7}$$

Here the sheath is assumed to be located on the right boundary, so that $\boldsymbol{s} \cdot \boldsymbol{b} = -b_x$. The wavenumber components must also satisfy the electrostatic dispersion relation in the plasma, which is given by

$$k_\perp^2 \varepsilon_\perp + k_\|^2 \varepsilon_\| = 0 \tag{4.8}$$

Consequently, one can solve Equations (4.6) and (4.8) (or Equations (4.7) and (4.8) when the required conditions are satisfied) to determine $k_x$ and $k_y$ for given $\omega$ and $k_z$. Similar to the way the analytical solution in 1D geometry is obtained (see Section 3.5.1), the Newton-Raphson method can be effectively applied for this calculation.

Now we are ready to investigate the characteristics of the SPW (specifically, the wavenumber component parallel to the sheath surface) by varying several quantities
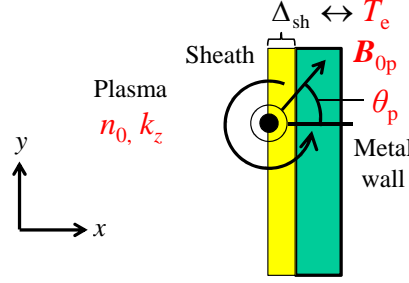
114

Figure 4-18: The quantities varied in the electrostatic sheath mode analysis.

in the electrostatic sheath mode analysis. Here, consider varying the plasma density, angle and magnitude of the poloidal component of the background magnetic field, electron temperature, and toroidal wavenumber component as schematically shown in Figure 4-18. For each case only one quantity is varied with other parameters fixed at their default values (specified in Section 4.4.1). Although Equation (4.7) is well satisfied for the present calculation condition except in the case where the poloidal angle of the background magnetic field is varied, Equation (4.6) is employed throughout the analysis to assure accuracy of the results.

Figure 4-19 shows the variations of the real and imaginary parts of $k_y$ at the sheath-plasma interface as functions of the plasma density with semi-logarithmic scale for the horizontal axis. Here the red and blue lines indicate the higher and lower plasma density values considered here, and the green line points out the density value at the lower hybrid resonance observed in Figure 4-13b. Notice that the variation pattern becomes completely opposite at the lower hybrid density $n_{LH}$. According to this result, the SPW only appears for the plasma density greater than the lower hybrid density since for $n_0 < n_{LH}$, $Im(k_y)$ largely exceeds $Re(k_y)$, so that the SPW is quickly damped before its wave motion is emerged on the sheath. For the density values considered here, the corresponding wavelengths are calculated using one root for each case at $3.6 \times 10^{-2}$ m for $n_0 = 2.0 \times 10^{18}$ m$^{-3}$ and $1.5 \times 10^{-2}$ m for $n_0 = 6.0 \times 10^{17}$ m$^{-3}$, which agree well with the numerical results shown in Figure 4-16.

Figure 4-20 shows the variations of $Re(k_y)$ and $Im(k_y)$ at the sheath-plasma in-
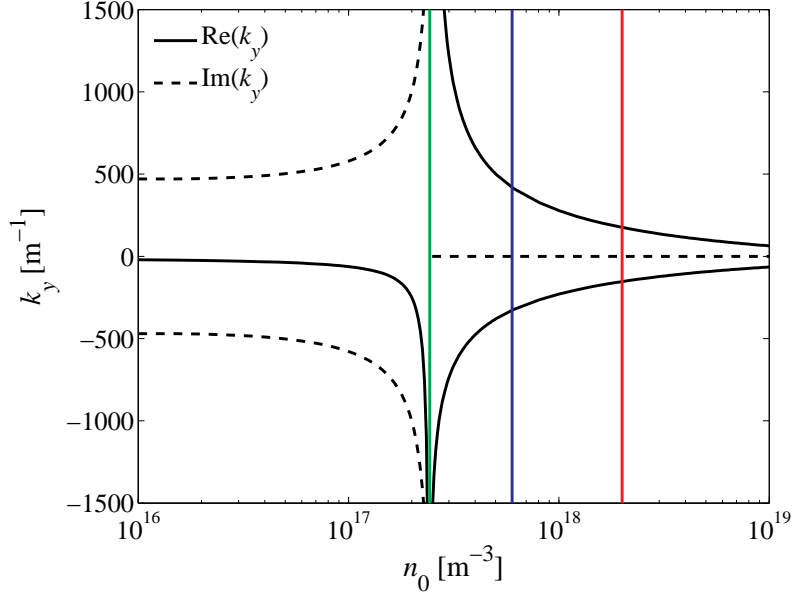
Figure 4-19: Plot of the real and imaginary parts of $k_y$ at the sheath-plasma interface as functions of the plasma density. The red and blue lines indicate the higher and lower plasma density values considered here, and the green line shows the position of the lower hybrid resonance.

terface as functions of the poloidal angle of the background magnetic field for two density values; $n_0 = 2.0 \times 10^{18}$ m$^{-3}$ and $n_0 = 1.0 \times 10^{17}$ m$^{-3}$. Here the poloidal angle $\theta_p$ is defined such that $\theta_p = 0$ when the direction of $\boldsymbol{B}_{0p}$ is identical with the positive direction of the $x$ axis (see Figure 4-18). Also, the red line in Figure 4-20 indicates the default angle (this also applies to the rest of the analysis in this section). It is observed for a higher density value that $|\text{Re}\,(k_y)|$ rapidly increases at two specific angles ($\theta_p = \pi/2,\ 3\pi/2$), indicating that the wavelength of the SPW gets shorter as the contact angle between the magnetic field line and the wall approaches zero and thus, fine grids are required in the vicinity of the sheath where the magnetic field lines are almost parallel to the wall. For a lower density value ($n_0 < n_{\text{LH}}$), although $|\text{Re}\,(k_y)|$ grows to infinity at the two specific angles, $\text{Im}(k_y)$ always dominates $\text{Re}(k_y)$, so the wave behavior should not be observed on the sheath.

Figure 4-21 shows the plots of $\text{Re}(k_y)$ and $\text{Im}(k_y)$ at the sheath-plasma interface as functions of the magnitude of the poloidal component of the background magnetic
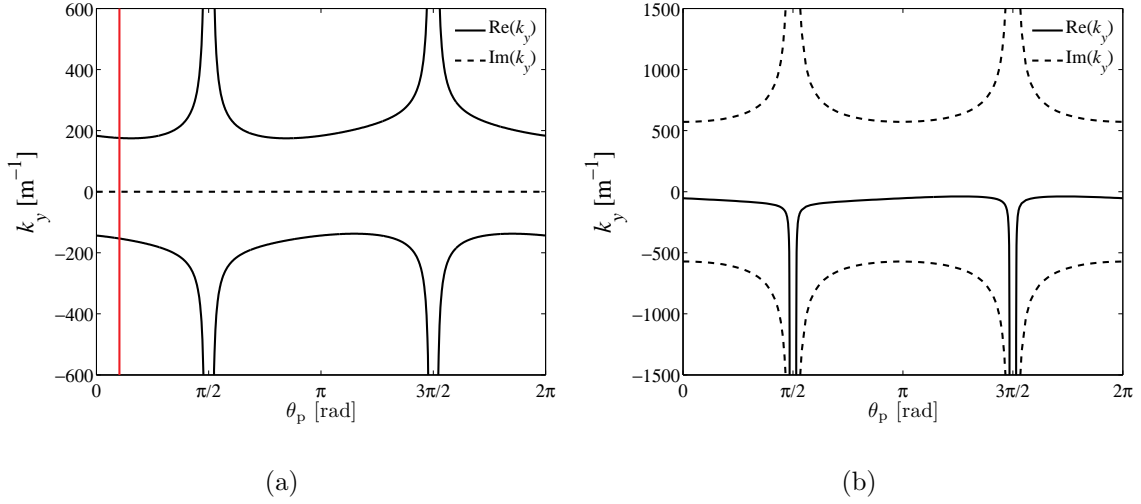
116

Figure 4-20: Plots of the real and imaginary parts of $k_y$ at the sheath-plasma interface as functions of the poloidal angle of the background magnetic field for: (a) $n_0 = 2.0 \times 10^{18}$ m$^{-3}$, and (b) $n_0 = 1.0 \times 10^{17}$ m$^{-3}$. The red line indicates the default parameter.

field for the two plasma density values. Here only the magnitude of the poloidal component, $|\boldsymbol{B}_{0\mathrm{p}}|$, is enlarged or lessened by multiplying its default value by the amplification factor $\alpha_{\mathrm{BP}}$, while the poloidal angle $\theta_{\mathrm{p}}$ is unchanged from its default value. It is seen for large values of plasma density that the real wavenumber component rapidly decreases for lower values of $\alpha_{\mathrm{BP}}$, but gradually decreases for $\alpha_{\mathrm{BP}} \gtrsim 1$ with an increase of $\alpha_{\mathrm{BP}}$. On the other hand, the value of $|\mathrm{Re}\,(k_y)|$ is always much smaller than that of $|\mathrm{Im}\,(k_y)|$ for a smaller density value (smaller than $n_{\mathrm{LH}}$) as for the results in the $n_0$ and $\theta_{\mathrm{p}}$ variations.

Figure 4-22 shows the plots of $\mathrm{Re}(k_y)$ and $\mathrm{Im}(k_y)$ as functions of the electron temperature for the two plasma density values. Recall that $\Delta_{\mathrm{sh}} \propto \lambda_{\mathrm{De}} \propto T_{\mathrm{e}}^{1/2}$ for the thermal sheath; thus, the variation of $T_{\mathrm{e}}$ directly affects the sheath width. For a higher density value it is observed that the wavenumber of the SPW gradually decreases with an increase in temperature. Again, the variation pattern for the lower density is almost the opposite of that for the higher density.

Lastly, Figure 4-23 shows the plots of $\mathrm{Re}(k_y)$ and $\mathrm{Im}(k_y)$ as functions of the

(a)

(b)

Figure 4-21: Plots of the real and imaginary parts of $k_y$ at the sheath-plasma interface as functions of the amplification factor in the poloidal component of the background magnetic field for: (a) $n_0 = 2.0 \times 10^{18}$ m$^{-3}$, and (b) $n_0 = 1.0 \times 10^{17}$ m$^{-3}$. The red line indicates the default parameter.



(a)

(b)

Figure 4-22: Plots of the real and imaginary parts of $k_y$ at the sheath-plasma interface as functions of the electron temperature for: (a) $n_0 = 2.0 \times 10^{18}$ m$^{-3}$, and (b) $n_0 = 1.0 \times 10^{17}$ m$^{-3}$. The red line indicates the default parameter.
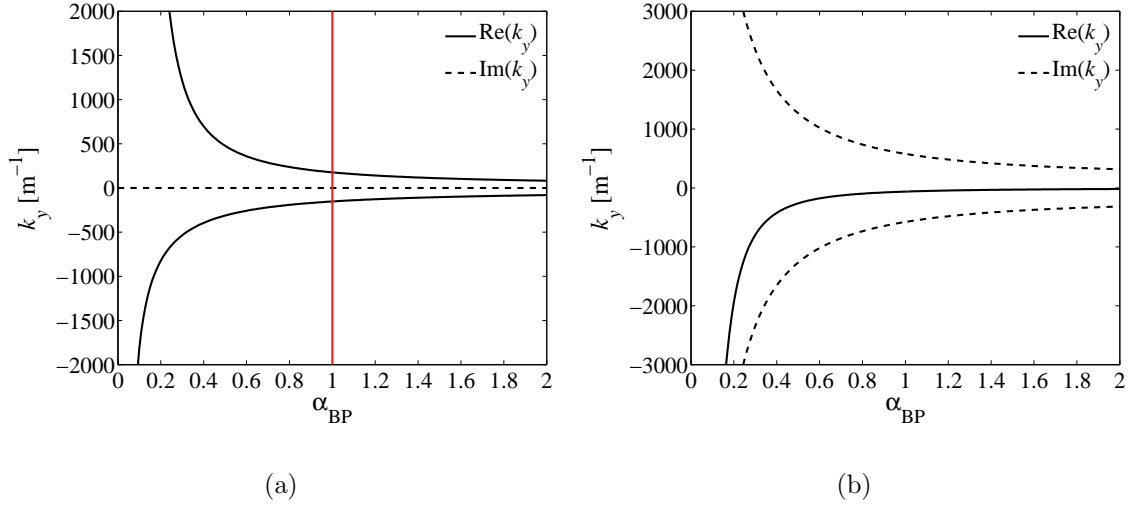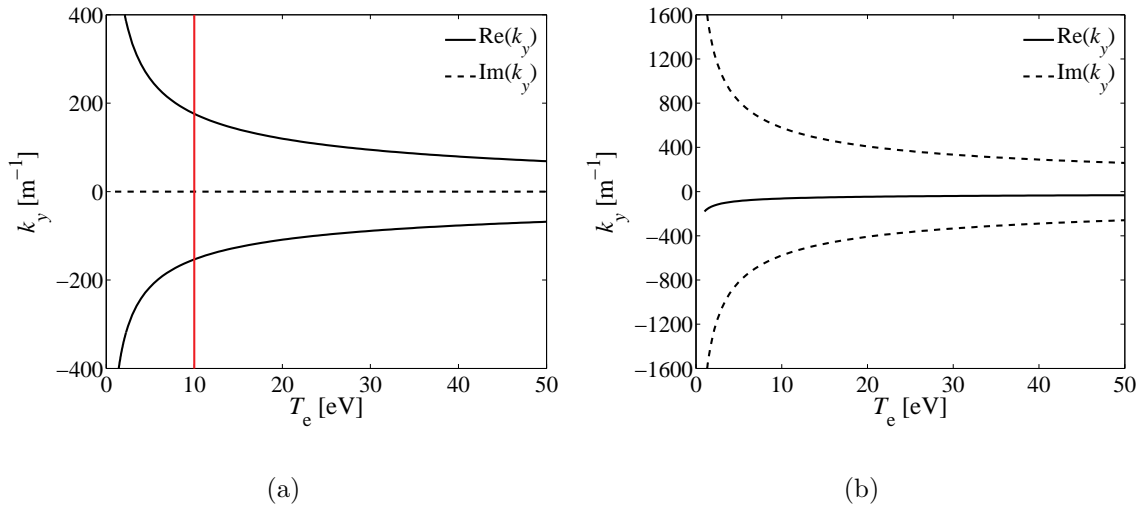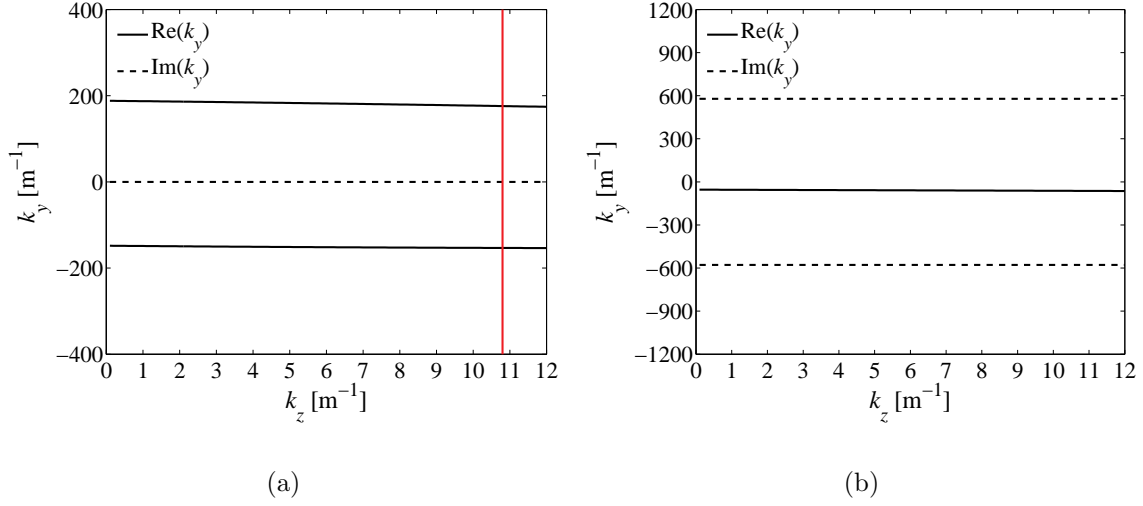
Figure 4-23: Plots of the real and imaginary parts of $k_y$ at the sheath-plasma interface as functions of the toroidal wavenumber component for: (a) $n_0 = 2.0 \times 10^{18}$ m$^{-3}$, and (b) $n_0 = 1.0 \times 10^{17}$ m$^{-3}$. The red line indicates the default parameter.

toroidal wavenumber component for the two plasma density values. As seen, the wavenumber component $k_y$ at the sheath-plasma interface is almost independent of $k_z$ (for a given range of $k_z$).

In summary, the SPW only appears for the plasma density greater than the lower hybrid density, and its wavelength depends mainly on the plasma density, magnitude of the poloidal component of the background magnetic field, and electron temperature when the condition $|(\boldsymbol{s} \cdot \boldsymbol{b})\, \boldsymbol{s}| \gtrsim |\boldsymbol{b} - (\boldsymbol{s} \cdot \boldsymbol{b})\, \boldsymbol{s}|$ is satisfied.

### 4.4.3 Numerical Analysis of the RF Sheath Interaction for Constant $n_0$ and Varying $B_0$

As a last example of this section, consider the case where the background magnetic field has a variation along the thermal sheath surface. Here the $x$ component of the background magnetic field is given by

$$B_{0x} = \frac{2}{3} \tilde{B}_{0x} \left[ 1 - \frac{1}{2} \cos\left( \frac{2y}{L_y} \pi \right) \right] \tag{4.9}$$

119

where $\tilde{B}_{0x} = 1.5$ T, while the other components are fixed at $B_{0y} = 0.5$ T and $B_{0z} = 4.0$ T. The density value is constant at $n_0 = 2.0 \times 10^{18}$ m$^{-3}$. All other input parameters are unchanged from the previous example in Section 4.4.1.

Figure 4-24 shows the filled contour plots of the real and imaginary parts of the parallel electric field component, and the corresponding variations along the sheath are shown in Figure 4-25. It is observed that the wavelength of the SPW varies along the sheath surface; the wavelength becomes shorter with distance from the antenna in accordance with the analytical predictions shown in Figures 4-20a and 4-21a. It is also interesting to see that the decay length of the SPW becomes shorter with a decrease in the SPW wavelength.

## 4.5 Nonlinear Sheath-Plasma Interactions in 2D Slab Geometry

The discussion for the 2D domain so far focused on the linear sheath-plasma interaction, and the numerical results were only given for the plasma density values greater than the lower hybrid density $n_{\mathrm{LH}}$. This section aims to solve propagating SW-sheath nonlinear interactions in the 2D slab geometry. This problem may be more important than the previous numerical example from a practical point of view, since the SW electric field parallel to the magnetic field line can be largely intensified by the parallel component (to the magnetic field line) of the antenna current, and the resulting sheath potential can be quite large ($\sim$ kV), which enhances the wall sputtering. It is also important to confirm if the phenomena observed in the 1D analysis (in Section 4.2) appear even in the 2D case.

The calculation model used here is the same as in the previous section (shown in Figure 4-12) except that the thermal sheath is now replaced with the RF sheath which includes the electric field contribution. The calculation domain and antenna position are determined such that $L_x = 0.7$ m, $L_y = 0.3$ m, $L_{\mathrm{ant}} = 0.05$ m, and
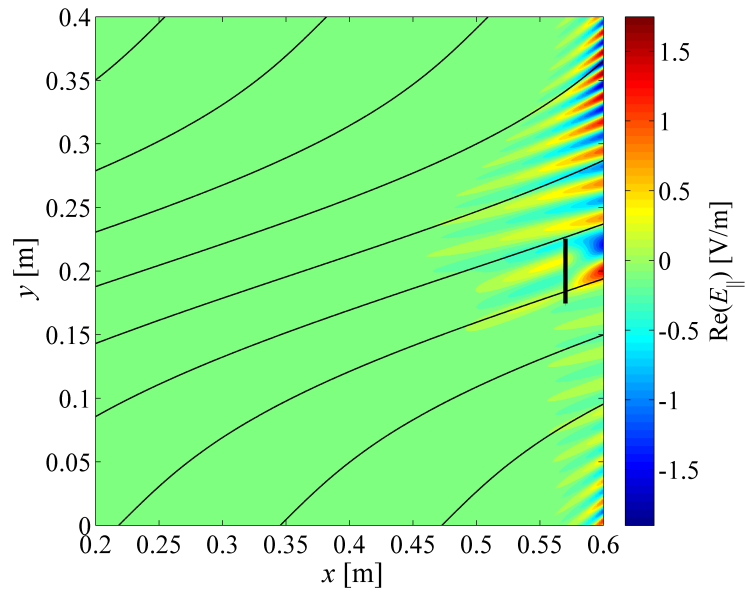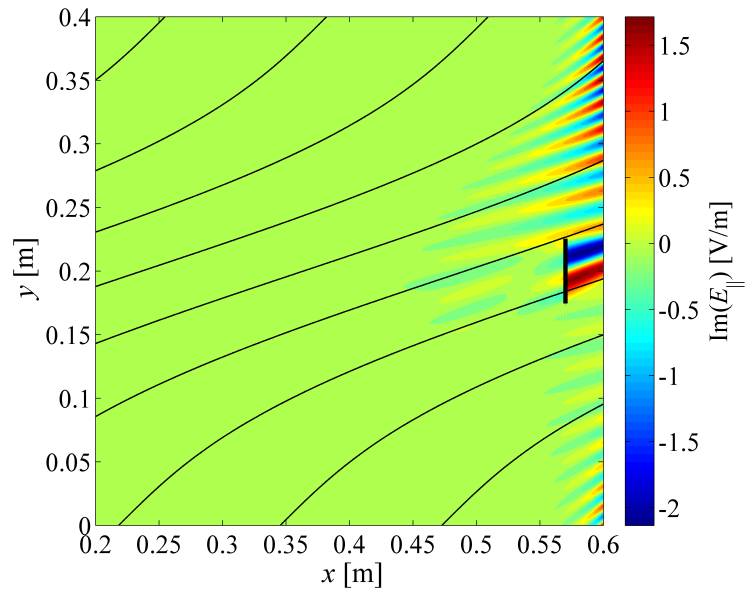
Figure 4-24: Filled contour plots of the real (a) and imaginary (b) parts of the parallel electric field component for a varying $\boldsymbol{B}_0$ field under the thermal sheath boundary condition.
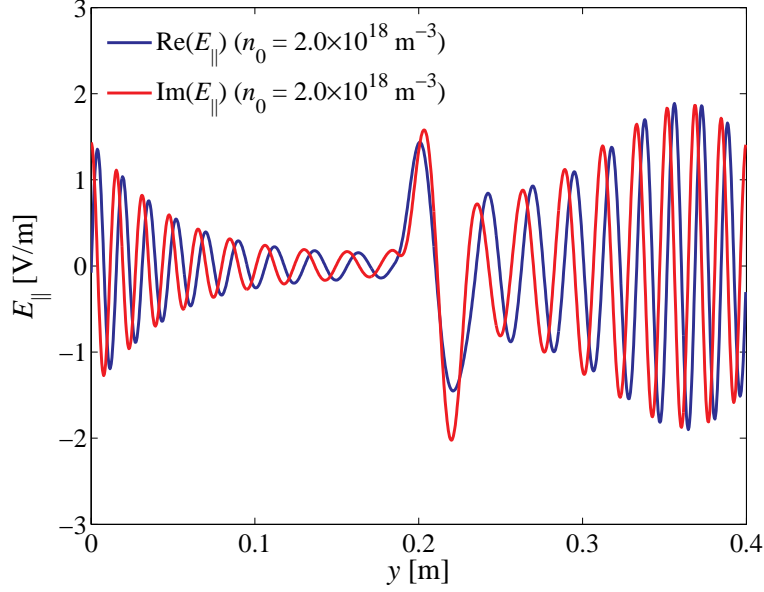
Figure 4-25: Plot of the real and imaginary parts of the parallel electric field component on the thermal sheath where the value of $B_{0x}$ is sinusoidally varied.

$D_{\text{lw-ant}} = 0.65$ m. The plasma density and background magnetic field are assumed to be constant; $n_0 = 1.0 \times 10^{17}$ m$^{-3}$, and $B_{0x} = 1.5$ T, $B_{0y} = 0.5$ T, and $B_{0z} = 4.0$ T. For this density value the SW propagates in the cold plasma according to the results shown in Figure 4-13. Thus, one is required to form an absorbing layer on the left-hand side of the domain; here it is formed with $\nu_0 = 3.0 \times 10^{11}$ s$^{-1}$, $x_{\text{abs}} = 0$ m, and $\lambda_\nu = 0.05$ m (see Equation (2.103)). The other parameters fixed in this analysis are $f = 80$ MHz, $T_{\text{e}} = 10$ eV, $k_z = 10.8$ m$^{-1}$, $C_{\text{sh}} = 0.6$, and $\varepsilon_{\text{err}} = 1.0 \times 10^{-3}$. A uniform mesh which includes $841 \times 961$ grid points ($420 \times 480$ nine-node elements) is used for the finite element discretization. In this analysis the strength of the antenna current, specifically the value of $K_{\text{max}}$ in Equation (4.4) is varied in the range of 1–320 A/m.

Figures 4-26, 27, and 28 show the filled contour plots of the real and imaginary parts of the parallel electric field component, which is normalized by dividing it by the maximum surface current value, for $K_{\text{max}} = 1$, 60, and 160 A/m, respectively. It is observed that the SWs are propagating along the field lines, but the distribution patterns are clearly different among these three cases; the normalized wave amplitude

122

in the edge plasma is enhanced for a large value of $K_{\mathrm{max}}$ (particularly, $K_{\mathrm{max}} = 160$ A/m), while it is not seen for $K_{\mathrm{max}} = 1$ A/m. In fact, the difference in the electric field distribution pattern was also observed in the analysis for the 1D domain (see Figure 4-2). One of the reasons for this phenomenon may be explained by the phase change in the reflected wave, which is demonstrated below using a simplified condition.

Suppose that a SW is propagating in a low density plasma with a constant uniform background magnetic field ($\boldsymbol{B}_0 = B_{0x}\boldsymbol{e}_x$). Further, assume that the sheath is formed on the right-most boundary ($x = x_{\mathrm{R}}$) of the plasma-filled domain; thus, there are incident (from left to right) and reflected (from right to left) waves in the vicinity of the metal wall as schematically shown in Figure 4-29. Here the perpendicular wavenumber components are imposed such that $k_y = 0$ and $k_z = k_{\mathrm{t}}$, so that one can write $k_\parallel = k_x$ and $k_\perp = k_z$. For this simplified condition the parallel wavenumber component can be easily obtained from the SW dispersion relation (2.23) as follows:

$$k_\parallel = \pm k_{\mathrm{r}} \tag{4.10}$$

where

$$k_{\mathrm{r}} = \frac{\omega}{c} \left[ \frac{\varepsilon_\perp}{\varepsilon_\parallel} \left( \varepsilon_\parallel - n_\perp^2 \right) \right]^{1/2} \tag{4.11}$$

Then the electric field in the plasma is expressed as

$$\boldsymbol{E} = \left( C_1 \tilde{\boldsymbol{E}}_1 \mathrm{e}^{ik_{\mathrm{r}}x} + C_2 \tilde{\boldsymbol{E}}_2 \mathrm{e}^{-ik_{\mathrm{r}}x} \right) \mathrm{e}^{i(k_{\mathrm{t}}z - \omega t)} \tag{4.12}$$

where $C_1$, $C_2$ are arbitrary constants, and $\tilde{\boldsymbol{E}}_1$, $\tilde{\boldsymbol{E}}_2$ are the polarization eigenvectors corresponding to $k_x = \pm k_{\mathrm{r}}$, respectively. In the SW limit the electric field is governed
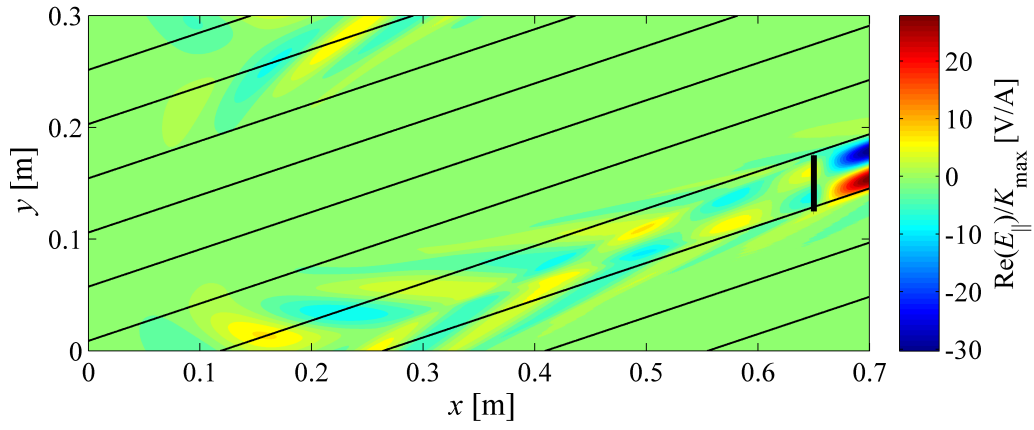
(a)
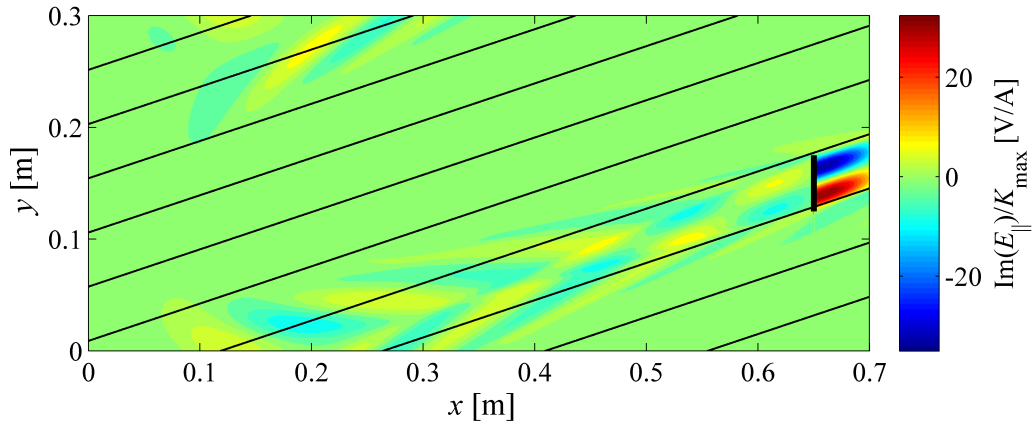


(b)

Figure 4-26: Filled contour plots of the real (a) and imaginary (b) parts of the parallel electric field component for $K_{\max} = 1$ A/m under the nonlinear sheath boundary condition.
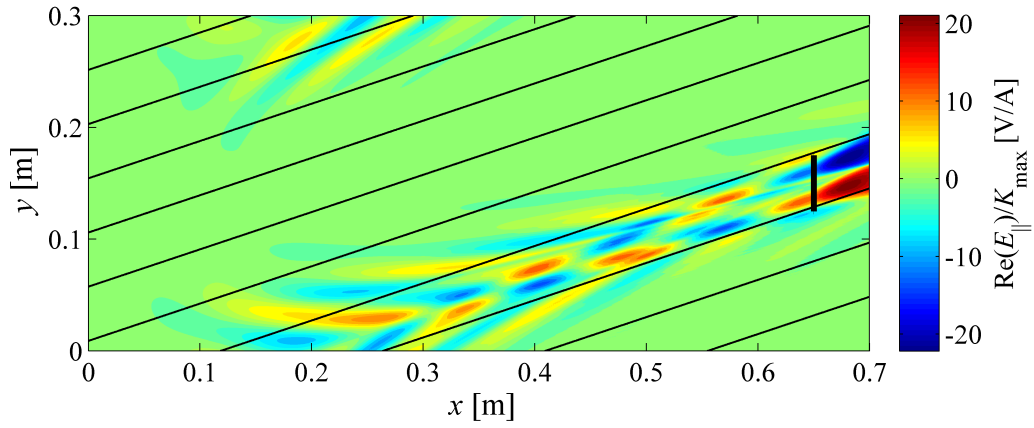
(a)
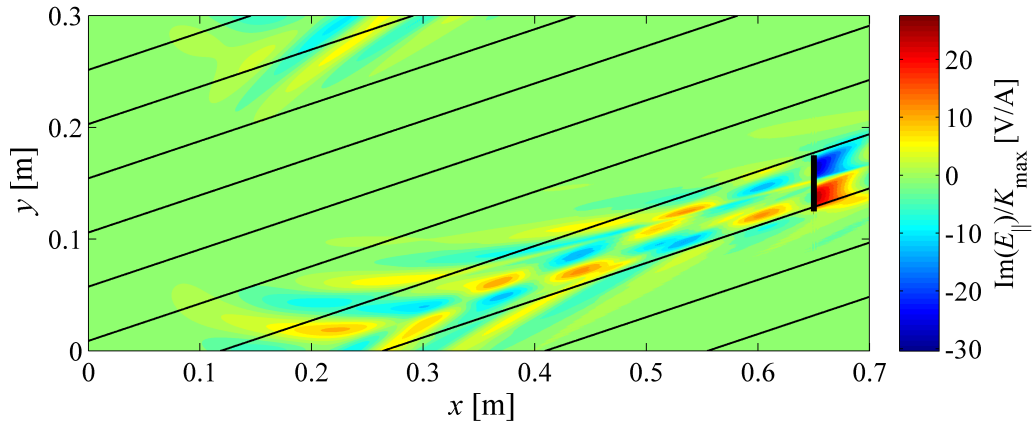


(b)

Figure 4-27: Filled contour plots of the real (a) and imaginary (b) parts of the parallel electric field component for $K_{\max} = 60$ A/m under the nonlinear sheath boundary condition.
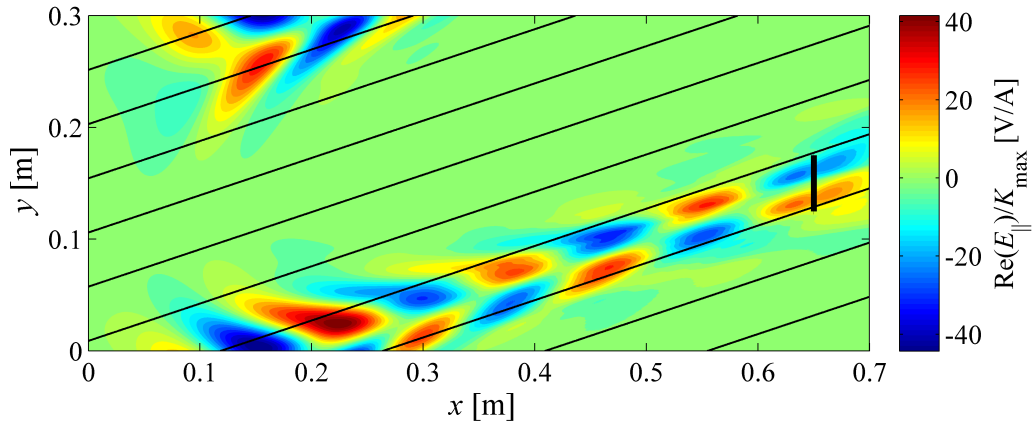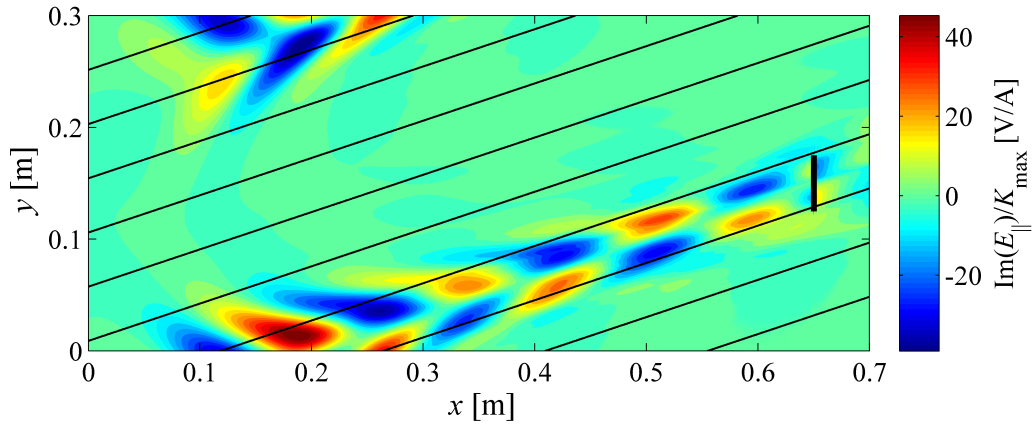
Figure 4-28: Filled contour plots of the real (a) and imaginary (b) parts of the parallel electric field component for $K_{\max} = 160$ A/m under the nonlinear sheath boundary condition.
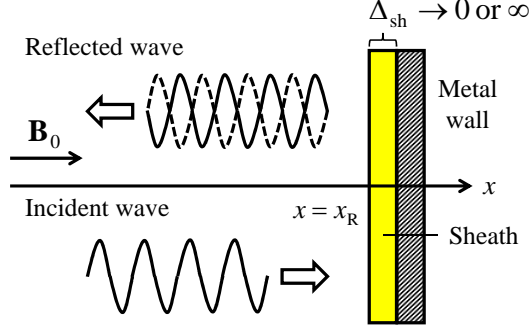
Figure 4-29: Slab model used for the demonstration of the phase change in the reflected wave.

by the following equation (see Equation (2.31)):

$$
\begin{pmatrix} \varepsilon_\perp - n_\parallel^2 & n_\perp n_\parallel \\ n_\perp n_\parallel & \varepsilon_\parallel - n_\perp^2 \end{pmatrix} \begin{pmatrix} E_z \\ E_x \end{pmatrix} = \begin{pmatrix} 0 \\ 0 \end{pmatrix}
\tag{4.13}
$$

Here, let us specify that $\tilde{E}_{z1} = \tilde{E}_{z2} = 1$. Then the expressions of $\tilde{E}_{x1}$ and $\tilde{E}_{x2}$ are given by

$$
\tilde{E}_{x1} = -\tilde{E}_{x2} = -\frac{\varepsilon_\perp - n_\parallel^2}{n_\perp n_{\mathrm{r}}}
\tag{4.14}
$$

where $n_{\mathrm{r}} = ck_{\mathrm{r}}/\omega$ and $n_\perp = ck_{\mathrm{t}}/\omega$.

Now consider the two opposite limits in the sheath boundary condition; $\Delta_{\mathrm{sh}} \to 0$ and $\Delta_{\mathrm{sh}} \to \infty$. In the former and latter cases the sheath boundary condition reduces to the conducting-wall and insulating boundary conditions (i.e., $\boldsymbol{E}_{\mathrm{t}} = \boldsymbol{0}$ and $D_{\mathrm{n}} = 0$), respectively, for a finite wave source. In this analysis they are simplified to $E_z = 0$ and $E_x = 0$, so that one gets

$$
\begin{aligned}
C_1 \tilde{E}_{z1} e^{ik_{\mathrm{r}} x_{\mathrm{R}}} + C_2 \tilde{E}_{z2} e^{-ik_{\mathrm{r}} x_{\mathrm{R}}} = 0 \qquad &\text{(for conducting-wall BC)} \\
C_1 \tilde{E}_{x1} e^{ik_{\mathrm{r}} x_{\mathrm{R}}} + C_2 \tilde{E}_{x2} e^{-ik_{\mathrm{r}} x_{\mathrm{R}}} = 0 \qquad &\text{(for insulating BC)}
\end{aligned}
\tag{4.15}
$$

Substituting the expressions for the polarization eigenvector components into Equa-

tion (4.15), we obtain the expressions of $C_2$ with respect to $C_1$. Consequently, the electric fields in the plasma corresponding to the two limits are

$$\boldsymbol{E} = \begin{cases} C_1 \left[ \tilde{\boldsymbol{E}}_1 \mathrm{e}^{ik_\mathrm{r}x} - \tilde{\boldsymbol{E}}_2 \mathrm{e}^{ik_\mathrm{r}(2x_\mathrm{R}-x)} \right] \mathrm{e}^{i(k_\mathrm{t}z-\omega t)} & (\Delta_\mathrm{sh} \to 0) \\ C_1 \left[ \tilde{\boldsymbol{E}}_1 \mathrm{e}^{ik_\mathrm{r}x} + \tilde{\boldsymbol{E}}_2 \mathrm{e}^{ik_\mathrm{r}(2x_\mathrm{R}-x)} \right] \mathrm{e}^{i(k_\mathrm{t}z-\omega t)} & (\Delta_\mathrm{sh} \to \infty) \end{cases} \tag{4.16}$$

Observe that the signs of the reflected wave are opposite. In other words, the phase shift occurs with an amount of $\pi$. This is the same result found in the 2D resonance cone analysis [34].

The waves that reflect from the right boundary and return to the plasma interfere with the left-going waves launched directly by the antenna. The interference will be constructive or destructive depending on the parallel wavenumber component, the distance between the antenna and the wall along the field line, and whether there is a phase change on reflection. For fixed wavenumber and antenna-to-wall distance the interference behavior could be determined by the phase shift caused by the presence of the sheath. The phase shift should occur smoothly between the two opposite limits in the sheath boundary condition, so that one can see an intermediate electric field pattern as shown in Figure 4-27.

Figure 4-30 shows the variations of the normalized normal component of the electric displacement on the sheath surface for five different antenna current values. It is seen that the normalized quantity decreases with an increase of the antenna current, which is a similar behavior to the result shown in Figure 4-4b, indicating that the sheath boundary condition approaches the quasi-insulating limit. It is also observed that the distribution pattern becomes spread out as the maximum antenna current increases (in the present condition). Figure 4-31 shows the variations of the rectified sheath potential corresponding to the five antenna currents. The maximum sheath potential value increases with an increase of the antenna current, which was also observed in the previous analysis in the 1D domain (see Figure 4-5a).
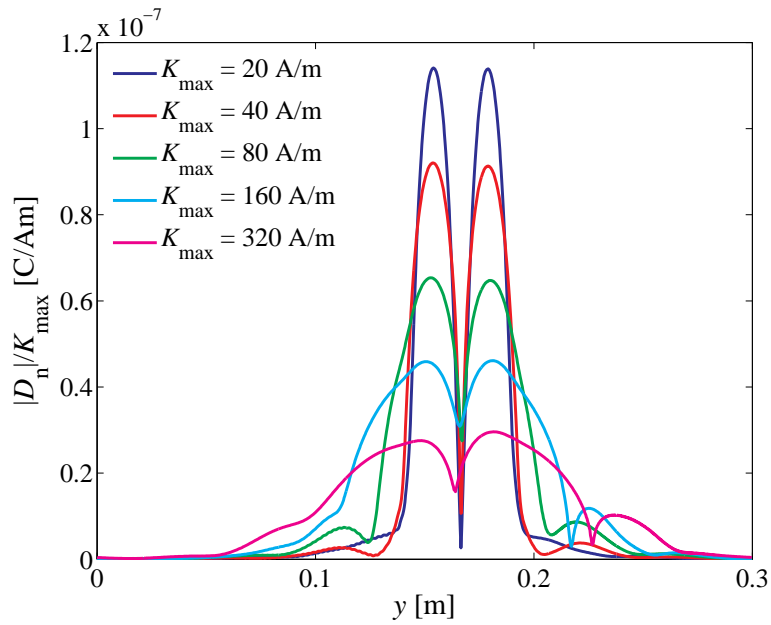
Figure 4-30: Normalized normal component of the electric displacement vs. $y$ at the right boundary for five different antenna current values.
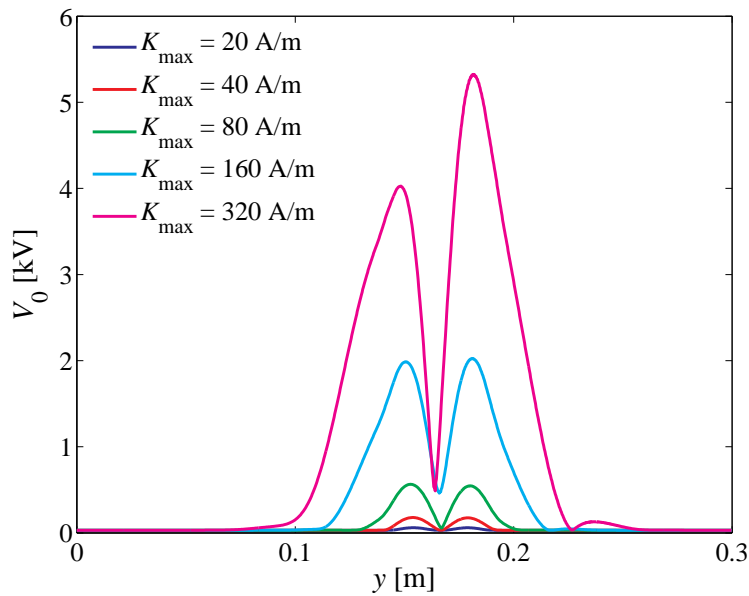


Figure 4-31: Rectified sheath potential vs. $y$ at the right boundary for five different antenna current values.

## 4.6 RF Sheath-Plasma Interactions in an Alcator C-Mod Scale Device

As a last numerical example, propagating SW-sheath nonlinear interaction problems are considered on the scale equivalent to the Alcator C-Mod device. Figure 4-32 shows a schematic diagram of an Alcator C-Mod poloidal cross section with representative measurements. Here this poloidal cross section is further simplified to the slab geometry used in the previous sections (shown in Figure 4-12) by taking $L_y$ as the circumferential length of the outer wall. With this approximation the curvature effect of the wall is neglected. However, in general this contribution to the sheath-plasma interaction is considered to be small for this large-scale device (see Section 2.7.3). Other major approximations are (1) the plasma density is assumed to be constant; (2) relating to this, there are no reflected waves (due to the lower hybrid resonance) from the core plasma side; and (3) the background magnetic field is assumed to be spatially constant. The purpose of this section is to investigate a characteristic order of the sheath potential and its sensitivity to parameters in the RF sheath-plasma interactions in a large-size domain comparable to Alcator C-Mod. Admittedly, the present model is still far from the realistic tokamak condition. Nevertheless, a series of calculations will provide some important insight into the localized RF sheath formation on the material surface near the antenna.

The important scaling to assess the numerical results here is

$$V_0 \sim C_{\text{sh}} V_{\text{sh}} \sim \mathcal{C} \frac{b_{\text{n}}^4 E_{\parallel}^4}{n_{\text{e0}}^2 T_{\text{e}}} \tag{4.17}$$

where $\mathcal{C}$ is the product of fundamental constants. Equation (4.17) can be easily derived from Equations (2.97), (2.100) and the approximation that $D_{\text{n}} \simeq \varepsilon_0 \varepsilon_{\parallel} E_{\parallel} b_{\text{n}}$ for $\left|\varepsilon_{\parallel}\right| \gg |\varepsilon_{\perp}|, |\varepsilon_{\times}|$ (see Section 4.4.2). Note that $E_{\parallel}$ has a dependence on $b_{\text{n}}$, $n_{\text{e0}}$, and $T_{\text{e}}$ through the sheath boundary condition.
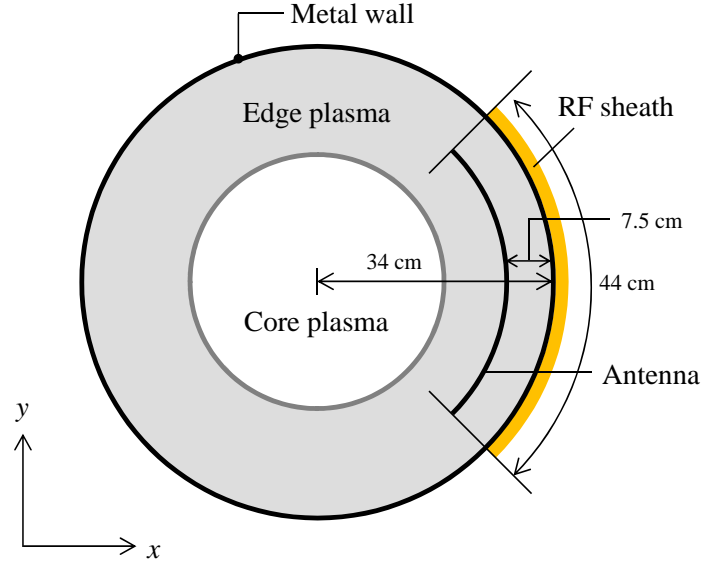
Figure 4-32: Schematic diagram of a simplified Alcator C-Mod poloidal cross section.

Based on the definition in Figure 4-12, two kinds of slab domains, which are called slab 1 and slab 2 here, are used depending on the tilt angle of the magnetic field lines. In both domains the following three lengths are fixed: $L_y = 2.14\,(\simeq 2\pi \times 0.34)$ m, $L_x - D_{\text{lw-ant}} = 0.075$ m, and $L_{\text{ant}} = 0.44$ m. The number of grid points is also fixed at $921 \times 1201$ ($460 \times 600$ nine-node elements), and 81 grid points (40 grid elements) are provided between the antenna and the sheath (right wall). In slab 1, $L_x = 3.0$ m and the absorbing layer on the left-hand side of the domain is formed with $\nu_0 = 2.0 \times 10^{11}$ s$^{-1}$ and $\lambda_\nu = 0.3$ m. In slab 2, $L_x = 1.5$ m and the absorbing layer is formed with $\nu_0 = 1.0 \times 10^{11}$ s$^{-1}$ and $\lambda_\nu = 0.1$ m (in both cases $x_{\text{abs}} = 0$ m).

The first numerical analysis is focused on the effect of the tilt angle of the magnetic field lines to the sheath and antenna current. To investigate this, the following two sets of poloidal components of the background magnetic field are particularly considered: $B_{0x} = 1.5$ T, $B_{0y} = 0.5$ T (case 1) and $B_{0x} = 0.5$ T, $B_{0y} = 1.5$ T (case 2). In these cases the toroidal background magnetic field component is fixed at $B_{0z} = 4.0$ T. In order to obtain accurate numerical results, case 1 and case 2 are calculated using slab 1 and slab 2, respectively. The other parameters are fixed at $n_0 = 1.0 \times 10^{17}$ m$^{-3}$,

$f = 80$ MHz, $T_e = 10$ eV, $k_z = 10.8$ m$^{-1}$, $C_{sh} = 0.6$, and $\varepsilon_{err} = 1.0 \times 10^{-3}$.

Figure 4-33 shows the filled contour plots of the real part of the parallel electric field component in case 1 and case 2 for $K_{max} = 1$ A/m. First, compared to the result shown in Figure 4-26a, it is found in Figure 4-33a that the electric field strength is largely reduced (compare the maximum and minimum values in the colorbar between the two results). Since the plasma density and background magnetic field are the same in these cases, this reduction is attributed to the increase in the antenna length (or decrease in the gradient of the antenna current strength in its length direction). In connection with this, the sheath potential values, which are calculated using four different antenna current values in case 1, in Figure 4-34 are much smaller compared to the results shown in Figure 4-31. Considering that the maximum antenna current in Alcator C-Mod can be estimated at around 5 kA/m and the measured sheath potential values are the order of hundred volts [23], the predictions shown in Figure 4-34 seem to be more realistic. In most cases the sputtering effect starts to emerge when the sheath potential exceeds 100V; thus, one can anticipate from these numerical results that the experimental configuration of Alcator C-Mod would lead to enhanced sputtering.

Second, it is seen in Figure 4-33b that the electric field strength in case 2 is increased by approximately three times compared to the result in case 1 when the magnetic field lines intersect with the antenna at a smaller angle. This occurs because the parallel electric field component is directly intensified by the projection of the antenna current to the magnetic field lines (i.e., $J_{\|ext} = \boldsymbol{J}_{ext} \cdot \boldsymbol{b}$).

Figure 4-35 shows the variations of $\left|E_\|\right|_{max}$ and $\left|b_n E_\|\right|_{max}$ as functions of the poloidal angle $\theta_p$ defined in Figure 4-18 for $K_{max} = 300$ A/m and $|\boldsymbol{B}_{0p}| = 1.58$ T, $B_{0z} = 4.0$ T. Here $\left|E_\|\right|_{max}$ is the maximum value of the parallel electric field component on the sheath, and slab 1 is used for the calculations when the poloidal angle of the magnetic field lines is equal to or less than 65°, while slab 2 is used for the other cases. It is found that the value of $\left|b_n E_\|\right|_{max}$ is insensitive to $\theta_p$. Therefore,
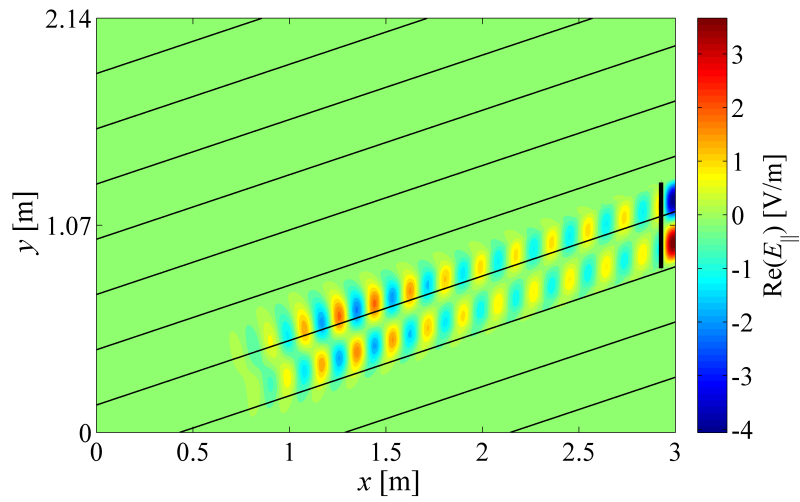
(a)



(b)
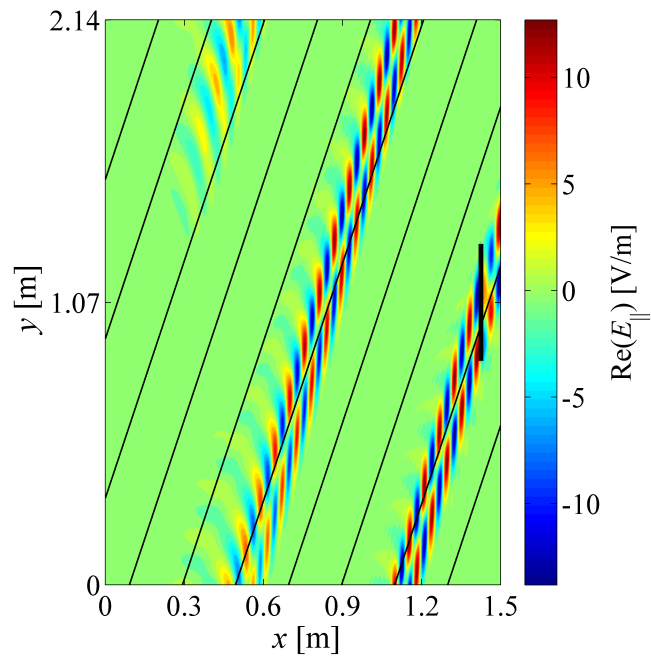
Figure 4-33: Filled contour plots of the real part of the parallel electric field component for $K_{\max} = 1$ A/m with two different poloidal components of the background magnetic field: (a) $B_{0x} = 1.5$ T, $B_{0y} = 0.5$ T (case 1); and (b) $B_{0x} = 0.5$ T, $B_{0y} = 1.5$ T (case 2).
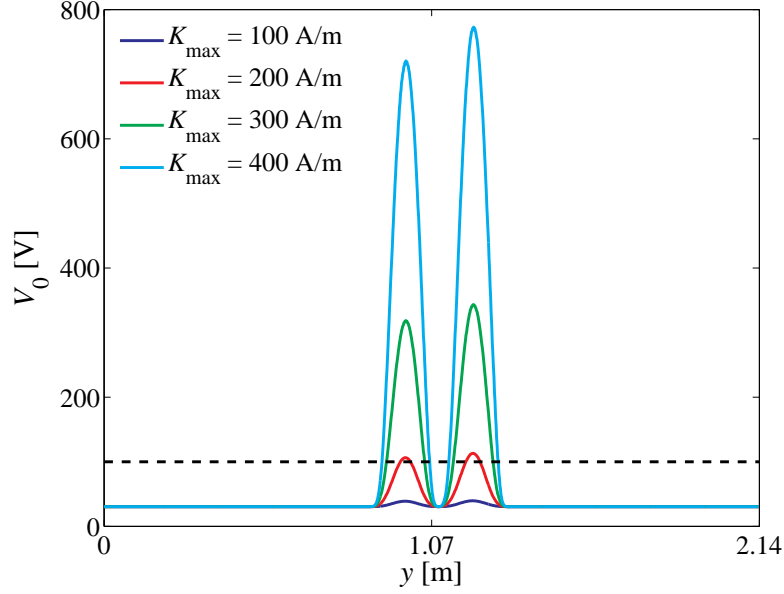
Figure 4-34: Rectified sheath potential vs. $y$ for four different antenna current values for $B_{0x} = 1.5$ T, $B_{0y} = 0.5$ T, and $B_{0z} = 4.0$ T (case 1). The horizontal dashed line indicates that $V_0 = 100$ V, where the sputtering starts to matter.

according to Equation (4.17), the sheath potential values in case 1 and case 2 should become comparable under the condition where $n_{e0}$ and $T_e$ are constant. This is verified in the results shown in Figure 4-36, where the rectified sheath potential variations are compared between the two cases for $K_{max} = 300$ A/m.

The angle dependence on the rectified sheath potential is also investigated by varying the toroidal angle $\theta_t$. Using the toroidal angle, the components of the background magnetic field are defined as follows:

$$B_{0x} = |\boldsymbol{B}_0| \sin \theta_t \cos \theta_p$$

$$B_{0y} = |\boldsymbol{B}_0| \sin \theta_t \sin \theta_p$$

$$B_{0z} = |\boldsymbol{B}_0| \cos \theta_t$$

where $|\boldsymbol{B}_0| = 4.3$ T. Figure 4-37 shows the variations of $\left|E_\parallel\right|_{max}$ and $\left|b_n E_\parallel\right|_{max}$ as functions of the toroidal angle $\theta_t$ with the poloidal angle $\theta_p$ fixed at $40°$ for $K_{max} = 300$

134
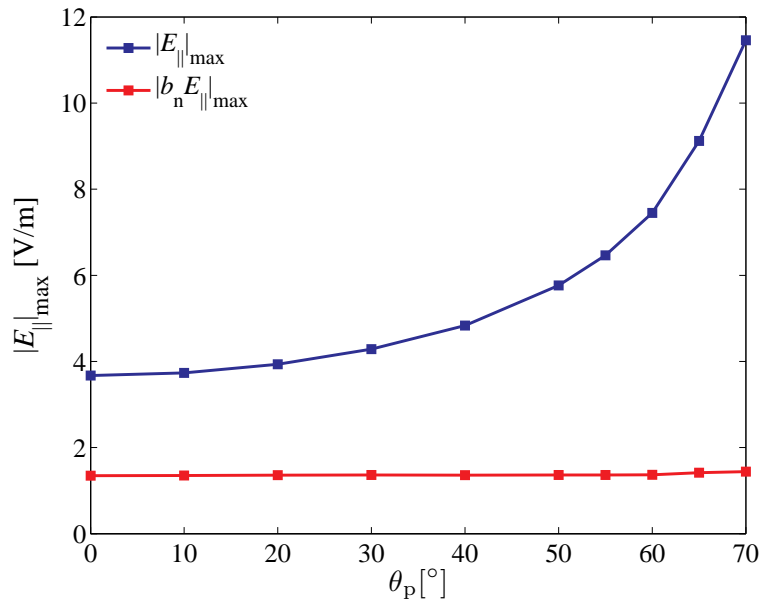
Figure 4-35: Plot of $\left|E_{\parallel}\right|_{\max}$ and $\left|b_{\mathrm{n}}E_{\parallel}\right|_{\max}$ as functions of the poloidal angle of the background magnetic field for $K_{\max} = 300$ A/m, $\left|\boldsymbol{B}_{0\mathrm{p}}\right| = 1.58$ T, and $B_z = 4.0$ T.
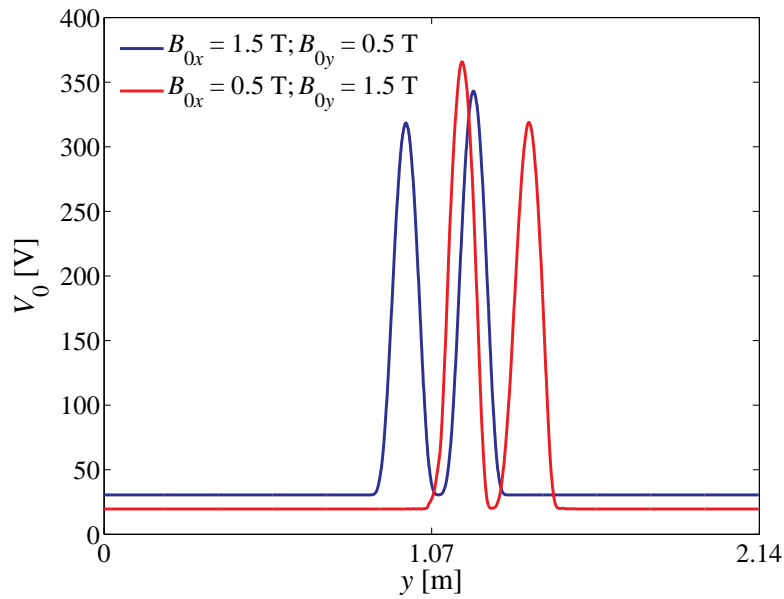


Figure 4-36: Comparison of the rectified sheath potential variation for $K_{\max} = 300$ A/m between the two examples employing different poloidal components of the background magnetic field.
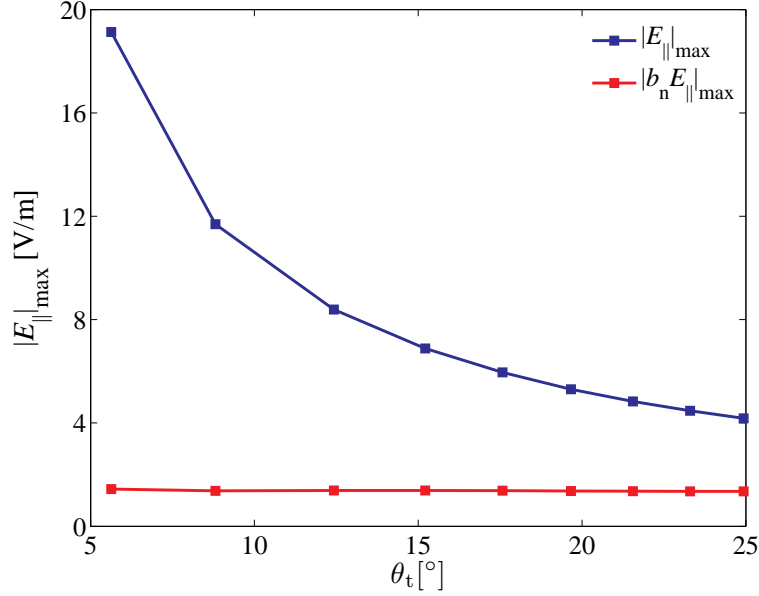
Figure 4-37: Plot of $\left|E_{\parallel}\right|_{\max}$ and $\left|b_{\mathrm{n}} E_{\parallel}\right|_{\max}$ as functions of the toroidal angle of the background magnetic field for $K_{\max} = 300$ A/m, $|\boldsymbol{B}_0| = 4.3$ T, and $\theta_{\mathrm{p}} = 40°$.

A/m. Again, it is confirmed that the value of $\left|b_{\mathrm{n}} E_{\parallel}\right|_{\max}$ is insensitive to $\theta_{\mathrm{t}}$. There is a subtlety in the electric field strength affected by the magnitudes of the poloidal and toroidal background magnetic field components, which might be clarified by an analytical work.

From these numerical results, it could be concluded that the sheath potential on the material surface in the close vicinity of the antenna current strap can be insensitive to the direction of the background magnetic field in the RF sheath dominated regime ($\sim$kV), if the contact angle between the magnetic field line and the sheath surface is not too small, so that the approximation $D_{\mathrm{n}} \simeq \varepsilon_0 \varepsilon_{\parallel} E_{\parallel} b_{\mathrm{n}}$ is valid.

As a last numerical examination, a series of calculations is conducted to investigate the sheath potential variation depending on the plasma density and electron temperature with the antenna current and background magnetic field fixed. Figure 4-38 shows the filled contour plots of the maximum rectified sheath potential $V_{\max}$ (on the sheath) as a function of the plasma density and electron temperature for $K_{\max} = 300$ A/m, and $B_{0x} = 1.5$ T, $B_{0y} = 0.5$ T, $B_{0z} = 4.0$ T. Here a comparison

is made between the approximate analytical result and the nonlinear self-consistent numerical result. Figure 4-38a is obtained using Equation (4.17) with the assumption that $E_\parallel$ is independent of $n_0$ ($= n_{e0}$) and $T_e$, and the numerical result is only provided at $n_0 = 1.0 \times 10^{17}$ m$^{-3}$ and $T_e = 10$ eV. Figure 4-38b is obtained from the numerical results calculated by the rfSOL code in the range of $n_0 = 1.0$–$2.0 \times 10^{17}$ m$^{-3}$ and $T_e = 5$–$10$ eV. Both figures are drawn by employing $6 \times 6$ sheath potential values. Although the overall trends are qualitatively similar between the two cases, the variation range in the numerical result is significantly reduced compared to that in the analytical prediction: the lowest and highest values of $V_{\mathrm{max}}$ are 86 V and 686 V, respectively, in Figure 4-38a, while they are 133 V and 510 V in Figure 4-38b. The contour lines at $V_{\mathrm{max}} = 200$ V and 150 V are compared in Figure 4-39. It is seen that the contour line of the numerical result at $V_{\mathrm{max}} = 150$ V significantly deviates from that of the analytical prediction (recall that the latter is drawn using a one-point numerical result around $V_{\mathrm{max}} = 300$ V, and hence the deviation is smaller at $V_{\mathrm{max}} = 200$ V). The difference comes from the fact that the numerical solution (the first-order electric field) is obtained (1) so as to satisfy the sheath boundary condition, and (2) by taking into account the dependence on parameters in the antenna coupling to $E_\parallel$. It should be emphasized from this comparison that the present nonlinear self-consistent code plays a major role in accurate quantitative evaluation of the RF sheath potential, which sensitively varies depending on the plasma density and electron temperature.

Lastly, Figure 4-40 shows how the contour line at $V_0 = 200$ V shifts on the parameter plane for $n_0$ and $T_e$ with an increase in the antenna current. Since higher antenna current yields an increased electric field, the contour line shifts to the higher plasma density or higher electron temperature side according to the scaling shown in Equation (4.17).
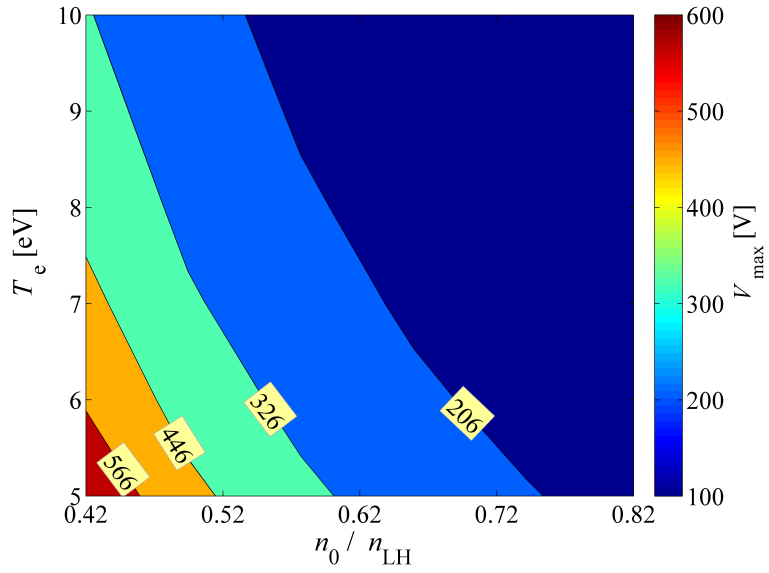
(a)
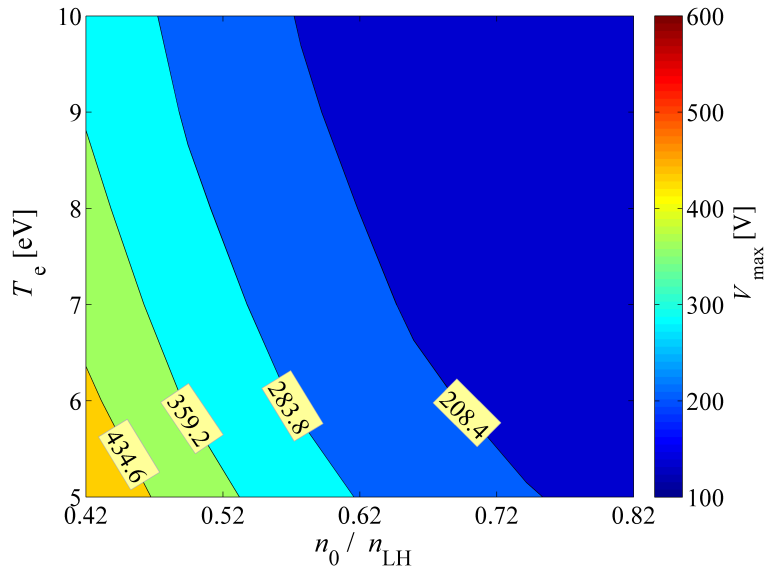


(b)

Figure 4-38: Filled contour plots of the maximum rectified sheath potential vs. plasma density and electron temperature for $K_{max} = 300$ A/m, and $B_{0x} = 1.5$ T, $B_{0y} = 0.5$ T, $B_{0z} = 4.0$ T: (a) analytical prediction with $D_n$ fixed; and (b) nonlinear self-consistent numerical result.
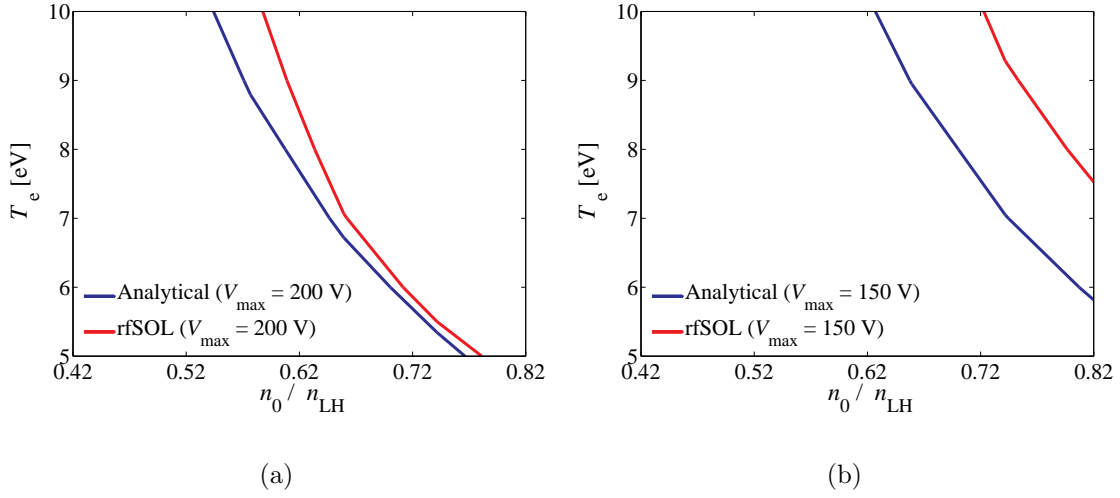
Figure 4-39: Comparison of the contour lines at $V_{max} = 200$ V (a) and $V_{max} = 150$ V (b) between the analytical prediction and the numerical result obtained by employing the rfSOL code. Here, $K_{max} = 300$ A/m, and $B_{0x} = 1.5$ T, $B_{0y} = 0.5$ T, $B_{0z} = 4.0$ T.
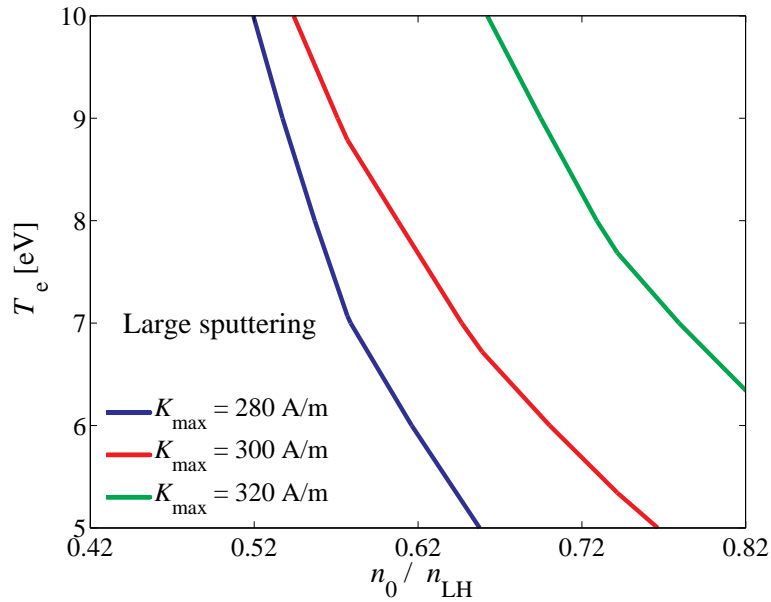


Figure 4-40: Contour lines at $V_{max} = 200$ V obtained by nonlinear self-consistent numerical simulation with three different antenna current values for $B_{0x} = 1.5$ T, $B_{0y} = 0.5$ T, and $B_{0z} = 4.0$ T.

# Chapter 5

# Development of the Finite Element Wave-Packet Method

## 5.1  Prologue

In the previous chapters the nonlinear sheath-plasma interactions in the SOL have been numerically solved under various conditions, and many interesting phenomena have been discovered. One of the important next steps will be to further increase the spatial resolution, together with complexity of the boundary geometry, in order to capture unidentified multiscale behaviors, especially, slow waves whose wavelengths are much smaller compared to the characteristic length of the domain. In particular, if resonance is involved in the calculation domain, conventional numerical methods require a sufficiently fine mesh to accurately capture fine-scale variations in the vicinity of the resonance region. In this case, even though most of the domain should not require a fine mesh, one still has to provide fine discretization for almost the entire domain, since in general we cannot predict precisely prior to the analysis where resonance will occur. Much effort has been devoted to the development of computer programs to solve wave propagations in hot tokamak plasmas [59–61]. However, as described in Section 3.4, there are currently several limits related to memory size even

if a highly sophisticated simulator, such as the computer system at NERSC, is employed; for this reason, 3D simulation is still a challenge for most of the fusion plasma problems. It is true that the above-mentioned difficulty will be gradually solved with improvement of computational performance from the hardware point of view, but we can also achieve this goal by developing more efficient interpolation functions used for the discretization of governing equations. Based on this standpoint, the last topic of this thesis is directed to the development of a new finite element procedure for multiscale wave equations with application to plasma waves. Below is the summary of the previously published paper [62].

To solve wave propagation problems accurately, the spectral method [63] or spectral finite element method have been used [64–66] and good results have been obtained in certain analyses. However, these methods can be computationally expensive, and more importantly, the methods show intrinsic difficulties in satisfying the boundary conditions for arbitrarily-shaped domains. Since in many wave propagation analyses, the domain considered is geometrically complex, the available spectral techniques may not be effective.

Another possibly more efficient approach is to utilize basic interpolation functions that are enriched with waves. This means in essence to construct special interpolation functions that are more amenable to capture the desired response. This approach is rather natural to increase the effectiveness of the finite element method for the solution of specific problems, and has been pursued for a long time, like for example in the analysis of wave propagations [67–69], global local solutions [70, 71], piping analyses [72], the development of beam elements [73], and in fluid flow analyses [74, 75]. Such methods have lately also been referred to as partition of unity methods or extended finite element methods, see for example [76–79]. In addition, recently, discontinuous Galerkin methods [80] and related techniques have been researched for the solution of wave propagation problems, but these techniques can be computationally expensive to use.

Whenever such a problem-specific method is proposed, the generality for a specific class of problems and effectiveness are crucial. For plasma wave problem solutions, Pletzer et al. proposed a wave-packet approach using Gabor functions as envelopes [81]. Although this method has several good features, five parameters need to be selected, where it is difficult to find near optimal choices. Also, since the values of the Gabor functions are nonzero in the entire calculation domain, a cutoff value has to be defined. Furthermore, it is difficult to incorporate general boundary conditions.

The objective in this chapter is to present a finite element scheme in which basic finite element interpolations are used enriched with wave packets. The method is quite simple and is based on the standard finite element method [52] and spectral method [63], but does not have the above-mentioned disadvantages. It turns out that the resulting interpolation functions have the same structure as those proposed in References [67,68] but can be applied to a much broader range of problems. Specifically, the procedure can also be used to solve a range of plasma wave propagation problems, for example in which mode conversion occurs. In these cases, waves with dramatically different wavelengths can exist in localized regions, which are determined by sophisticated plasma models considering kinetic effects. An important point is that the governing equations corresponding to the kinetic model include integrals, since the dielectric tensor is evaluated by integrating over the whole of velocity space and past particle trajectory time. For that reason, the methods referenced above [67–69,76,77] cannot directly be used to such plasma wave problems, because they use solutions of some specific differential equations. The approach presented here utilizes classical finite element interpolations with spectral enrichments, and can be applied to the equations including integrals as well as general differential equations. The combined interpolation technique can be used to easily satisfy Dirichlet boundary conditions and solve for many different wavenumbers in one solution.

In this chapter, first, the proposed numerical procedure is presented in detail, and then the solutions of some test problems are given, including a problem modeling

wave behavior in plasmas. It will be shown that the proposed finite element method gives more accurate results than the conventional finite element method for wave propagation problems. While this chapter only considers 1D linear problems, there is considerable intrinsic potential of the method to be effective for multi-dimensional and even nonlinear solutions.

## 5.2   Finite Element Wave-Packet Approach

The method proposed here is based on three important features: the technique can be thought of as using the interpolations of the traditional finite element method enriched by waves, the resultant global coefficient matrix is sparse as in finite element methods, and the boundary conditions are easily incorporated. The purpose of this section is to describe each feature in detail.

### 5.2.1   Foundation of the Numerical Method

The basis of the proposed scheme is a weak form of the weighted residual method [52]. Consider a general 1D ordinary differential equation written as $\mathcal{L}[u]+f(x)=0$, where $\mathcal{L}$ is an ordinary differential operator. Let $\hat{u}$ be an approximate numerical solution. The numerical solution $\hat{u}$ is determined such that the following integral equation is satisfied:

$$\int_{\Omega} h(x)\left(\mathcal{L}[\hat{u}] + f(x)\right) d\Omega + \int_{\Gamma} h(x)\left(\mathcal{B}[u] - \mathcal{B}[\hat{u}]\right) d\Gamma = 0 \tag{5.1}$$

where $h(x)$ is a weight function, $\mathcal{B}$ is an operator for the boundary term, $\Omega$ and $\Gamma$ denote the calculation domain and its boundary, respectively. Using the standard Galerkin approach, the numerical solution and weight function are given by the same type of interpolation functions, which are formulated next.

144

## 5.2.2 Linear, Quadratic, and Hermitian Wave-Packet Interpolation Functions

The interpolation functions are constructed by multiplying sinusoidal functions by well-known finite element interpolation functions. First, the numerical solution $\hat{u}$ and the weight function $h$ are expressed using the linear or quadratic wave-packet interpolation functions $g_{(i,j)}$ as follows:

$$\hat{u}(x) = g_{(i,j)}(x) u_{(i,j)} \tag{5.2}$$

$$h(x) = g^*_{(i',j')}(x) h_{(i',j')} \tag{5.3}$$

where the superscript $*$ denotes the complex conjugate; $u_{(i,j)}$, $h_{(i',j')}$ are nodal complex values in the coordinate-frequency space identified by the global node number $i$ and the harmonic number $j$. Here the summation convention applies to the subscripts $i$ and $j$. Since the proposed method utilizes a finite element interpolation function as an envelope function, the value of the envelope function is one at some nodal point $x_k$ and zero at $x_j$ $(j \neq k)$. This allows the functions $g_{(i,j)}$ to be defined in each grid element, and the linear wave-packet interpolation functions are locally expressed as

$$g_{(\alpha,j)}(\xi) = \frac{1}{2}(1 + \xi_\alpha \xi) \exp\left[2\pi i \nu_j \left(x_e + \frac{\Delta x}{2}\xi\right)\right] \tag{5.4}$$

Similarly, for the quadratic envelope one gets

$$g_{(\alpha,j)}(\xi) = \left[\frac{\xi_\alpha \xi}{2}(1 + \xi_\alpha \xi) + \left(1 - \xi_\alpha^2\right)\left(1 - \xi^2\right)\right] \exp\left[2\pi i \nu_j \left(x_e + \frac{\Delta x}{2}\xi\right)\right] \tag{5.5}$$

where $i$, $x_e$, $\Delta x$, and $\xi$ are the imaginary unit, $x$-coordinate at the center of an element, length of an element, and coordinate variable in the calculation space $(-1 \leq \xi \leq 1)$, respectively; the physical space is then related to the calculation space by $x = x_e + (\Delta x/2)\xi$. The subscript $\alpha$ denotes the local node number, and the values of $\xi_\alpha$ are
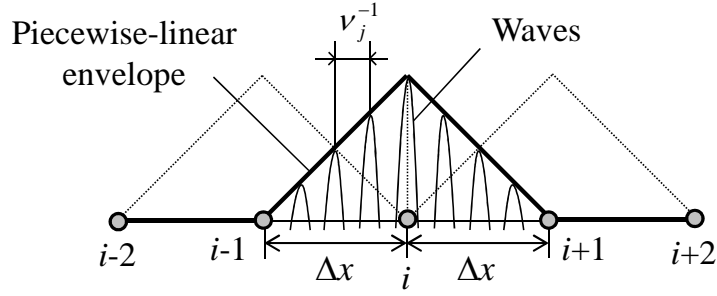
Figure 5-1: Schematic diagram of a linear wave-packet interpolation function.

$\xi_{1,2} = -1, 1$ for the linear case and $\xi_{1,2,3} = -1, 1, 0$ for the quadratic case, respectively. The wavenumbers $2\pi\nu_j$ are determined by $\nu_j = j\nu$, where $\nu$ is the fundamental frequency and $j$ is an integer in the range $-(N_F - 1)/2 \leq j \leq (N_F - 1)/2$ with the cutoff number of harmonics $N_F$. Here $N_F \geq 1$ is an odd integer. The schematic profile of a linear wave-packet interpolation function is shown in Figure 5-1. As we will see in the numerical examples in Section 5.4, the quadratic wave-packet interpolation is actually more effective.

Another possibly more efficient wave-packet approach can be established by employing Hermitian cubic beam functions [52] where then the nodal values and also the derivative values at the nodes are used. This makes the expressions for the numerical solution and weight function slightly different from Equations (5.2) and (5.3):

$$\hat{u}(x) = g_{(i,j)}(x)\,\tilde{u}_{(i,j)} \tag{5.6}$$

$$h(x) = g^*_{(i',j')}(x)\,\tilde{h}_{(i',j')} \tag{5.7}$$

Here the Hermitian wave-packet interpolation functions and corresponding nodal complex values comprise two different expressions:

$$g_{(i,j)} = \begin{cases} g^1_{(i,j)} & \text{for } 1 \leq i \leq N_x \\ g^2_{(k,j)} & \text{for } N_x + 1 \leq i \leq 2N_x \end{cases} \tag{5.8}$$

146

$$
\tilde{u}_{(i,j)} =
\begin{cases}
u_{(i,j)} & \text{for } 1 \leq i \leq N_x \\[2mm]
u'_{(k,j)} & \text{for } N_x + 1 \leq i \leq 2N_x
\end{cases}
\tag{5.9}
$$

(same applies to $\tilde{h}_{(i,j)}$) where $N_x$ is the total number of nodes, and the value of the subscript $k$ is related to the value of $i$ by $k = i - N_x$. In a similar way to the linear and quadratic wave-packet interpolations, the functions in Equation (5.8) can be written locally as follows:

$$
\begin{aligned}
g^1_{(\alpha,j)} (\xi) &= \frac{1}{4} (\xi + \xi_\alpha)^2 (-\xi_\alpha \xi + 2) \exp \left[ 2\pi i \nu_j \left( x_{\mathrm{e}} + \frac{\Delta x}{2} \xi \right) \right] \\
g^2_{(\alpha,j)} (\xi) &= \frac{\Delta x}{8} (\xi + \xi_\alpha)^2 (\xi - \xi_\alpha) \exp \left[ 2\pi i \nu_j \left( x_{\mathrm{e}} + \frac{\Delta x}{2} \xi \right) \right]
\end{aligned}
\tag{5.10}
$$

where $\xi_{1,2} = -1, 1$. The real-valued profiles of the Hermitian wave-packet interpolation functions are shown in Figure 5-2.

For a real-valued solution, we can easily derive the following restrictions from Equations (5.2) and (5.6):

$$
\begin{aligned}
u_{(\alpha,j)} &= u^*_{(\alpha,-j)} \\
u'_{(\alpha,j)} &= u'^*_{(\alpha,-j)}
\end{aligned}
\tag{5.11}
$$

where the equation involving derivatives is of course only considered for the Hermitian wave-packet interpolation functions. These relations reduce the number of unknowns to half and consequently, the size of the global matrix to a quarter. Using Equation (5.11), for example, we can modify the linear wave-packet interpolation functions as follows:

$$
\begin{aligned}
\hat{u}(x) &= g^{\mathrm{a}}_{(\alpha,0)} u_{(\alpha,0)} + \sum_{j=1}^{(N_{\mathrm{F}}-1)/2} \left[ g^{\mathrm{b}}_{(\alpha,j)} u^{(\mathrm{R})}_{(\alpha,j)} + g^{\mathrm{c}}_{(\alpha,j)} u^{(\mathrm{I})}_{(\alpha,j)} \right] \\
&= g_{(\alpha,m)} \tilde{u}_{(\alpha,m)}
\end{aligned}
\tag{5.12}
$$
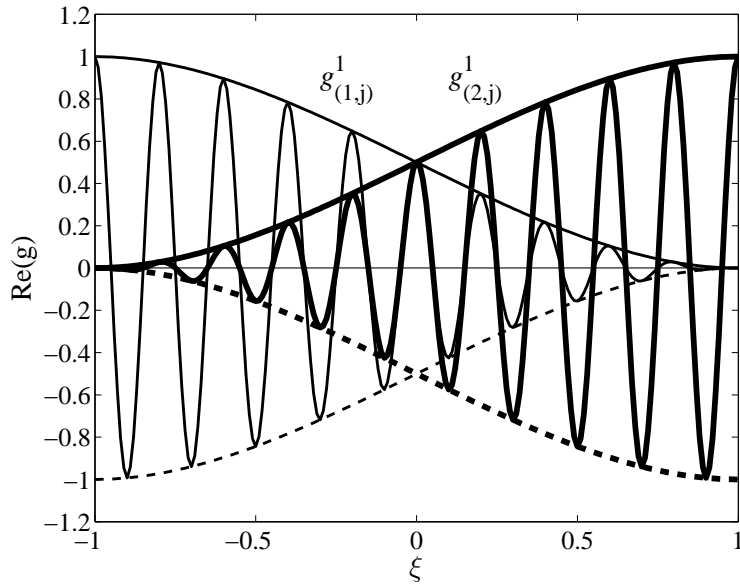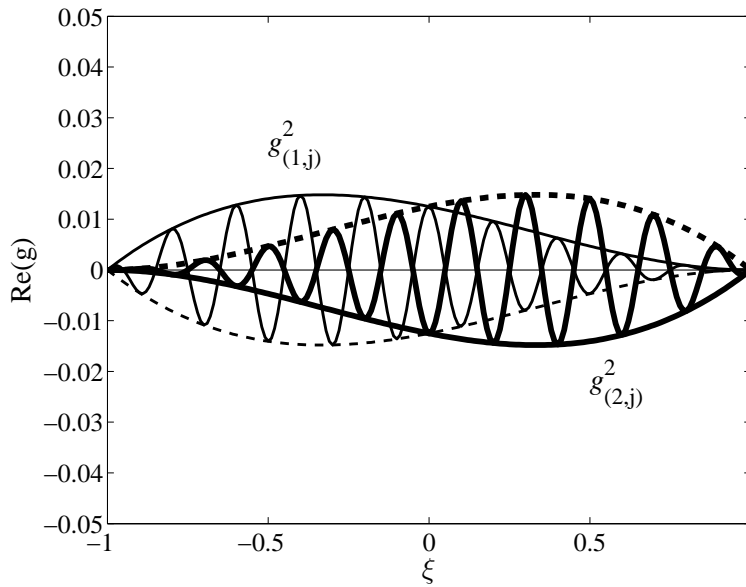
Figure 5-2: Profiles of the Hermitian wave-packet interpolation functions together with their envelope functions for $\Delta x = 0.1$ and $\nu_j = 100$: (a) plot of $\text{Re}\left[g^1_{(\alpha,j)}\right]$ vs. $\xi$; and (b) plot of $\text{Re}\left[g^2_{(\alpha,j)}\right]$ vs. $\xi$.

with

$$g^{\mathrm{a}}_{(\alpha,0)} = \frac{1}{2}\left(1 + \xi_\alpha \xi\right)$$

$$g^{\mathrm{b}}_{(\alpha,j)} = \left(1 + \xi_\alpha \xi\right) \cos\left[2\pi\nu_j\left(x_{\mathrm{e}} + \frac{\Delta x}{2}\xi\right)\right] \qquad (5.13)$$

$$g^{\mathrm{c}}_{(\alpha,j)} = -\left(1 + \xi_\alpha \xi\right) \sin\left[2\pi\nu_j\left(x_{\mathrm{e}} + \frac{\Delta x}{2}\xi\right)\right]$$

$$g_{(\alpha,m)} = \begin{cases} g^{\mathrm{a}}_{(\alpha,0)} & \text{for } m = 0 \\[2mm] g^{\mathrm{b}}_{(\alpha,j)} & \text{for } 1 \leq m \leq (N_{\mathrm{F}} - 1)/2 \\[2mm] g^{\mathrm{c}}_{(\alpha,k)} & \text{for } (N_{\mathrm{F}} - 1)/2 + 1 \leq m \leq N_{\mathrm{F}} - 1 \end{cases} \qquad (5.14)$$

$$\tilde{u}_{(\alpha,m)} = \begin{cases} u_{(\alpha,0)} & \text{for } m = 0 \\[2mm] u^{(\mathrm{R})}_{(\alpha,j)} & \text{for } 1 \leq m \leq (N_{\mathrm{F}} - 1)/2 \\[2mm] u^{(\mathrm{I})}_{(\alpha,k)} & \text{for } (N_{\mathrm{F}} - 1)/2 + 1 \leq m \leq N_{\mathrm{F}} - 1 \end{cases} \qquad (5.15)$$

where $u^{(\mathrm{R})}_{(\alpha,j)}$, $u^{(\mathrm{I})}_{(\alpha,j)}$ are the real and imaginary parts of $u_{(\alpha,j)}$, respectively, and the subscripts $j$, $k$, and $m$ in Equations (5.14) and (5.15) are related to one another by $j = m$, $k = m - (N_{\mathrm{F}} - 1)/2$. Of course, if we consider a general plasma wave, the numerical solution is always complex, and hence Equations (5.11) to (5.15) are not applicable.

An interesting observation is that for $j = 0$ all the wave-packet interpolation functions given in Equations (5.4), (5.5), and (5.10) reduce to the usual finite element interpolation functions as a result of $\nu_j = j\nu = 0$. Thus, for $N_{\mathrm{F}} = 1$, the present interpolation scheme consists only of the conventional finite element interpolation functions, and indeed the present wave-packet approach becomes identical to the conventional finite element method when $N_{\mathrm{F}} = 1$ (see Section 5.2.3). We will see that this property leads to a straightforward treatment of the boundary conditions.

The present scheme results in a relatively low computational cost since the global

$2 \times N_x \times N_F$

0          0

0          0

0          0

0          0

0          0

0          0

$N_F$

$u_{(1,-(N_F-1)/2)}$

$u_{(N_x,(N_F-1)/2)}$

$u'_{(1,-(N_F-1)/2)}$

$u'_{(N_x,(N_F-1)/2)}$

$\begin{matrix} 1 & & 0 \\ & \ddots & \\ 0 & & 1 \end{matrix}$

Boundary conditions
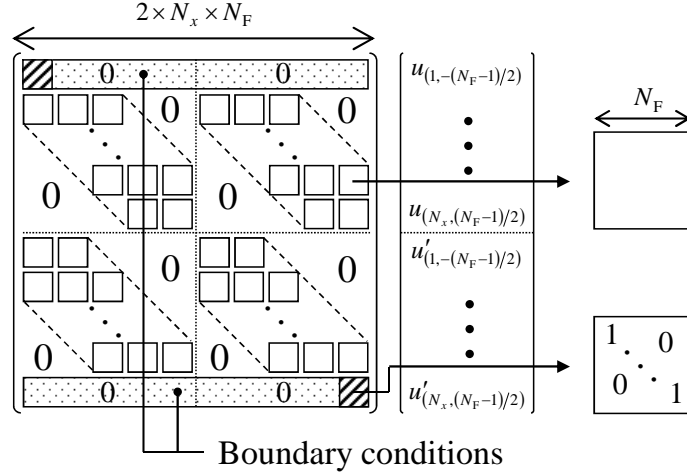
Figure 5-3: An example of the structure of the global matrix for the analysis using the Hermitian finite element wave-packet method.

matrix is sparse. This sparsity is due to the local interpolation of wave packets. As an example, the distribution of the global matrix elements for the case of using the Hermitian functions is shown in Figure 5-3, where the nonzero regions are block-diagonalized with a regular bandwidth of $3N_F$.

As an illustration, consider a 1D sine-wave problem described by $u'' + \alpha^2 u = 0$ in the range $0 \leq x \leq 1$ subject to the boundary condition $u(0) = 0$, $u'(1) = \alpha$. Here $\alpha$ is a constant with $\cos \alpha = 1$. The exact solution for this problem is then given by $u = \sin(\alpha x)$. Figure 5-4a shows a numerical solution obtained by the linear finite element wave-packet approach for $\alpha = 4\pi$, $\nu = 0.5$, $N_x = 2$, and $N_F = 9$. As seen, with only one element used, we obtain virtually the exact analytical result. This is the desired result since the method is based on the Fourier decomposition technique, so that any smooth function should be reproduced by the combination of sinusoidal waves with different wavenumbers regardless of the value of $N_x$. Figure 5-4b is a semi-log plot of the error norm, which is defined by $\|L^2\| \equiv \left[ \int (u - \hat{u})^2 \, dx / \int u^2 dx \right]^{1/2}$, as a function of $N_F$. We notice that the error decreases logarithmically with the number of harmonics for $N_F \geq 5$. Due to this feature, the present wave-packet approach can

yield more accurate results compared to the conventional finite element method by orders of magnitude.

## 5.2.3 Imposing the Boundary Conditions

An important feature of the present method is the ease of imposing the boundary conditions. Consider a 1D problem governed by a certain differential equation. When imposing the Dirichlet boundary condition, we choose a weight function whose value is forced to be zero at the boundary in the same way as in the conventional Galerkin finite element method. But an important point to notice is that the interpolated nodal values $u_{(i,j)}$ (or $\tilde{u}_{(i,j)}$) are not identical to the nodal values of the numerical solution $\hat{u}(x)$. Thus, for example, if we intend to exactly satisfy the Dirichlet boundary condition at the boundary $x = x_b$ (the right-hand side boundary), the following equality must be satisfied:

$$\hat{u}(x_b) = u_b = \begin{cases} g_{(i,j)}(x_b) u_{(i,j)} & \text{for the linear and quadratic cases} \\ g_{(i,j)}(x_b) \tilde{u}_{(i,j)} & \text{for the Hermitian case} \end{cases} \tag{5.16}$$

For $u_b$ being real, Equation (5.16) leads to

$$\begin{cases} \sum_{j=-(N_F-1)/2}^{(N_F-1)/2} \left[ \cos(2\pi\nu_j x_b) u_{(N_x,j)}^{(R)} - \sin(2\pi\nu_j x_b) u_{(N_x,j)}^{(I)} \right] = u_b \\ \sum_{j=-(N_F-1)/2}^{(N_F-1)/2} \left[ \sin(2\pi\nu_j x_b) u_{(N_x,j)}^{(R)} + \cos(2\pi\nu_j x_b) u_{(N_x,j)}^{(I)} \right] = 0 \end{cases} \tag{5.17}$$

where we note that Equation (5.17) does not lead to a unique solution for $N_F > 1$. However, the following choice always satisfies the boundary condition for any $\nu$ and
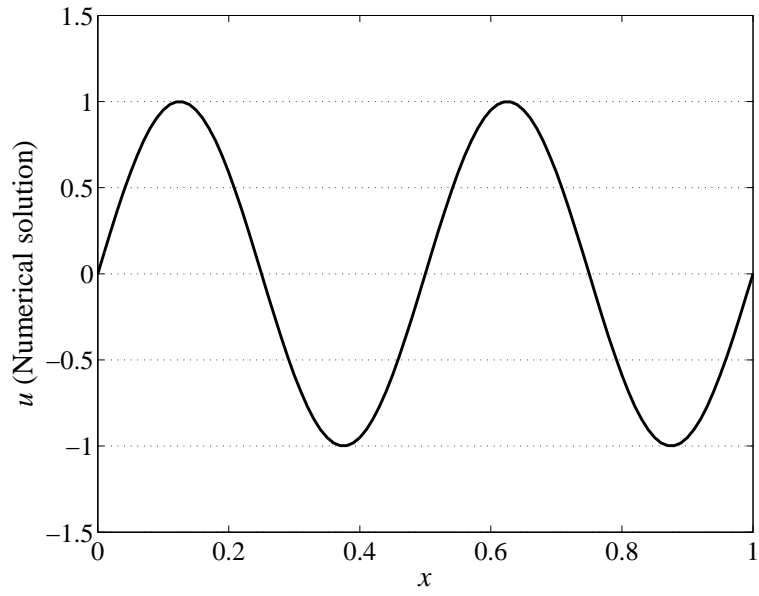
(a)
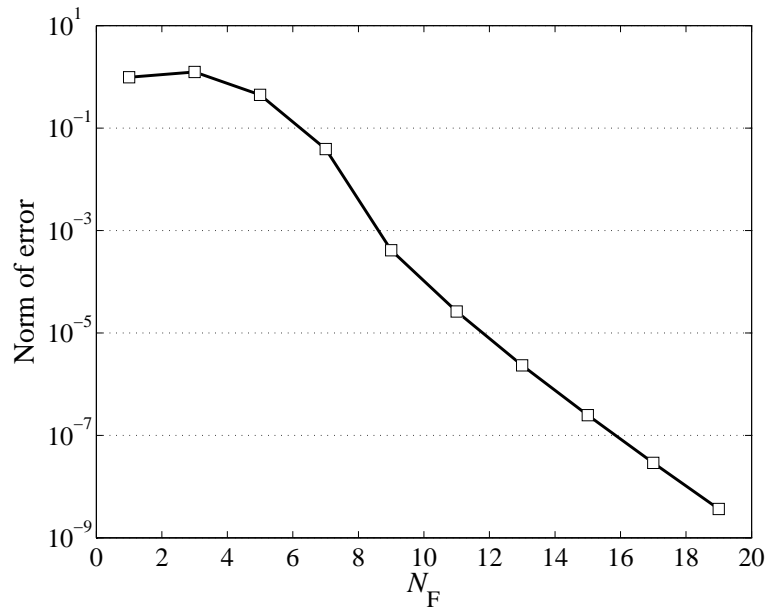


(b)

Figure 5-4: The numerical results obtained by the linear finite element wave-packet method for $\nu = 0.5$, $N_x = 2$: (a) the calculated wave for $N_F = 9$; and (b) the norm of error as a function of $N_F$.

$x_{\mathrm{b}}$:

$$u^{(\mathrm{R})}_{(N_x,j)} = \begin{cases} u_{\mathrm{b}} & \text{for } j = 0 \\ 0 & \text{for } j \neq 0 \end{cases}$$

$$u^{(\mathrm{I})}_{(N_x,j)} = 0$$

(5.18)

This corresponds to the concept of imposing the exact boundary value in the conventional finite element component ($j = 0$). Note that Equation (5.18) is consistent with the statement in Section 5.2.2; the present scheme reduces to the conventional finite element method for $N_{\mathrm{F}} = 1$.

On the other hand, the proposed method only approximately satisfies the Neumann boundary conditions, again as in the conventional finite element method. For the linear or quadratic wave-packet approach, the value of the weight function at the boundary can be arbitrary. The boundary term in the discretized equation is calculated in the same way as in the standard finite element method. For the Hermitian wave-packet approach, we specify $h'_{(i,j)} = 0$ at the Neumann boundary and choose the boundary nodal values in a similar way to the Dirichlet boundary condition as follows:

$$u'^{(\mathrm{R})}_{(N_x,j)} = \begin{cases} u'_{\mathrm{b}} & \text{for } j = 0 \\ 0 & \text{for } j \neq 0 \end{cases}$$

$$u'^{(\mathrm{I})}_{(N_x,j)} = 0$$

(5.19)

Here we assume that the Neumann boundary condition is imposed at $x = x_{\mathrm{b}}$. In general, the above choice does not exactly satisfy the Neumann boundary condition

because

$$\left. \frac{d\hat{u}}{dx} \right|_{x=x_{\mathrm{b}}} = \frac{2}{\Delta x} \left( \frac{dg^1_{(\alpha=2,j)}(\xi)}{d\xi} u_{(\alpha=2,j)} + \frac{dg^2_{(\alpha=2,j)}(\xi)}{d\xi} u'_{(\alpha=2,j)} \right) \Bigg|_{\xi=1, x=x_{\mathrm{b}}}$$

$$= \frac{2}{\Delta x} \frac{dg^1_{(2,j)}(\xi)}{d\xi} u_{(2,j)} \Bigg|_{\xi=1, x=x_{\mathrm{b}}} + u'_{\mathrm{b}}$$

(5.20)

In general, the first term on the right-hand side is nonzero, and thus $d\hat{u}/dx|_{x=x_{\mathrm{b}}} \neq u'_{\mathrm{b}}$. For $N_{\mathrm{F}} = 1$, the scheme reduces to the conventional Hermitian finite element method, and then the Neumann boundary condition is exactly satisfied.

## 5.3   A Required Condition in $\nu$

In the present scheme, we need to specify three numerical parameters: $N_x$, $N_{\mathrm{F}}$, and $\nu$. Here one required condition for a proper choice of $\nu$ is derived by relating it to the value of $N_x$.

First of all, an important point is that every integral in the locally discretized equations can be written in the following form:

$$I = \int_{-1}^{1} \left( \sum_{n=0}^{\infty} C_n \xi^n \right) \exp\left( a\xi + b \right) d\xi$$

(5.21)

where

$$a = \pi i \left( \nu_j - \nu_{j'} \right) \Delta x$$
$$b = 2\pi i \left( \nu_j - \nu_{j'} \right) x_{\mathrm{e}}$$

(5.22)

Here $n \geq 0$ takes integer values, and the $C_n$ are the coefficients determined depending on the differential equations considered. Now define

$$F(n) \equiv \int_{-1}^{1} \xi^n \exp\left( a\xi + b \right) d\xi$$

(5.23)

154

Then Equation (5.21) is simply expressed by $I = \sum_{n=0} C_n F(n)$. Consider first the case of $\nu_j \neq \nu_{j'}$ (i.e., $j \neq j'$). For $n \geq 1$ one can rewrite Equation (5.23) as follows:

$$F(n) = \left[ \frac{\xi^n}{a} \exp(a\xi + b) \right]_{-1}^{1} - \frac{n}{a} F(n-1) \tag{5.24}$$

For $n = 0$ we have

$$F(0) = \int_{-1}^{1} e^{a\xi + b} d\xi = \frac{1}{a} \left( e^{a+b} - e^{-a+b} \right) \tag{5.25}$$

Thus, using Equations (5.24) and (5.25) we obtain $F(n)$ for any value of $n$ through successive calculations. For $\nu_j = \nu_{j'}$ ($j = j'$), the integral in Equation (5.23) is easily solved as follows:

$$F(n) = \int_{-1}^{1} \xi^n d\xi = \frac{1}{n+1} \left[ 1 - (-1)^{n+1} \right] \tag{5.26}$$

These analytical expressions are desirable since we do not need to apply any numerical integration to the integral shown in Equation (5.21); consequently, the computation of each term is fast without a numerical error due to numerical integration.

Now, using Equations (5.24) and (5.26), consider the following two important limits: $|a| \to \infty$ and $|a| \to 0$. Assume that a given differential equation is discretized by properly choosing finite element wave-packet interpolation functions. For $|a| \to \infty$, we find that $|I_{j=j'}| / |I_{j \neq j'}| \to \infty$ and $|I_{j=j'}| \to \infty$ for $j \neq 0$ in a non-sparse block $(i, i')$, where $|I_{j=j'}|$ and $|I_{j \neq j'}|$ are the integrals obtained by adding up all the discretized derivative terms for $j = j'$ and $j \neq j'$, respectively, expressed in the form of Equation (5.21). On the other hand, for $|a| \to 0$, we find that $|I_{j \neq j'}| / |I_{j=j'}| \to \infty$ and $|I_{j \neq j'}| \to \infty$ in a non-sparse block $(i, i')$. Of course, the numerical solutions for these cases do not make any sense. Therefore, a required condition should be $|a| \sim 1$, i.e., $\nu \Delta x \sim 1$, for which the magnitude of every term in Equation (5.21) is about like in the conventional finite element discretization ($j = j' = 0$). The physical

interpretation to this constraint is that the waves in the wave packet should have at least one wavelength in a grid element (see Figure 5-1).

## 5.4   Numerical Results

In this section the performance of the finite element wave-packet approach is illustrated using three test examples. The problems considered here are a wave propagation through different media, a problem described by the Airy-type equation, whose exact solution is available for comparison with the numerical results, and a problem described by the Wasow equation, which models the mode-conversion behavior of RF waves in plasmas. The last two examples are chosen from Reference [81]. All solutions are obtained using uniform meshes, and when the solution accuracies of the proposed approach are compared with the accuracy obtained using the conventional finite element method, the fact that the solutions are real is employed and the same number of unknowns is used (see Section 5.2.2).

### 5.4.1   Wave Propagation through Different Media

Consider the wave propagation problem through different media in the domain $0 \leq x \leq 2$, which is described by the following equation:

$$\frac{d^2u}{dx^2} + \alpha^2 u = 0 \tag{5.27}$$

where $\alpha^2 = \alpha_{\mathrm{I}}^2$ for $0 \leq x < 1$ and $\alpha^2 = \alpha_{\mathrm{II}}^2$ for $1 < x \leq 2$. We assume that $\sin \alpha_{\mathrm{I}} = \sin \alpha_{\mathrm{II}} = 0$ and $\cos \alpha_{\mathrm{I}} = \cos \alpha_{\mathrm{II}}$ subject to the boundary conditions $u(0) = 0$ and $u'(2) = \alpha_{\mathrm{II}}$. The exact solution is then $u_{\mathrm{I}} = (\alpha_{\mathrm{II}}/\alpha_{\mathrm{I}}) \sin(\alpha_{\mathrm{I}} x)$ in the range $0 \leq x < 1$ and $u_{\mathrm{II}} = \sin(\alpha_{\mathrm{II}} x)$ in $1 < x \leq 2$. Here we consider two cases: $\alpha_{\mathrm{I}} = 8\pi$, $\alpha_{\mathrm{II}} = 4\pi$ in case 1 and $\alpha_{\mathrm{I}} = 64\pi$, $\alpha_{\mathrm{II}} = 8\pi$ in case 2.

The local (within a grid element) discretized equation for Equation (5.27) is:

$$\int_{\Omega^e} \left( \frac{dg^*_{(\alpha,j')}}{dx} \frac{dg_{(\beta,j)}}{dx} - \alpha^2 g^*_{(\alpha,j')} g_{(\beta,j)} \right) dx \cdot u_{(\beta,j)} - g^*_{(\alpha,j')} \frac{du}{dx} \bigg|_{\text{boundary}} = 0 \qquad (5.28)$$

As for the parameters used in the numerical scheme, the number of envelope positions (i.e., nodes), cutoff number of harmonics, and fundamental frequency are set at $N_x = 9$, $N_F = 5$, $\nu = 1.8$ ($N_x = 21$, $N_F = 11$, $\nu = 6.0$) for the linear, quadratic wave-packet methods and $N_x = 5$, $N_F = 5$, $\nu = 1.5$ ($N_x = 11$, $N_F = 11$, $\nu = 6.0$) for the Hermitian wave-packet method in case 1 (case 2).

The profiles of the numerical solutions obtained by the Hermitian wave-packet method are shown in Figure 5-5. Figure 5-6 shows the comparison of the numerical error $(\hat{u}-u)$ for the linear, quadratic, and Hermitian wave-packet approaches. As seen, the error is considerably smaller if we use higher-order envelope functions, although the difference between the quadratic and Hermitian wave packets is small for this problem. Figure 5-7 shows the comparison of the numerical error between the present wave-packet method and the conventional finite element method with $N_x = 25$ in case 1 and $N_x = 121$ in case 2, both of which utilize the Hermitian interpolation functions. We see that the numerical results obtained using the Hermitian wave-packet method are several orders of magnitude more accurate than the results obtained using the standard finite element method. Especially, the result in Figure 5-7b demonstrates that a sufficient number of harmonics yields rapid convergence for a smooth function as for the standard Fourier series (see Figure 5-4b).

## 5.4.2 Airy-Type Equation

Second, the methods are applied to the following second-order differential equation:

$$\frac{d^2u}{dx^2} + \alpha^2 \left(1 - 2x\right) u = 0 \qquad (5.29)$$
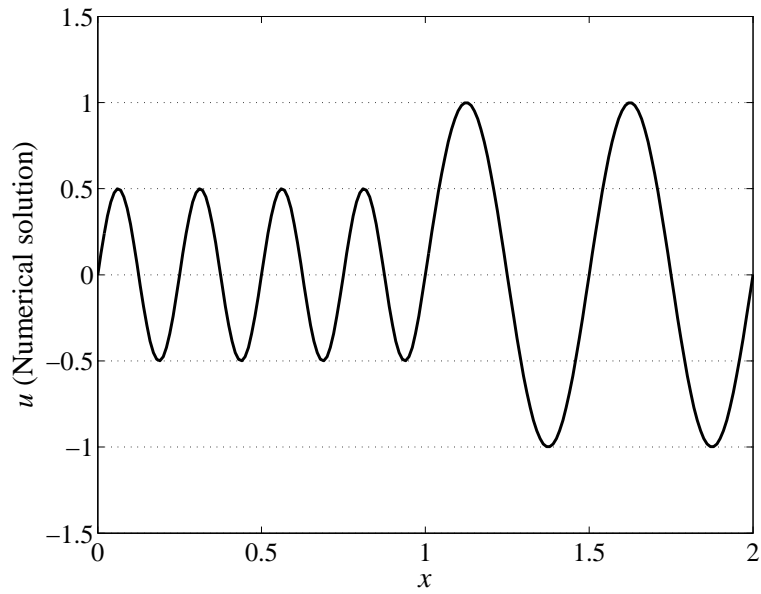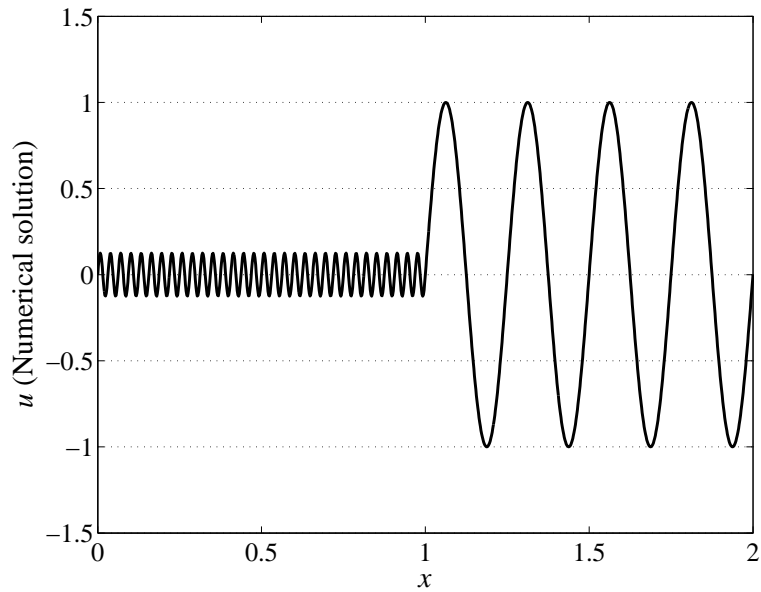
Figure 5-5: Numerical solutions of the wave propagation problem through different media: (a) $u = 0.5 \sin(8\pi x)$ in $0 \leq x < 1$ and $u = \sin(4\pi x)$ in $1 < x \leq 2$ (case 1); (b) $u = 0.125 \sin(64\pi x)$ in $0 \leq x < 1$ and $u = \sin(8\pi x)$ in $1 < x \leq 2$ (case 2).

158
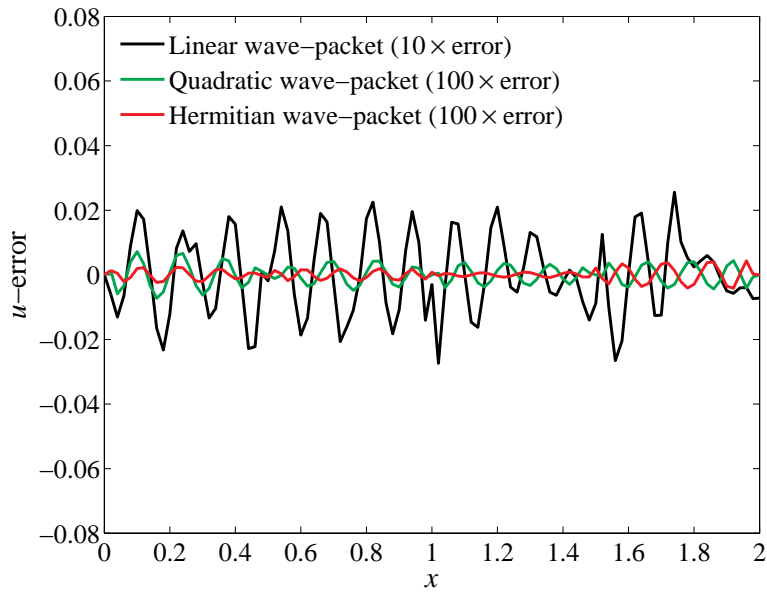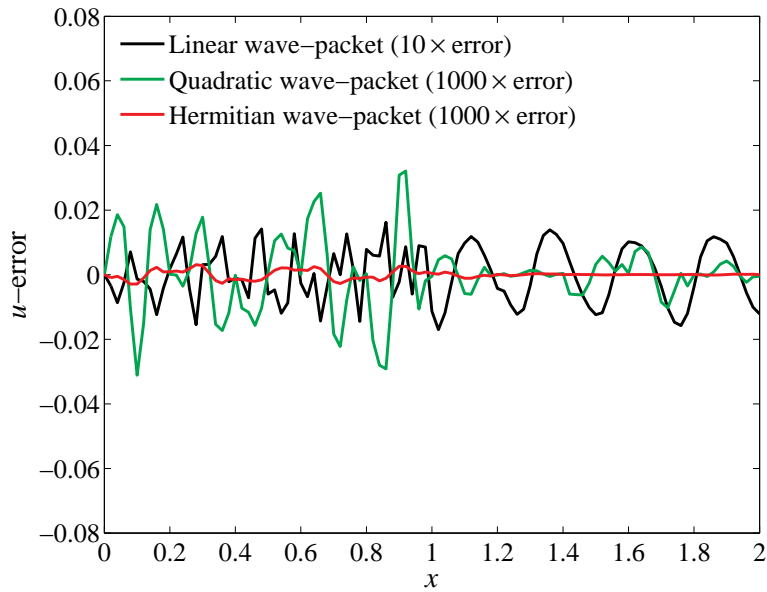
Figure 5-6: Comparison of the numerical error for the wave propagation problem through different media among the three different wave-packet methods: (a) case 1; and (b) case 2.
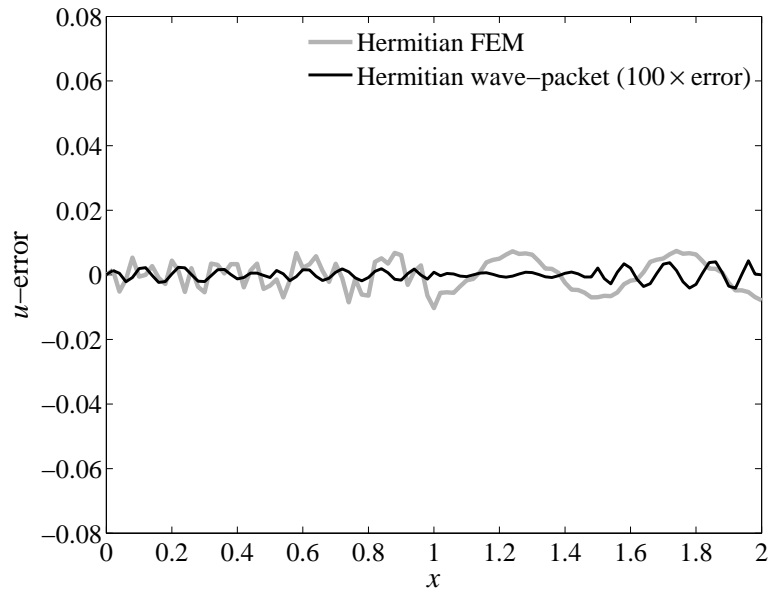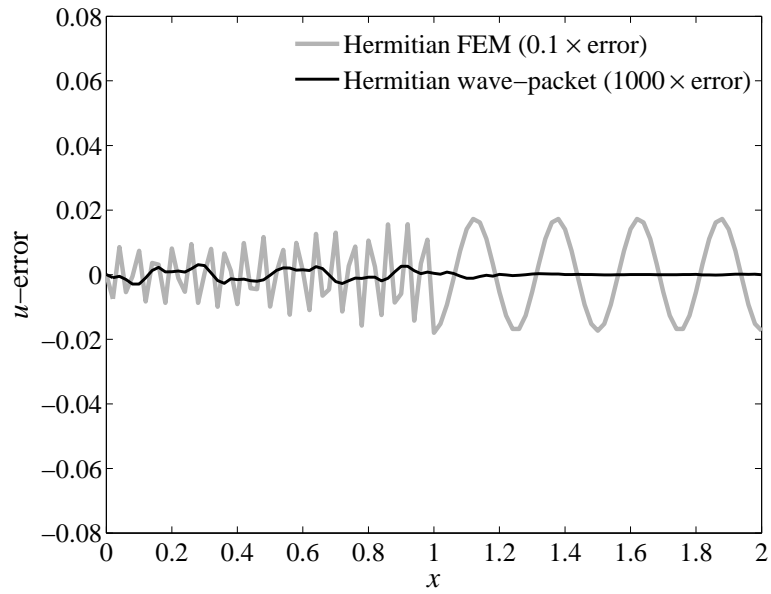
Figure 5-7: Comparison of the numerical error for the wave propagation problem through different media between the finite element wave-packet method and the conventional finite element method: (a) case 1; and (b) case 2.
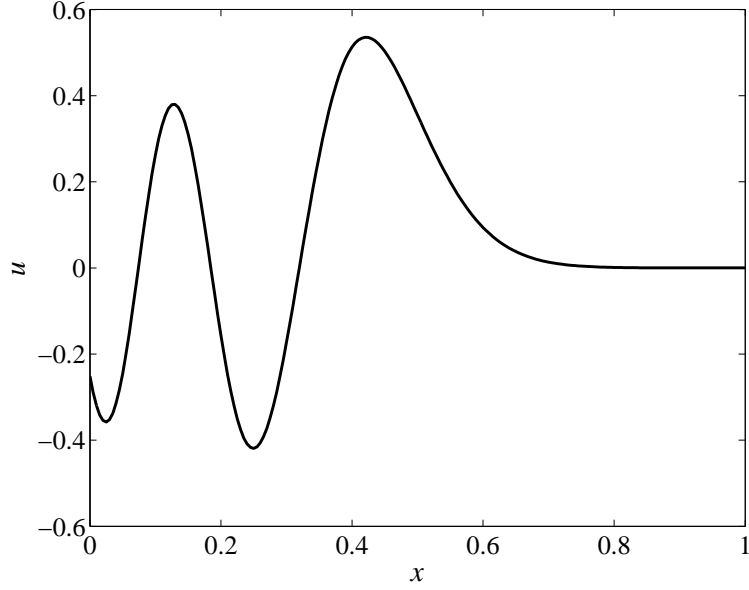
Figure 5-8: Exact solution of the Airy-type equation for $\alpha = 21\pi/2$.

in the domain $0 \leq x \leq 1$ whose exact solution is described by the Airy function:
$u = \text{Ai}\left[(\alpha/2)^{2/3}(2x-1)\right]$. Here the coefficient $\alpha$ is fixed at $21\pi/2$ (the same value as
in Reference [81]), and the corresponding boundary conditions are given by $u'(0) = -8.3239$ and $u'(1) = -9.8696\times10^{-5}$. Figure 5-8 shows the profile of the corresponding
exact solution. The fundamental frequency, numbers of the envelope position and
Fourier mode are $\nu = 2.0$, $N_x = 9$ for the linear, quadratic cases, $N_x = 5$ for the
Hermitian case, and $N_F = 5$.

Figure 5-9 gives the numerical error for the three different wave-packet approaches.
As before, the errors obtained using the higher-order wave-packet interpolations are
much smaller than the error obtained using the linear interpolation. Also, it is ob-
served that the higher-order finite element wave-packet methods are comparable in
accuracy with the Gabor element method developed by Pletzer et al. [81]. Figure
5-10 shows the comparison of the numerical error between the present wave-packet
method and the conventional finite element method (with $N_x = 25$), both of which
utilize the Hermitian interpolation functions. Again, it is observed that the numerical
result using the Hermitian wave-packet method is much more accurate; note that the
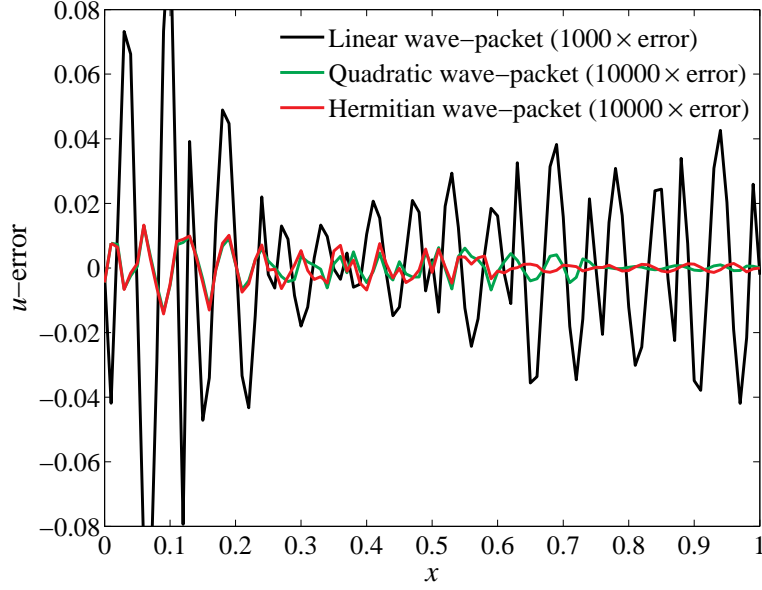
Figure 5-9: Comparison of the numerical error for the Airy-type equation among the three different wave-packet methods.

error-scale differs by two orders of magnitude.

## 5.4.3 Wasow Equation

Lastly, we consider the numerical solution of the Wasow equation, which models the mode conversion effects of RF waves in plasmas. The equation considered here is given by

$$\left\{\frac{d^2}{dx^2} + k^2 \left[1 - 0.5\left(x - 0.5\right)\right]\right\} \left\{\frac{d^2}{dx^2} + k^2 \left[1 - 160\left(x - 0.5\right)\right]\right\} u + \alpha u = 0 \quad (5.30)$$

in the domain $0 \le x \le 1$ where $k^2 = 2 \times 10^3$ and $\alpha = 8 \times 10^6$ subject to the boundary condition $u\left(0\right) = 0$, $u\left(1\right) = 1$ and $u'\left(0\right) = u'\left(1\right) = 0$ (the same boundary condition as in Reference [81]). Equation (5.30) implies the formation of multiscale waves with different wavenumbers by a factor of 320. Here a comparison is made between the finite element wave-packet method and the conventional finite element method, both utilizing the Hermitian interpolation functions which can be straightforwardly applied

162

Figure 5-10: Comparison of the numerical error for the Airy-type equation between the finite element wave-packet method and the conventional finite element method.

to this fourth-order equation. As for numerical parameters, we choose $\nu = 10.5$, $N_x = 10$, and $N_{\mathrm{F}} = 11$, and compare the results with a conventional finite element calculation.

Since an analytical solution to this problem is not available, we first calculate the problem with a very fine mesh using the conventional finite element method that employs the Hermitian interpolation functions, and utilize the obtained result as a "quasi-exact" solution. Figure 5-11 shows the numerical solution obtained with 1000 grid elements. We see that the fast and slow waves are coupled on the left half of the domain (see Figure 5-11b), while only the SW having a shorter wavelength is evanescent on the right half. This is also confirmed in Equation (5.30); although the sign of $r_1 = k^2 \left[1 - 0.5 \left(x - 0.5\right)\right]$ is always positive in the entire domain, the sign of $r_2 = k^2 \left[1 - 160 \left(x - 0.5\right)\right]$ changes from positive to negative at $x = 0.5$. The former corresponds to propagation of the FW at every point, whereas the latter corresponds to evanescence of the SW on the right half of the domain. The mixing of these very different waves makes it more difficult to accurately solve the Wasow equation

163
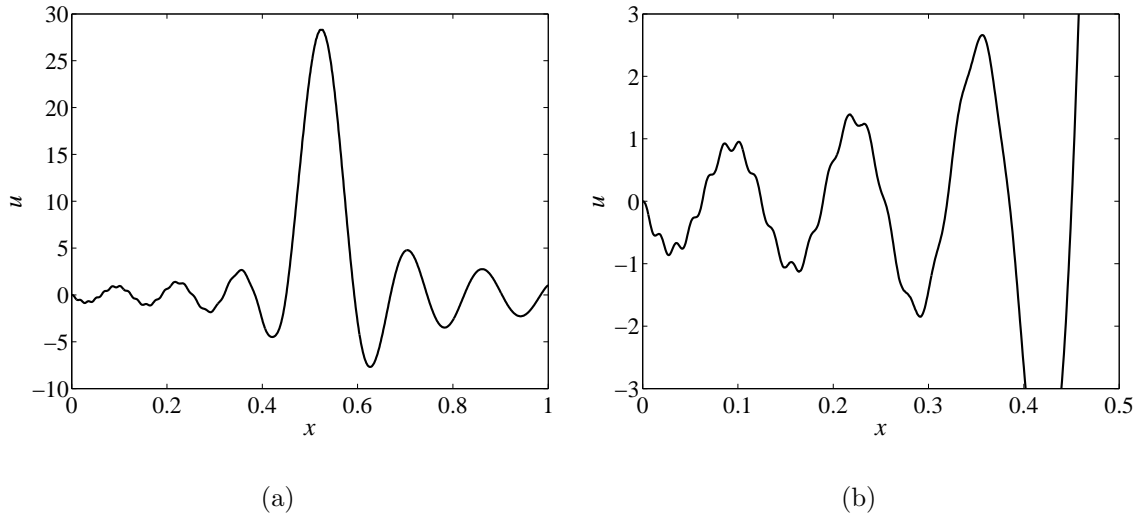
Figure 5-11: Numerical solution of the Wasow equation: (a) macroscopic oscillation; and (b) fine-scale oscillation.

compared to the equations in the previous problems.

A comparison of the numerical error ($\hat{u} - u_{\text{quasi-exact}}$) between the finite element wave-packet method and the conventional finite element method is shown in Figure 5-12. Again, the present wave-packet approach gives a more accurate numerical result compared to the conventional finite element solution.

## 5.5 Conclusions

In this chapter a finite element wave-packet method was presented for the analysis of waves through media, and some illustrative problems were solved. The method is in particular directed to solve waves in plasmas accurately with reasonable computational cost. The key idea is to enrich the usual finite element interpolations with wave packets. We see that this approach results into some favorable features drawing from both, conventional finite element and spectral methods. First, the interpolation functions are locally defined in the same way as in the conventional finite element method, which is effective for programming. Second, this local definition
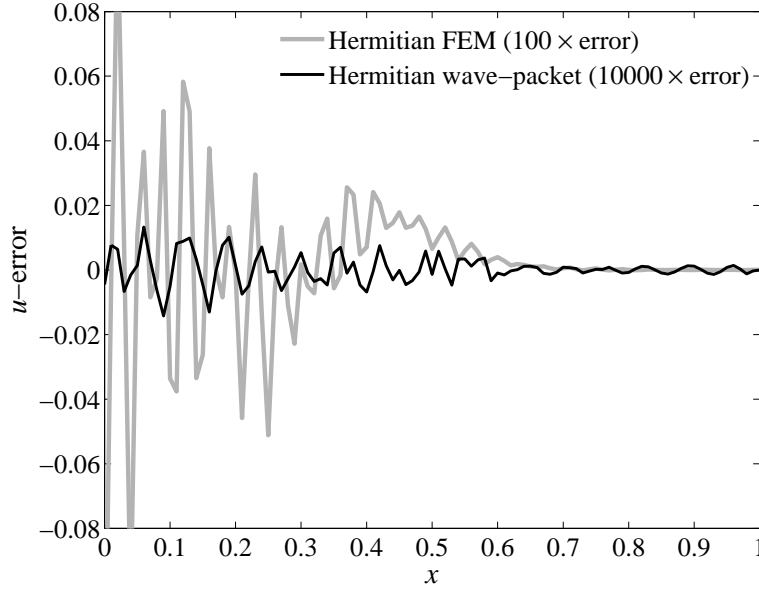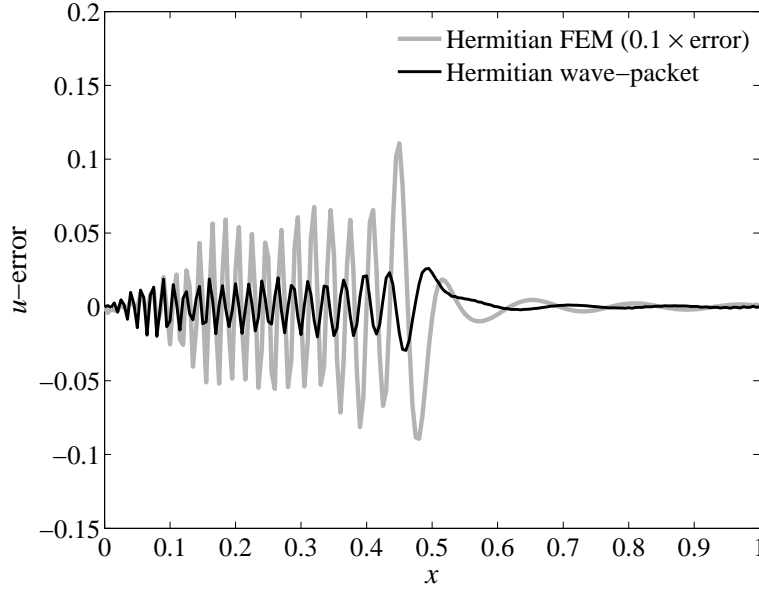
Figure 5-12: Comparison of the numerical error for the Wasow equation between the finite element wave-packet method and the conventional finite element method.

results in the formation of a sparse global matrix. Third, all the integrals in the discretized equation are analytically solved, yielding simple expressions (of course, numerical integration could be used and probably has to be used for wave equations of higher dimensions). Fourth, the boundary conditions are easily incorporated into the discretized equation. In fact, the Dirichlet and Neumann boundary conditions are treated in a similar way as in the conventional finite element method. Fifth, using the wave packets can give more accurate results than using the corresponding conventional finite element methods under the same computational costs.

Plasma wave equations can be far more complex than the 1D equations solved here, but the 1D equations/solutions exhibit some of the fundamental characteristics of these more complex waves. In further research the method should be applied to and tested in two- and three-dimensional solutions with nonuniform meshes. Also, a mathematical convergence analysis should be pursued to identify the rate and order of convergence, and the optimal value of fundamental frequency.

# Chapter 6

# Conclusions and Future Work

## 6.1 Conclusions

This thesis has presented two main numerical schemes and revealed various 2D properties caused by self-consistent RF sheath-plasma interactions in the ICRF. Regarding the new numerical schemes, first, the numerical code that solves self-consistent RF sheath-plasma interactions in the SOL for ICRF heating was developed for the first time based on the nonlinear finite element method, and named "rfSOL." Second, the finite element wave-packet method was developed for the purpose of solving for multiscale plasma waves in the tokamak poloidal plane accurately with reasonable computational cost. The validity of the rfSOL code was confirmed through comparisons with an analytical solution in the 1D closed domain and the results of the local dispersion relation in Chapter 3. Also, it was demonstrated using three test examples that the finite element wave-packet method yields much more accurate results compared to the conventional finite element method in Chapter 5.

The present numerical results that contribute to the efforts on the RF sheath-plasma interaction problems are summarized as follows. In the 1D analysis with constant plasma density a similar variation pattern of the rectified sheath potential to the results shown in References [34, 35] was obtained, which supports the validity

of the analytical models proposed by Myra and D'Ippolito. It was also confirmed that the sheath boundary condition reduces to the quasi-insulating boundary condition, in which the normal electric displacement normalized by the surface current value vanishes, in the limit where the sheath width goes to infinity. Further, in the numerical analysis employing a varying plasma density profile, multiple roots were found in the process of increasing the antenna current. With the help of graphical solution, it was confirmed that the presence of the multiple roots is attributed to a combination of box resonance effects of the confined propagating slow wave together with nonlinearity of the sheath boundary condition. It was clarified by introducing dissipation into the problem that the root jumping mechanism can involve hysteresis.

In a 2D slab geometry sheath-plasma waves were identified for the first time by means of numerical simulation, and their characteristics were investigated through the electrostatic 2D sheath mode analysis. An important consequence is that the sheath-plasma wave only appears if the plasma density is greater than the lower hybrid density. It was found that the wavelength of the sheath-plasma wave depends mainly on the plasma density, magnitude of the poloidal component of the background magnetic field, and electron temperature when the contact angle between the magnetic field line and the wall is not too small. In addition, it was revealed for a varying background magnetic field that the decay length of the sheath-plasma wave into the plasma becomes shorter with a decrease of its wavelength.

For the plasma density lower than that at the lower hybrid resonance, it was demonstrated in the 2D slab geometry that propagating slow waves yield large sheath potential values, which can reach the order of kV for parameters similar to those of Alcator C-Mod. A similar trend to the analysis in the 1D domain was observed in the variation of the normalized normal electric displacement, which assures the validity of the quasi-insulating limit. An analytical investigation with a simplified condition showed that the phase shift can be the cause for the variation of the electric field distribution pattern along the magnetic field lines.

In the numerical analysis corresponding to an Alcator C-Mod scale device, it was discovered that the key parameters which determine the magnitude of the RF sheath potential are the parallel electric field strength, contact angle between the magnetic field line and the sheath, electron density, and electron temperature. Furthermore, it was demonstrated that the sheath potential in the close vicinity of the antenna can be insensitive to the direction of the background magnetic field in the RF sheath dominated regime for constant plasma density and straight magnetic field lines, if the contact angle between the magnetic field line and the sheath is sufficiently large. This is a significant consequence that could help elucidate the effect of the rotated antenna, which will be examined in the Alcator C-Mod experiments soon.

As a matter of course, a more refined treatment of the geometry of the magnetic field, SOL, and wall together with accurate plasma density and temperature profiles will be required for an accurate prediction. Nevertheless, the simulation code (rfSOL) that was developed in this thesis work is extensible with modifications to arbitrary vessel geometry and magnetic field configurations (see next section), and eventually it should be possible using this code to make an accurate quantitative prediction for the RF sheath potential at specific locations on the wall structure in existing tokamaks as well as in a reactor scale device such as ITER.

## 6.2 Future Work on the rfSOL Code

### 6.2.1 Developmental Direction

The road map for establishing a practically useful numerical code that possesses an accurate predictive capability for a realistic tokamak geometry is shown in Figure 6-1. As Chapter 4 has shown, the present rfSOL code solves various problems in step 1 at a satisfactory level, and if a certain condition is met (which will be clarified in the next subsection), the code can also solve some problems in step 2. The ultimate goal is to combine the rfSOL code to the core-plasma solver (or it might be more
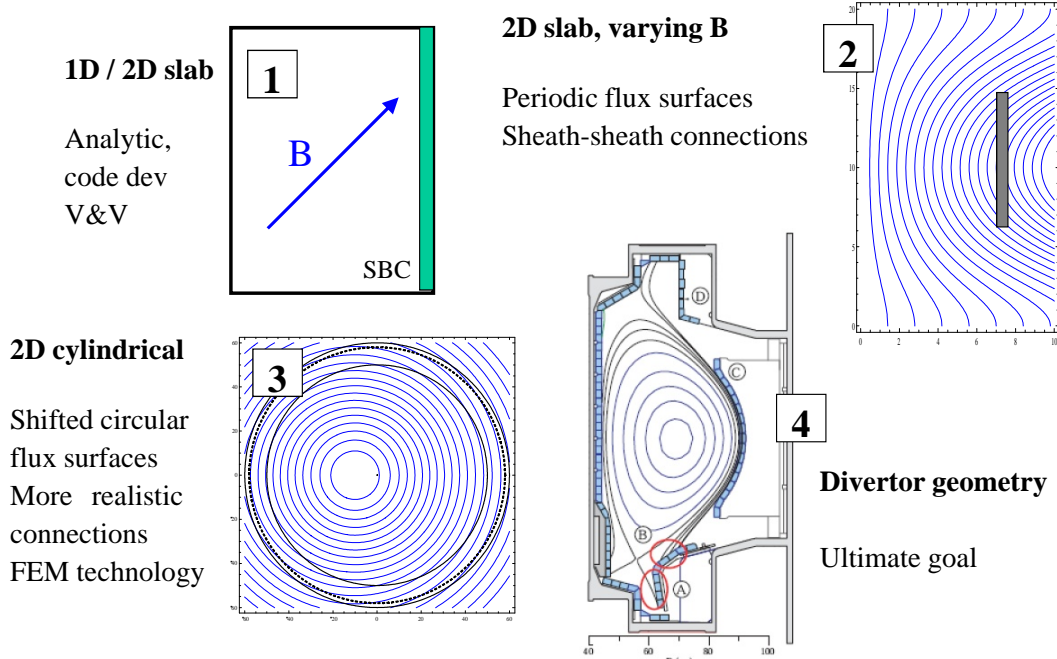
Figure 6-1: Progression of the rfSOL models towards realism (courtesy of J.R. Myra).

straightforward to replace the cold plasma equation with the hot plasma equation in the present approach) and solve the problem in a realistic divertor geometry (see the diagram in step 4). It is not a difficult issue to generalize the scheme so as to apply the rfSOL code to a curved geometry as shown in the diagram in step 3 when we employ the formulation presented in Section 3.2.4. However, even for a simple 2D slab geometry considered in this thesis, there still remain several things that need to be improved.

First, in order to take into account the sheath power dissipation, it would be important to introduce a small imaginary part into the scalar dielectric constant in the sheath. According to the analytical model given in [33], this imaginary part is inversely proportional to the instantaneous sheath voltage $V_{\mathrm{sh}}$, so that its effect may be less important if the sheath potential reaches the order of kV. However, if $V_{\mathrm{sh}}$ is relatively small (but much larger than the thermal sheath potential), the resistive part of the sheath dielectric would become more significant and enhance nonlinearity

in the sheath boundary condition.

Second, more importantly, there is a singularity in the sheath boundary condition. This singularity cannot be avoided when considering the real tokamak geometry problem with varying background magnetic fields, and thus must be settled in an appropriate way. The details are described in the next subsection.

## 6.2.2   Singularity Problem

According to the result shown in Figure 4-20, the wavenumber component tangential to the sheath surface rapidly increases to infinity when the magnetic field line approaches parallel to the wall (or when $\boldsymbol{b} \cdot \boldsymbol{s} = b_{\mathrm{n}} \to 0$, where $\boldsymbol{b}$ and $\boldsymbol{s}$ are the unit vectors along the background magnetic field and perpendicular to the sheath surface, respectively). This behavior is similar to the lower hybrid resonance; therefore if this singular point is included in the calculation domain, unwanted numerical oscillation is triggered from that point no matter how fine the grids are. On the other hand, the tangential electric field component should vanish when $b_{\mathrm{n}} \to 0$, since in that case most of the electrons do not escape to the wall, and thus, the ion-rich sheath is not formed (recall that the sheath boundary condition reduces to the conducting-wall boundary condition for $\Delta_{\mathrm{sh}} \to 0$). However, this does not help to avoid the difficulty mentioned above since the tangential electric field component is not exactly zero in the close vicinity of the singular point. Of course, if the calculation domain does not include the point where $b_{\mathrm{n}} = 0$ on the sheath, an accurate and converged numerical result can be obtained as shown in Figure 4-24 (see also Equation (4.9)).

In order to tackle this singularity problem, the following two methods have been proposed: (1) add the diffusion term in the sheath boundary condition, and/or (2) add the imaginary part (dissipation) in the dielectric tensor components. Both approaches are successful "mathematically" (i.e., the unstable numerical oscillation disappears) if large artificial coefficients are used for them. However, it turns out that important physics on the sheath surface, such as sheath-plasma waves, can also be damped out

due to these artificial parameters. Further, it is not clear if a good-looking numerical result, which is finally obtained by manipulating the artificial coefficients by try and error, is physically correct.

Another approach would be to modify the sheath boundary condition so as to lessen the tangential wavenumber component in the vicinity of the singular points to the extent where the sheath-plasma wave can be resolved with a given grid resolution. A simple way, which appears to be effective, is to switch the boundary condition to $\boldsymbol{E}_\mathrm{t} = \boldsymbol{0}$ for $k_\mathrm{t} \geq k_\mathrm{crit}$, where $k_\mathrm{crit}$ is a critical value below which the sheath boundary condition is accurately discretized by given grids. However, this approach causes a discontinuity in the gradient of $\boldsymbol{E}_\mathrm{t}$, which makes the numerical simulation unstable.

A promising remedy is to replace the discretization method for the sheath boundary condition with a 1D spectral approach. At least, this will prevent unwanted grid-scale oscillations. Although the global matrix size will be expanded with the number of harmonics, this approach is worth pursuing to proceed towards the ultimate goal of the rfSOL code development.

## 6.3 Future Work on the Wave-Packet Approach

As briefly described in Section 5.5, the most important next step is to establish the method that gives the optimal value of the fundamental frequency. This value is seemingly related to the solution of the characteristic equation corresponding to the differential equation considered, but it is not that simple since it is confirmed that the optimal value also depends on the grid resolution. Once a successful method is devised, it would be straightforward to extend the finite element wave-packet procedure to 2D applications; for example, the approach used in Reference [82] would be effective.

# Appendix A

# Calculations of the Integrals in Finite Element Discretization

## A.1 Integrals in Maxwell's Equation

The integrals appeared in the discretized Maxwell's equation can be analytically calculated by applying the element average techniques to the Jacobian and the components of the cofactor matrix. In a nine-node element shown in Figure 3-1, the coordinate $\boldsymbol{x}$ is expressed as

$$\boldsymbol{x} = N_\alpha^{(1)} \boldsymbol{x}_\alpha \tag{A.1}$$

where $N_\alpha^{(1)}$ is the local bilinear interpolation functions defined as

$$N_\alpha^{(1)}(\xi, \eta) = \frac{1}{4}(1 + \xi_\alpha \xi)(1 + \eta_\alpha \eta) \tag{A.2}$$

Here the summation convention applies to the subscript $\alpha$, which denotes the local node number at the apexes of an element (i.e., $\alpha = 1, \ldots, 4$). Using the expression

(A.1), the Jacobian $J$ is approximately calculated in the 2D space as follows:

$$J = \begin{vmatrix} \frac{\partial x}{\partial \xi} & \frac{\partial y}{\partial \xi} \\ \frac{\partial x}{\partial \eta} & \frac{\partial y}{\partial \eta} \end{vmatrix} = \begin{vmatrix} \frac{\partial N_\alpha^{(1)}}{\partial \xi} x_\alpha & \frac{\partial N_\beta^{(1)}}{\partial \xi} y_\beta \\ \frac{\partial N_\alpha^{(1)}}{\partial \eta} x_\alpha & \frac{\partial N_\beta^{(1)}}{\partial \eta} y_\beta \end{vmatrix}$$

$$= \frac{1}{16} \begin{vmatrix} x_\alpha \xi_\alpha (1 + \eta_\alpha \eta) & y_\beta \xi_\beta (1 + \eta_\beta \eta) \\ x_\alpha \eta_\alpha (1 + \xi_\alpha \xi) & y_\beta \eta_\beta (1 + \xi_\beta \xi) \end{vmatrix} \tag{A.3}$$

$$\simeq \frac{1}{16} \begin{vmatrix} x_\alpha \xi_\alpha & y_\beta \xi_\beta \\ x_\alpha \eta_\alpha & y_\beta \eta_\beta \end{vmatrix} \equiv J_{\mathrm{e}}$$

where the subscript $\beta$ denotes the local node number (same as for the subscript $\alpha$). This procedure corresponds to the central point approximation; the value of the Jacobian in a grid element is evaluated at $\xi = \eta = 0$. Similarly, the components of the cofactor matrix, $A_{ij}$ $(i, j = 1, 2)$, are evaluated as follows:

$$\begin{pmatrix} \frac{\partial \xi}{\partial x} & \frac{\partial \eta}{\partial x} \\ \frac{\partial \xi}{\partial y} & \frac{\partial \eta}{\partial y} \end{pmatrix} = \frac{1}{J} \begin{pmatrix} \frac{\partial y}{\partial \eta} & -\frac{\partial y}{\partial \xi} \\ -\frac{\partial x}{\partial \eta} & \frac{\partial x}{\partial \xi} \end{pmatrix} \simeq \frac{1}{J} \begin{pmatrix} (A_{11})_0 & (A_{12})_0 \\ (A_{21})_0 & (A_{22})_0 \end{pmatrix} \tag{A.4}$$

where

$$\begin{aligned} (A_{11})_0 &= \frac{1}{4} \eta_\alpha y_\alpha, & (A_{12})_0 &= -\frac{1}{4} \xi_\alpha y_\alpha \\ (A_{21})_0 &= -\frac{1}{4} \eta_\alpha x_\alpha, & (A_{22})_0 &= \frac{1}{4} \xi_\alpha x_\alpha \end{aligned} \tag{A.5}$$

It is then straightforward to calculate the integrals in Equations (3.14)-(3.16) analytically. Due to the characteristics of the finite element interpolation functions, calculations can be conducted over an element $\Omega_{\mathrm{e}}$ using the local shape functions $N_\alpha$, $N_\beta$, and $N_\gamma$ (see Equation (3.6)). The results are shown below:

$$\int_{\Omega_{\mathrm{e}}} N_\alpha N_\beta d\Omega = J_{\mathrm{e}} [NN]_\xi [NN]_\eta$$

$$\int_{\Omega_e} \frac{\partial N_\alpha}{\partial x} N_\beta d\Omega = (A_{11})_0 \left[N'N\right]_\xi \left[NN\right]_\eta + (A_{12})_0 \left[NN\right]_\xi \left[N'N\right]_\eta$$

$$\int_{\Omega_e} N_\alpha \frac{\partial N_\beta}{\partial x} d\Omega = (A_{11})_0 \left[NN'\right]_\xi \left[NN\right]_\eta + (A_{12})_0 \left[NN\right]_\xi \left[NN'\right]_\eta$$

$$\int_{\Omega_e} \frac{\partial N_\alpha}{\partial y} N_\beta d\Omega = (A_{21})_0 \left[N'N\right]_\xi \left[NN\right]_\eta + (A_{22})_0 \left[NN\right]_\xi \left[N'N\right]_\eta$$

$$\int_{\Omega_e} N_\alpha \frac{\partial N_\beta}{\partial y} d\Omega = (A_{21})_0 \left[NN'\right]_\xi \left[NN\right]_\eta + (A_{22})_0 \left[NN\right]_\xi \left[NN'\right]_\eta$$

$$\int_{\Omega_e} \frac{\partial N_\alpha}{\partial x} \frac{\partial N_\beta}{\partial x} d\Omega = \frac{1}{J_e} \Big[ (A_{11})_0^2 \left[N'N'\right]_\xi \left[NN\right]_\eta + (A_{12})_0^2 \left[NN\right]_\xi \left[N'N'\right]_\eta$$
$$+ (A_{11})_0 (A_{12})_0 \left( \left[N'N\right]_\xi \left[NN'\right]_\eta + \left[NN'\right]_\xi \left[N'N\right]_\eta \right) \Big]$$

$$\int_{\Omega_e} \frac{\partial N_\alpha}{\partial y} \frac{\partial N_\beta}{\partial x} d\Omega = \frac{1}{J_e} \Big( (A_{11})_0 (A_{21})_0 \left[N'N'\right]_\xi \left[NN\right]_\eta + (A_{12})_0 (A_{22})_0 \left[NN\right]_\xi \left[N'N'\right]_\eta$$
$$+ (A_{12})_0 (A_{21})_0 \left[N'N\right]_\xi \left[NN'\right]_\eta + (A_{11})_0 (A_{22})_0 \left[NN'\right]_\xi \left[N'N\right]_\eta \Big)$$

$$\int_{\Omega_e} \frac{\partial N_\alpha}{\partial x} \frac{\partial N_\beta}{\partial y} d\Omega = \frac{1}{J_e} \Big( (A_{11})_0 (A_{21})_0 \left[N'N'\right]_\xi \left[NN\right]_\eta + (A_{12})_0 (A_{22})_0 \left[NN\right]_\xi \left[N'N'\right]_\eta$$
$$+ (A_{11})_0 (A_{22})_0 \left[N'N\right]_\xi \left[NN'\right]_\eta + (A_{12})_0 (A_{21})_0 \left[NN'\right]_\xi \left[N'N\right]_\eta \Big)$$

$$\int_{\Omega_e} \frac{\partial N_\alpha}{\partial y} \frac{\partial N_\beta}{\partial y} d\Omega = \frac{1}{J_e} \Big[ (A_{21})_0^2 \left[N'N'\right]_\xi \left[NN\right]_\eta + (A_{22})_0^2 \left[NN\right]_\xi \left[N'N'\right]_\eta$$
$$+ (A_{21})_0 (A_{22})_0 \left( \left[N'N\right]_\xi \left[NN'\right]_\eta + \left[NN'\right]_\xi \left[N'N\right]_\eta \right) \Big]$$

$$\int_{\Omega_e} N_\alpha N_\beta N_\gamma d\Omega = J_e \left[NNN\right]_\xi \left[NNN\right]_\eta$$

where

$$[NN]_\xi = \frac{\xi_\alpha \xi_\beta}{6} + \frac{1}{30} \left( 32 - 28\xi_\alpha^2 - 28\xi_\beta^2 + 27\xi_\alpha^2 \xi_\beta^2 \right)$$

$$[NN]_\eta = \frac{\eta_\alpha \eta_\beta}{6} + \frac{1}{30} \left( 32 - 28\eta_\alpha^2 - 28\eta_\beta^2 + 27\eta_\alpha^2 \eta_\beta^2 \right)$$

$$[N'N]_\xi = \frac{2}{3} (\xi_\alpha - \xi_\beta) + \frac{\xi_\alpha \xi_\beta}{2} (2\xi_\alpha - \xi_\beta)$$

$$[NN']_\xi = \frac{2}{3}\left(\xi_\beta - \xi_\alpha\right) + \frac{\xi_\alpha\xi_\beta}{2}\left(2\xi_\beta - \xi_\alpha\right)$$

$$[N'N]_\eta = \frac{2}{3}\left(\eta_\alpha - \eta_\beta\right) + \frac{\eta_\alpha\eta_\beta}{2}\left(2\eta_\alpha - \eta_\beta\right)$$

$$[NN']_\eta = \frac{2}{3}\left(\eta_\beta - \eta_\alpha\right) + \frac{\eta_\alpha\eta_\beta}{2}\left(2\eta_\beta - \eta_\alpha\right)$$

$$[N'N']_\xi = \frac{\xi_\alpha\xi_\beta}{2} + \frac{2}{3}\left(2 - 3\xi_\alpha^2\right)\left(2 - 3\xi_\beta^2\right)$$

$$[N'N']_\eta = \frac{\eta_\alpha\eta_\beta}{2} + \frac{2}{3}\left(2 - 3\eta_\alpha^2\right)\left(2 - 3\eta_\beta^2\right)$$

$$
\begin{aligned}
[NNN]_\xi =& \frac{32}{35} + \frac{1}{15}\left(\xi_\alpha\xi_\beta + \xi_\beta\xi_\gamma + \xi_\gamma\xi_\alpha\right) - \frac{88}{105}\left(\xi_\alpha^2 + \xi_\beta^2 + \xi_\gamma^2\right) \\
&- \frac{1}{60}\left(\xi_\alpha^2\xi_\beta\xi_\gamma + \xi_\alpha\xi_\beta^2\xi_\gamma + \xi_\alpha\xi_\beta\xi_\gamma^2\right) \\
&+ \frac{83}{105}\left(\xi_\alpha^2\xi_\beta^2 + \xi_\beta^2\xi_\gamma^2 + \xi_\gamma^2\xi_\alpha^2\right) - \frac{103}{140}\xi_\alpha^2\xi_\beta^2\xi_\gamma^2
\end{aligned}
$$

$$
\begin{aligned}
[NNN]_\eta =& \frac{32}{35} + \frac{1}{15}\left(\eta_\alpha\eta_\beta + \eta_\beta\eta_\gamma + \eta_\gamma\eta_\alpha\right) - \frac{88}{105}\left(\eta_\alpha^2 + \eta_\beta^2 + \eta_\gamma^2\right) \\
&- \frac{1}{60}\left(\eta_\alpha^2\eta_\beta\eta_\gamma + \eta_\alpha\eta_\beta^2\eta_\gamma + \eta_\alpha\eta_\beta\eta_\gamma^2\right) \\
&+ \frac{83}{105}\left(\eta_\alpha^2\eta_\beta^2 + \eta_\beta^2\eta_\gamma^2 + \eta_\gamma^2\eta_\alpha^2\right) - \frac{103}{140}\eta_\alpha^2\eta_\beta^2\eta_\gamma^2
\end{aligned}
$$

The definitions of $\xi_\alpha$, $\xi_\beta$, and $\xi_\gamma$ are the same as that of $\xi_\alpha$ in Equation (3.6). In the same way, the values of $\eta_\alpha$, $\eta_\beta$, and $\eta_\gamma$ are followed by the definition of $\eta_\alpha$ in Equation (3.6).

## A.2  Integrals in the Sheath Boundary Condition

Unlike the integrals in the discretized Maxwell's equation, the integrals in the discretized sheath boundary condition can be analytically calculated without approximation (i.e., without a one-point integration). However, the calculations are largely simplified when the element average is applied to the derivatives of $\Delta_{\mathrm{sh}}\kappa$ as shown in

Equation (3.27). Here the values of $\langle \Delta_{\text{sh}} \rangle_{\text{e}}$ and $\langle d\Delta_{\text{sh}}/dy \rangle_{\text{e}}$ are calculated as follows:

$$\langle \Delta_{\text{sh}} \rangle_{\text{e}} \equiv \frac{1}{\Gamma_{\text{e}}^{\text{S}}} \int_{\Gamma_{\text{e}}^{\text{S}}} \Delta_{\text{sh}} d\Gamma^{\text{S}} = \left( \frac{1}{\Gamma_{\text{e}}^{\text{S}}} \int_{\Gamma_{\text{e}}^{\text{S}}} N_{\alpha}^{\text{S}} d\Gamma^{\text{S}} \right) (\Delta_{\text{sh}})_{\alpha} = A_{\alpha} (\Delta_{\text{sh}})_{\alpha} \tag{A.6}$$

$$\left\langle \frac{d\Delta_{\text{sh}}}{dy} \right\rangle_{\text{e}} \equiv \frac{1}{\Gamma_{\text{e}}^{\text{S}}} \int_{\Gamma_{\text{e}}^{\text{S}}} \frac{d\Delta_{\text{sh}}}{dy} d\Gamma^{\text{S}} = \left( \frac{1}{\Gamma_{\text{e}}^{\text{S}}} \int_{\Gamma_{\text{e}}^{\text{S}}} \frac{dN_{\alpha}^{\text{S}}}{dy} d\Gamma^{\text{S}} \right) (\Delta_{\text{sh}})_{\alpha} = B_{\alpha} (\Delta_{\text{sh}})_{\alpha} \tag{A.7}$$

where $N_{\alpha}^{\text{S}}$ is the local quadratic functions defined in a three-node element. The coefficients $A_{\alpha}$ and $B_{\alpha}$ are given by

$$A_{\alpha} = \frac{1}{2} \left( \frac{4}{3} - \xi_{\alpha}^2 \right) \to A_1 = \frac{1}{6}, \quad A_2 = \frac{1}{6}, \quad A_3 = \frac{2}{3} \tag{A.8}$$

$$B_{\alpha} = \frac{\xi_{\alpha}}{\Gamma_{\text{e}}^{\text{S}}} \to B_1 = -\frac{1}{\Gamma_{\text{e}}^{\text{S}}}, \quad B_2 = \frac{1}{\Gamma_{\text{e}}^{\text{S}}}, \quad B_3 = 0 \tag{A.9}$$

As a consequence of this approximation, one is only required to calculate the integrals shown in Equation (3.32), whose calculations can be conducted over an element $\Gamma_{\text{e}}^{\text{S}}$ using the local shape functions $N_{\alpha}^{\text{S}}$, $N_{\beta}^{\text{S}}$, and $N_{\gamma}^{\text{S}}$ (see Equation (3.19)). The results are as follows:

$$\int_{\Gamma_{\text{e}}^{\text{S}}} N_{\alpha}^{\text{S}} N_{\beta}^{\text{S}} d\Gamma^{\text{S}} = J_{\text{e}} [NN]_{\xi}$$

$$\int_{\Gamma_{\text{e}}^{\text{S}}} N_{\alpha}^{\text{S}} N_{\beta}^{\text{S}} N_{\gamma}^{\text{S}} d\Gamma^{\text{S}} = J_{\text{e}} [NNN]_{\xi}$$

$$\int_{\Gamma_{\text{e}}^{\text{S}}} N_{\alpha}^{\text{S}} \frac{dN_{\beta}^{\text{S}}}{dy} N_{\gamma}^{\text{S}} d\Gamma^{\text{S}} = \frac{4}{15} \left( -\xi_{\alpha} + 2\xi_{\beta} - \xi_{\gamma} \right) + \frac{1}{12} \xi_{\alpha} \xi_{\beta} \xi_{\gamma}$$

$$+ \frac{1}{15} \left( -7\xi_{\alpha}^2 \xi_{\beta} + 6\xi_{\alpha}\xi_{\beta}^2 + 6\xi_{\beta}^2\xi_{\gamma} - 7\xi_{\beta}\xi_{\gamma}^2 + \xi_{\gamma}^2\xi_{\alpha} + \xi_{\gamma}\xi_{\alpha}^2 \right)$$

$$+ \frac{1}{20} \left( -2\xi_{\alpha}^2 \xi_{\beta}^2 \xi_{\gamma} - 2\xi_{\alpha}\xi_{\beta}^2\xi_{\gamma}^2 + 9\xi_{\alpha}^2\xi_{\beta}\xi_{\gamma}^2 \right)$$

$$\int_{\Gamma_e^{S}} N_\alpha^{S} N_\beta^{S} \frac{dN_\gamma^{S}}{dy} d\Gamma^{S} = \frac{4}{15} \left( -\xi_\alpha - \xi_\beta + 2\xi_\gamma \right) + \frac{1}{12} \xi_\alpha \xi_\beta \xi_\gamma$$

$$+ \frac{1}{15} \left( \xi_\alpha^2 \xi_\beta + \xi_\alpha \xi_\beta^2 - 7\xi_\beta^2 \xi_\gamma + 6\xi_\beta \xi_\gamma^2 + 6\xi_\gamma^2 \xi_\alpha - 7\xi_\gamma \xi_\alpha^2 \right)$$

$$+ \frac{1}{20} \left( 9\xi_\alpha^2 \xi_\beta^2 \xi_\gamma - 2\xi_\alpha \xi_\beta^2 \xi_\gamma^2 - 2\xi_\alpha^2 \xi_\beta \xi_\gamma^2 \right)$$

The definitions of $\xi_\alpha$, $\xi_\beta$, and $\xi_\gamma$ are the same as that of $\xi_\alpha$ in Equation (3.19). Here, $J_e = \Gamma_e^{S}/2$.

# Appendix B

# Derivative Expressions of the Discretized Boundary Condition

The global matrix $\boldsymbol{K}^{(n)}$ appeared in the Newton-Raphson iteration algorithm consists of the derivative of the discretized entire vector $\boldsymbol{f}$ with respect to the solution $\hat{\boldsymbol{E}}$ and can be explicitly obtained using the discretized governing equations derived in Section 3.2. In this appendix a procedure to obtain the derivative expressions of the discretized sheath boundary condition is partly demonstrated. Although the calculations are straightforward, they will clarify the effectiveness of the element-average technique that is applied to the sheath width since this method largely simplifies the derivation of the derivative expressions. The derivatives of the discretized Maxwell's equation are easily obtained from Equations (3.14)–(3.16) and are thus omitted here.

For simplicity, let us consider the case where the sheath boundary condition is imposed on a flat wall lying in the $y$-$z$ plane. In Section 3.2.3 we derived the discretized sheath boundary condition on the left wall, which is repeated here for convenience.

$$G_{yi} = \sum_m G_{yi}\big|_{\mathrm{e}(m)} = \sum_m \left( \left[ N_i^{\mathrm{S}} N_j^{\mathrm{S}} \right] \hat{E}_{yj}^{\mathrm{S}} - \mathcal{S}_{ijk}^{y\mathrm{L}} \kappa_{jk} \right)\Big|_{\mathrm{e}(m)} = 0 \tag{B.1}$$

$$G_{zi} = \sum_m G_{zi}|_{\mathrm{e}(m)} = \sum_m \left( \left[ N_i^{\mathrm{S}} N_j^{\mathrm{S}} \right] \hat{E}_{zj}^{\mathrm{S}} - i\mathcal{S}_{ijk}^{z\mathrm{L}} \kappa_{jk} \right)\Big|_{\mathrm{e}(m)} = 0 \tag{B.2}$$

where

$$\begin{aligned}
\mathcal{S}_{ijk}^{y\mathrm{L}} &= \mathcal{T}_{ijkl}^{y\mathrm{L}} (\Delta_{\mathrm{sh}})_l, \quad \mathcal{S}_{ijk}^{z\mathrm{L}} = \mathcal{T}_{ijkl}^{z\mathrm{L}} (\Delta_{\mathrm{sh}})_l \\
\mathcal{T}_{ijkl}^{y\mathrm{L}} &= A_l^{\mathrm{e}(m)} \left[ N_i^{\mathrm{S}} \tilde{N}_j^{\mathrm{S}} \tilde{N}_k^{\mathrm{S}} \right] + B_l^{\mathrm{e}(m)} \left[ N_i^{\mathrm{S}} N_j^{\mathrm{S}} N_k^{\mathrm{S}} \right] \\
\mathcal{T}_{ijkl}^{z\mathrm{L}} &= k_z A_l^{\mathrm{e}(m)} \left[ N_i^{\mathrm{S}} N_j^{\mathrm{S}} N_k^{\mathrm{S}} \right] \\
\kappa_{jk} &= \varepsilon_{xxk}^{\mathrm{S}} \hat{E}_{xj}^{\mathrm{S}} + \varepsilon_{xyk}^{\mathrm{S}} \hat{E}_{yj}^{\mathrm{S}} + \varepsilon_{xzk}^{\mathrm{S}} \hat{E}_{zj}^{\mathrm{S}}
\end{aligned} \tag{B.3}$$

Here, note that the element-averaged sheath width and its derivative are expressed as

$$\begin{aligned}
\langle \Delta_{\mathrm{sh}} \rangle_{\mathrm{e}(m)} &= A_l^{\mathrm{e}(m)} (\Delta_{\mathrm{sh}})_l \\
\left\langle \frac{d\Delta_{\mathrm{sh}}}{dy} \right\rangle_{\mathrm{e}(m)} &= B_l^{\mathrm{e}(m)} (\Delta_{\mathrm{sh}})_l
\end{aligned} \tag{B.4}$$

where the subscript $l$ denotes the global node number. The coefficients $A_l^{\mathrm{e}(m)}$ and $B_l^{\mathrm{e}(m)}$ are defined such that they possess specific values given by Equations (A.8) and (A.9) at the grid nodes constituting the element e($m$). The expression of $G_{yi}|_{\mathrm{e}(m)}$ in Equation (B.1) is easily divided into real and imaginary parts as follows:

$$\begin{aligned}
G_{yi}^{(\mathrm{R})}\Big|_{\mathrm{e}(m)} &= \left[ N_i^{\mathrm{S}} N_j^{\mathrm{S}} \right] \hat{E}_{yj}^{\mathrm{S}(\mathrm{R})} - \mathcal{S}_{ijk}^{y\mathrm{L}} \kappa_{jk}^{(\mathrm{R})} \\
G_{yi}^{(\mathrm{I})}\Big|_{\mathrm{e}(m)} &= \left[ N_i^{\mathrm{S}} N_j^{\mathrm{S}} \right] \hat{E}_{yj}^{\mathrm{S}(\mathrm{I})} - \mathcal{S}_{ijk}^{y\mathrm{L}} \kappa_{jk}^{(\mathrm{I})}
\end{aligned} \tag{B.5}$$

where the superscripts R and I denote the real and imaginary parts of the quantity, respectively. Notice that $\mathcal{S}_{ijk}^{y\mathrm{L}}$ and $\mathcal{S}_{ijk}^{z\mathrm{L}}$ are real values. Recalling that the sheath width is expressed as

$$(\Delta_{\mathrm{sh}})_l = \left( \alpha_{\mathrm{sh}} |\kappa|^3 + \beta_{\mathrm{sh}} \right)_l \tag{B.6}$$

where

$$\alpha_{\text{sh}} = \left(\frac{eC_{\text{sh}}}{T_{\text{e}}}\right)^3 \lambda_{\text{De}}^4, \quad \beta_{\text{sh}} = C_{\text{th}}\lambda_{\text{De}} \tag{B.7}$$

the derivative expression of $G_{yi}^{(\text{R})}\Big|_{\text{e}(m)}$ with respect to $\hat{E}_{xn}^{\text{S(R)}}$ (where the subscript $n$ denotes the global node number) is given by

$$\frac{\partial G_{yi}^{(\text{R})}}{\partial \hat{E}_{xn}^{\text{S(R)}}}\Bigg|_{\text{e}(m)} = -\frac{\partial \mathcal{S}_{ijk}^{y\text{L}}}{\partial \hat{E}_{xn}^{\text{S(R)}}}\kappa_{jk}^{(\text{R})} - \mathcal{S}_{ijk}^{y\text{L}}\frac{\partial \kappa_{jk}^{(\text{R})}}{\partial \hat{E}_{xn}^{\text{S(R)}}}$$

$$= -\mathcal{T}_{ijkn}^{y\text{L}}(\alpha_{\text{sh}})_n \frac{\partial |\kappa_n|^3}{\partial \hat{E}_{xn}^{\text{S(R)}}}\kappa_{jk}^{(\text{R})} - \mathcal{S}_{ink}^{y\text{L}}\varepsilon_{xxk}^{\text{S(R)}}$$

$$= -3\mathcal{T}_{ijkn}^{y\text{L}}\kappa_{jk}^{(\text{R})}(\alpha_{\text{sh}})_n |\kappa_n| \left(\kappa_n^{(\text{R})}\varepsilon_{xxn}^{\text{S(R)}} + \kappa_n^{(\text{I})}\varepsilon_{xxn}^{\text{S(I)}}\right) - \mathcal{S}_{ink}^{y\text{L}}\varepsilon_{xxk}^{\text{S(R)}}$$

Here, it is assumed that the node $n$ is included in the element $\text{e}(m)$. Note that the summation convention does not apply to the subscript $n$, and $\varepsilon_{xxk}^{\text{S}}$ has both real and imaginary parts due to the assumption that the electron mass is a complex-valued quantity (see Section 2.5). Similarly, the derivatives of $G_{yi}^{(\text{R})}\Big|_{\text{e}(m)}$ with respect to the other real and imaginary parts of the electric field components are calculated as follows:

$$\frac{\partial G_{yi}^{(\text{R})}}{\partial \hat{E}_{yn}^{\text{S(R)}}}\Bigg|_{\text{e}(m)} = \left[N_i^{\text{S}}N_n^{\text{S}}\right] - 3\mathcal{T}_{ijkn}^{y\text{L}}\kappa_{jk}^{(\text{R})}(\alpha_{\text{sh}})_n |\kappa_n| \left(\kappa_n^{(\text{R})}\varepsilon_{xyn}^{\text{S(R)}} + \kappa_n^{(\text{I})}\varepsilon_{xyn}^{\text{S(I)}}\right) - \mathcal{S}_{ink}^{y\text{L}}\varepsilon_{xyk}^{\text{S(R)}}$$

$$\frac{\partial G_{yi}^{(\text{R})}}{\partial \hat{E}_{zn}^{\text{S(R)}}}\Bigg|_{\text{e}(m)} = -3\mathcal{T}_{ijkn}^{y\text{L}}\kappa_{jk}^{(\text{R})}(\alpha_{\text{sh}})_n |\kappa_n| \left(\kappa_n^{(\text{R})}\varepsilon_{xzn}^{\text{S(R)}} + \kappa_n^{(\text{I})}\varepsilon_{xzn}^{\text{S(I)}}\right) - \mathcal{S}_{ink}^{y\text{L}}\varepsilon_{xzk}^{\text{S(R)}}$$

$$\frac{\partial G_{yi}^{(\text{R})}}{\partial \hat{E}_{xn}^{\text{S(I)}}}\Bigg|_{\text{e}(m)} = 3\mathcal{T}_{ijkn}^{y\text{L}}\kappa_{jk}^{(\text{R})}(\alpha_{\text{sh}})_n |\kappa_n| \left(\kappa_n^{(\text{R})}\varepsilon_{xxn}^{\text{S(I)}} - \kappa_n^{(\text{I})}\varepsilon_{xxn}^{\text{S(R)}}\right) + \mathcal{S}_{ink}^{y\text{L}}\varepsilon_{xxk}^{\text{S(I)}}$$

$$\frac{\partial G_{yi}^{(\text{R})}}{\partial \hat{E}_{yn}^{\text{S(I)}}}\Bigg|_{\text{e}(m)} = 3\mathcal{T}_{ijkn}^{y\text{L}}\kappa_{jk}^{(\text{R})}(\alpha_{\text{sh}})_n |\kappa_n| \left(\kappa_n^{(\text{R})}\varepsilon_{xyn}^{\text{S(I)}} - \kappa_n^{(\text{I})}\varepsilon_{xyn}^{\text{S(R)}}\right) + \mathcal{S}_{ink}^{y\text{L}}\varepsilon_{xyk}^{\text{S(I)}}$$

$$\left. \frac{\partial G_{yi}^{(\mathrm{R})}}{\partial \hat{E}_{zn}^{\mathrm{S(I)}}} \right|_{\mathrm{e}(m)} = 3\mathcal{T}_{ijkn}^{y\mathrm{L}} \kappa_{jk}^{(\mathrm{R})} \left(\alpha_{\mathrm{sh}}\right)_n |\kappa_n| \left(\kappa_n^{(\mathrm{R})} \varepsilon_{xzn}^{\mathrm{S(I)}} - \kappa_n^{(\mathrm{I})} \varepsilon_{xzn}^{\mathrm{S(R)}}\right) + \mathcal{S}_{ink}^{y\mathrm{L}} \varepsilon_{xzk}^{\mathrm{S(I)}}$$

The derivatives of $\left. G_{yi}^{(\mathrm{I})} \right|_{\mathrm{e}(m)}$ are given by

$$\left. \frac{\partial G_{yi}^{(\mathrm{I})}}{\partial \hat{E}_{xn}^{\mathrm{S(R)}}} \right|_{\mathrm{e}(m)} = -3\mathcal{T}_{ijkn}^{y\mathrm{L}} \kappa_{jk}^{(\mathrm{I})} \left(\alpha_{\mathrm{sh}}\right)_n |\kappa_n| \left(\kappa_n^{(\mathrm{R})} \varepsilon_{xxn}^{\mathrm{S(R)}} + \kappa_n^{(\mathrm{I})} \varepsilon_{xxn}^{\mathrm{S(I)}}\right) - \mathcal{S}_{ink}^{y\mathrm{L}} \varepsilon_{xxk}^{\mathrm{S(I)}}$$

$$\left. \frac{\partial G_{yi}^{(\mathrm{I})}}{\partial \hat{E}_{yn}^{\mathrm{S(R)}}} \right|_{\mathrm{e}(m)} = -3\mathcal{T}_{ijkn}^{y\mathrm{L}} \kappa_{jk}^{(\mathrm{I})} \left(\alpha_{\mathrm{sh}}\right)_n |\kappa_n| \left(\kappa_n^{(\mathrm{R})} \varepsilon_{xyn}^{\mathrm{S(R)}} + \kappa_n^{(\mathrm{I})} \varepsilon_{xyn}^{\mathrm{S(I)}}\right) - \mathcal{S}_{ink}^{y\mathrm{L}} \varepsilon_{xyk}^{\mathrm{S(I)}}$$

$$\left. \frac{\partial G_{yi}^{(\mathrm{I})}}{\partial \hat{E}_{zn}^{\mathrm{S(R)}}} \right|_{\mathrm{e}(m)} = -3\mathcal{T}_{ijkn}^{y\mathrm{L}} \kappa_{jk}^{(\mathrm{I})} \left(\alpha_{\mathrm{sh}}\right)_n |\kappa_n| \left(\kappa_n^{(\mathrm{R})} \varepsilon_{xzn}^{\mathrm{S(R)}} + \kappa_n^{(\mathrm{I})} \varepsilon_{xzn}^{\mathrm{S(I)}}\right) - \mathcal{S}_{ink}^{y\mathrm{L}} \varepsilon_{xzk}^{\mathrm{S(I)}}$$

$$\left. \frac{\partial G_{yi}^{(\mathrm{I})}}{\partial \hat{E}_{xn}^{\mathrm{S(I)}}} \right|_{\mathrm{e}(m)} = 3\mathcal{T}_{ijkn}^{y\mathrm{L}} \kappa_{jk}^{(\mathrm{I})} \left(\alpha_{\mathrm{sh}}\right)_n |\kappa_n| \left(\kappa_n^{(\mathrm{R})} \varepsilon_{xxn}^{\mathrm{S(I)}} - \kappa_n^{(\mathrm{I})} \varepsilon_{xxn}^{\mathrm{S(R)}}\right) - \mathcal{S}_{ink}^{y\mathrm{L}} \varepsilon_{xxk}^{\mathrm{S(R)}}$$

$$\left. \frac{\partial G_{yi}^{(\mathrm{I})}}{\partial \hat{E}_{yn}^{\mathrm{S(I)}}} \right|_{\mathrm{e}(m)} = \left[N_i^{\mathrm{S}} N_n^{\mathrm{S}}\right] + 3\mathcal{T}_{ijkn}^{y\mathrm{L}} \kappa_{jk}^{(\mathrm{I})} \left(\alpha_{\mathrm{sh}}\right)_n |\kappa_n| \left(\kappa_n^{(\mathrm{R})} \varepsilon_{xyn}^{\mathrm{S(I)}} - \kappa_n^{(\mathrm{I})} \varepsilon_{xyn}^{\mathrm{S(R)}}\right) - \mathcal{S}_{ink}^{y\mathrm{L}} \varepsilon_{xyk}^{\mathrm{S(R)}}$$

$$\left. \frac{\partial G_{yi}^{(\mathrm{I})}}{\partial \hat{E}_{zn}^{\mathrm{S(I)}}} \right|_{\mathrm{e}(m)} = 3\mathcal{T}_{ijkn}^{y\mathrm{L}} \kappa_{jk}^{(\mathrm{I})} \left(\alpha_{\mathrm{sh}}\right)_n |\kappa_n| \left(\kappa_n^{(\mathrm{R})} \varepsilon_{xzn}^{\mathrm{S(I)}} - \kappa_n^{(\mathrm{I})} \varepsilon_{xzn}^{\mathrm{S(R)}}\right) - \mathcal{S}_{ink}^{y\mathrm{L}} \varepsilon_{xzk}^{\mathrm{S(R)}}$$

Following the same procedure as above, one can obtain the derivative expressions of $\left. G_{zi}^{(\mathrm{R})} \right|_{\mathrm{e}(m)}$ and $\left. G_{zi}^{(\mathrm{I})} \right|_{\mathrm{e}(m)}$ with respect to the solution vector components.

# Bibliography

[1] J.W. Tester, E.M. Drake, M.J. Driscoll, M.W. Golay, and W.A. Peters. *Sustainable Energy: Choosing Among Options*. The MIT Press, 2005.

[2] Statistical Review of World Energy 2010 (pdf)

(see http://www.bp.com/centres/energy/index.asp).

[3] J.W. Tester. Overview of the Energy Supply Portfolio. Class material in Sustainable Energy, 2008.

[4] J.P. Freidberg. *Plasma Physics and Fusion Energy*. Cambridge University Press, 2007.

[5] F.W. Perkins. ICRF heating theory. *IEEE Transactions on Plasma Science* 1984; **12**: 53–63.

[6] J.R. Myra, D.A. D'Ippolito, D.A. Russell, L.A. Berry, E.F. Jaeger, and M.D. Carter. Nonlinear ICRF-plasma interactions. *Nuclear Fusion* 2006; **46**: S455–S468.

[7] J.-M. Noterdaeme and G. Van Oost. The interaction between waves in the ion cyclotron range of frequencies and the plasma boundary. *Plasma Physics and Controlled Fusion* 1993; **35**: 1481–1511.

[8] H.S. Butler and G.S. Kino. Plasma sheath formation by radio-frequency fields. *Physics of Fluids* 1963; **6**: 1346–1355.

[9] F.W. Perkins. Radiofrequency sheaths and impurity generation by ICRF antennas. *Nuclear Fusion* 1989; **29**: 583–592.

[10] R. Van Nieuwenhove and G. Van Oost. Experimental evidence for sheath effects at the ICRF antenna and ensuing changes in the plasma boundary during ICRF on TEXTOR. *Journal of Nuclear Materials* 1989; **162**–**164**: 288–291.

[11] J.R. Myra, D.A. D'Ippolito, and M.J. Gerver. Faraday screen sheaths and impurity production during ion cyclotron heating. *Nuclear Fusion* 1990; **30**: 845–858.

[12] D.A. D'Ippolito, J.R. Myra, M. Bureš, and J. Jacquinot. A model of sheath-driven impurity production by ICRF antennas. *Plasma Physics and Controlled Fusion* 1991; **33**: 607–642.

[13] D.A. D'Ippolito and J.R. Myra. Low-power fast wave antenna loading as a radio-frequency sheath diagnostic. *Physics of Plasmas* 1996; **3**: 420–426.

[14] R. Van Nieuwenhove and G. Van Oost. Experimental study of sheath currents in the scrape-off layer during ICRH on TEXTOR. *Plasma Physics and Controlled Fusion* 1992; **34**: 525–532.

[15] D.A. D'Ippolito, J.R. Myra, J. Jacquinot, and M. Bures. Radio-frequency-sheath-driven edge plasma convection and interaction with the H mode. *Physics of Fluids* 1993; **B5**: 3603–3617.

[16] J.R. Myra, D.A. D'Ippolito, and Y.L. Ho. Three-dimensional analysis of antenna sheaths. *Fusion Engineering and Design* 1996; **31**: 291–312.

[17] J.R. Myra and D.A. D'Ippolito. Scrape-off layer profile modifications by convective cells. *Physics of Plasmas* 1996; **3**: 699–701.

[18] D.A. D'Ippolito, J.R. Myra, J.H. Rogers, K.W. Hill, J.C. Hosea, R. Majeski, G. Schilling, J.R. Wilson, G.R. Hanson, A.C. England, and J.B. Wilgen. Analysis of RF sheath interactions in TFTR. *Nuclear Fusion* 1998; **38**: 1543–1563.

[19] R. Majeski, P.H. Probert, T. Tanaka, D. Diebold, R. Breun, M. Doczy, R. Fonck, N. Hershkowitz, T. Intrator, G. McKee, P. Nonn, J. Pew, and J. Sorensen. The Phaedrus-T antenna system. *Fusion Engineering and Design* 1994; **24**: 159–172.

[20] J.R. Myra, D.A. D'Ippolito, J.A. Rice, and C.S. Hazelton. Radio-frequency sheath mitigation by insulating antenna limiters. *Journal of Nuclear Materials* 1997; **249**: 190–198.

[21] B. Lipschultz, D.A. Pappas, B. LaBombard, J.E. Rice, D. Smith, and S.J. Wukitch. A study of molybdenum influxes and transport in Alcator C-Mod. *Nuclear Fusion* 2001; **41**: 585–596.

[22] S.J. Wukitch, T. Graves, Y. Lin, B. Lipschultz, A. Parisot, M. Reinke, P.T. Bonoli, M. Porkolab, I.H. Hutchinson, E. Marmar, and the Alcator C-Mod Team. Alcator C-Mod ion cyclotron antenna performance. *Proceedings of the 21st IAEA Fusion Energy Conference 2006*; IAEA-CN-149/FT/1–6.

[23] S.J. Wukitch, Y. Lin, B. LaBombard, B. Lipschultz, D. Whyte, and the Alcator C-Mod Team. Ion cyclotron antenna impurity production and real time matching in Alcator C-Mod. *Proceedings of the 22nd IAEA Fusion Energy Conference 2008*; EX/P6–23.

[24] L. Colas, V. Basiuk, B. Beaumont, A. Bécoulet, G. Bosia, S. Brémond, M. Chantant, F. Clairet, A. Ekedahl, E. Faudot, A. Géraud, M. Goniche, S. Heuraux, G.T. Hoang, G. Lombard, L. Millon, R. Mitteau, P. Mollard, K. Vulliez, and the Tore Supra team. Key results of long pulse ICRH operation in Tore Supra. *Nuclear Fusion* 2006; **46**: S500–S513.

[25] T. Hellsten and M. Laxåback. Influence of coupling to spectra of weakly damped eigenmodes in the ion cyclotron range of frequencies on parasitic absorption in rectified radio frequency sheaths. *Physics of Plasmas* 2005; **12**: 032505.

[26] J. Hosea, R.E. Bell, B.P. LeBlanc, C.K. Phillips, G. Taylor, E. Valeo, J.R. Wilson, E.F. Jaeger, P.M. Ryan, J. Wilgen, H. Yuh, F. Levinton, S. Sabbagh, K. Tritz, J. Parker, P.T. Bonoli, R. Harvey, and HSTX Team. High harmonic fast wave heating efficiency enhancement and current drive at longer wavelength on the National Spherical Torus Experiment. *Physics of Plasmas* 2008; **15**: 056104.

[27] J.R. Myra, D.A. D'Ippolito, and M. Bures. Far field sheaths from waves in the ion cyclotron range of frequencies. *Physics of Plasmas* 1994; **1**: 2890–2900.

[28] D.A. D'Ippolito, J.R. Myra, E.F. Jaeger, and L.A. Berry. Far-field sheaths due to fast waves incident on material boundaries. *Physics of Plasmas* 2008; **15**: 102501.

[29] G. Bekefi. *Radiation Processes in Plasmas.* Wiley, 1966.

[30] J.R. Myra, D.A. D'Ippolito, D.W. Forslund, and J.U. Brackbill. Sheath-plasma waves and anomalous loading in ion-Bernstein-wave experiments. *Physical Review Letters* 1991; **66**: 1173–1176.

[31] K. Takayama, H. Ikegami, and S. Miyazaki. Plasma resonance in a radio-frequency probe. *Physical Review Letters* 1960; **5**: 238–240.

[32] R.L. Stenzel. Instability of the sheath-plasma resonance. *Physical Review Letters* 1988; **60**: 704–707.

[33] D.A. D'Ippolito and J.R. Myra. A radio-frequency sheath boundary condition and its effect on slow wave propagation. *Physics of Plasmas* 2006; **13**: 102508.

[34] J.R. Myra and D.A. D'Ippolito. Resonance cone interaction with a self-consistent radio-frequency sheath. *Physical Review Letters* 2008; **101**: 195004.

[35] D.A. D'Ippolito and J.R. Myra. Analytic model of near-field radio-frequency sheaths. I. Tenuous plasma limit. *Physics of Plasmas* 2009; **16**: 022506.

[36] J.R. Myra and D.A. D'Ippolito. Slow-wave propagation and sheath interaction in the ion-cyclotron frequency range. *Plasma Physics and Controlled Fusion* 2010; **52**: 015003.

[37] D.A. D'Ippolito and J.R. Myra. Analytic model of near-field radio-frequency sheaths. II. Full plasma dielectric. *Physics of Plasmas* 2010; **17**: 072508.

[38] M.A. Lieberman. Analytical solution for capacitive RF sheath. *IEEE Transactions on Plasma Science* 1988; **16**: 638–644.

[39] V.A. Godyak. Dynamic model of the electrode sheaths in symmetrically driven rf discharges. *Physical Review A* 1990; **42**: 2299–2312.

[40] E.F. Jaeger, L.A. Berry, J.S. Tolliver, and D.B. Batchelor. Power deposition in high-density inductively coupled plasma tools for semiconductor processing. *Physics of Plasmas* 1995; **2**: 2597–2604.

[41] M.D. Carter, P.M. Ryan, D. Hoffman, W.S. Lee, D. Buchberger, and V. Godyak. Combined rf and transport effects in magnetized capacitive discharges. *Journal of Applied Physics* 2006; **100**: 073305.

[42] R. Maggiora, G. Vecchi, V. Lancellotti, and V. Kyrytsya. Efficient 3D/1D self-consistent integral-equation analysis of ICRH antennae. *Nuclear Fusion* 2004; **44**: 846–868.

[43] V. Lancellotti, D. Milanesio, R. Maggiora, G. Vecchi, and V. Kyrytsya. TOPICA: an accurate and efficient numerical tool for analysis and design of ICRF antennas. *Nuclear Fusion* 2006; **46**: S476–S499.

[44] B. Van Compernolle, R. Maggiora, G. Vecchi, D. Milanesio, and R. Koch. Implementation of sheath effects into TOPICA. *Proceedings of the 35th EPS Conference on Plasma Physics 2008*; **32** (ECA): P–2.105.

[45] F.F. Chen. *Introduction to Plasma Physics and Controlled Fusion* (second edition). Springer, 1984.

[46] T.H. Stix. *Waves in Plasmas*. American Institute of Physics, 1992.

[47] N.S. Krasheninnikova and X. Tang. Equilibrium properties of the plasma sheath with a magnetic field parallel to the wall. *Physics of Plasmas* 2010; **17**: 063508.

[48] J.R. Myra. Electromagnetic sheath boundary condition. Private communication, 2009.

[49] J.R. Myra. Electrostatic sheath boundary condition in curvilinear coordinates. Private communication, 2009.

[50] C.D. Child. Discharge from hot CaO. *Physical Review (Series I)* 1911; **32**: 492–511.

[51] I. Langmuir. The effect of space charge and initial velocities on the potential distribution and thermionic current between parallel plane electrodes. *Physical Review* 1923; **21**: 419–435.

[52] K.J. Bathe. *Finite Element Procedures*. Prentice-Hall, 1996.

[53] K. Appert, T. Hellsten, J. Vaclavik, and L. Villard. Textbook finite element methods applied to linear wave propagation problems involving conversion and absorption. *Computer Physics Communications* 1986; **40**: 73–93.

[54] M. Brambilla. Numerical simulation of ion cyclotron waves in tokamak plasmas. *Plasma Physics and Controlled Fusion* 1999; **41**: 1–34.

[55] A. Fukuyama, S. Murakami, A. Sonoda, and M. Honda. Integrated full wave analysis of RF heating and current drive in toroidal plasmas. *Proceedings of the 21st IAEA Fusion Energy Conference 2006*; IAEA-CN-149/TH/P6–10.

[56] O. Meneghini, S. Shiraiwa, and R. Parker. Full wave simulation of lower hybrid waves in Maxwellian plasma based on the finite element method. *Physics of Plasmas* 2009; **16**: 090701.

[57] W.H. Press, S.A. Teukolsky, W.T. Vetterling, and B.P. Flannery. *Numerical Recipes: The Art of Scientific Computing* (third edition). Cambridge University Press, 2007.

[58] MUltifrontal Massively Parallel Solver (MUMPS 4.9.2) Users' guide, 2009.

[59] M. Brambilla and T. Krucken. Numerical simulation of ion cyclotron heating of hot tokamak plasmas. *Nuclear Fusion* 1988; **28**: 1813–1833.

[60] E.F. Jaeger, L.A. Berry, E. D'Azevedo, D.B. Batchelor, and M.D. Carter. All-orders spectral calculation of radio-frequency heating in two-dimensional toroidal plasmas. *Physics of Plasmas* 2001; **8**: 1573–1583.

[61] J.C. Wright, P.T. Bonoli, M. Brambilla, F. Meo, E. D'Azevedo, D.B. Batchelor, E.F. Jaeger, L.A. Berry, C.K. Phillips, and A. Pletzer. Full wave simulations of fast wave mode conversion and lower hybrid wave propagation in tokamaks. *Physics of Plasmas* 2004; **11**: 2473–2479.

[62] H. Kohno, K.J. Bathe, and J.C. Wright. A finite element procedure for multiscale wave equations with application to plasma waves. *Computers and Structures* 2010; **88**: 87–94.

[63] G.E. Karniadakis and S. Sherwin. *Spectral/hp Element Methods for Computational Fluid Dynamics* (second edition). Oxford University Press, 2005.

[64] S. Gopalakrishnan, A. Chakraborty, and D.R. Mahapatra. *Spectral Finite Element Method.* Springer-Verlag, 2008.

[65] A.N. Beris, R.C. Armstrong, and R.A. Brown. Spectral/finite-element calculations of the flow of a Maxwell fluid between eccentric rotating cylinders. *Journal of Non-Newtonian Fluid Mechanics* 1987; **22**: 129–167.

[66] J. Steppeler. A Galerkin finite element-spectral weather forecast model in hybrid coordinates. *Computers & Mathematics with Applications* 1988; **16**: 23–30.

[67] R.J. Astley. Wave envelope and infinite elements for acoustical radiation. *International Journal for Numerical Methods in Fluids* 1983; **3**: 507–526.

[68] P. Bettess. A simple wave envelope element example. *Communications in Applied Numerical Methods* 1987; **3**: 77–80.

[69] P. Bettess and E. Chadwick. Wave envelope examples for progressive waves. *International Journal for Numerical Methods in Engineering* 1995; **38**: 2487–2508.

[70] V. Avanessian, S.B. Dong, and R. Muki. Forced asymmetric vibrations of an axisymmetric body in contact with an elastic half-space − a global-local finite element approach. *Journal of Sound and Vibration* 1987; **114**: 45–56.

[71] T. Belytschko and Y.Y. Lu. Global-local finite element-spectral-boundary element techniques for failure analysis. *Computers & Structures* 1990; **37**: 133–140.

[72] K.J. Bathe and C. Almeida. A simple and effective pipe elbow element − linear analysis. *Journal of Applied Mechanics* 1980; **47**: 93–100.

[73] E.N. Dvorkin, D. Celentano, A. Cuitino, and G. Gioia. A Vlasov beam element. *Computers & Structures* 1989; **33**: 187–196.

[74] H. Kohno and K.J. Bathe. A flow-condition-based interpolation finite element procedure for triangular grids. *International Journal for Numerical Methods in Fluids* 2006; **51**: 673–699.

[75] B. Banijamali and K.J. Bathe. The CIP method embedded in finite element discretizations of incompressible flows. *International Journal for Numerical Methods in Engineering* 2007; **71**: 66–80.

[76] J.M. Melenk and I. Babuška. The partition of unity finite element method: Basic theory and applications. *Computer Methods in Applied Mechanics and Engineering* 1996; **139**: 289–314.

[77] I. Babuška and J.M. Melenk. The partition of unity method. *International Journal for Numerical Methods in Engineering* 1997; **40**: 727–758.

[78] N. Sukumar, N. Moes, B. Moran, and T. Belytschko. Extended finite element method for three-dimensional crack modelling. *International Journal for Numerical Methods in Engineering* 2000; **48**: 1549–1570.

[79] T.P. Fries and T. Belytschko. The intrinsic XFEM: a method for arbitrary discontinuities without additional unknowns. *International Journal for Numerical Methods in Engineering* 2006; **68**: 1358–1385.

[80] K.J. Bathe (ed.). Computational fluid and solid mechanics. *Proceedings of the Third MIT Conference on Computational Fluid and Solid Mechanics 2005*. Elsevier, 2005.

[81] A. Pletzer, C.K. Phillips, and D.N. Smithe. Gabor wave packet method to solve plasma wave equations. *Proceedings of the 15th Topical Conference on Radio Frequency Power in Plasmas 2003*; **694**: 503–506.

[82] H. Kohno and K.J. Bathe. Insight into the flow-condition-based interpolation finite element approach: solution of steady-state advection-diffusion problems. *International Journal for Numerical Methods in Engineering* 2005; **63**: 197–217.